Quantum size effects in Mg epilayers on Si(111): Enhancement of photoelectron yield and oxidation rate

Von der Fakultät für Physik der Universität Duisburg-Essen
zur Erlangung des akademischen Grades
Dr.rer.nat
genehmigte Dissertation
vorgelegt von

Ulrich Johannes Hagemann
aus
Best / Niederlande

Duisburg, im Juli 2014

Tag der mündlichen Prüfung
28.11.2014
Gutachter
Prof. Dr. Hermann Nienhaus und Prof. Dr. Klaus Schierbaum

Kurzfassung

In dieser Arbeit wurden nicht-adiabatische Effekte bei der Oxidation verschiedener Magnesium- und Siliziumoberflächen untersucht. Dünnschicht-Schottkydioden ermöglichen die Detektion von den, von der Reaktion chemisch angeregten, Elektron-Loch Paaren als Chemoströme und erlauben so die Aufzeichnung der Reaktionskinetik.

Kristalline Mg-Filme von nur wenigen Monolagen (ML) Dicke wurden auf die *p*-dotierte Si(111) 7x7 Rekonstruktion aufgedampft. Die Beschränkung des Elektronensystems auf wenige ML führt zu einer Oszillation der elektronischen Zustandsdichte an der Fermienergie (DOS (E_F)). Diese wurde mit Valenzbandspektroskopie (UPS) gemessen. Hohe Zustandsdichten führen zu einem Anstieg der Reaktionsrate und zu einer Oxidation der zweiten atomaren Lage des Mg, wie mittels Röntgenphotoemissionsspektroskopie (XPS) gezeigt werden konnte. Die niedrige Probentemperatur von 110 K verhindert, bei Proben ohne erhöhte DOS (E_F), eine Tiefenoxidation über die erste Lage hinaus.

Mg-Schichten, die auf Ag/*p*-Si(111) Schottkydioden aufgedampft wurden, zeigen eine starke Abhängigkeit des detektierten Stroms von der Dicke des Silberfilms. Für eine Schichtdicke von 45 nm wird ein Maximum des Stroms detektiert. Dies kann mit dem Effekt der Oberflächenplasmonen gekoppelten Chemoluminiszenz (SPCC) erklärt werden. Die Reaktion von Mg mit O_2 emittiert Photonen, die Oberflächenplasmonen im Silberfilm anregen. Diese zerfallen radiativ an der Ag/Si Grenzfläche und werden im Silizium als Strom detektiert. Eine Simulation der Ag/Si Grenzfläche in der abgeschwächten Totalreflexion Geometrie (ATR) ergibt ein Absorptionsmaximum für die emittierte Strahlung für eine Silberschichtdicke von 46 nm.

Drei verschiedene Siliziumoberflächen wurden elektrisch kontaktiert und dann O_2 ausgesetzt. Die Wasserstoff-passivierte *p*-Si(111) Oberfläche zeigte keine Sauerstoffaufnahme und daher auch keinen Chemostrom durch die Diode. Die reine *p*-Si(111) Oberfläche zeigt hingegen eine Sauerstoffaufnahme. Da jedoch an dieser Oberfläche keine elektrische Leitfähigkeit existiert, kann kein Strom detektiert werden. Da hingegen die Oberfläche der *p*-Si(111) 7x7 Rekonstruktion sowohl elektrisch leitfähig als auch chemisch sehr reaktiv ist, ist für diese Oberfläche ein Strom und Sauerstoffaufnahme nachweisbar. Es kann gezeigt werden, dass dieser Strom ein Verschiebungsstrom ist.

Während der UPS Messungen an kristallinen Mg-Schichten wurde eine starke Lyman α Emission aus der UV-Quelle gefunden, obwohl reines Neon-, Argon- oder Heliumgas verwendet wurden. Diese Lyman α Linie wurden verwendet, um die Anregungsenergieabhängigkeit der Photoelektronenemission des Magnesiumfilms zu untersuchen. Die Erzeugung der Wasserstofflinien kann durch einen quasi-resonanten Energietransfer zwischen den Wasserstoffmolekülen und Edelgasexzimeren erklärt werden.

Abstract

The subject of this thesis are non-adiabatic effects during the oxidation of different magnesium and silicon surfaces. In the chemicurrent setup different Schottky diodes served as high-pass filters to detect highly energetic electron-hole pair excitations as a current through the device. This detection of the current allowed monitoring of the reaction kinetics.

Crystalline Mg films, with a thickness of only a few monolayers (ML), were grown on the *p*-doped Si(111) 7x7 reconstruction, forming thin film Schottky diodes. Quantum size effects as a result of the confinement of the electron system in the z-direction lead to a thickness dependent increase in the oxidation rate of the Mg surface. Valence band photoemission spectroscopy (UPS) measurements indicate that the electronic density of states at the Fermi edge, which oscillates due to the existence of Quantum well states, is the driving force behind this change in reactivity. X-ray photoemission spectroscopy (XPS) reveals that for these highly reactive films, not only the first but also the second atomic layer reacts to MgO. The low sample temperature of 110 K hinders bulk oxidation for samples that do not show quantum size effects.

Thin Mg films that were deposited on Ag/*p*-Si(111) diodes showed current intensities, upon exposure to molecular oxygen, that depend on the Ag film thickness. A maximum in the detected current is found for an Ag layer with a thickness of 45 nm. It was possible to attribute this phenomenon to the effect of surface plasmon coupled chemiluminescence (SPCC). MgO formation emits chemiluminescence photons, which excite surface plasmons in the silver film. These decay radiatively at the Ag/Si interface and are detected as a current. Simulations of this interface in the attenuated total reflection (ATR) geometry reveal a maximum of absorption of the silver film at a thickness of 46 nm.

Oxidation of the hydrogen passivated *p*-Si(111) surface and the depassivated *p*-Si(111) surface do not show a detectable chemicurrent. XPS measurements reveal that, while the former does not react with oxygen, the latter does show oxygen uptake. However, as the surface has virtually no electronic surface conductivity, no current can be measured. The *p*-Si(111) 7x7 reconstruction, which does react with oxygen, has a large enough surface conductivity to allow detection of a chemicurrent. The chemicurrent trace can be interpreted to be a displacement current.

Strong Lyman α emission from the UV-source is found when it is operated with Ar, Ne or He. Combined with the regular noble gas photon lines, this allows the measurement of the total photoyield for thin, crystalline Mg films and investigation of the thickness dependence of the photoemission cross-section. The Lyman α emission can be explained by a resonant energy transfer process between noble gas excimers and hydrogen molecules.

Contents

1. Introduction

1.1. Surface reactivity and quantum size effects

"Surface reactions have an important place in modern technology. At present, 90% of all chemicals are produced via a heterogeneously catalyzed process, where a reaction occurs on the surface of a catalyst. Integrated circuits are made by using a reaction to deposit films on the surface of a semiconductor..." [Mas96].

As Richard Masel points out in his introduction to his book *Chemical kinetics and catalysis* surface reactions play a vital role in a lot of economically important areas. This is also depicted by Figure 1.1, adapted from [McC01]. Areas like fuel production, energy conversion and corrosion strongly depend on the kinetics of surface reactions. Due to this great importance, much effort has been devoted to increase the understanding and to gain control of surface reactivity [McC01, Mas96].

Many different methods, from the fields of photo- and electrochemistry [Anp96, HHV07], have been developed to gain the ability to tune the surface reactivity. A different approach is to gain influence on the substrates electronic structure by controlling the geometric structure. As the valence elec-

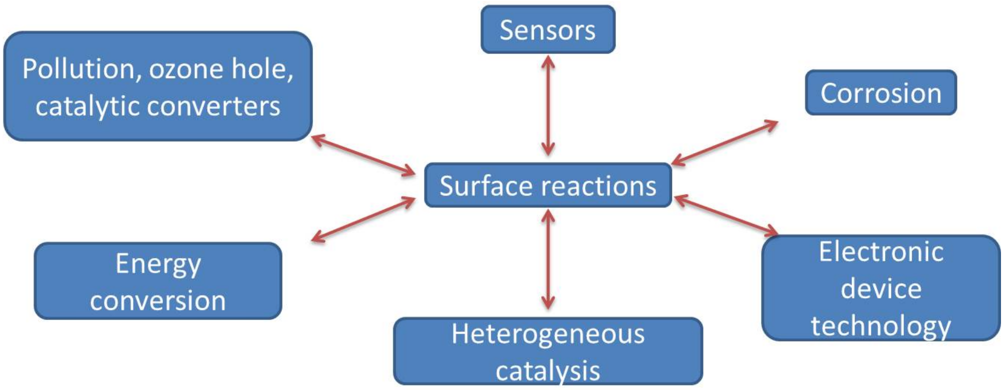

Figure 1.1.: Schematic diagram of the influence of surface reactions in different areas. Adapted from [McC01].

trons of the substrate participate strongly in chemical reactions, the electronic density of states at the Fermi level, (DOS(E_F)), is essential for the reaction rate and reaction kinetics [HL08, Som94]. It is possible to influence the DOS(E_F) by inducing defects or adatoms on the surface [SLG+03, Bel03] or by nanostructuring the surface [Mor01, Ros04]. Preparing ∼nm thin metal films on a substrate effectively confines the electronic system of the metal in the z-direction and leads to the existence of quantum well states which induce a variation in the electronic density of states. This variation changes the reactivity of the metal surface [ABL+04, DCB04, ZZF+08]. With the chemicurrent setup applied in this work it is possible monitor the reaction kinetics *in situ* [Nie02]. Combining this setup with the preparation of thin metal films showing quantum size effects, facilitates the investigation of the interplay of the density of states, reaction rate and reaction kinetics.

1.2. Non-adiabatic effects during chemical reactions at surfaces

Reaction energies of chemical reactions are typically a few electron volts (eV). The possible dissipation channels for this released energy are schematically shown in Figure 1.2. At long time scales, the energy will heat the metal surface via the generation of phonons. Phonons only have energies of ∼ meV and thus multiple phonon excitations have to take place to dissipate all the reaction energy. If this happens in a type of direct energy transfer, the process is called adiabatic, meaning that there is no excitation of the electronic system. This is in contrast to the non-adiabatic pathways, where the energy goes into the electronic system of the surface before heating the lattice through electron-phonon coupling. Non-adiabatic pathways include the excitation of hot electron-hole (e-h) pairs, the emission of exoelectrons into vacuum and the emission of chemiluminescence photons. The energies dissipated in these processes can be up to several eV. Hence, it is possible to transfer the entire released reaction energy in a single step.

Exoemission of electrons has been detected for a multitude of systems and experiments [GA72, Gre97, Nie02, Kri11]. A problem that occurs in exoemission detection is one of intensity. The surface barrier is on the order of a few electron volts (eV) [HG94], which limits the number of electrons that are able to cross. With a suitable device, however, it is possible to detect these e-h pairs inside the metal film. The chemicurrent setup has been established in the 90s to detect this internal exoemission by employing metal-semiconductor contacts, also called Schottky diodes [NBG+99, GNWM01, NBG+00, Nie02]. These diodes have a barrier which is of the order of 0.5 eV for Silicon based diodes [Mön04, SN06]. This is much lower than the surface barrier that needs to be crossed for electron exoemission. As the transmission across the barrier decreases exponentially

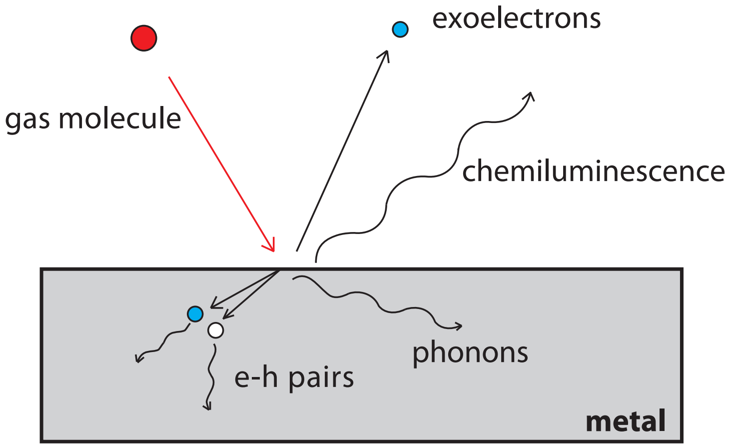

Figure 1.2.: Possible dissipation pathways for the energy released during a exothermic reaction of a gas molecule with a metal surface. The different dissipation channels are the generation of heat in the surface via phonon excitation, which is an adiabatic process. Non-adiabatic pathways include the emission of chemiluminescence photons, the emission of exoelectrons and the excitation of electron-hole pairs in the metal surface.

with the barrier height, the internal detection is orders of magnitude more sensitive than external detection. The energy-space diagram in Figure 1.3 depicts the process of e-h pair detection in the chemicurrent setup. A reactive gas particle, here an O_2 molecule, reacts with the metal surface. This reaction releases energy which can excite the electronic system via the generation of an electron-hole pair. When the metal film thickness is not much larger than the inelastic mean free path of the majority charge carrier, here the hole as the silicon is *p*-doped, the hole can travel ballistically through the metal film towards the Schottky barrier. Only those holes, which have a kinetic energy larger than the Schottky barrier height Φ_p can cross the barrier and be detected as a current through the device.

A drawback of this measurement scheme is the inability to spectroscopically investigate the detected charge carriers with a single device. This is because the barrier height cannot be changed and the detected current represents an integral over all electron energies above the barrier height. One possible solution is the fabrication of metal-insulator-metal (MIM) or metal-insulator-semiconductor (MIS) devices, which give access to spectroscopic data by varying a bias voltage [SDH13, MHDW11, KGK$^+$10]. However these devices are difficult to fabricate with reproducible quality and properties. Furthermore, the influence of the insulating oxide layer is fairly large and impedes the interpretation

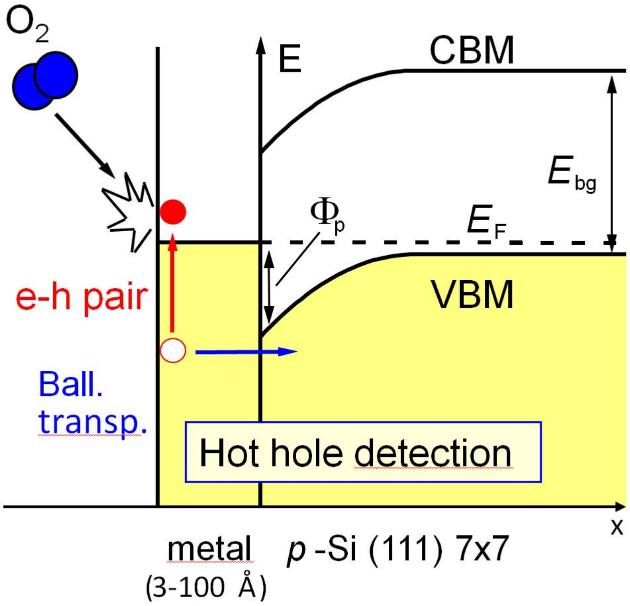

Figure 1.3.: Energy-space diagram for the hot-hole detection of a metal-silicon contact, also called a Schottky diode. A Schottky barrier Φ_p is formed at the metal-Si interface, due to the bending of the valence band maximum and conduction band minimum (VBM and CBM), which serves as a high-pass filter for the majority charge carriers. When a reactive molecule or atom, here O_2, reacts with the metal surface a hot electron-hole pair can be excited. If the excitation energy of the e-h pair is high and the metal film thin enough the majority charge carrier, here the hole as the silicon is *p*-doped, can travel ballistically into the semiconductor. The dashed line gives the Fermi energy E_F, and E_bg denotes the silicon band-gap.

of experimental results.

Another possible method to circumvent this is to change the metal-semiconductor interface by using a different semiconductor surface. This changes the barrier height while it retains the metal surface. But a new device has to be prepared for each barrier height. Nonetheless, this has been done for the oxidation of magnesium films for three different interfaces/barrier heights [NG06]. For this thesis, three additional interfaces were prepared to solidify the spectroscopic description of the hot-charge carrier distribution of this reaction.

Chemiluminescence has also been investigated thoroughly for the oxidation of magnesium and other reactions [Kas74, GA72, GN04, Gla05, Kri11, BKHN13, AG09]. The effect of surface plasmon coupled chemiluminescence (SPCC) on the other hand is a fairly new concept. An object emits photons, due to chemical excitations, which in turn excite surface plasmons in a silver layer. These plasmons decay radiatively and can thus be detected as light [CMA+07, AG09]. Just recently our group has managed to exploit the SPCC effect to greatly enhance the detected current during the chlorination of potassium [BKHN13]. The same method is used here to investigate the oxidation of thin magnesium films on silver/silicon Schottky diodes.

1.3. Thesis Outline

The experimental and theoretical basics are discussed in chapter 2. This covers the theory of Schottky diodes and their application in the chemicurrent setup. Furthermore both the theoretical concepts and experimental evidence for quantum size effects and non-adiabatic effects during oxide growth on magnesium surfaces are presented.

The chapters 3 and 4 demonstrate the experimental setup and measurement techniques as well as the sample preparation scheme that are the basis of the experiments in this work.

The electronic and structural properties of crystalline magnesium films are presented in chapter 5. The latter are determined by low energy electron diffraction (LEED) and photoelectron emission spectroscopy (XPS and UPS). Temperature dependent current-voltage (IV) curves are used to obtain the electronic properties.

The results and analysis of chemicurrent measurements during the oxidation of ML thin, crystalline Mg films are covered in chapter 6. The influence of quantum size effects on the reactivity of the Mg film is revealed.

The subsequent chapter 7 gives the results and interpretation of oxidation of polycrystalline Mg films on Ag/Si Schottky diodes. For this system the SPCC effect enhances the detected current in comparison to previous data on diodes without the intermediate silver layer.

Chapter 8 depicts the oxidation of three different silicon (111) surfaces. A displacement current is detected during the growth of the first ~ 0.2 ML of oxide on the Si(111) 7x7 reconstruction.

Chapter 9 concludes the experimental results of this work by presenting the emission of hydrogen α radiation from a UV-source operated with pure He, Ne or Ar.

The final chapter 10 summarizes the outcome of chapters 6 to 9 and gives an outlook on possible subsequent experiments.

A list of Figures and a list of Tables is given at the end of the thesis, after the bibliography. A list of abbreviations follows this introduction.

AFM	atomic force microscopy
BEEM	ballistic electron emission microscopy
DFT	density functional theory
EELS	electron energy-loss spectroscopy
LEED	low-energy electron diffraction
SEM	scanning electron microscopy
UPS	ultraviolet photoelectron spectroscopy
XPS	x-ray photoelectron spectroscopy
CBM	conduction band minimum
DOS	density of states
E_F	Fermi energy
e-h pair	electron-hole pair
H α	main photoemission line of hydrogen
FE	Fermi edge
FWHM	full width at half maximum
MIGS	metal-induced gap states
ML	monolayer
QWS	quantum well state
SPCC	surface plasmon coupled chemiluminescence
SPP	surface plasmon polariton
SS	surface state
VBM	valence band maximum
UHV	ultra high vacuum

Table 1.1.: List of abbreviations

2. Experimental and theoretical principles

2.1. Schottky diodes

Barrier height and electronegativity concept

The electric properties of metal semiconductor contacts have been investigated extensively in the past. The first description of their rectifying behavior was given by Braun in 1875, who worked with metal sulfide interfaces [Bra75]. Schottky developed the theory to describe this phenomenon in 1939 [Sch39]. Their useful applicability to serve as detectors for hot charge carriers created during chemical reactions at metal surfaces has been demonstrated repeatedly in recent years [NBG$^+$99, Nie02, NG06, HKN10, BKHN13].

A short introduction into the theory on Schottky diodes will be given. A deeper and more detailed insight into the matter can be found in the books of Sze [SN06] and Mönch [Mön04]. The discussion will be for p-doped semiconductors but it can be applied to n-doped substrates as well.

The origin of the rectifying behavior of Schottky contacts can be visualized by a Gedankenexperiment proposed by Mönch [Mön04] and schematically shown in Figure 2.1. The idea is to form a metal semiconductor contact by slowly reducing the distance between the metal and the semiconductor surface until they form an immediate and abrupt interface. When the two surfaces are at infinite distance from each other, their valance and conduction bands are flat, right up to the surface - for surfaces free of surface states. In thermal equilibrium, the work functions of metal ϕ_m and semiconductor ϕ_s are usually not equal, resulting in an electric field E inside the vacuum gap when the distance is reduced. The electric field is given by

$$E = \frac{\phi_\mathrm{m} - \phi_\mathrm{s}}{e_0 a}, \tag{2.1}$$

where a denotes the distance between the two surfaces. This results in a surface charge on both surfaces of opposite sign. The surface charge generates an extended space-charge layer in the semiconductor reaching several nm into the bulk. Screening of electric fields in semiconductors with a dopant concentration of n_b is described by their Debye length $L_\mathrm{D}^2 = \epsilon_b \epsilon_0 k_\mathrm{B} T / e_0^2 n_b$ which is on

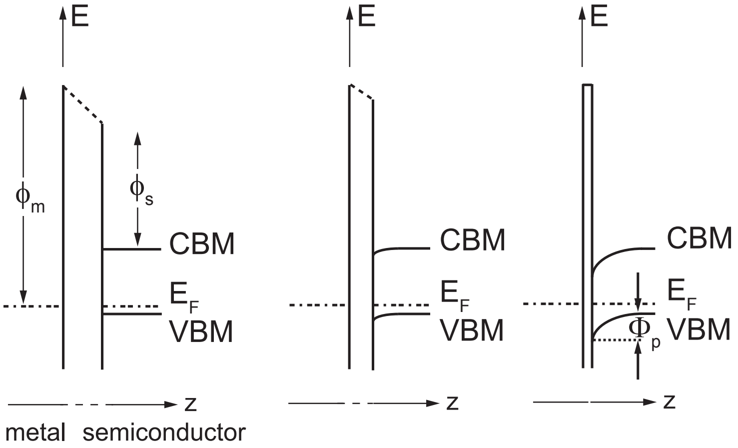

Figure 2.1.: Development of a Schottky barrier when reducing the metal-semiconductor distance. In this picture the interface is assumed to be free of states. Adapted from [Mön04].

the order of 5 to 50 nm for typical semiconductors - $\epsilon_b = 12.5$, 10^{16} cm^{-3} $< n_b <$ 10^{18} cm^{-3}. In the metal, the surface charge is screened much more efficiently within the Thomas-Fermi screening length on the order of inter-atomic distances. This screening length is this small due to the high electron density in metals [Kit66, SN06].

In the case of p-doped semiconductors, the space-charge layer leads to acceptor (hole) depletion at the surface, thus the valence and conductance bands bend downwards. But the major effect on the band bending arises from so-called metal induced gap states (MIGS), which form at the interface [Mön95]. These states are due to the effect of Bloch-like electronic states of the metal decaying into the space-charge region of the semiconductor and resulting in a surface charge Q_{MIGS}. When the abrupt contact is formed, the Fermi energies E_{F} of metal and semiconductor are aligned. Thus, the charge Q_{MIGS} has to be compensated by a surface charge Q_{m} in the metal of same magnitude and opposite sign. It is possible to show that Q_{MIGS} is proportional to the electronegativity difference between metal and semiconductor

$$Q_{\mathrm{MIGS}} \propto \chi_m - \chi_s. \tag{2.2}$$

A rather lengthy calculation yields the homogeneous barrier height Φ_{hom} for the majority charge carriers [Mön95]

$$\Phi_{\mathrm{hom}} = \Phi_{\mathrm{CNL}} + S_{\chi}(\chi_m - \chi_s). \tag{2.3}$$

The charge neutrality level Φ_{CNL}, also called branch-point energy or zero-charge barrier, is the energy where the MIGS are equally valance-like and conductance-like and the charge Q_{MIGS} becomes

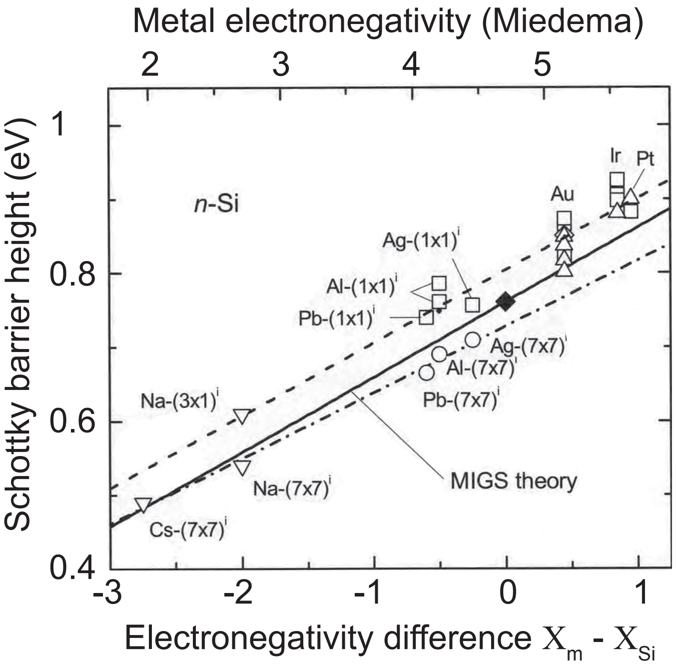

Figure 2.2.: Barrier heights for n-Si Schottky contacts versus the electronegativity difference between the metal and Si. Taken from [Mön04].

zero. Φ_{CNL} as well as the slope parameter S_χ are different for each semiconductor substrate. Figure 2.2 shows the example of n-doped silicon, where the Schottky barrier height is plotted versus the electronegativity difference between metal and semiconductor [Mön04]. The prediction by the MIGS theory is given as a solid line, with Φ_{CNL} as the black diamond. The dashed and dashed-dotted lines represent least-square fits to the data for the unreconstructed (1x1) and reconstructed (7x7) Si interface, showing that the precise geometric and electronic nature of the semiconductor at the interface influences the barrier height. The charge neutrality levels for n- and p-doped semiconductors have to add up to approximately the semiconductor band gap. Thus, from slopes of the fit lines in Figure 2.2, one can deduce for the barrier height for a contact between a metal and p-doped Si(111) 7x7 [Mön04]

$$\Phi_{\mathrm{p}} = 0.43 - 0.089 \cdot (\chi_m - 4.7)\ [eV]. \tag{2.4}$$

For the diodes used in this work, Mg thin films on p-Si(111) 7x7, this equation is valid, as seen later in chapter 5.1.

Thermionic emission theory

The current in Schottky diodes is transported by the majority charge carriers, which means electrons in the case of n- and holes for p-type semiconductors. Several contributions add up to the net current flowing through a metal semiconductor contact [SN06]

- Tunneling current through the barrier is only relevant for large dopant concentrations. The space charge layer, and with that the barrier itself, narrows and electron tunneling through the barrier becomes possible. This is responsible for most ohmic contacts.
- Thermionic emission current across the potential barrier. Dominant for semiconductors like Si or GaAs with a high electron mobility and moderate dopant concentrations - e.g. for Si $n_D < 10^{17}$ cm^{-3}.
- Recombination in the space charge region.
- Injection of electrons/holes and recombination in the neutral region of the semiconductor. Negligible if $\Phi_p > 2 \cdot k_\mathrm{B}T$ [SN06].

For the diodes and the experimental conditions used in this work the thermionic emission is at least an order of magnitude larger than the other effects [SN06]. This is why it will solely be discussed here.

Several assumptions are made to apply this theory. The barrier height Φ_p has to be larger than $k_\mathrm{B}T$. This is easily fulfilled because it is around 0.5 eV for metal Si contacts, see Figure 5.5, and $k_\mathrm{B}T$ is 0.025 eV at room temperature. Furthermore thermal equilibrium is supposed to be established at the surface plane of emission. If a net charge flow should exist it is assumed to have no effect on the thermal equilibrium.

Thermionic emission theory describes the current-voltage relation by the following equation [SN06]

$$I(V,T) = I_0(T) \cdot \left(\mathrm{e}^{-\frac{e_0 V}{k_\mathrm{B}T}} - 1\right) \tag{2.5}$$

$$\text{with } I_0(T) = AA^{**}T^2 \cdot \mathrm{e}^{-\frac{e_0 \Phi_\mathrm{hom}(T)}{k_\mathrm{B}T}} . \tag{2.6}$$

I is the total current through the device, A the active diode area, A^{**} the effective Richardson constant and Φ_hom the homogeneous barrier height of the diode. Equation 2.6 describes an ideal diode and real diodes often poorly resemble this form. Therefore equation 2.6 is modified to the following form [SN06]

$$I(V,T) = I_0(T) \cdot \left(\mathrm{e}^{-\frac{e_0 V - RI(V,T)}{n(T) k_\mathrm{B} T}} - 1 \right) \tag{2.7}$$

$$\text{with } I_0(T) = AA^{**}T^2 \cdot \mathrm{e}^{-\frac{e_0 \Phi_\text{eff}(T)}{k_\mathrm{B} T}} \tag{2.8}$$

using the effective barrier Φ_eff, the serial resistance R and the ideality factor $n(T)$. The higher the influence on the total current of other current contributions is in comparison to the thermionic emission, the larger the $n(T)$ parameter will be. $n(T)$ and Φ_eff can be deduced from a current voltage (IV) curve. Taking the derivative of the logarithm of the current with respect to the current yields the value for n(T) as

$$\frac{1}{n(T)} = \frac{k_\mathrm{B} T}{e_0} \frac{\delta \ln I}{\delta U}. \tag{2.9}$$

The value for the effective barrier height Φ_eff is obtained by extrapolating the current in forward direction to $U = 0$ V. Equation 2.8 then reads

$$\Phi_\text{eff} = \frac{k_\mathrm{B} T}{e_0} \ln \left(\frac{A^{**}T^2}{I_0} \right). \tag{2.10}$$

The serial resistance R in real diodes is responsible for a voltage drop at the device $U_R = I \cdot R$ and is obtained by the maximum current in the linear high voltage regime of a Schottky diode. For the diodes in this work the current I at a voltage of $|U| = 1$ V was chosen for the determination of R. With the parameters n and Φ_eff obtained from the IV measurements, it is possible to determine the homogeneous barrier height from a series of temperature dependent IV curves by plotting the effective barrier heights as a function of the corresponding ideality factor [Mön04]. As was mentioned above, the current is influenced by other contributions than the thermionic emission and those might also show a certain temperature dependence. By recording temperature dependent IV measurements one can single out the effect of thermionic emission on a single diode and determine the homogeneous barrier height Φ_hom [Mön04].

If this temperature data is not available one can do the evaluation for a multitude of diodes of the same structure and interface, preferably at the same temperature. When plotting those $\Phi_\text{eff}(n)$ values one can again extrapolate to Φ_hom. Both methods should yield the same result for the metal semiconductor system. This procedure has been presented by Schmitsdorf *et al* [SKM97, SM99, Mön04] and has been successfully applied for a long time to determine barrier heights of Schottky diodes.

The deviation of real diodes from the ideal form is explained by Tung [Tun91] by the existence of so called low barrier patches, regions of interface inhomogeneities and locally reduced barrier height.

Laterally this patches are smaller than the width of the depletion layer in the semiconductor. Barrier heights can also be determined using other methods like ballistic electron emission microscopy (BEEM), internal photoemission spectroscopy and capacitance voltage (CV) measurements. BEEM is also performed in our group and the resulting barrier height of these measurements agree rather well with the IV method - e.g. for Ag/Si diodes [Ber12].

Photocurrents

Schottky diodes are highly sensitive detectors of infrared radiation and have been used for this purpose since the 1960s, see [SB10] and references therein. A problem arises, when one plans to use these diodes as detectors for very small currents in the pA range in an UHV chamber. Direct light can be omitted by covering all chamber windows and shutting off all light sources inside the UHV. This does however not shield the diode from infrared radiation from the chamber walls. The barrier Φ_{hom} of a Schottky diode filters the low energy part of the Planck distribution that is given by

$$N(E)dE = \frac{8\pi}{h^3c^3}\frac{E^2}{\mathrm{e}^{\frac{E}{k_\mathrm{B}T}}-1}dE. \tag{2.11}$$

The Mg/Si diodes used in this work have a homogeneous barrier height of ~ 0.57 eV and thus detect only photons of the high energy tail far away from the emission maximum. This is shown in Figure 2.3. The Photon number at this photon energy is roughly seven orders of magnitude smaller than in the maximum of the Planck distribution and so the radiation from the chamber walls is small enough to not interfere with the chemicurrents measured during the experiment. The diode is sensitive enough to measure a photovoltage at low temperatures, see left panel in Figure 5.1.

2.2. Chemicurrents

In this work Schottky diodes are used to detect majority charge carrier flow generated by a chemical reaction at the metal surface. Due to its origin in the chemical reaction this charge flow is called chemicurrent [Nie02]. In the following part the discussion will be about holes, which are the majority charge carriers for p-type semiconductors. The discussion is similar for n-doped semiconductors. The principle of chemicurrent detection is depicted in a schematic drawing shown in Figure 2.4. A hole that is excited at the metal-vacuum interface, travels ballistically through the metal film. When the metal film thickness is not much larger than the mean free path of the electron, the electron can reach the metal-semiconductor interface without loosing kinetic energy. If it has a sufficient energy it crosses the Schottky barrier and enters the semiconductor. It is impossible for the hole to tunnel

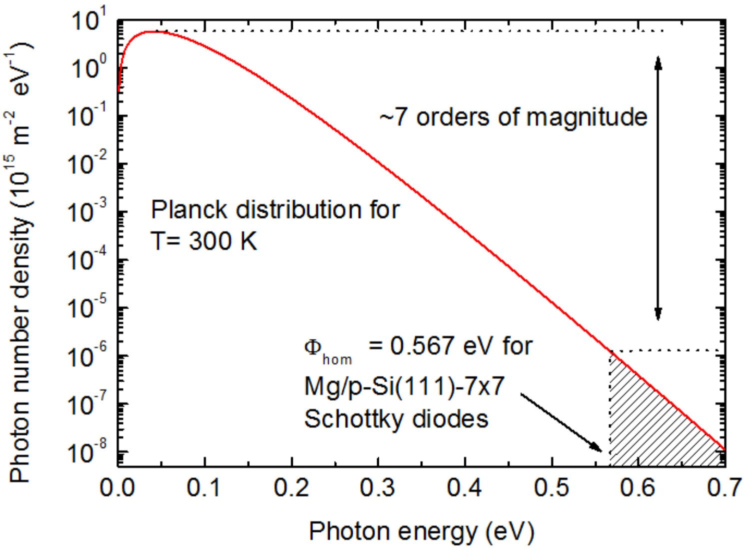

Figure 2.3.: Photon number density plotted as a function of photon energy at a black body temperature of $T = 300$ K. The lower detection limit of Mg/p-Si(111) 7x7 diodes is determined by the homogeneous barrier height of ~ 0.57 eV. The photon number has decreased by 7 orders of magnitude from the maximum.

through the barrier, due to the large width of the depletion layer. As typical chemical reactions are in the order of a few eV and barrier heights on Si are around 0.5 eV the hole is not allowed to loose energy due to inelastic collision if it is to be detected. Thus the principle of detecting electronic excitations is best described by ballistic transport of the holes through the metal film.

The three step model, which has been put forth by Nienhaus [Nie02] is now commonly used to describe the chemicurrent process. It is, in its essence, similar to the four step model of ballistic electron injection used for the description of BEEM measurements given by Bell and Kaiser [KB88]. The efficiency $\alpha(t)$ with which a hole, that is excited at the metal surface can be detected in the semiconductor is determined by three factors:

1. the efficiency $D(\mathbf{k}, t)$ of the chemical reaction to create a charge carrier of a given sufficient energy $E(\mathbf{k}, t)$,
2. the transport of charge carriers through the metal film and their attenuation $A(\mathbf{k}, t)$ and
3. the transport above the barrier given by the crossing probability $T(\mathbf{k}, t)$.

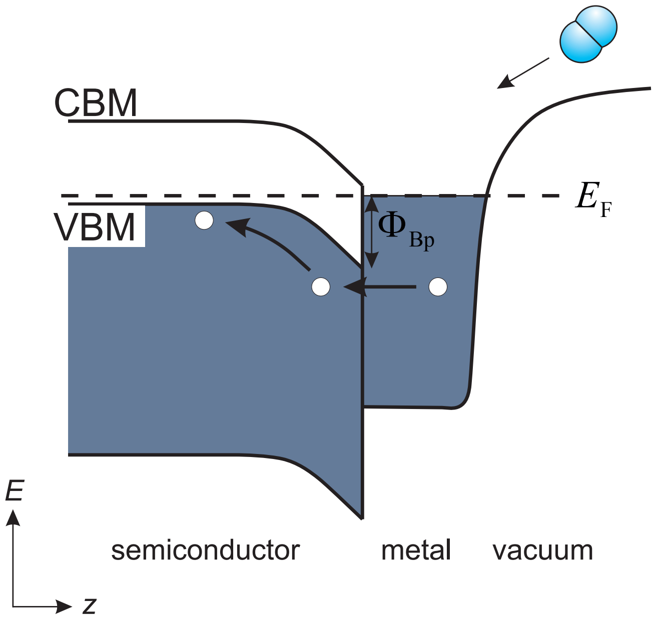

Figure 2.4.: Schematic description of the chemicurrent process. A gas molecule reacts with the metal surface and an electron-hole pair is generated. As the semiconductor is *p*-type the hole travels ballistically across the Schottky barrier and is detected as a current. Adapted from [Kri11, Nie02].

Integration over total k-space yields for $\alpha(t)$

$$\alpha(t) = \int_0^\infty \int_{4\Pi} d\Omega dk D(\mathbf{k},t) A(\mathbf{k},t) T(\mathbf{k},t) P(\mathbf{k},t). \tag{2.12}$$

The factor $P(\mathbf{k},t)$ describes additional contribution to the net current due to recombination, impact ionization and other loss and gain processes in the semiconductor.
This efficiency $\alpha(t)$ determines the chemicurrent I_{cc}

$$I_{\mathrm{cc}} = \alpha(t) e_0 R(t). \tag{2.13}$$

$R(t)$ is the reaction rate. If n-multiple reaction steps are involved the above equation has to be summed over all n.
It is clear from all the above that for an efficient detection the metal film thickness cannot be much larger than the mean-free path length of holes in the film. The attenuation factor $A(\mathbf{k},t)$ from equation 2.12 is given by Beers law and decays exponentially with film thickness d [Bee52, Nie02]

$$A(\mathbf{k},t) \sim \mathrm{e}^{(-\frac{d}{\lambda_m})}. \tag{2.14}$$

λ_m is the attenuation length for the hot charge carriers. If the charge carriers do not travel perpendicular through the film a $\cos(\Theta)$ dependence of the angle between the carriers k-vector and the surface has to be included.

2.3. Quantum size effects

Quantum size effects (QSE) are properties of small crystals and structures that arise from spatial confinement of the electronic system in at least one dimension. Many quantum size effects are attributed to the rise of quantum well states like magic numbers in thin film growth [HWC+03], work function oscillations [LZC07, PWC+02], transport properties [JL75] or changes in surface reactivity [ABL+04]. As electronic devices are miniaturized as much as possible, quantum size effects begin to play an important role in modern physics and are investigated thoroughly.

Quantum well states

These discrete states form when electrons are confined in space by a high potential well. A basic model of a free electron confined in a one-dimensional box - the thin film - is given by T.C. Chiang [Chi00] as a basic idea of the quantum well concept.

Only discrete wave vectors k are allowed for quantum well states, as the standing wave pattern has to fit the geometry of the thin film of thickness d

$$k = \frac{n\pi}{d}, \tag{2.15}$$

where n is a quantum number. The energy values of these states are then given by

$$E = \frac{\hbar^2 k^2}{2m_e} = \frac{\hbar^2}{2m_e}\frac{n\pi}{d}. \tag{2.16}$$

Here m_e is the mass of a free electron. Now one can give the wave function in dependence on the quantum number n as

$$\psi(z) \propto \sin\left(\frac{n\pi z}{d}\right). \tag{2.17}$$

The quantum number n equals the number of maxima of the probability density.

In real solids the electron dispersion will not be simply parabolic, as given in equation 2.16, but show some deviations. But it has been shown previously, and will also be seen from the data in this work that in the case of thin magnesium films the dispersion of the Mg electrons is basically free-electron-like (see chapter 5.3.4).

For the case of thin Mg films the existence, position and form of the quantum well states have been

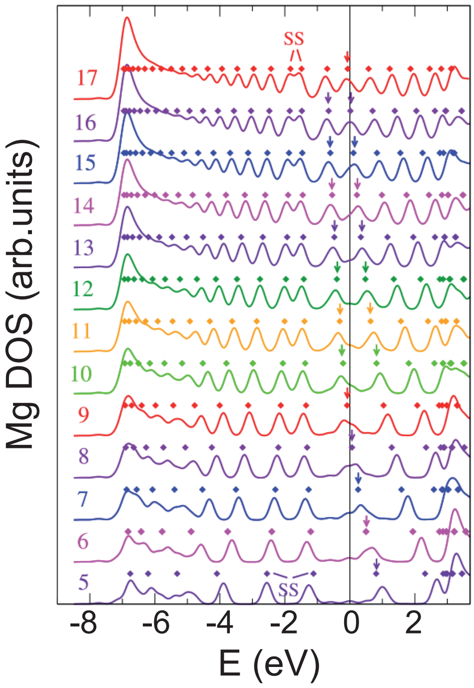

Figure 2.5.: Calculated density of states at Γ of the Mg(0001) surface on W(001). With increasing film thickness, denoted by the numbers on the left, additional states cross the Fermi energy into the valence band. These are called quantum well states. Taken from [BA08].

calculated using density functional theory by Binggeli and Altarelli [BA08]. Their result is given in Figure 2.5, where the electron density of states of monolayer thin magnesium (0001) films on tungsten (001) is plotted versus the binding energy. The important part of this graph is the region of the Fermi edge, where formerly unoccupied states cross into the valence band with increasing film thickness. In this case at around 9 and 16 monolayers film thickness. These two states are the first and second quantum well state of this system.

Similar results are obtained from photoemission experiments - explained in more detail in the following chapters - on thin Mg(0001) films on Si(111) 7x7, see Figure 2.6. Looking again at the region around the Fermi edge, one can see that additional states appear with increasing film size, as long as the film is crystalline. The 8 ML film, black solid line, shows only one QWS and it is close to E_F. For the 17 ML Mg film, red solid line, the first QWS has shifted to roughly 0.75 eV binding energy and a second QWS appears at the Fermi edge. For 24 ML, blue solid line, a third QWS has appeared at the Fermi edge. A polycrystalline film of 10 ML of Mg, green solid line, does not show quantum well states as the confinement of the electronic system is not sufficiently good.

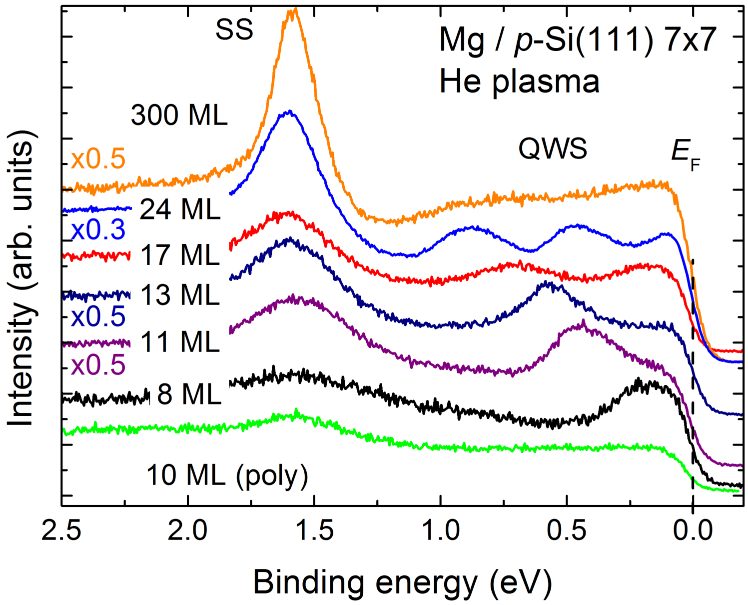

Figure 2.6.: UPS photoemission data of Mg films of different thickness and crystal structure prepared in this work. With increasing film thickness additional states cross the Fermi edge and appear as occupied states in the valence band of the metal. For very high thicknesses, orange solid line, these discrete states form a continuum and are no longer discernible. For a polycrystalline film, green solid line, no quantum well states can be detected.

For very thick films the discrete quantum well states basically form a continuum and are no longer discernible as discrete states, as can be seen in the case of a 300ML film, orange solid line. Just by looking at this graph one can guess another important quantum size effect. The density of states at the Fermi energy is not constant but it changes with film thickness. Every time an additional quantum well state crosses the Fermi energy the DOS (E_F)increases, until the QWS has shifted to higher binding energies. It will be shown later, in chapter 6, that the change in density of states at the Fermi energy is responsible for surprisingly large differences in chemical reactivity between different film thicknesses.

QSE in the reactivity of Mg surfaces

A publication that was of great motivation for this work was written by Aballe *et al* in 2004 [ABL$^+$04]. The authors present their results on the oxidation of crystalline Mg films on the tungsten (110) surface. With low-energy electron microscopy (LEEM) they were able to define the monolayer

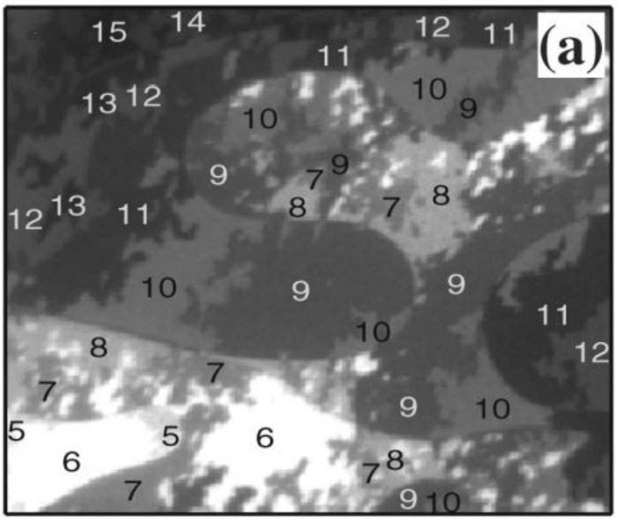

Figure 2.7.: 30 µm^2 image of a Mg film on W(110). The image was recorded at 1.3 eV electron energy and the numbers indicate the number of atomic layers in that area. Taken from [ABL$^+$04].

thickness of their heterogeneous Mg films. In a 30 µm^2 large area it was possible to identify film thicknesses between 7-15 ML, as shown in Figure 2.7. The thickness was determined by observing the change in reflectivity during the growth process. All those different film sizes show well defined quantum well states.

These type of films were oxidized by exposing them to molecular oxygen at a substrate temperature of 50°C. The oxide growth was monitored using x-ray photoelectron emission microscopy (XPEEM) on the different Mg layers. It was found that, at any fixed oxygen exposure, the areas where the Mg film was 7ML thick were oxidized more strongly than other thicknesses, see Figure 2.8.

The upper panel shows the electron density of states at the Fermi edge ($\mathrm{DOS_{EF}}$). It has a maximum at 7ML film thickness and decreases towards higher and lower thicknesses. The reason for this is, that at roughly 7ML a quantum well state crosses the Fermi level into the valence band. This is in slight contrast to the theoretical calculations by Binggeli, where the maximum is at 9 ML.

The lower panel panel gives the relative intensity of the Mg 2p oxide component from XPEEM measurements compared to the total Mg 2p intensity in dependence on film thickness (on the x-axis) and oxygen exposure (different exposures represented by different symbols). For the smallest exposure investigated the difference in the oxidation ratio of the different layers is roughly a factor of 2. With increasing exposures the relative difference in the oxidation level between the different

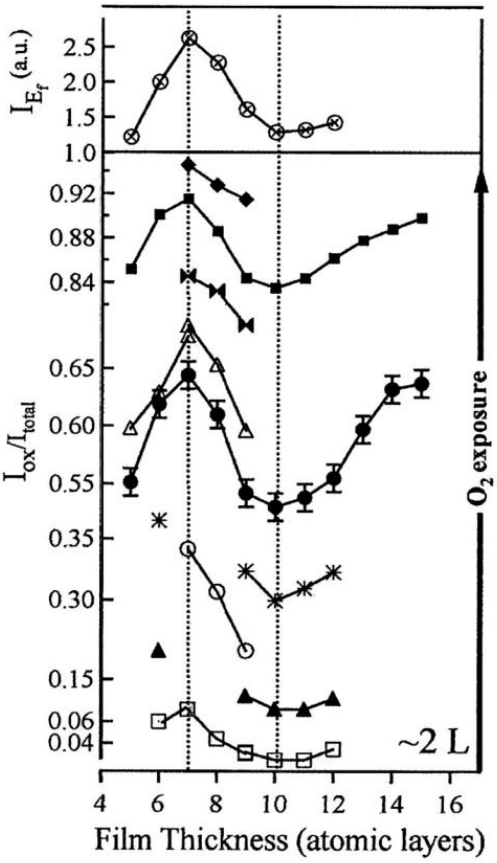

Figure 2.8.: Upper panel: Photoemission intensity at the Fermi edge before oxidation. Lower panel: Relative intensity of the oxide component of the Mg 2p peak versus the layer thickness in ML after different oxygen exposures. The oxygen exposure is increased from bottom to top. Taken from [ABL$^+$04].

thicknesses decreases. The authors argue that the high density of states at the Fermi edge is directly responsible for the increased level of oxidation for the different thicknesses.

With the chemicurrent setup, presented in chapter 3.3, we are able to detect the internal exoemission current generated by the oxidation of Mg. When certain thicknesses show an increased level of oxidation this could possibly be visible in the chemicurrent trace. The chemicurrent might be affected by quantum size effects and the existence of quantum wells. One has to be careful though, as the two experiments do not measures exactly the same quantity. XPEEM measures the resulting chemical phase in the MgO layer after the oxidation is stopped. The chemicurrent measures the reactivity of the surface in situ via the second electron transfer- see chapter 2.5. The detected chemicurrent is the integral over the entire Mg surface. As the surface consists of areas of different film thickness, with one dominating thickness, the ML dependence of the chemicurrent is probably smeared out. This is not the case for the XPEEM experiment, as they measure only on a definite ML thick micro-region.

2.4. Oxide growth: Nucleation and growth model

Metal oxide growth has been studied for a very long time. In this work the nucleation and growth model published by Hudson and Holloway in 1974 will be discussed [HH74]. Their paper is based on work by Avrami [Avr39, Avr40, Avr41] and Johnson and Mehl [JM39]. While Hudson and Holloway applied their description to the oxidation of clean Ni films it was successfully applied to different systems. Our group used it to describe the oxidation of polycrystalline magnesium films [GN04, Gla05] and of polycrystalline aluminum layers [Ger14]. The nucleation and growth model describes the oxide growth of up to 1 ML thickness. The key message is, that oxygen molecules are incorporated into the film only at the edges of oxide islands or at defect sites. They impinge on the surface, diffuse on flat terraces until they hit a step edge and react with the metal atoms there. The model is not applicable to subsurface oxidation or comparable mechanisms. A schematic of the nucleation and growth model is given in Figure 2.9.
Five main assumptions are made for this model [HH74]:

1. physically adsorbed oxygen on the surface has a mean stay time τ_p and a diffusion coefficient D_s.
2. oxygen can only dissociate at perimeter sites, not on flat terraces.
3. the resulting oxide islands are assumed to be circular.
4. τ_p and D_s do not differ between the covered and the free metal surface.
5. Oxide island nucleation is slow compared to total time of oxide formation.

In the next step one has to identify the rate limiting step for oxide growth. If the oxygen impingement rate from the vacuum onto the metal surface is the rate limiting step then the reaction rate would be constant until the surface is completely covered. This is usually - and in this work - not the case.
The growth rate is normally limited by either surface diffusion of the physisorbed oxygen molecule or by the incorporation of the oxygen at the island perimeter sites. For the former case the number

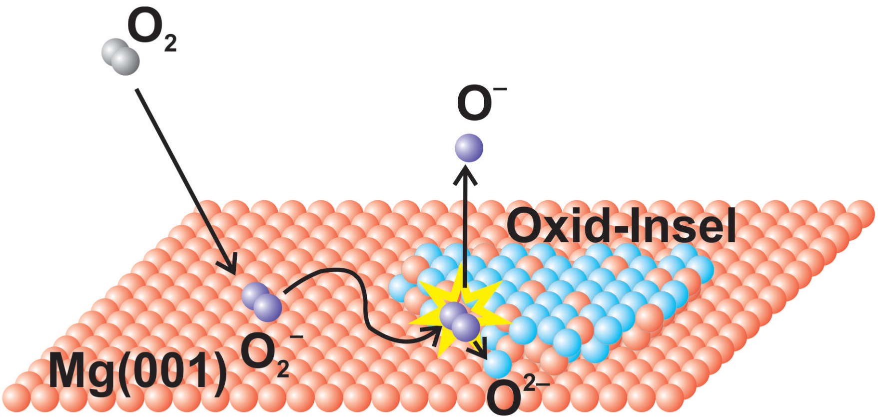

Figure 2.9.: Schematic of the nucleation and growth process. An O_2 molecule impinges on the surface, diffuses there until it hits a island border. There it dissociates, with one oxygen atom forming the MgO bond and the other leaving the surface again or reacting at a different surface site. The minus signs give the charge states of the molecules, corresponding to a first and second electron transfer from the Mg surface to the molecule. The electron transfers will be discussed in section 2.5. This drawing was made by Hermann Nienhaus.

of molecules reaching a perimeter site is determined by the diffusion coefficient and the mean stay time. The latter is dominated by a constant describing the incorporation and also depends on the mean stay time. In either case the coverage Θ at a given time $t > 0$ obeys the following formula [HH74]

$$1 - \Theta = \exp(-K_i N_0 q^2 t^2), \tag{2.18}$$

where N_0 represents the number of nucleation sites at time $t = 0$ s and q is the oxygen flux onto the sample. The K_i factor contains all the given surface factors and thermodynamic properties like the diffusion constant, mean stay time, incorporation constant, vibrational frequencies etc. K_i is assumed to be independent of the time and has the same value for the oxide and the metal surface - see assumption 4 [HH74]. N_0 is the number of nucleation sites existent at time $t = 0$ s, the beginning of oxidation. A preoxidized sample can be described by this model substituting the t^2 factor with a $(t - t_0)^2$. t_0 could then be taken as a measure for the level of the oxygen coverage at $t = 0$ s. q is the oxygen flux onto the sample surface. The time development of the coverage and its derivative are shown in Figure 2.10, as black and red solid lines. The coverage is described by an S-shaped increase. The derivative of the coverage has a distinct maximum at a coverage of 0.4 ML.

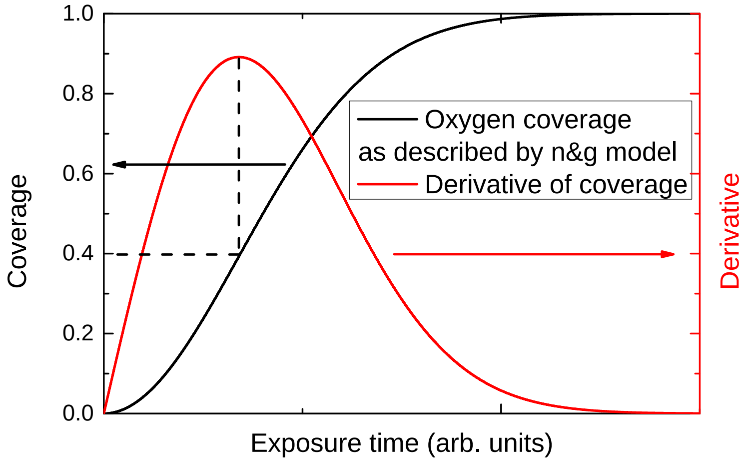

Figure 2.10.: Schematic depicting the time evolution of the nucleation and growth model [HH74]. The maximum of the derivative, which is proportional to the detected current, is found at a coverage of 0.4 ML in the case of constant flux q and K_i. As can be deducted from equation 2.18, the coverage at the maximum of the derivative does not depend on the value of q or K_i, as long as these parameters do not change with time.

As has been mentioned this model was successfully applied to polycrystalline Mg films and the detected chemicurrent traces could be linked to the oxide growth rate. But there was a trend visible, that the more crystalline the metal films were, the less well suited was the nucleation and growth model to describe the detected signal [Gla05]. It will be shown in this work that assumption 4, the indistinguishability of D_s and τ_p between the oxide and the metal surface, seems not to be valid for crystalline films.

To describe the detected chemicurrent traces it has to be assumed that the detected chemicurrent is proportional to the reaction rate. Thus, it is proportional to the derivative of the oxygen coverage. If a large number of oxide islands and defects are present on the surface, the current trace will not start at zero, but at a slightly elevated level, described by the factor t_0,

$$I_{cc} \propto \frac{d\Theta(t)}{dt} = 2K_iN_0q^2(t-t_0)\cdot\exp(-K_iN_0q^2(t-t_0)^2). \tag{2.19}$$

The maximum of the derivative occurs at a oxygen coverage of 0.4 ML, independent of the precise value of K_i or q.

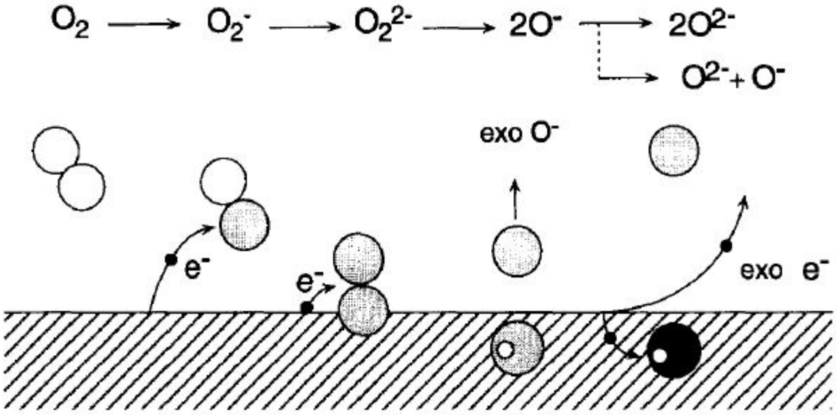

Figure 2.11.: Schematic depicting the proposed harpooning model and the direct dissociation of oxygen molecules at a metal surface. Two electrons transfers to the molecule result in its dissociation and the incorporation of one highly excited oxygen atom into the metal surface. Electron-hole pairs, exoelectrons or chemiluminescence may be generated by this second electron transfer and the deexcitation of the absorbed oxygen atom. Taken from [Gre94].

The derivative becomes more difficult if K_i and/or the oxygen flux are time dependent.

$$\begin{aligned} I_{cc} \propto \exp(-K_i(t-t_0)\ N_0\ q(t-t_0)^2\ (t-t_0)^2)\cdot \\ \Big[2\cdot K_i(t-t_0)\ N_0\ q(t-t_0)^2\ (t-t_0) \\ +\frac{dK_i(t-t_0)}{dt}\ N_0\ q(t-t_0)^2\ (t-t_0)^2 \\ +2\cdot K_i(t-t_0)\ N_0\ \frac{dq(t)}{dt}(t-t_0)^2\Big]. \end{aligned} \tag{2.20}$$

Equation 2.20 is used in chapter 6.3 to describe the chemicurrent traces.

2.5. Harpooning: Model for electron transfer to oxygen molecules at metal surfaces

A theoretical model to describe the non-adiabatic effects of metal surfaces was put forth by Greber and Böttcher [Gre94, GFG+94, Gre97] in the 90s. Figure 2.11 gives the basic idea of the theory. In total two electron transfers are needed to fill the molecule. As the oxygen molecule approaches the metal surface a first electron transfer occurs, which is called harpooning. This takes place relatively far away from the surface and with the molecule moving slowly. The slow velocity allows the electron to tunnel resonantly into the O_2 affinity level.

The singly charged molecule accelerates towards the surface because the charge strongly feels the image force from the surface. The forming O_2^{2-} with the second electron transfer happens much closer to the surface.

O_2^{2-} is highly unstable and the molecule dissociates. One of the ions could leave the surface into vacuum if it obtains enough energy. These ions have been detected in the vacuum, but only in a small fraction [GGM$^+$93]. It is more probable that both ions undergo the last reaction step, only at different surface sites. In this last step the oxygen ion is again accelerated towards the surface and its 2p orbital is rapidly pushed below the Fermi energy of the metal surface. Thus, a highly excited hole state exists on the molecule. It can be deexcited by a resonant charge transfer and the excitation of a hot electron-hole pair in the metal. These electron-hole pairs can be detected using the chemicurrent setup.

Other deexcitation mechanisms, like chemiluminescence or Auger processes, resulting in exoemission of electrons are possible. The existence of the former is shown and discussed in chapter 7. Electron emission into vacuum is not investigated in this work.

2.6. Surface plasmon coupled chemiluminescence

The idea of surface plasmon coupled chemiluminescence (SPCC) is, that chemically induced excited electronic states of a particle couple to surface plasmon modes in a thin metal film. The decay of these modes results in turn in a highly directional and p-polarized light emission from the backside of the material [CMA$^+$07, AG09]. Figure 2.12, taken from [AG09] shows the setup (panel A) of the first SPCC experiment, a Kretschmann-Raether like configuration. A chemiluminescent dye is dispersed on a 10 nm silicon oxide covered 47 nm silver film that is deposited on glass. The glass in turn is placed on a hemispherical prism. A detector measures the angular dependence of light emission for the front side of the sample (free space) and the backside of the prism (SPCC), shown in Panel B. The backside emission is highly directional and p-polarized. The wavelengths of the emitted light is the same for front and backside, see panel C. The effect of SPCC is closely related to the effects of surface plasmon coupled emission (SPCE) and surface plasmon resonance (SPR) [Lak07].

That light can excite surface plasmon was discussed by Raether [Rae88]. The argument for surface plasmon excitation at an ATR (attenuated total reflection) coupler in the Kretschmann, or

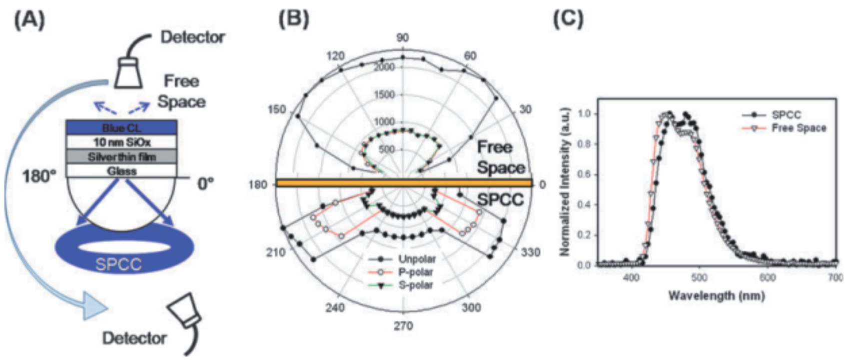

Figure 2.12.: Panel A) Setup of the experiment to detect SPCC from 47nm thick silver films. Panel B) Angular dependence of free space (front-side of sample) and SPCC (backside of prism) emission. Panel C) Wavelength of emitted light. Taken from [AG09].

Kretschmann-Raether - see also Figure 7.10, configuration will be given here. One needs matching of the k-vectors of the light and surface plasmon to have the possibility for surface plasmon excitation by light and vice versa.
The wavevector of light is given by

$$k = \sqrt{\epsilon_i}\frac{\omega}{c} \tag{2.21}$$

where ϵ_i is the dielectric constant of the medium. When light is reflected at a metal/dielectric interface the projection of the momentum onto the metal surface, with ϵ_m the dielectric function of the metal, is described by [Rae88]

$$k_x = \sqrt{\epsilon_m}\frac{\omega}{c}\sin(\theta_0). \tag{2.22}$$

For a surface plasmon the Maxwell equations in the absence of other external forces read [PSCE07],

$$\text{rot}\,\vec{H}_i = \epsilon_i \frac{1}{c}\frac{\delta}{\delta t}\vec{E}_i, \tag{2.23}$$

$$\text{rot}\,\vec{E}_i = -\frac{1}{c}\frac{\delta}{\delta t}\vec{H}_i, \tag{2.24}$$

$$\text{div}\ (\epsilon_i \vec{E} i) = 0, \tag{2.25}$$

$$\text{div}\,\vec{H}_i = 0, \tag{2.26}$$

where the index i denotes the metal $i = m$ and the dielectric sample $i = s$ at both sides of the interface. A wave that propagates along such an interface has to have an electric field component normal to the surface. Thus surface oscillations with an electric field parallel to the interface, s-polarized oscillations, do not exist. The electric and magnetic field of a p-polarized surface oscillation are written as [PSCE07]

$$\vec{E}_i = (E_{i,x}, 0, E_{i,z}) \exp(-\kappa_i |z|) \exp(i(k_i x - \omega t)), \tag{2.27}$$

$$\vec{H}_i = (0, E_{i,y}, 0) \exp(-\kappa_i |z|) \exp(k_i x - \omega t). \tag{2.28}$$

Electric and magnetic fields at the interface have to be continuous as well as the wave vector k, $k = k_m = k_s$. Entering the definitions of the electric and magnetic field into Maxwell's equations and applying the necessity of continuity at the interface yields the dispersion relation of a surface plasmon as

$$k_{\mathrm{sp}}(\omega) = \frac{\omega}{c} \sqrt{\frac{\epsilon_m \epsilon_s}{\epsilon_m + \epsilon_s}}. \tag{2.29}$$

For $\epsilon_m = \epsilon_s = 1$ we again get the same results as for light in vacuum, see equation 2.21. The condition for surface plasmon excitation is thus [PSCE07]

$$\sqrt{\epsilon_m} \frac{\omega}{c} \sin(\theta_0) = \frac{\omega}{c} \sqrt{\frac{\epsilon_m \epsilon_s}{\epsilon_m + \epsilon_s}}. \tag{2.30}$$

This excitation of surface plasmons leads to a minimum in the totally reflected intensity in the ATR geometry [Rae88], see Figure 7.11. In our setup we generate chemiluminescence light by oxidizing a thin Mg film, which is deposited on silver. The chemiluminescence light excites surface plasmons in the silver film, which decay radiatively and are thus detected in our Schottky diode as a current. The intensity of this film is dependent on the thickness of the silver film, as is expected for SPR and SPCC effects [PSCE07].

2.7. Photoyield from metallic surfaces

Absorption of UV-photons at metal surfaces via the excitation of electron-hole pairs can be described within the concept developed by Feibelman [Fei82] and later applied by Liebsch [Lie97] to describe the electron photoyield of a metal surface. Starting from the quasi-static Maxwell equations Feibelman derives the so-called d-parameters $\mathrm{d}_{\|}(\omega)$ and $\mathrm{d}_{\perp}(\omega)$. They specify the normal and parallel components of the integrated surface polarization - equations 4.64 and 4.65 in [Lie97]. As the intensity of the photoyield depends only on $\mathrm{d}_{\perp}(\omega)$ and not on $\mathrm{d}_{\|}(\omega)$ [Lie97], the latter will not be discussed here in detail. $\mathrm{d}_{\perp}(\omega)$ is the centroid of the charge density induced by an external photon field [Fei82, Lie97].

The surface polarization induced by an external electric field, e.g. emission from a UV-light source, at a metal surface is illustrated in Figure 2.13, taken and calculated by Liebsch [Lie97]. The dashed line gives the classical picture, where $\mathrm{d}_{\|}(\omega) = \mathrm{d}_{\perp}(\omega) = 0$. While this is just a step function with a

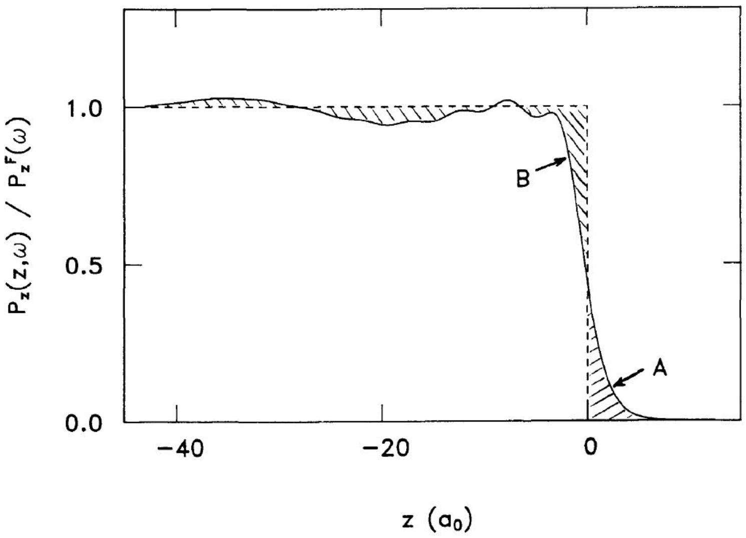

Figure 2.13.: Schematic illustration of polarization $P_z(\omega)$ near a metal surface induced by an external field. The dashed curve implies the classic picture. $\mathrm{d}_\perp\omega$ is determined by the difference between the areas A and B [Lie97]. Taken from [Lie97].

constant polarization up to the metal surface at $z = 0$ and a polarization of zero in vacuum. The result of the microscopic picture is given by the solid line. The difference between the classical and non-classical description is largest immediately at the interface. If one looks closely the polarization at the metal surface is not exactly 1/2, but slightly smaller. One of the features of the microscopic description is the displacement of the effective location of the surface [Lie97]. $\mathrm{d}_\perp(\omega)$ is determined by the difference between the ruled areas A and B [Lie97] and is a complex quantity.
The dependency of the real and imaginary parts of $\mathrm{d}_\perp(\omega)$ on the light frequency ω for a semi-infinite jellium surface is given in Figure 2.14. The Imaginary part reaches it maximum at a frequency around $\omega = 0.8 \cdot \omega_\mathrm{p}$, where ω_p is the bulk plasmon frequency of the semi-infinite system. At the same frequency the real part is zero. The photoyield $\Upsilon(\omega)$ is given by Liebsch as

$$\Upsilon(\omega) = 2\sqrt{2}\,\frac{\omega}{c}\left(1 - \frac{\omega^2}{{\omega_\mathrm{p}}^2}\right)\mathrm{Im}\ d_\perp(\omega) \tag{2.31}$$

Due to its dependence on Im $\mathrm{d}_\perp(\omega)$, the photoyield is largest at an incident photon frequency of 0.8 times the bulk plasmon frequency, according to Figure 2.14. It also vanishes when the photon frequency ω equals that of the bulk plasmon ω_p. However, this is only true as long as the film is not too thin. For thin films the centroid of the induced charge density changes with film thickness and leads to a thickness dependence of the photoyield. This, in fact, leads to a photoyield maximum at

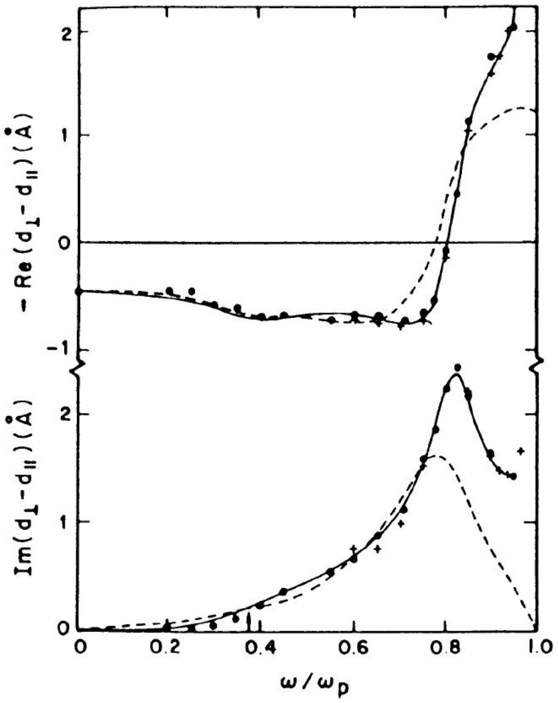

Figure 2.14.: Frequency dependence of the real and imaginary parts of $\mathrm{d}_{\perp}(\omega)$ [Lie97].

the bulk plasmon frequency [Lie97, ARH02b, BSH^{+}01].

This is illustrated by theoretical calculations, left panel of Figure 2.15, and experiments, right panel in Figure 2.15. The left panel shows the calculated value of the centroid of the charge density induced by an external field $\mathrm{d}_{\perp}(\omega)$ in dependence on the frequency of the photon field. The system consists of a thin Na overlayer (0.25 ML to 2 ML) on Al. The dotted lines denote the results for realistic Na layers, the solid lines those for jellium-like overlayers. The value of $\mathrm{d}_{\perp}(\omega)$ changes dramatically with film thickness. For the two maxima at a coverage of $\Theta = 2$ ML the photon frequency is close to that of the bulk and surface plasmon of the Na, at 5.9 eV and 4.8 eV respectively. With increasing film thickness further, the contribution of the bulk plasmon vanishes, as shown by experiment [BH99, BBH04] and theoretically by equation 2.31.

The right panel in Figure 2.15 gives the results of constant initial state measurements of the photoyield from a 11 ML thin Mg film on a Si(111) 7x7 substrate in dependence of the incident photon energy. At photon energies above the Mg bulk plasmon energy of $\hbar\omega_{\mathrm{p}} = 10.7$ eV, see chapter 5.3.3, no photoyield is detected. For photon energies $\leq \hbar\omega_{\mathrm{p}}$ two maxima, labeled ω_{p} and ω_{m}, are found. Their energetic positions correspond to energies close to the bulk plasmon and surface multipole

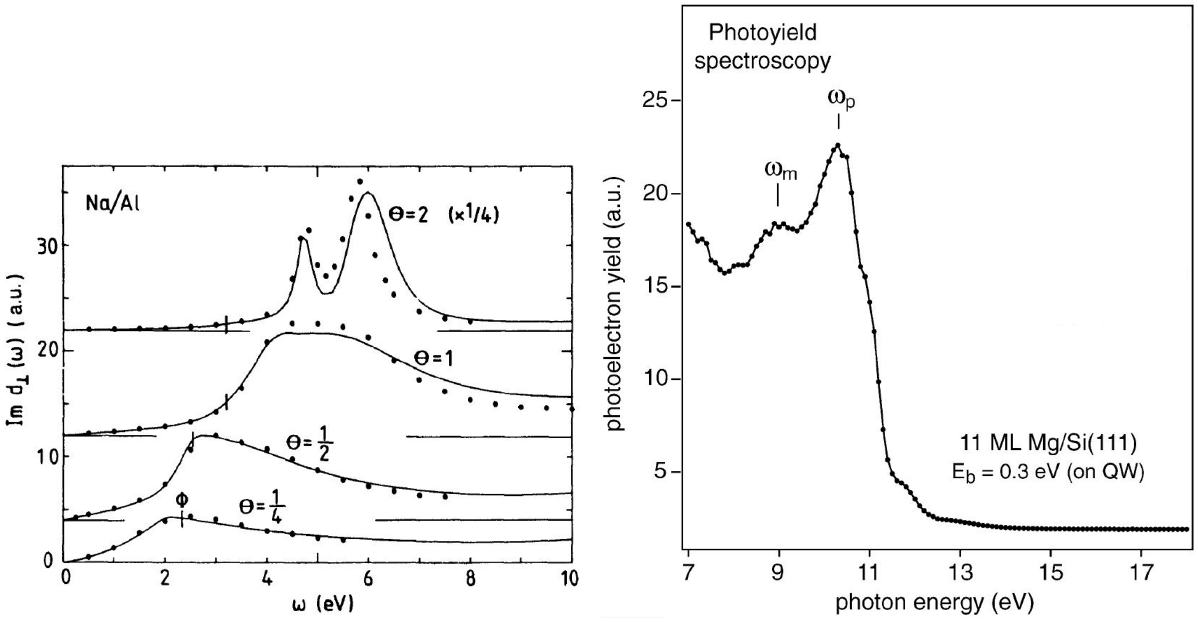

Figure 2.15.: Left panel: Calculated values for $\mathrm{d}_\perp(\omega)$ in dependence on photon frequency and coverage of a Na covered Al surface. The dotted and solid lines give the result for realistic and jellium overlayers, respectively. The dot-dashed line in the bottommost panel gives the image density of the uncovered surface [Lie97, IL90]. Θ gives the overlayer coverage in ML. Right panel: Constant initial state measurements of the photoyield from a 11 ML thin Mg film on Si using UV-light [ARH02b].

plasmon energies. This experiment proves that for ultrathin, crystalline Mg films on Si the photoyield, and with that the centroid of the induced charge density Im $\mathrm{d}_\perp(\omega)$, is largest close to the bulk plasmon energy. For thick Mg layers it is predicted to be close to the surface plasmon energy by equation 2.31. This has been shown in experiments, e.g. for aluminum bulk crystals [LPF79]. The transition from the thin to thick film regime, from the photoyield maximum being at ω_p to it being close to ω_m, has not been measured or calculated before.

3. Experimental Setup

3.1. Ultra high vacuum system

The UHV system, in which most of the experiments for this work have been performed, consists of two large chambers called the analysis chamber and the preparation chamber. A third smaller chamber is used as a quick load-lock system. Each chamber can be vented separately without affecting the pressure in the others. The preparation chamber was pumped by an ion getter pump. The analysis chamber was pumped by a turbomolecular pump (TMP). Both chambers had base pressure of below $2 \cdot 10^{-10}$ mbar. The load-lock system was pumped by a TMP, backed by a membrane pump. A sorption pump was used to quickly evacuate the load-lock system after insertion of a sample.

This work was started at a different vacuum system, very alike in set-up and usage. The main difference was the lower quality of the hemispherical analyzer. It was there that the low energy electron diffraction (short LEED) images were recorded. This system was presented previously in detail [HKN10, Hag09]. It was used for the measurements in chapters 7 and 8.

3.1.1. Preparation chamber

The preparation chamber was used for metal film deposition and chemicurrent measurements. The sample could be positioned in two different positions inside the chamber. In the first one, which is on the main manipulator, the sample can be cooled down to 120 K by a liquid nitrogen cryostat and heated to about 500 K using a ceramic heat plate. A pivoted mechanism allows the electrical connection to the metal film to perform current-voltage or chemicurrent measurements.

In this position the metal films are deposited onto the sample. To this end, a Knudsen-cell type evaporator is installed in the chamber, equipped with a shutter to shut off the atom beam. Metals available for deposition included gold, silver, magnesium and lead. The atom flux from the evaporator can be determined by a quartz micro-balance, which can be moved into the molecular beam.

The second sample position allows flashing the sample up to 1400 K via electronic heating to produce the 7x7 reconstruction of the Si(111) surface.

Although this chamber is called the preparation chamber, there are also some means of analysis available. In this position it is possible with the use of a cylindrical mirror analyzer (CMA) with an integrated electron gun to perform auger electron spectroscopy (AES) as well as electron energy loss spectroscopy (EELS) to check the cleanliness of the samples and metal films. AES and EELS have not been performed with the CMA in this work, but rather in the analysis chamber using an electron gun and hemispherical analyzer.

A quadrupole mass spectrometer allows analysis of the residual gases in the chamber. The pressure is measured by an uncalibrated Bayard-Alpert hot filament gauge and a cold cathode gauge.

A high precision dosing valve, which leads to a small gas inlet system, can be opened to fill the chamber with different gases. In this work only molecular oxygen was used.

3.1.2. Analysis chamber

This chamber contains most of the analysis tools used in this work. A Phoibos 100 hemispherical analyzer with multi-channel detection by SPECS is used to detect electrons emitted from the sample. A XR 50 dual anode x-ray source and a UVS-10/35 ultraviolet- (UV-) photon source by SPECS are available for chemical analysis of the sample and it can be switched between the two sources within a minute.

In this work the Al Kα line at 1486.5 eV and the Mg Kα at 1256.3 eV were used for XPS. All available UV-photon energies are given in table 4.1 in chapter 4.

The UV lamp is pumped by a turbomolecular pump backed by a rotary vane pump. To minimize the contamination of the gas inlet system whenever the gas bottle is switched, the inlet system is repeatedly purged with the new gas and pumped by a rotary vane pump, before the high precision valve to the UV source is opened. Also the inlet system is constantly kept under noble gas atmosphere when not in use. This does not avoid completely any water contamination and thus a tiny increase in the O_2 signal in the UPS is sometimes visible after a new gas bottle was installed.

During the last few months of the experimental work to this thesis a EKF 1000 electron source by Omicron was installed into the chamber, with an energy range between 0.1 and 5 keV. This gun was used for the EELS measurements.

The sample position in the chamber can be altered using a manipulator and the sample can also be cooled down to around 125K. Unless otherwise stated all XPS and UPS measurements in this work were recorded at room temperature.

The pressure in the main chamber is measured by a uncalibrated Bayard-Alpert hot filament gauge and a cold cathode gauge.
The hemispherical analyzer of the second UHV system, in which the experiments presented in chapters 7 and 8 were done, is a well-used HA 150 by VSW. Its transmission and resolution are not as good as for the Phoibos 100 and so the spectra shown in this work have a lower resolution and signal intensity.

3.2. Sample preparation

The semiconducting substrates used in this work were mainly one side polished, Boron doped p-Si(111) samples with a resistivity of 7.5 Ωcm, a thickness of 0.508 mm and a maximum miss-cut of 0.35°. The Si surface was protected by a thick oxide layer, which was removed prior to insertion of the samples into UHV by dipping the samples in buffered hydrofluoric acid. The backside of the samples was highly doped with Boron to achieve an ohmic back-contact. The backside doping and the slicing of the wafer into 12x10 mm pieces was done at the Fraunhofer Group for Microelectronics in Duisburg. The depth profiles of the backside doping is given in the appendix C.

Wetchemical etching The first step of cleaning the Si pieces was to immerse them in ultra-pure water and manually stir them for a few minutes with the aim of removing small dust particles from the surface. For the samples used it was impossible to put them into an ultrasonic bath, because small pieces of Si tended to sliver off the sample edges, due to a non-perfect slicing of the wafer.
The samples were then taken out of the water, blown dry with Argon gas and put into VLSI grade Isopropanol for a few minutes to remove any organic compounds on the Si. The samples were again blown dry with Argon, immersed in water again to remove any residual Isopropanol.
After drying the samples yet again, they are put into buffered HF for 3 minutes. This effectively removes the silicon oxide and terminates the free dangling-bonds of the Si surface with hydrogen [Mön95]. Because this step of the cleaning process was done beneath an extractor hood in a regular lab, one was able to see the amount of dust particles in the acid increasing within a minute. That was the reason why the Teflon dish was twice emptied almost completely after 60 seconds each and refilled with fresh buffered HF. The sample stayed completely immersed in the acid during this process. The buffered HF consists of 34.8% ammonium fluoride and 6.5% hydrofluoric acid in aqueous solution.

UHV preparation The samples were put onto the sample holder and into the load-lock chamber. This was the only time, where the sample was not covered or in a clean environment, before it is being put into vacuum. For the 2 m distance between the Flow-box and the load-lock chamber, the samples were carried upside down, to minimize the amount of dust on the substrate. Within 10 minutes of taking the samples out of the HF they were inserted into vacuum.

In UHV the samples were put into the flasher position. A lot of different flashing procedures have been tested to achieve the Si(111) 7x7 reconstruction. The best, in respect to the magnesium surface state quality, cleanliness of the surface and electronic properties of the diode, and the procedure which was used in this work, was to heat the sample to 610°C and leave it there till the pressure has dropped to below 10^{-8} mbar again. The pressure rise was mostly due to water that had attached itself to the sample holder and clips while being out of vacuum and the desorption of the hydrogen termination on the Si surface.

Then the sample was flashed to 730°C repeatedly for 5 seconds each, with a minimum of 15 seconds cooldown time in between. If the pressure rose above $7 \cdot 10^{-8}$ mbar during the first step the flashing was stopped. It was resumed after the pressure dropped below 10^{-8} mbar again. The sample temperature was measured with a pyrometer calibrated for silicon. As it could not measure temperatures below 600°C we calibrated the flasher once with a thermocouple (TC) welded to a thin molybdenum plate for lower temperatures. The TC and the pyrometer showed basically the same temperatures for $T > 600°\text{C}$. Figure 3.1 is a screenshot of the LabView program controlling the flashing process. It shows the set (red) and measured (white) temperatures of the silicon substrate during three flashing steps.

As the current at the sample is measured as well, one can use the flasher without the pyrometer and use the current as the control parameter. This is necessary if one wants to heat to temperatures below 600°C.

The sample was transferred onto the manipulator and cooled down to below 120 K. If magnesium was to be evaporated onto the substrate it was done with the use of a 7x8 mm^2 shadow mask. The evaporation temperature of the Mg cell was 288°C for most experiments, to minimize oxygen pollution on the sample. 288°C is the equivalent to an evaporation rate of about 0.22 nm/min or 0.81 ML/min. After evaporation the sample was usually moved to the analysis chamber for chemical investigation. As it was not cooled during those measurements it was annealed to room temperature in this process. For chemicurrent (cc) and current voltage (IV) measurements the sample was transferred back into the preparation chamber, where it was cooled back down to liquid nitrogen temperatures and electrically contacted by a pivoted gold ball.

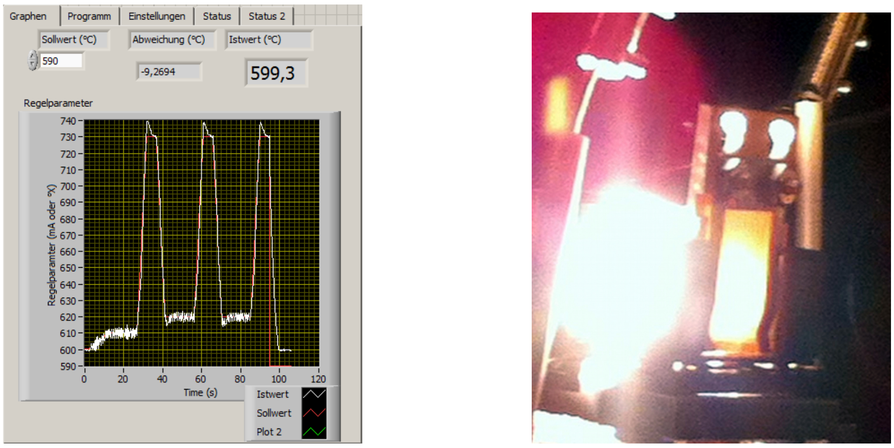

Sollwert (°C) 590

Abweichung (°C) -9,2694

Istwert (°C) 599,3

Figure 3.1.: Left panel: Screenshot of the LabView flashing program. It shows the temperature of the Si substrate during flashing. Right panel: Photograph of the sample during flashing. The color of the substrate is homogeneous for large areas of the sample.

3.3. Sample holder and electrical setup

Sample holder The sample holder is shown in the left panel in Figure 3.2. The sample holder itself, the windings and the nuts are made of niobium. The clip holding the sample in place is made of molybdenum. Between the sample holder and the clip is an aluminum oxide piece, which is shown at the top of the photograph. The same is the case between the clip and the nuts. In this way the Si front-side does not have an electrical contact to the sample holder. This is important, as the Si(111) 7x7 surface is conducting [HST$^+$03] and one has to take precaution not to get a short-circuit. For each sample the resistance between the Mo clip and the Nb holder was measured prior to insertion into UHV to avoid electrical contact between the two. In a newer version the Mo clip looks slightly different to avoid contact to the windings and the main body.

Electrical setup For the chemicurrent and current/voltage measurements the metal film was contacted with a pivoted gold contact. A schematic of the setup is shown in the right panel of Figure 3.2. The copper part on the left is attached, thermally connected, but electrically isolated, to the liquid nitrogen cooling in the chamber. With the screw on the right the stainless steel glider was used to firmly press the sample holder onto the cooled copper. The copper is thermally connected

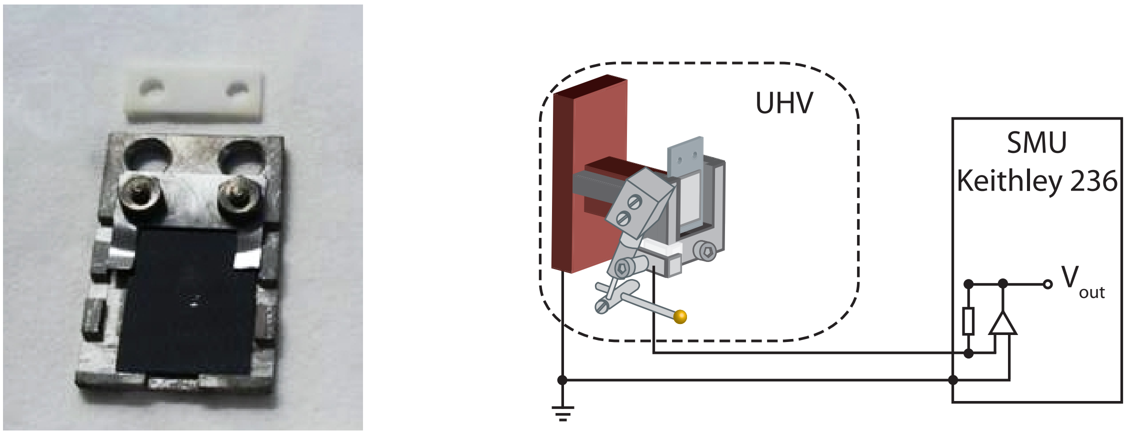

Figure 3.2.: Left: Photograph of the sample holder. The sample holder, winding and nuts are made of niobium. The clip is molybdenum and the ceramic is Al_2O_3. Right: Schematic of the electrical setup for the chemicurrent and IV measurements. Adapted from [Kri11].

to the liquid nitrogen tank. Fixed to the copper part, close to the front side, is the thermocouple for determination of the sample temperature. The stainless steel part holding the gold ball is again electrically isolated to the glider. Attached to the gold ball part is an unshielded cable leading to an electrical feed-through. In air a coax cable leads to the source measure unit (SMU) 236 by Keithley, that was used for all IV and CC measurements. The gold contact is called the front contact.
Another cable wiring of the same type leads from the copper to the SMU. This is called the back contact. In all measurements this contact was kept on earth potential, unless otherwise stated. For IV measurements the voltage was applied to the front contact, during CC measurements it was kept at zero bias.

3.4. Oxidation experiments

For the detection of chemicurrents during chemical reactions the diodes are electrically connected as described above. There are different ways of exposing the diode to the reactive gas. In this work, all experiments were performed by filling the chamber with clean molecular oxygen through a high precision leak valve. Usually the base pressure after preparation was in the range of a few 10^{-10} mbar. By opening the valve the chamber is flooded with O_2 up to pressures around $3 \cdot 10^{-8}$ mbar. As the sample does not face the leak valve one can describe the O_2 flux using kinetic gas theory. The impingement rate of thermal gases is then given by [Jou12]

$$z_\mathrm{F} = \frac{n\bar{c}}{4}. \tag{3.1}$$

Here $\bar{c} = \sqrt{\frac{8k_\mathrm{B}T}{\pi m_g}}$ is the average velocity of the particles and $n = \frac{p}{k_\mathrm{B}T}$ the oxygen density [Jou12]. As the oxygen partial pressure in the chamber is dominating by at least one order of magnitude it is valid to use the total chamber pressure as the value for p in this equation. With the particle temperature $T = 295$ K and mass $m_g = 32$ amu we get

$$z_\mathrm{F} = 2.67 \cdot 10^{24} \cdot p[\mathrm{mbar}] \frac{1}{m^2 s}.$$

Typical values in this work are $p = 3 \cdot 10^{-8}$ mbar and $\mathrm{A_{Mg}} = 0.56 \cdot 10^{-4}$ m^2. For these parameters the total $\mathrm{O_2}$ flux onto the Mg film per second is

$$q_{\mathrm{O_2}} = 4.49 \cdot 10^{12} \frac{\mathrm{O_2}}{s}.$$

4. Experimental Techniques

4.1. Photoemission spectroscopy

The effect of photoemission was first measured by Hertz in the 1880s [Her87] and further investigated by Lenard and Einstein [Len00, Len02, Ein05]. These first experiments allowed to measure the work function ϕ_{m} of metals by detecting the kinetic energy of emitted electrons under the influence of monochromatic light with $E = h\nu$. They found that the maximum kinetic energy of electrons emitted from a metal is dependent on the frequency of the light and is given by

$$E_{kin,max} = h\nu - \phi_{\mathrm{m}}. \tag{4.1}$$

The development of photoemission spectroscopy (PES) using x-rays (XPS) by Siegbahn and coworkers in the 1960s [SNS58, NSS57] opened the door to a wide range of applications and was awarded the Nobel Prize for Physics in 1981 [Sie81]. This technique, called Electron Spectroscopy for Chemical Analysis by Siegbahn (ESCA), allows the characterization of the surface composition, the chemical state of adsorbates and of reaction products. Using ultraviolet light (UPS) one can determine the atomic or molecular energy levels in the valence region close to the Fermi energy with high precision. Photoemission spectroscopy is usually softly divided into three energy regimes, the ultraviolet (5 - 100 eV), soft x-ray (100 - 1000 eV) and the x-ray regime ($>$ 1000 eV). Photoemission spectroscopy is highly surface sensitive. This is determined by the mean free path (or escape depth) of electrons in elements. This has been studied in great detail and a universal curve, with data for all elements, is shown in Figure 4.1 taken from [Lüt10]. This curve shows that for electrons with a kinetic energy in the ultraviolet the escape depth is between 2 and 5 Å. For electrons directly excited by x-rays this value increases to about 10 to 20 Å.

Only a brief introduction into this technique will be given in this work. For a more detailed view on photoelectron spectroscopy the textbook 'Photoelectron Spectroscopy' by Hüfner is recommended [Hüf03].

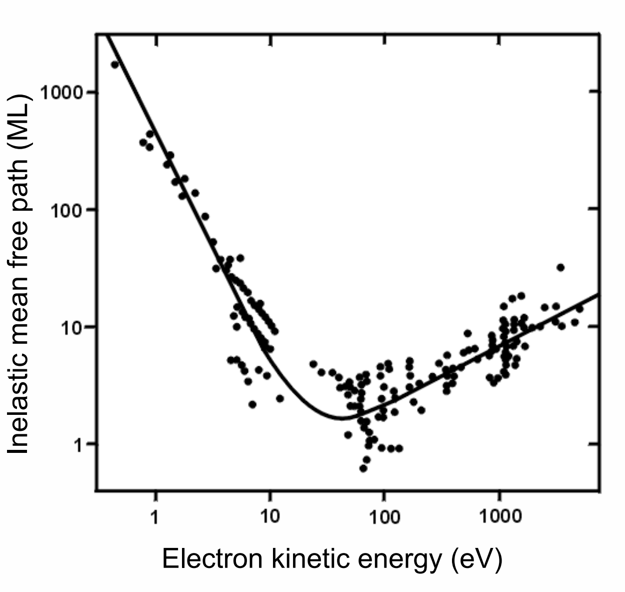

Figure 4.1.: Inelastic mean free path as a function of electron energy. Taken from [Lüt10].

4.1.1. X-ray photoemission spectroscopy

The basic principle of XPS, as it is used today, is still quite similar to the first experiments in the last century. High energy x-ray light is used to ionize atoms or molecules on the surface. The emitted core level electrons have a characteristic kinetic energy E_{kin} depending on their chemical environment in the surface. Measuring the kinetic energy of the electrons, with the knowledge of the x-ray excitation energy $h\nu$, allows determination of the electron binding energy E_{b}:

$$E_{\mathrm{b}} = h\nu - E_{\mathrm{kin}} - \phi_{\mathrm{a}}. \tag{4.2}$$

ϕ_{a} is the work function of the analyzer and has to be deducted, when referencing the binding energy to the Fermi level. The binding energy is highly sensitive to changes in surface composition. Differences in stoichiometry for example may lead to a chemical shift of the binding energy [MRB^{+}14, Hüf03]. Thus, by measuring the binding energy, it is possible to determine the charge state of an element, for example the oxidation state of metals.

The photoemission process is shown schematically in Figure 4.2. An electron from a core level (here 1s) is excited by the incident photon with an energy $h\nu$. If it does not scatter inelastically inside the volume, the electron it is emitted into vacuum with the kinetic energy $h\nu - E_{\mathrm{b}}$. To be detected in the analyzer it has to cross its work function ϕ_{a} so that the resulting detected binding energy equals equation 4.2. If the photon flux is not monochromatic, but consists of two photon energies

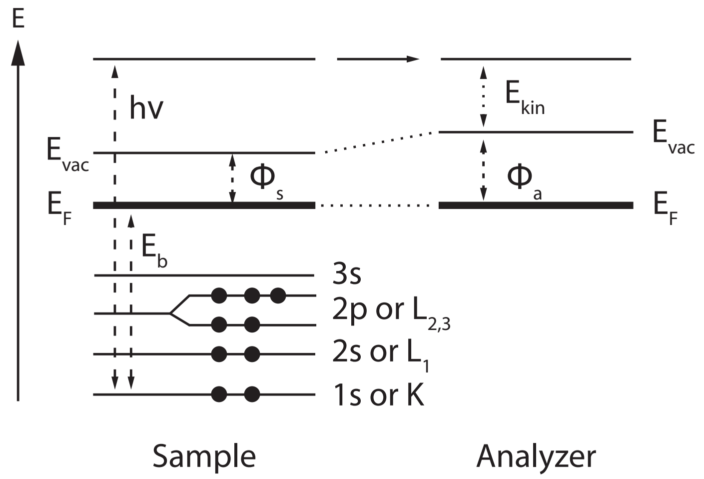

Figure 4.2.: Schematic of the x-ray photoemission process. A core level electron is excited by an incident photon $h\nu$. The electron leaves the surface and is detected in the analyzer.

$h\nu_1$ and $h\nu_2$, then the electrons excited by $h\nu_2 < h\nu_1$, originating from the same electronic state, are shifted by $\Delta E_{\text{kin}} = h\nu_1 - h\nu_2$ on the kinetic energy scale. If $h\nu_2$ is not known, then it can be calculated by measuring this value ΔE, as can be seen in Figure 4.3:

$$\begin{aligned} h\nu_2 &= h\nu_1 - \Delta E, \\ \Delta E &= E_{\text{kin},1} - E_{\text{kin},2}. \end{aligned} \tag{4.3}$$

ΔE can easily be measured as the difference in energetic position on the kinetic energy scale. From this schematic overview it is clear that PES only measures occupied states. To gain information of unoccupied states other methods, like inverse photoemission, can be used [Lüt10, HG94].

4.1.2. Ultraviolet photoemission spectroscopy

The basic concept of UPS is the same as in XPS. The difference lies in the used light sources and with that the available energy range and resolution [CL78]. The most common light source in laboratories is a discharge lamp, usually used with Helium, to produce light with up to 40.8 eV. The natural line width of the He I line is 3 meV, while for x-rays it is somewhat below 1 eV [SPEb]. The photon energies and relative intensities of the UV-lines used in this work are given in table 4.1. This high resolution makes UPS the perfect tool for analyzing electronic density of states in the valence region of an element. Energies of atomic and molecular orbitals, surface or quantum well states and also the determination of the work function of a (metal) substrate are accessible with UPS. The valence

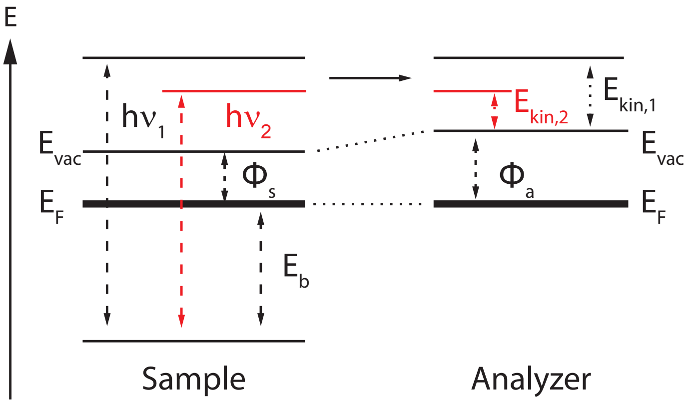

Figure 4.3.: Kinetic energy differences for electrons from the same electronic state excited by non-monochromatic photon flux with two photon energies $h\nu_1$ and $h\nu_2$.

electrons close to the Fermi edge are the ones which are in general responsible for any chemical reaction, therefor the study of valence electrons is of great interest [Hüf03]. Another advantage of UPS is that the photoionisation cross-sections are higher than in XPS for most elements [YL85].
Electrons that are excited can loose parts of their kinetic energy by scattering inelastically with for example impurities in the film. This is usually a more dramatic effect for UPS than XPS. The signal arising from the core levels in XPS is energetically far away from the large amount of slow electrons near the low energy cutoff. In UPS this is often not the case so one has to correct the spectra for these secondary electrons. In this work this is done using a inelastic electron background function presented by Li *et al* [LZH93]. The background correction is presented in the appendix in section A.
UPS was applied in this work to determine the work function of the surface, the crystallinity of the surface, via measurement of surface and quantum well states, determination of the electronic density of states at the Fermi energy and to detect photon excited plasmon decay in the Mg surface.

4.1.3. Hemispherical Analyzer

To detect electrons excited by the different light sources we used a hemispherical analyzer (HSA) [SPEa, RT90]. A schematic of a HSA is shown in Figure 4.4. Electrons emitted from the sample fly into the lens system, get focused and collimated and enter the hemispheres through a slit of variable size. The electrostatic field between the hemispheres diverts the path of the electrons and only those with the appropriate energy can fly through the exit slit. If they are too slow they will

Gas	Excitation energy (eV)	relative Intensity
He	21.22	100
He II	40.82	20
Ne	16.85 / 16.67	100
Ne II	26.9 / 27.8	20 / 10
Ar	11.83 / 11.62	100 / 80
Ar II	13.48 / 13.30	16 / 10
H α	10.2	100
H_2	7.7	

Table 4.1.: Excitation energies and relative intensities of the different noble gas emission lines used in this work. The relative intensities of the secondary lines depend on the condition of the discharge and the values given are only approximate [CL78, Ste89, SPEb].

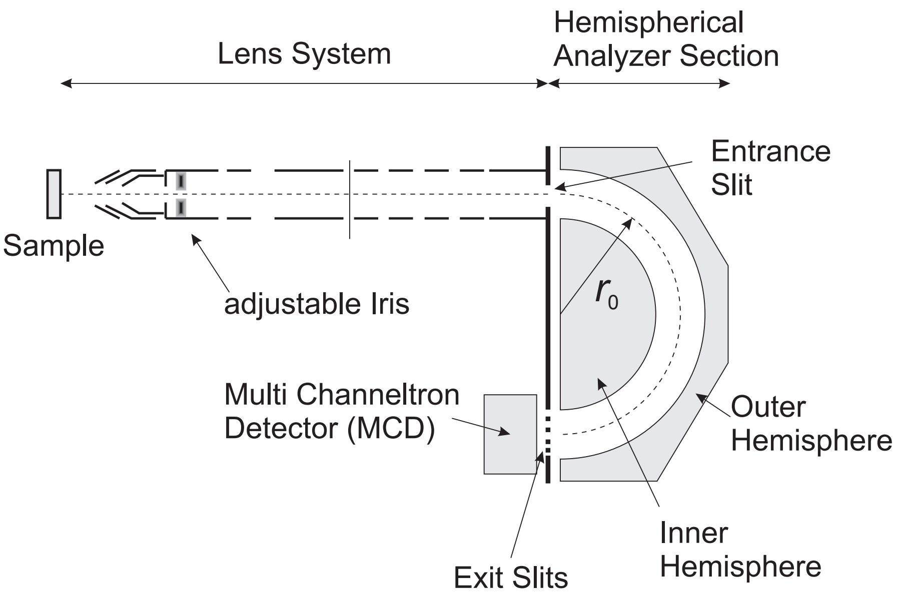

Figure 4.4.: Schematic drawing of a hemispherical analyzer. Taken and adapted from [Kri11].

hit the inner hemisphere and be lost for detection, as are the electrons that are too fast and collide with the outer. A trajectory of an electron that has the right energy to be detected is given by the dashed line. The voltage between the hemispheres is altered slightly to allow electrons with a different kinetic energy to pass through the exit slit. In this way the analyzer spectroscopically detects electrons.

The resolution of the analyzer is defined by the mean radius $r_0 = \frac{r_{in}+r_{out}}{2} = 100$ cm of the hemispheres and the kinetic energy of the electrons passing through. In this work all the measurements were recorded in the Fixed Analyzer Transmission mode. The electrons are decelerated to a fixed pass energy at the entrance slit and in this way the spectral resolution is constant for all detected lines.

The lens system can be tuned to a myriad of different magnification modes, most commonly used are low (3.5 x 10 mm^2 acceptance area with usual rectangular slit size), medium (1.4 x 4 mm^2) and high (0.7 x 2 mm^2) magnification. From low to high this increases spatial resolution, but decreases the angular resolution. Decreasing the Iris diameter increases angular resolution. The best that can be achieved is an acceptance angle of ±1°, but decreasing the Iris diameter decreases the count rate quite drastically [SPEa].

In this work the entrance slit can be varied between different rectangular and circular sizes. The exit slit was always fixed at being completely open.

4.2. LEED

Low energy electron diffraction is a widely used method to determine the crystallographic quality of a crystalline sample and to obtain information about atomic surface structure [HG94, Lüt10]. Slow electrons with kinetic energies between 20 and 500 eV, which results in de Broglie wavelengths of $\lambda = 0.5$ to 3 Å, hit a sample surface and are diffracted. The resulting diffraction pattern can be seen on fluorescent screen. A typical three-grid LEED setup is shown schematically in the left panel of Figure 4.5 [Lüt10].

Electrons are generated by a heated filament, get accelerated and focused, by the electron optics A-D, and then enter the field-free space between the last grid and the sample. After they get diffracted at the sample surface they hit the fluorescent screen and can be detected by a camera, which is looking at the screen from the backside. If the electron beam hits the sample perpendicular to the surface the resulting image has a simple correlation to the surface structure. The image that is detected on the fluorescent screen is proportional to the projection of the Ewald sphere in k-space. The curvature of the Ewald sphere in k-space, right panel in Figure 4.5, is reproduced by

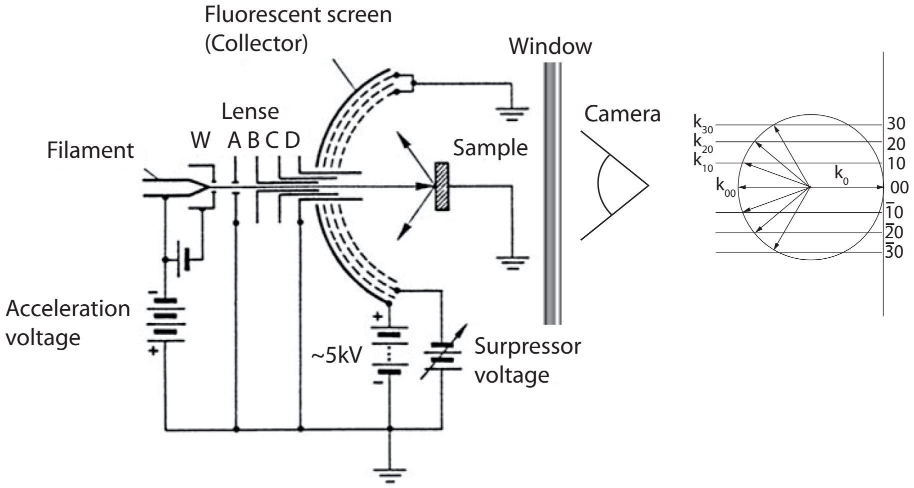

Figure 4.5.: Schematic of a three-grid LEED optics for electron diffraction experiments. The integrated electron gun consists of a heated filament, a Wehnelt cylinder (W) and the electron optics (A-D). Taken and adapted from [Lüt10] and [HG94].

the curvature of the fluorescent screen in real space [HG94]. Thus, the LEED image gives the periodicity in k-space without any deformation [HG94]. With increasing electron energy the de Broglie wavelength becomes shorter which results in a larger radius of the Ewald sphere and smaller angles between the different spots. In the image detected by the camera the diffraction pattern moves closer to the 00-spot. Because of the low kinetic energy of the electrons LEED is easily perturbed by stray magnetic fields [HG94].

Electrons are also scattered inelastically at the sample surface. These are scattered in wide angles and produce a background intensity on the fluorescent screen. A suppressor voltage can be applied to the central grid, Figure 4.5, to prevent these electrons from reaching the screen [Lüt10]. In this work LEED was used to check the quality of the H:passivated silicon substrates, of the Si(111) 7x7 reconstruction as well as the crystallinity of the prepared magnesium and silver films.

4.3. EELS

As the name suggests electron energy loss spectroscopy (EELS) is a technique to analyze the kinetic energy loss of electrons when they are scattered at a sample surface [Lüt10]. A mono-energetic electron beam is created, scattered on the sample surface and detected at a certain angle in an electron analyzer - in this work the aforementioned HSA. The energy loss and signal intensity of the inelastically scattered electrons give insight into, amongst other things, the excitation of phonons, plasmons and adsorbate vibrations at the surface.

In this work the kinetic energy of the incident electron beam was > 100 eV which is sufficient to investigate (multiple) plasmon excitations, as those are usually in the range of up to 20 eV [Rae80]. Due to the energetic width of the electron beam the resolution of normal EELS is in the area of 0.5 eV, which is sufficient enough to reveal plasmon losses. A detailed overview of EELS is given for example by Lüth [Lüt10].

5. Structural quality and electronic properties of crystalline Mg films

In this and the following chapters an important property of the prepared films is their thickness. This thickness is given either in nanometers (nm) or monolayers (ML), with 1 ML = 0.267 nm, 1 nm = 3.7 ML. As magnesium is a bilayer hcp crystal one could also call the above defined monolayer as half a bilayer.

5.1. Electronic properties: IV-characteristics

One of the goals of this work was to investigate the oxidation of crystalline magnesium films on a silicon substrate. The preparation of these films was discussed before in chapter 3.2 and a quite similar method was presented by Aballe *et al* [ARH02a]. In that work, it was shown that it is possible to grow Mg film on the Si(111) 7x7 surface in a way that the Mg surface state and Mg quantum well states can be detected. The problem in this work, was to achieve this quality of film structure and at the same time have sufficiently well developed electrical features for our large area devices, with $A = 0.56\ \text{mm}^2$. The Mg/Si interface should form a Schottky diode with a barrier height of between 0.5 and 0.8 eV as was measured experimentally [NG06, HKN10]. Theoretically the barrier heights of abrupt Mg / p Si(111) contacts is best described by the MIGS concept, as was discussed earlier in chapter 2.1 and in reference [Mön04]. In this model the homogeneous barrier height for p-doped silicon is given by

$$\Phi_{\text{hom},p} = (0.36 - 0.098(\chi_{\text{Mg}} - \chi_{\text{Si}}))\ [\text{eV}], \tag{5.1}$$

where $\chi_{\text{Si}} = 4.70$ and $\chi_{\text{Mg}} = 3.45$ are the Miedema electronegativities. This results in a predicted homogeneous barrier height of $\Phi_{\text{hom}} = 0.48$ eV. As has been shown in chapter 2.1 the surface structure at the metal silicon interface influences the experimentally determined barrier heights and the least squares fit to data on Si(111) 7x7 surfaces predicts the barrier height as [Mön95]

$$\Phi_{\text{p}} = 0.43 - 0.089 \cdot (\chi_m - 4.7)\ [\text{eV}]. \tag{5.2}$$

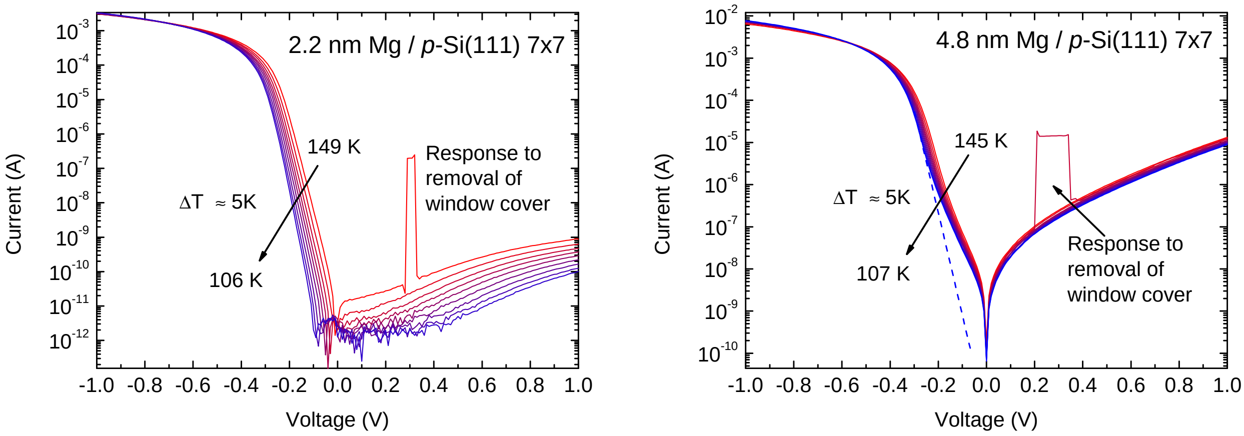

Figure 5.1.: IV-curves recorded during cooling of the sample to liquid nitrogen temperatures. Left panel: Temperature dependent IV-curves of a 2.2 nm thick Mg film on p-Si(111) 7x7. It represents a 'good' diode with a low reverse current and a shift of the minimal current value away from 0V for low temperatures. This shift is due to radiation from the chamber walls and the induced photovoltage. Right panel: Same for a 4.8 nm Mg film. This sample is an example for a defective diode. An ohmic like contribution is dominant around 0V and superimposed on the diodic part. The dashed blue line gives an idea how the diodic contribution to the IV-curve would look like. As was mentioned previously the chamber has to be completely dark because the samples are highly photosensitive.

The applied preparation procedure yielded a relatively low number of defective diodes. Only one sample in ten was not usable due to its electrical characteristics. But the difference in diode quality can be seen in Figure 5.1. The left panel shows a set of temperature dependent IV-curves for a 'good' diode with a low reverse current. The Mg film thickness is 2.2 nm. Color coded from red to blue is the decrease in sample temperature from 149 K to 106 K. The reverse current decreases with temperature. With decreasing temperature the total current minimum shifts from 0 V to ~ -0.1 V. This shift is due to the increasing photosensitivity of the diode and is generated by heat radiation from the chamber walls. The shift represents the induced photovoltage.

A similar set of temperature dependent IV-curves are given in the right panel for a 4.8 nm thick Mg film on p-Si(111) 7x7 and represents a defective, or 'bad', diode. An ohmic-like contribution is superimposed on the diodic behavior. From -1 V to -0.2 V the IV-curves look similar to the ones in the left panel. For higher voltage the ohmic contribution dominates the current. The diode is still photosensitive though, as can be seen in the current response at around 0.4 V to the removal

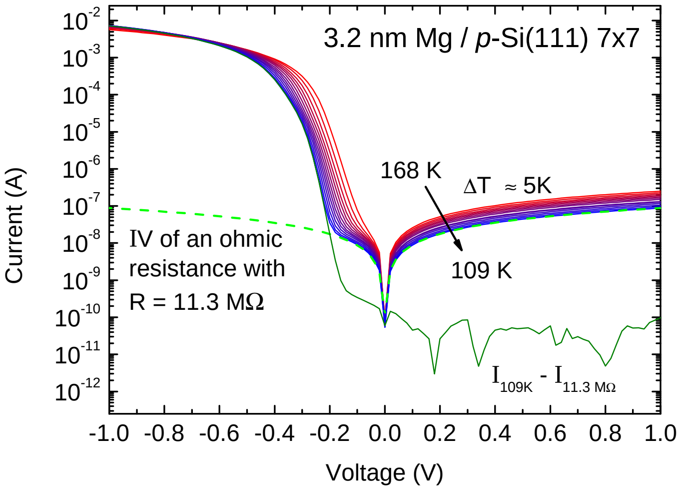

Figure 5.2.: IV-curves recorded during cooling of the sample with 3.2 nm Mg film thickness to liquid nitrogen temperatures. The green dashed line is the result of a linear fit to the reverse direction and a modeling of the ohmic contribution of a parallel resistance to the current. The resistance is $R_{\text{parallel}} = 11.3$ MΩ. The dark green line gives the resulting IV-curve when deduction the ohmic from the measured one at 109 K.

of one of the UHV-window covers.

The influence of such an ohmic contribution on the chemicurrent measurements is in a higher background and noise current. While the current at zero bias is on the order of 1 pA for a good diode, left panel Figure 5.1, it can go up to several hundred pA or even nA for a diode with a parallel ohmic resistance.

Such an ohmic contribution to forward IV-characteristics has been seen in the past by different groups [SM99, LSS^{+}95, NKG07] for different systems. It was tried to model these in different ways, mainly using different distributions of discretely distributed small areas of lowered barrier height. But the reverse direction of the current was always neglected. As can be seen very well in another example of these kind of diodes in Figure 5.2. In this Figure a third set of temperature dependent IV-curves for a 3.2 nm Mg / *p*-Si(111) 7x7 diode is plotted. Again one can clearly see an ohmic-like contribution dominating for reverse bias and at small forward bias. The green dashed line is the IV-curve of an ohmic contact with a resistance of 11.3 MΩ and an offset current of $I_0 = 113$ pA. The dark green line is the result when subtracting the ohmic IV-curve from the measured one at 109 K. This does not give as good a diodic IV-behavior as shown in the left panel of Figure 5.1, but it is a strong hint that it is in fact a parallel ohmic resistance in the MΩ range that gives rise to this

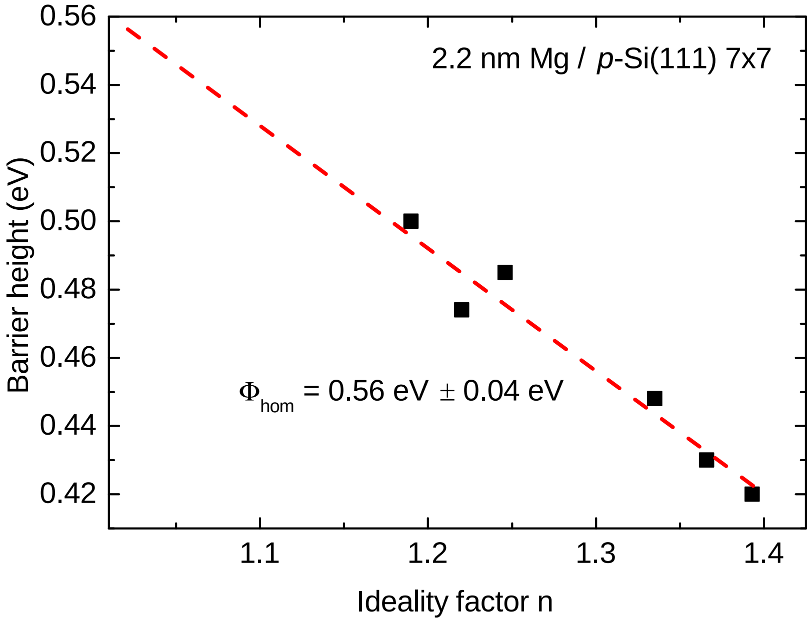

Figure 5.3.: Effective barrier heights are obtained by evaluation of the single, temperature dependent IV-curves. Plotting Φ_{eff} versus the corresponding ideality factor and extrapolation to $n = 1.01$ yields the homogeneous barrier height. Here $\Phi_{\text{hom}} = 0.56 \pm 0.04$ eV.

unwanted feature in the IV-measurements. The precise nature and origin of this parallel resistance is not known and as it does not influence the current detection, other than reducing the signal to noise ratio, it will not be discussed further here.

For each curve in Figure 5.1, also for those with a parallel resistance, one can obtain an effective barrier height and a corresponding ideality factor, using equation 2.8. Plotting these two values against each other, as was done in Figure 5.3 for the diode shown in the left panel of Figure 5.1, allows the determination of the homogeneous barrier height of this diode by extrapolation of a linear fit to an ideality factor of $n = 1.01$ [SKM97, SM99]. For this diode the homogeneous barrier height is $\Phi_{\text{hom}} = 0.56 \pm 0.04$ eV.
This determination of the homogeneous barrier was done for all the Mg diodes prepared in this work. Figure 5.4 shows a histogram of the determined homogeneous barrier heights. A Gaussian fit gives 0.567 ± 0.002 eV as the center of the distribution. The error is very small as the individual errors from the determination of the barrier height are not included in the fit. Thus, considering these errors the homogeneous barrier height of crystalline Mg films on p-Si(111) 7x7 surfaces has a

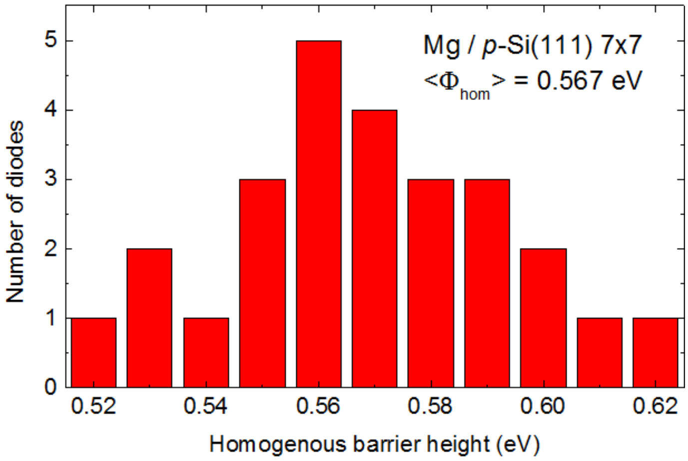

Figure 5.4.: Histogram of the determined homogeneous barrier heights for Mg / p-Si(111) 7x7 Schottky diodes.

value of 0.567 ± 0.04 eV.

The determined value of the barrier height is plotted in Figure 5.5 as the red circle with error bars. The black line gives the predicted value by the MIGS model - see equation 5.1 - and the gray circles are results from other experiments on different metal-silicon interfaces [Mön04]. The red circles give the results for metal-Si(111) 7x7 interfaces and the red line represents the least squares fit to that data, see chapter 2.1 and [Mön04]. The value for the diodes from this work is slightly higher than expected by the fit to the other Si(111) 7x7 contacts. The reason is probably that the assumption, that the Mg/Si(111) 7x7 interface prepared in this work represent an abrupt, clean and laterally homogeneous interface is not completely met.

An observation that was made in this work was, that when the flashing time and temperature of the Si substrate was increased, this lead to more pronounced Si(111) 7x7 surface states in UPS measurements. However, the electric quality of the samples decreased. The ohmic-like contribution increased and the number of samples, that could not be used for chemicurrent detection increased with it. The reason for this is not known.

5.2. Structural analysis with LEED

Figure 5.6 shows a series of LEED images on the Mg and Si surfaces of a prepared sample. The Mg film is 6 nm thick. In the first image the LEED spot is solely on uncovered Si and the 7x7 reconstruction is visible. From left to right and top to bottom the sample is then moved perpendicular

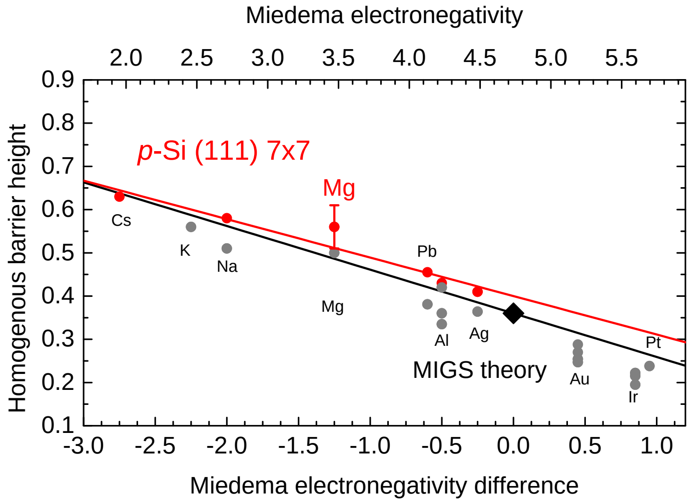

Figure 5.5.: Predicted barrier heights by the MIGS model (black line), equation 5.1 [Mön04]. Measured barrier heights are given by gray circles. The red line gives the least squares fit to data from Schottky diodes on Si(111) 7x7 substrates, red circles, given in the book by Mönch [Mön04] and follows equation 5.2. The red circle with error bars is the value for the Mg/p-Si(111) 7x7 diodes used in this work.

to the electron beam. One can see the Si spots losing intensity while the diffraction pattern from the Mg film emerges. This means the 7x7 reconstruction is completely intact in areas that were covered by the shadow mask during Mg evaporation. As this reconstruction is quite sensitive to oxygen uptake and oxygen uptake reduces the LEED intensity of the 7x7 spots strongly we can say that no detectable oxygen is adsorbed on the covered Si surface during deposition.

The atomic distance in the Si(111) surface is $540 \cdot \frac{\sqrt{2}}{2} = 380$ nm [Kit66]. The distance in the LEED image is 314 pixel (px). The distance of the equivalent Mg atoms is 370 px. This results in a Mg atomic distance of 322 nm which is, within the error margin, exactly the lattice constant of the Mg(0001) surface [Kit66].

The Mg spots are slightly elongated along the azimuthal direction. In the last image - bottom right - a red and blue line represent intensity profiles. These are shown in Figure 5.7 together with Lorenz fits to the spots. The half width of the fit is $\mathrm{w}_1 = 182$ px, $\mathrm{w}_2 = 203$ px and the perpendicular width is $\mathrm{w}_{2,perpend.} = 128$ px. The broadening of the spots due to rotational disorder of the Mg film can now be calculated by subtracting the radial half width of spot 2 from the half width of spot 1. This is the case because rotational disorder only elongates the spot along the diffraction ring and not perpendicular to it [HG94, Wal11]. Rotational disorder means that there are multiple

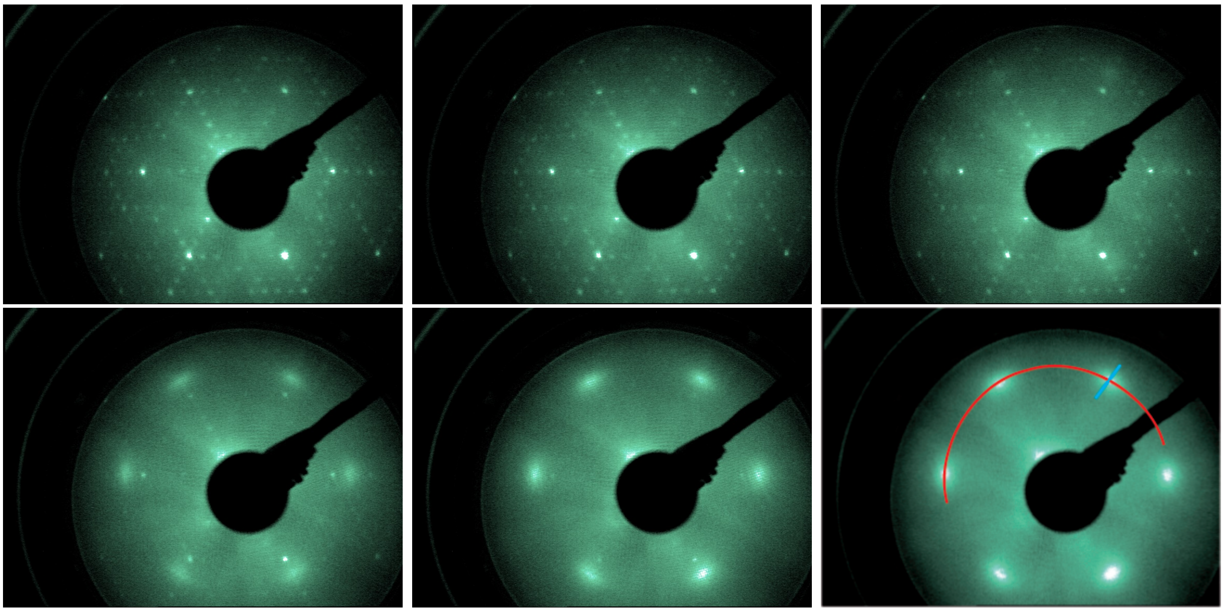

Figure 5.6.: LEED images of a crystalline 6 nm Mg film on the Si(111) 7x7 surface. The sample is moved perpendicular to the incident beam, so that the electron spot moves from the uncovered Si surface - that was protected by a shadow mask during Mg evaporation, top left - onto the Mg film - bottom right. The 7x7 reconstruction remains intact where it is not covered by Mg. This series was recorded at 85 eV primary electron energy. The red and blue line in the last scan represent line scans of the intensity profile.

domains of perfect crystal structure on the surface which are in-plane rotated against each other as is schematically shown in Figure 5.8. The radial half width gives the statistical disorder of the film, see below, and for a film without rotational disorder the half width along the azimuthal direction should be the same. The difference between the radial and azimuthal half widths can be converted into the degree of rotational disorder Φ by a rule of three [Wal11]

$$\frac{\Delta \mathrm{w}}{\Phi} = \frac{\mathrm{L}}{360^\circ}, \tag{5.3}$$

where L is the total length of the complete diffraction ring at the radius of the investigated spot. For this Mg film this results in a rotational disorder of $\Phi = \pm 3^\circ$.

Performing such profile scans for the Si spots yields a half width of w = 36 px in both directions. The general broadening of the Mg compared to the Si spots cannot be easily explained. Most likely it is due to statistically disordered steps and terraces on the metal surface [HG94, Wal11]. There is no evidence that tilted rotational disorder is responsible for the peak broadening, as there is no

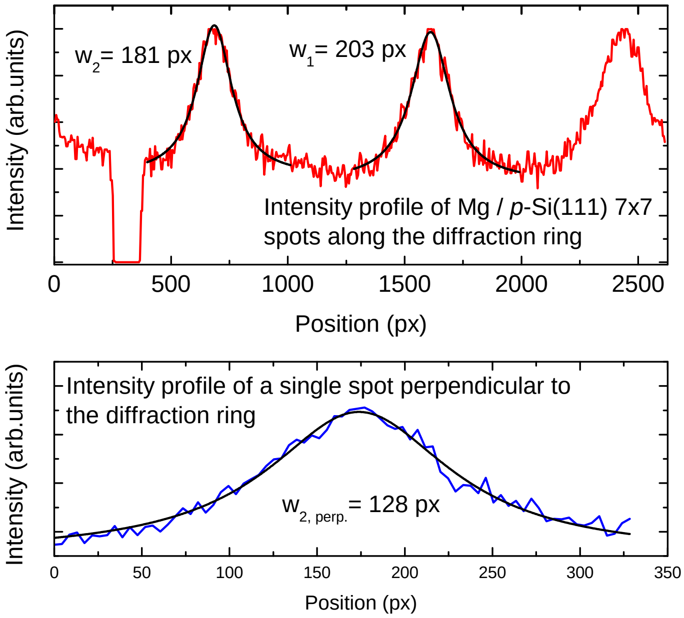

Figure 5.7.: Intensity profiles as indicated in Figure 5.6. The profiles are fitted by a Lorenz distribution.

visible energy dependence in the width of the peaks, as is the case for tilted mosaic structures.

5.3. Surface analysis using XPS, UPS and EELS

5.3.1. UPS

Surface and quantum well states

The film quality is also effectively checked with UPS, using He I light with 21.22 eV photon energy and recorded at normal emission. As was discussed above crystalline Mg (0001) films develop a surface state and thin films also show several quantum well states. These are accessible with UV light, as they are energetically close to the Fermi edge. Figure 5.9 shows UPS spectra of different samples of thin Mg films on Si. The Mg film thickness are 8 ML, black line, 17 ML, red line, 24 ML, blue line and 300 ML, orange line. The green sample of 10 ML thickness that is called 'poly', represents a polycrystalline Mg film which was deposited onto the sample at room temperature.
In the left panel of Figure 5.9 the complete spectra are shown. At about 17 eV binding energy one can see the sudden increase of the secondary electron background consisting of inelastically scattered electrons. At 0 eV binding energy is the Fermi edge of the metal film. The surface state

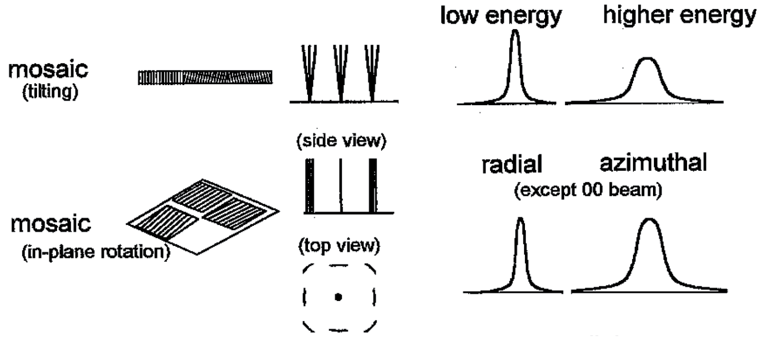

Figure 5.8.: Schematic drawing of the in-plane and tilted rotational disorder on crystalline surfaces. Taken from [Hen96].

(SS) at 1.6 eV binding energy below E_F is visible for all thicknesses and most pronounced for the thicker films. The feature at around 6 eV binding energy is a signature of oxygen adatoms on the Mg surface. This feature is quite pronounced due to the high photoionization cross section of oxygen in this photon energy range [YL85]. Another feature in the spectra are several peaks between 11 and 13 eV binding energy. These are photoemission lines of the surface and quantum well states due to the existence of H α radiation and will be discussed later in chapter 9.

The right panel of Figure 5.9 shows a high resolution scan of the surface state region up to the Fermi level E_{F} of the same five samples plus two samples with 11 ML and 13 ML film thickness. The surface state at $E_{\mathrm{b}} = 1.6$ eV becomes sharper and more pronounced for thicker films. At the same time the quantum well states (QWS) shift to higher binding energies towards the surface state. The Mg film that has been deposited at RT does show a surface state, but no quantum well states are visible. This means that increased surface roughness and/or increased small island formation destroy the quantum size effects leading to the formation of quantum well states. That is the reason why this film is assumed to be more polycrystalline.

The quantum well states offer a very precise way to determine the film thickness of the Mg layer as their energetic position relative to the Fermi edge is highly sensitive on this thickness. Additionally the film thickness was calibrated by measuring the deposition rate using a quartz micro-balance. The thickness determined in this way prior to deposition can be compared to the thickness determined by the energetic position of the QWS.

Aballe *et al* have done this before and their result is shown in the left panel of Figure 5.10, as the grey hollow circles [ARH02a]. Here the binding energies of the 1st to 4th quantum well state are plotted versus the Mg film thickness in monolayers. One can now calibrate our binding energies of

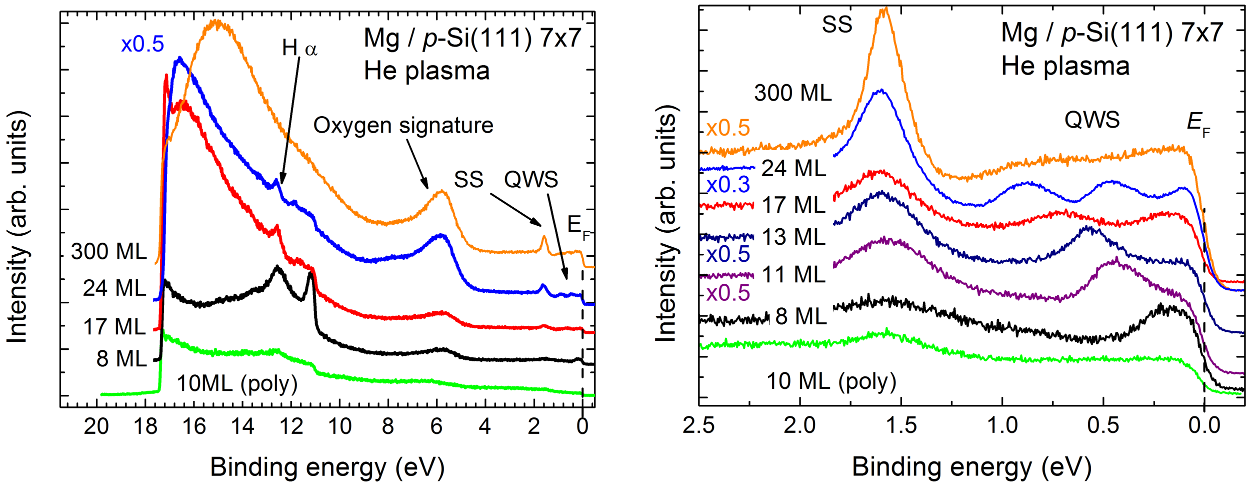

Figure 5.9.: UPS scans of Mg films of different thickness recorded in normal emission. The 10 ML polycrystalline (poly) film was deposited at room temperature, as opposed to the regular deposition at 100 K. Left panel: Complete He I spectra. Right panel: High resolution scan of the surface state and Fermi edge region with two additional film thicknesses.

the 1st QWS to the thicknesses measured by Aballe for the same binding energy. This was done and that data is plotted as the colored squares in the left panel of Figure 5.10. Both sets of data agree well with each other. Thickness differences between different samples of down to 0.1 ML can be resolved in this way. Even if this calibration is off in such a way, that the value of a single sample is slightly wrong, the succession of all samples is fixed. If the 1st QWS of sample A is at a higher binding energy than for sample B then the Mg film of sample A is thicker, no matter how small the energetic difference of the two positions might be.

As was mentioned earlier the Mg deposition rate is also determined by an uncalibrated quartz micro-balance prior to deposition. In the right panel of Figure 5.10 the thickness values determined with the quartz microbalance is compared to the thickness determined by the measured position of the QWS. This value is determined by comparing the 1st QWS position in UPS to the data by Aballe *et al* in the left panel of Figure 5.10. The blue line gives the bisectrix and the red line the fitted linear relationship between the two values. The slope of the red line is determined as $s_{\mathrm{Mg}} = d_{\mathrm{Mg}}/d_{\mathrm{QWS}} = 0.875 \pm 0.02$ and s_{Mg}^{-1} can be used as a tooling factor for the Mg oven.

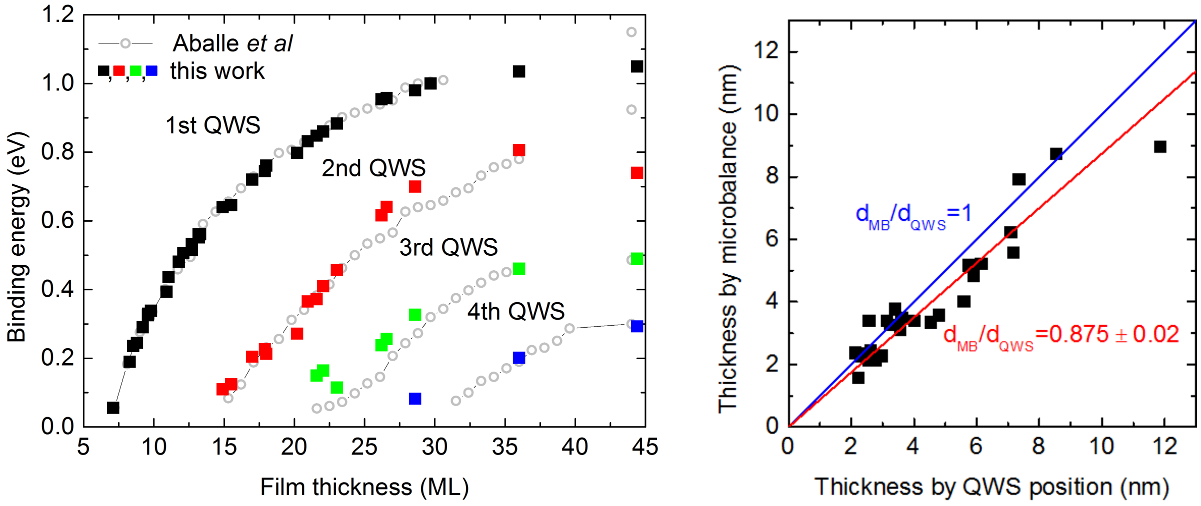

Figure 5.10.: Left panel: Calibrated dependence of the energetic position of the quantum well states on the film thickness. The grey hollow circles represent the data by Aballe *et al* [ARH02a]. The colored squares represent the data measured in this work on the binding energy of the 1st to 4th QWS. The comparioson of the binding energy of the 1st QWS with the result by Aballe determines the film thickness. Right panel: Comparison of thickness determined by the uncalibrated quartz micro-balance and the quantum well state position using reference [ARH02a]. They are proportional to each other with a factor of $d_{\mathrm{Mg}}/d_{\mathrm{QWS}} = 0.875 \pm 0.02$.

Work function

As was mentioned above in chapter 4.1.2 UPS can be used to determine the work function of metallic surfaces. By determining the onset of the electron signal E_{on} - around 17 eV binding energy in left panel of Figure 5.9 -, the position of the Fermi energy E_{F} and knowing the exact excitation energy $h\nu = 21.22$ eV the work function ϕ_{m} of the metal surface is calculated via:

$$\phi_m = h\nu - (E_{\mathrm{on}} - E_{\mathrm{F}}). \tag{5.4}$$

The result is shown in the left panel of Figure 5.11 - black circles - together with the result of a density functional theory (DFT) simulation by Li *et al* - red circles [LZC07] - versus the film thickness. The value for ϕ_{m} oscillates around 3.9 eV for films $d < 20$ ML and seems to remain constant at around 3.92 eV for thicker films. The calculation predicts minima in the work function at around 12 ML and 21ML. These minima are also present in the experimental results but shifted by about 3 ML to thinner films with the two minima at around 9 ML and 18 ML. The noise and

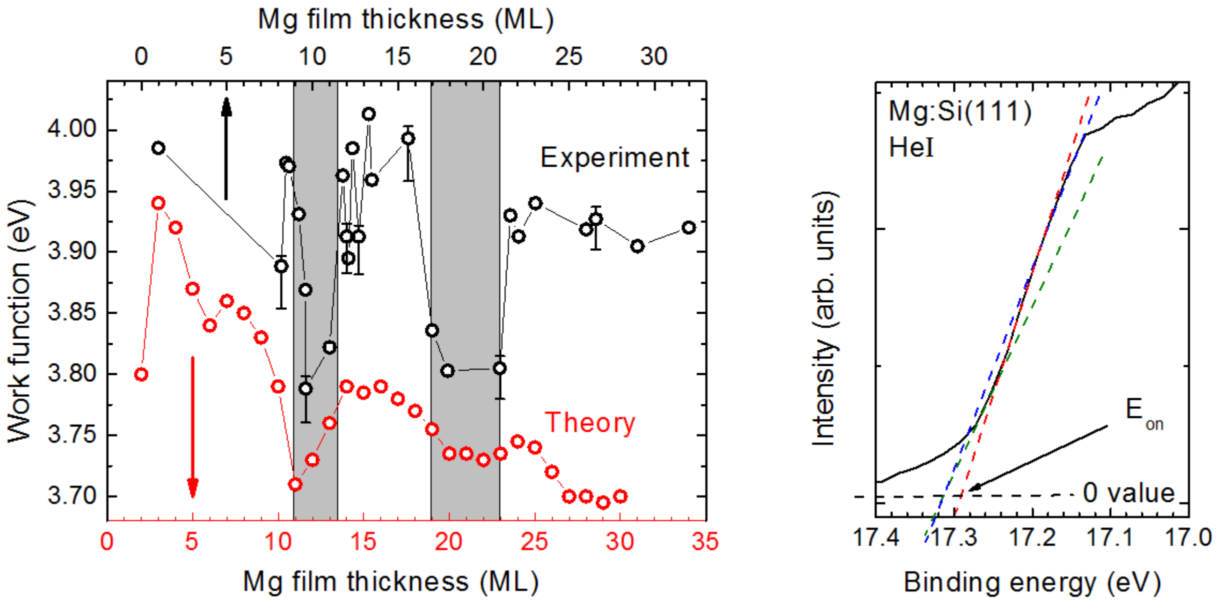

Figure 5.11.: Left panel: Experimentally determined - black circles - and calculated - red circles - work function of thin Mg films. The two minima, predicted by the calculations, at around 12 and 21ML are present in the experiment but shifted to thinner films at 9 and 18ML. Right panel: Example of error in determination of the onset value E_{on}. Red dashed line is a fit to the linear middle region of the onset. Blue and green are fits to the onset curve left and right of the central linear region. The error here is about 0.025 eV.

the error bars on the experimental values are quite large. This is mainly due to the problem in determining the precise onset value of the UPS signal.

To give an idea of the problem in the determination of E_{on} the right panel in Figure 5.11 shows a zoom into the onset region and three different ways of fitting the curve. The red dashed line is a fit to the linear middle region of the onset. The blue and green lines are fits to the onset curve left and right of the central linear region. The difference in the onset energy between those three different fits is about 0.025 eV. In this work I used the value determined by a fit to the central, linear part of the onset - red line. The other fits were used to give the error bars in Figure 5.11. The qualitative agreement between this measurement and the calculation is surprisingly adequate, as the work function determination was by no means in the focus of this work.

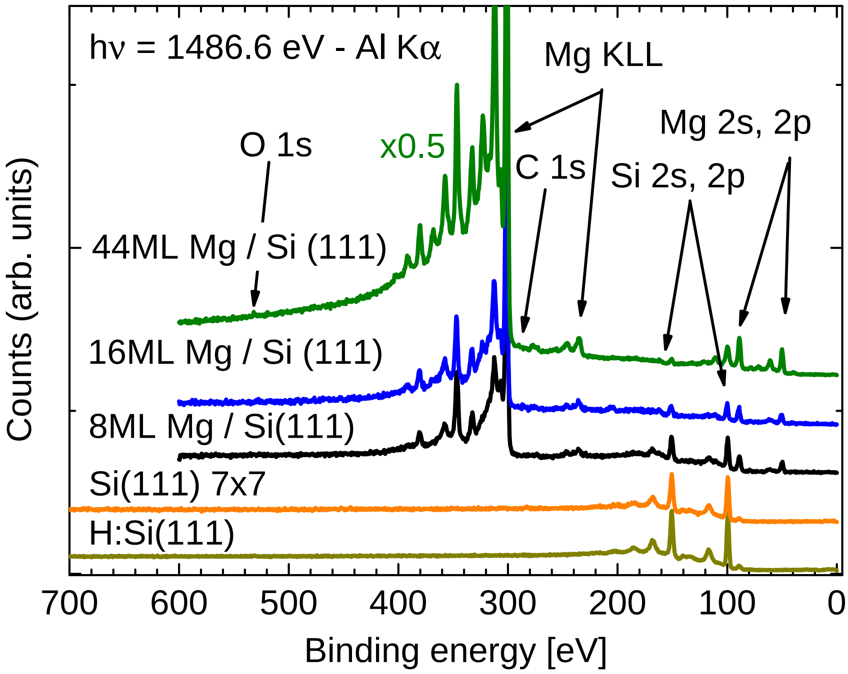

Figure 5.12.: XPS measurements of the three different stages of sample preparation. The scans for the as-prepared H-passivated Si surface, the flashed Si(111) 7x7 and the 8 ML Mg covered surface are all taken from the same sample. For comparison two more Mg covered samples are shown.

5.3.2. XPS

X-ray photoelectron spectroscopy is used for chemical analysis of the sample in all its preparation steps. Figure 5.12 gives the XPS spectra of the sample after etching, dark yellow line, flashing, orange line, and evaporation of Mg, black line, versus the binding energy. For the hydrogen passivated Si(111) surface only the Si peaks at 99 eV and 150 eV are visible in the spectrum [MSSB95, LM]. This is also the case when recording high resolution scans. The O 1s or C 1s peaks, at 531 eV and 284 eV binding energy respectively [MSSB95, LM], do not show.

The sample is flashed, as described above, and the corresponding XPS scan reveals a small carbon contamination of the surface of below 3% for the S(111) 7x7 reconstruction. Oxygen is still not detectable. Repeated flashing as well as flashing at higher temperatures lead to an increase in carbon content on the surface. The minimization of the C 1s peak is the main reason for the chosen preparation procedure presented in chapter 3.2.

After the deposition of Mg, in this case 8 ML, onto the flashed surface small amounts of oxygen are to be found on the surface. If one assumes the oxygen to be incorporated into the Mg film a contamination of below 1% is found. The same result is obtained for carbon. An increase in evaporation temperature leads to an increase of carbon and oxygen contamination, at 531 eV and 284 eV binding energy. Thus it is advisable to evaporate Mg at temperatures as low as possible while maintaining a reasonable evaporation time. For this reason the evaporation temperature of 561 K was chosen.

Two more scans of different samples are shown for larger Mg films of 16 and 44 ML thickness. Oxygen content stays at about 1 to 2% for the 44 ML sample, while the amount of detected carbon increases with increasing film thickness to about 4%.

5.3.3. Measurement of plasmon energy with EELS and XPS

In this work the plasmon energies of the different magnesium plasmons were measured in different ways, namely with EELS and XPS.

EELS

Figure 5.13 shows an energy loss spectrum measured in normal emission for electrons being scattered from a 11 ML Mg film with a primary electron energy of 569 eV. The angle between source and surface normal is $\phi_{\mathrm{SS}} = 53°$. The inset on the right shows the intensity of the elastic peak in comparison to the single plasmon losses. The peaks closest to the elastically reflected electrons can be identified as losses due to the excitations of a surface plasmon, green solid line, at $\hbar\omega_{\mathrm{SP}} = 7.26$ eV and a bulk plasmon, blue solid line, at $\hbar\omega_{\mathrm{BP}} = 10.68$ eV [Rae80]. The violet feature in between these two losses corresponds to the excitation of a multipole mode of the surface plasmon at an energy loss of $\hbar\omega_{\mathrm{MSP}} = 8.73$ eV. These values agree very well to those published previously like in [SWP92] with $\hbar\omega_{\mathrm{SP}} = 7.38$ eV, $\hbar\omega_{\mathrm{BP}} = 10.7$ eV and $\hbar\omega_{\mathrm{MSP}} = 8.73$ eV and in other works as well [Rae80, GKG^{+}07]. While the single plasmon losses of bulk and surface plasmon are quite similar in intensity, multiple losses behave quite differently. n-Multiple bulk plasmon excitations can be seen clearly up to $n_{\mathrm{bulk}} = 4$, with an energy loss of $4 \cdot \hbar\omega_{\mathrm{p}} \approx 43$ eV. On the other hand, the excitation of even only 2 surface plasmons by a single electron is almost undetectable. However, the combination of multiple bulk plasmon losses, up to $n_{\mathrm{bulk}} = 3$ and single surface plasmon loss, $n_{\mathrm{surface}} = 1$, by a single electron is visible, dark green line. This loss, located at a loss energy of 39.52 eV for $n_{\mathrm{bulk}} = 3$, is relatively intense, with roughly half the intensity of the pure multiple bulk plasmon

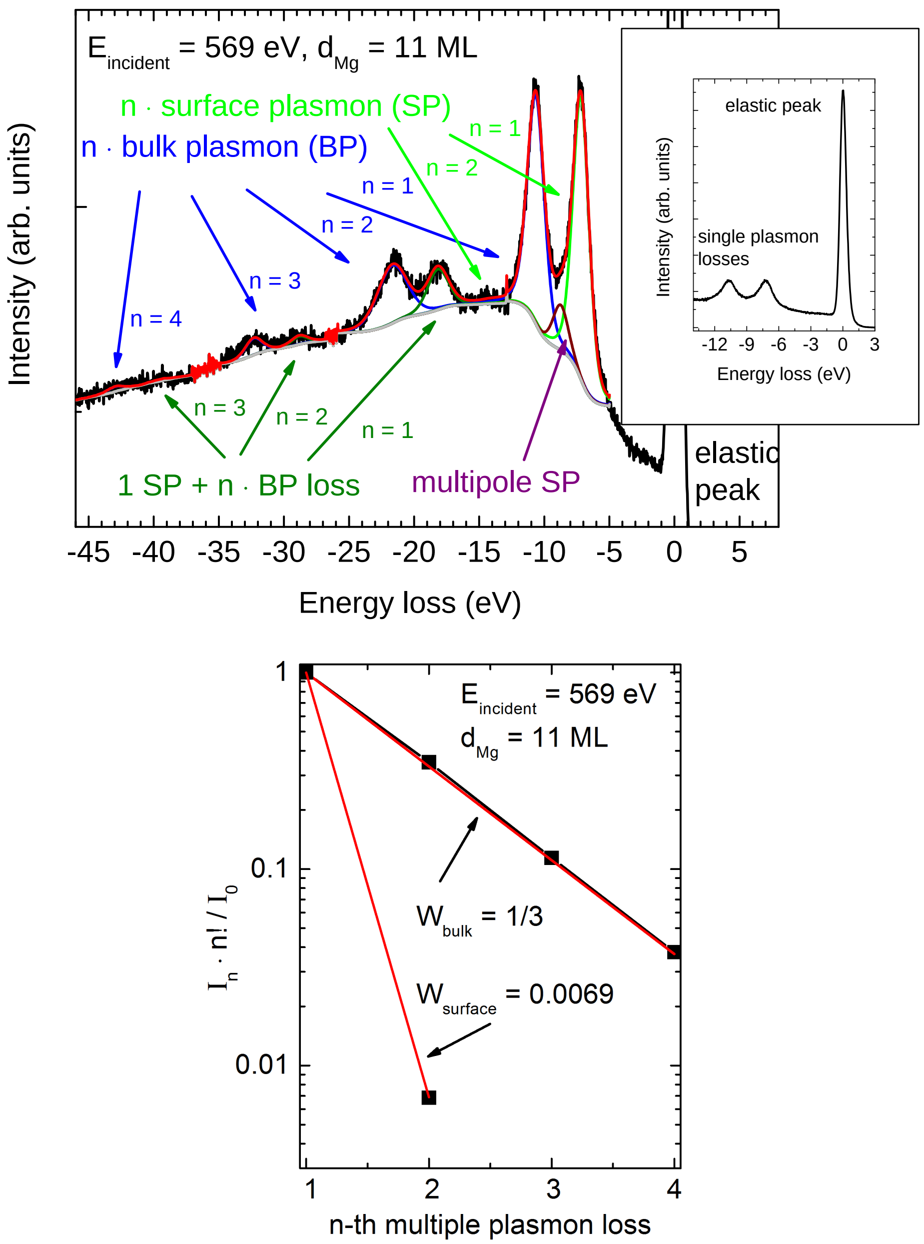

Figure 5.13.: Upper panel: Electron energy loss spectrum of a 11 ML Mg film on Si(111) 7x7. Primary electron energy is 569 eV. This spectra was recorded in normal emission, at an angle of 53° degrees between source and sample, a constant pass energy of 5 eV and a step size of 0.028 eV. Lower panel: Intensities of the n-th multiple bulk and surface plasmon loss. The red lines represent the corresponding Poisson distributions with the an excitation probability $W_{\text{bulk}} = \frac{1}{3}$ and $W_{\text{surface}} = 0.0069$.

loss with $n_{\text{bulk}} = 4$.

In general the excitation of multiple plasmon losses by electrons is governed by the Poisson distribution given through [Rae80]

$$P_{\text{n}} = \frac{1}{\text{n}!} W^{\text{n}} \text{e}^{-W}. \tag{5.5}$$

The value W, the probability to produce one plasmon energy loss, differs for bulk and surface plasmon excitation. As no multiple surface plasmon losses by a single electron are measurable, W is obviously smaller for the surface plasmon. The value for W can be determined by plotting the $I_n \cdot n!/I_0$ versus the order of the loss and identifying the slope. This was done in the lower panel in Figure 5.13. The intensities of the multiple losses for both the bulk and surface plasmon align along straight lines. The slope of the lines yields the excitation probabilities as $W_{\text{bulk}} = 1/3$ and $W_{\text{surface}} = 0.0069$. This huge difference of a factor of ~ 48 is at least partially due to the dependence of the excitation probability on the primary electron energy. Ibach shows that for surface losses of an impinging electron with a primary energy E_0 the scattering cross-section is $\frac{dS}{d\hbar\omega} \propto \frac{1}{E_0 cos(\theta)}$, while for bulk losses it is $\frac{dS}{d\hbar\omega} \propto \frac{1}{\sqrt{E_0} cos(\theta)}$ [IM82]. The difference due to the square root of the primary energy E_0 is a factor of 24 for $E_0 = 569$ eV, as in Figure 5.13. This still leaves a factor of $48/24 = 2$ that is most probably due to an error in the determination of the intensity of the double surface plasmon loss in Figure 5.13.

XPS

X-ray photoelectron spectroscopy offers an alternative way of measuring plasmon energies. Figure 5.14 shows the Mg 2p main peak at a binding energy of 49.48 eV and to higher binding energies the surface plasmon loss $\Delta E = 7.1$ eV, the single plasmon excitation $\Delta E = 10.87$ eV and the electron loss due to the excitation of two bulk plasmons by a single electron at $\Delta E = 21.65$ eV. These results again agree very well to literature data [KGM03]. Table 5.1 summarizes the determined plasmon energies.

Our determined values agree with other works. It is interesting to note the large span of values for the bulk plasmon between 10.2 eV and 11 eV. At the same time the FWHM ranges in between 0.5 eV and 0.8 eV. The reason for this is, that the loss function of a free electron gas is not a sharp resonance at the bulk plasmon energy $\hbar\omega_{\text{BP}}$ but rather a relatively broad continuum [Rae80]. Hence, it is possible that different methods yield different values. Secondly the structure of the film concerning defects, thickness, crystallinity etc. has an effect on the bulk plasmon energy as well. The experiments supplying the data for table 5.1 all have differently prepared Mg surfaces of different thickness. This would influence the measured bulk plasmon energy.

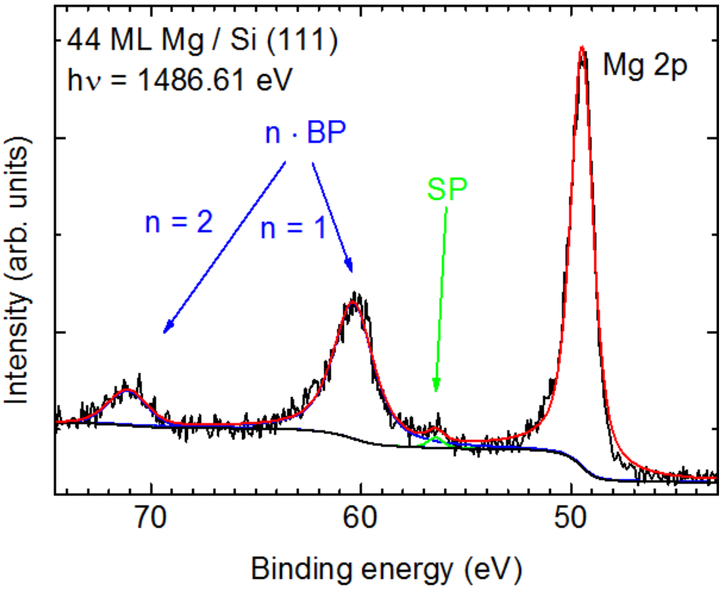

Figure 5.14.: Mg 2p main peak and plasmon region as measured for a 44 ML Mg film. This spectra was recorded in normal emission, at an angle of 45° degrees between source and sample, a constant pass energy of 20 eV and a step size of 0.08 eV.

$\hbar\omega_{\mathrm{SP}}$ [eV]	$\hbar\omega_{\mathrm{MSP}}$ [eV]	$\hbar\omega_{\mathrm{BP}}$ [eV]	$2 \cdot \hbar\omega_{\mathrm{BP}}$	Source
7.26	8.73	10.68	21.7	EELS
7.1	/	10.87	21.64	XPS
7.4	/	11	22	EELS [GKG+07]
7.38	8.73	10.7	/	EELS [SWP92]
7.34	/	10.85	21.3	XPS [KGM03]
Further values for $\hbar\omega_{\mathrm{BP}}$ [eV]:				
10.35eV [Che76], 10.2 eV [Sue65], 10.3 [AY74]				

Table 5.1.: Determined plasmon energies in eV from EELS and XPS in comparison to literature data.

5.3.4. Dispersion relation of the Mg surface state and evidence for an intact Si(111) 7x7 periodicity below the Mg film

Varying the emission angle of the electrons in respect to the surface normal enables the measurement of the dispersion relation of the magnesium surface state in UPS. It will be shown in chapter 9 that the photon flux emitted from a He, Ne or Ar plasma in our UV-source contains hydrogen α radiation as well. Hence, it is possible to measure the dispersion relation for two photon energies in a single scan. This is visible in Figure 5.9, where the electron signal between 11 and 13 eV binding energy is generated by incident H α radiation.

Figure 5.15 shows the He I and H α photoelectron signal from the same scan versus the electron binding energy. The upper panel represents the photoelectron signal for He I light and lower panel the same for H α light. The sample is rotated to vary the electron emission angle between -2.5° and 17.5° degrees. The hindmost scan represents an emission angle of -2.5°. Upon rotation the energetic position of the surface state moves towards the Fermi edge for both photon energies. The total shift is slightly different, because the different photons have a different wavevector parallel to the surface. At large emission angles the intensities are different between the different light sources, which is most likely due to the different $k_{||}$ values and a change in the photoionization cross section. $k_{||}$, the wavevector component of the emitted electrons parallel to the surface, is calculated via

$$k_{||} = sin(\alpha)\sqrt{\frac{2m_e \cdot (h\nu - \phi_{\mathrm{m}})}{\hbar^2}}. \tag{5.6}$$

Here α is the emission angle in respect to the surface normal, ϕ_{m} the work function of the Mg film and $h\nu$ the energy of the incident light.

The dispersion of the surface state for a 8 ML Mg film is shown in the upper panel of Figure 5.16 for photon energies of 10.2 eV (H) and 21.22 eV (He). The energetic position of the surface state in respect to the Fermi edge is plotted versus the parallel wavevector, as determined by equation 5.6. The red data points correspond to the H α signal and the black one to the He I signal. The shaded areas depict the projected bulk bands as determined from [BGGP86, CSFK99]. Both sets of data are fitted well by parabolic fits $y = A + B \cdot x^2$. The prefactor B is 1.6 times larger for the hydrogen light. Why the two curves in the upper part of Figure 5.16 differ is not clear.

The lower part of Figure 5.16 plots the same results as in the upper panel together with the results from Aballe *et al* [ARH02a]. The slopes determined in that work are slightly larger than in this work, but the overall agreement is satisfying.

Other references give the value of the band edges at $k_{||} = 0$ Å^{-1} somewhat lower [KHPF82] so that the values by Aballe are also well within the band gap.

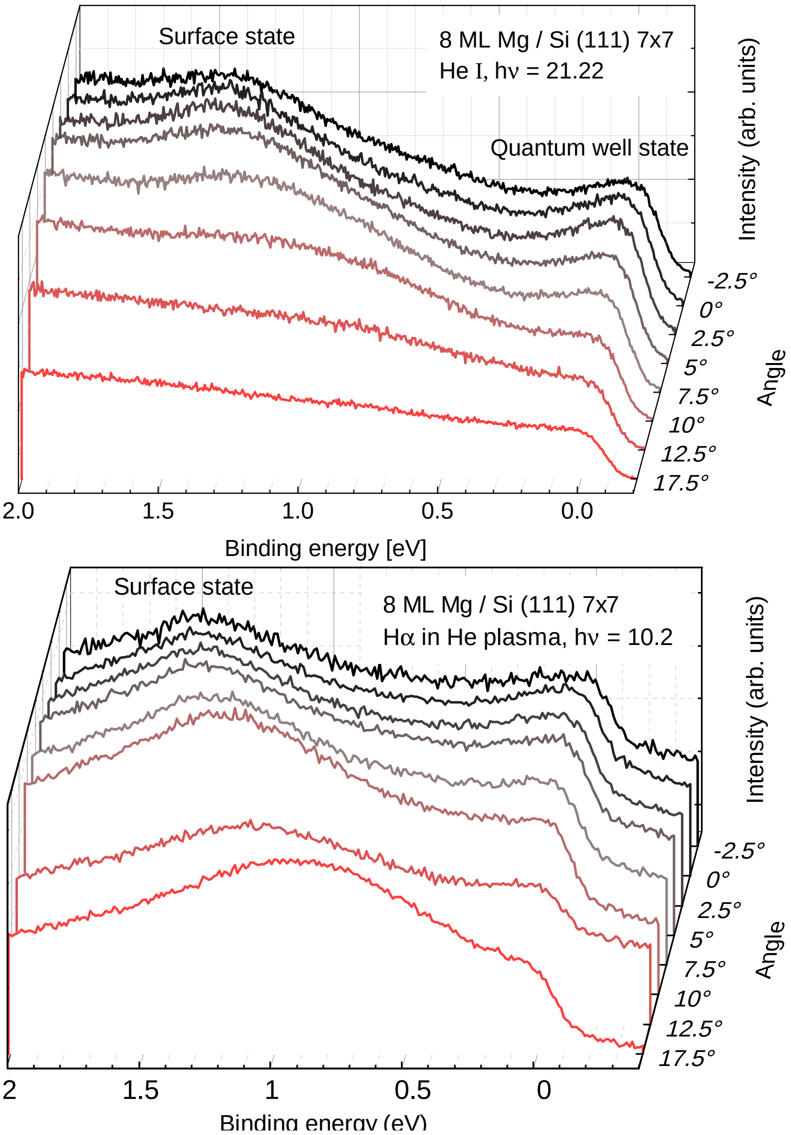

Figure 5.15.: Upper panel: UPS scans of a 8 ML thick Mg film on Si(111) 7x7 recorded under He I illumination. The emission angle is varied between -2.5° and 17.5°. The surface state decreases with increasing emission angle and shifts energetically towards the Fermi edge. The quantum well state, which is visible between -2.5° and 2.5° degrees vanishes quickly for higher angles. Lower panel: The same as upper panel, but showing the H α part of the scan.

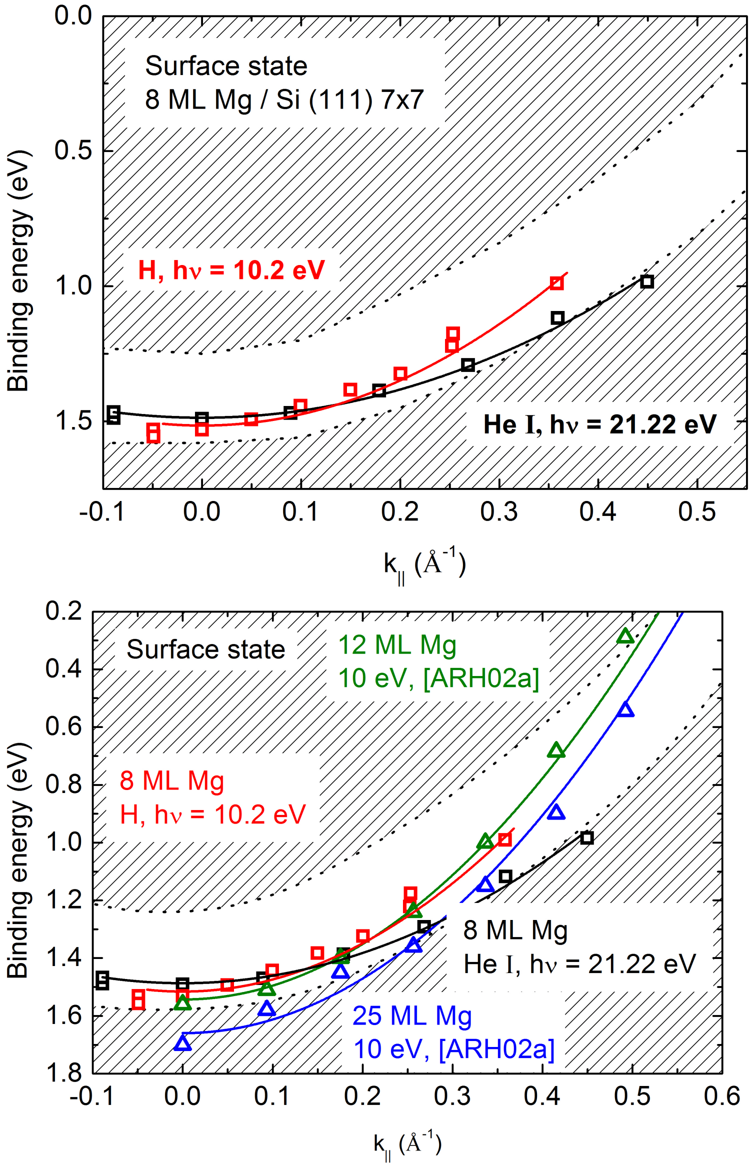

Figure 5.16.: Upper panel: Dispersion of the surface state if a 8ML thick Mg film on Si (111) 7x7 recorded using H α (red squares) and He I (black squares) radiation. The parabolic fit to the H α data has a steeper slope than for the helium light. The shaded regions depict the projected bulk bands as determined from [BGGP86, CSFK99]. Lower panel: Comparison to a 12 and a 25 ML Mg film by Aballe *et al* [ARH02a]. The slopes by Aballe are similar to each other, but steeper than the ones found for our samples. The shaded regions depict the projected bulk bands as determined from [BGGP86, CSFK99].

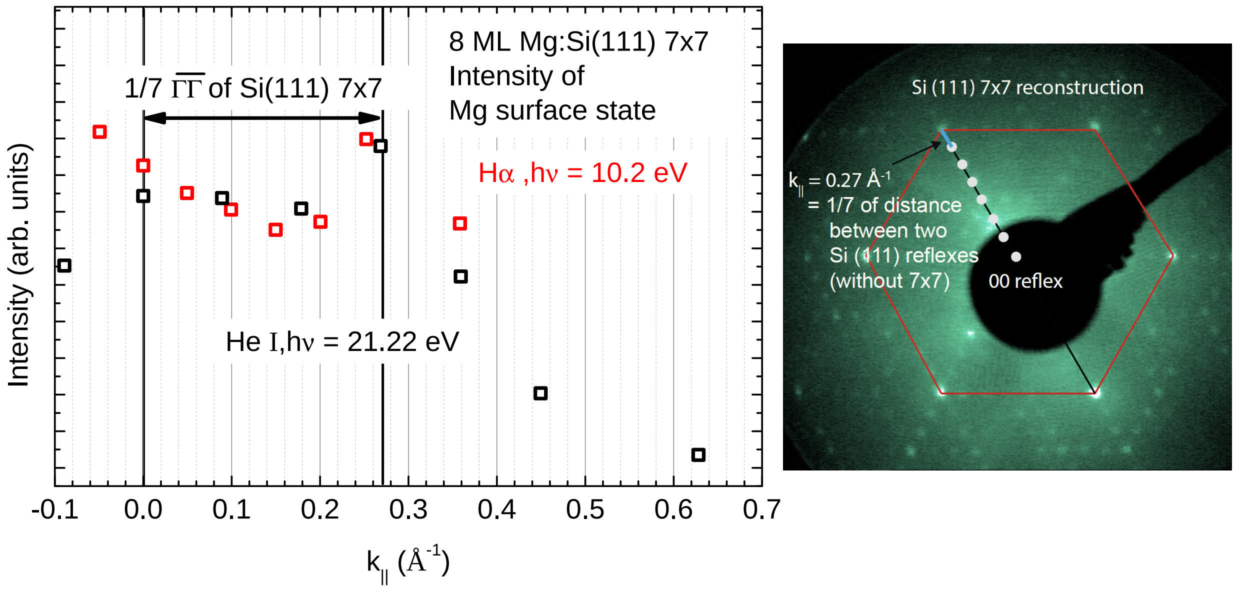

Figure 5.17.: Left panel: Angular dependent intensity of the surface state of a 8 ML Mg film on Si(111) 7x7 for He I and H α light. When $k_{||}$ is 1/7 of the distance of two neighboring points of the Si (111) reciprocal lattice the intensity suddenly increases. Right panel: Schematic of the distance between two neighboring points of the Si(111) reciprocal lattice and the Si (111) 7x7 reconstructions periodicity.

An interesting observation is made when one looks at the angular dependence of the intensity of the surface state as it is shown in the left panel of Figure 5.17. The intensity decreases with increasing angle and thus increasing $k_{||}$. But when $k_{||}$ equals exactly 1/7 of the distance of two neighboring points of the Si(111) reciprocal lattice, $k_{||} = 0.27$ Å^{-1}, the intensity suddenly increases for only this value. This coincides with the position of the first LEED spot of the 7x7 reconstruction of the Si (111) surface, shown schematically in the right panel of Figure 5.17. Obviously this increase is due to the periodicity of this reconstruction and resulting in constructive interference. The Mg film has to be sufficiently thin to allow for the substrate to influence the XPS signal.
The increase in Figure 5.17 is evidence to the fact that the periodicity of the 7x7 reconstruction is preserved upon the deposition of magnesium. This was also found to be the case for the deposition of silver and amorphous silicon [Mön95].

6. Oxidation of crystalline Mg surfaces

6.1. Oxidation of crystalline Mg surfaces

After electronic and chemical characterization (see chapter 5) the Mg diodes are exposed to clean molecular oxygen. The diodes are kept at temperatures around 100 K during the reaction. The current through the device and the pressure in the chamber are monitored at all times (see chapter 3.4). Figure 6.1 shows the measured current and chamber pressure for the oxidation of a 32 ML thick Mg film on Si(111). At $t = 0$ s the leak valve is opened. An immediate current is detected that increases with time to a certain maximum and decreases close to zero at later times. The pressure jumps to 10^{-8} mbar at $t = 0$ s and increases slightly with time. The general trace of the current has been explained before [Gla05, GN04] for polycrystalline Mg films on Si and will be discussed in detail in chapter 6.3. It has also been shown, using infrared internal photo emission (IR-IPE), that the current increase can not be attributed to the change of diode parameters, like the homogeneous barrier height or the effective diode area. Rather it could be demonstrated that the current is proportional to the oxygen uptake and the growth of an MgO layer [Gla05, GN04, NG06, Hag09].

To compare different measurements with each other it is necessary to normalize both axes in respect to the oxygen exposure, because the number of reactions per time step is directly proportional to the number of impinging atoms. For the time axis this was done by calculating the oxygen exposure in Langmuir via

$$L(t + \Delta t) = \frac{p(t + \Delta t) \cdot \Delta t}{1.33 \cdot 10^{-6}} + L(t). \tag{6.1}$$

One Langmuir corresponds to a coverage of roughly one monolayer when assuming a sticking coefficient of unity. Another way of calculating the exposure is to determine the impingement rate per second using equation 3.1 and dividing by the total number of surface atoms. Again assuming a sticking coefficient of unity this amounts to a monolayer coverage of the sample. These two normalizations are interchangeable. For the case of the prepared Mg(0001) surfaces 1 L = 0.548 ML coverage. In this work the x-axis is normalized to Langmuir exposure.

The y-axis was normalized by dividing the current by the chamber pressure.

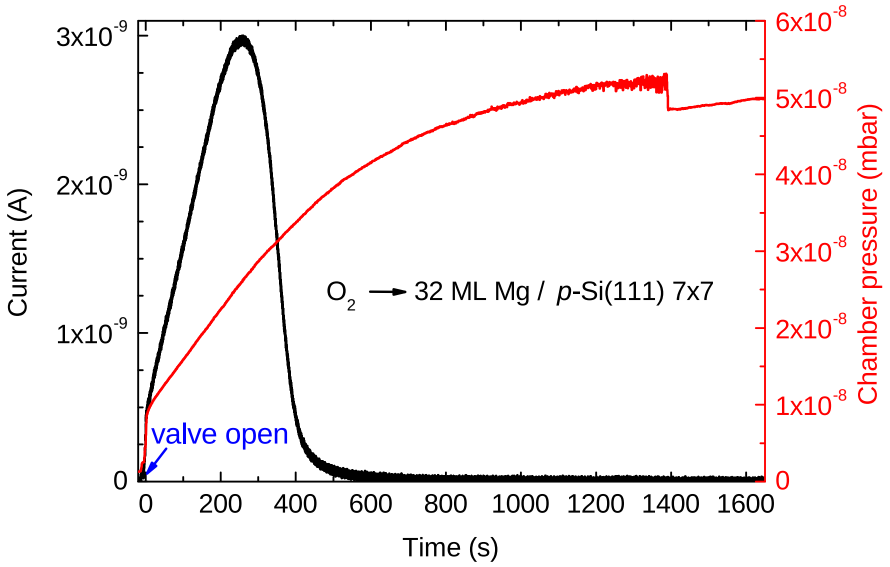

Figure 6.1.: Detected chemicurrent (black line) during the oxidation of a 32 ML Mg / Si(111) diode. At $t = 0s$ a high precision leak valve is opened to a O_2 reservoir. The O_2 pressure does not remain constant but increases with time (red line).

Figure 6.2 shows the normalized chemicurrents for four different diodes, each with a different Mg film thickness. Of these four different current traces, the red curve shows a quiet noisy signal. Experiments that showed current traces with a smaller signal to noise ratio then this one were not used in the evaluation of the data. Two main features can be seen immediately. The maximal current value I_{max} differs between the diodes. At the same time the width and the position of the maximum of the signal change. Generally all traces showing the maximum at later times also show a larger full width at half maximum. The value I_{max} is the maximum of the normalized current traces. As it is the one distinguishable current value in the trace it is used to compare the oxidation of different samples.

As is seen in Figure 6.2 I_{max} has a thickness dependence. Figure 6.3 shows all determined values for the maximal current versus the Mg film thickness of the corresponding diode.

Two regions of very large currents can be identified. Between film thicknesses of roughly 9-10 ML and 12-13 ML, made up by 7 different diodes in total, the measured I_{max} values are 2-3 times larger then for their neighboring diodes. These regions of increased current seem to be very sharply confined to certain thicknesses.

The second aspect to notice in Figure 6.3 is the general decrease of the current with increasing film

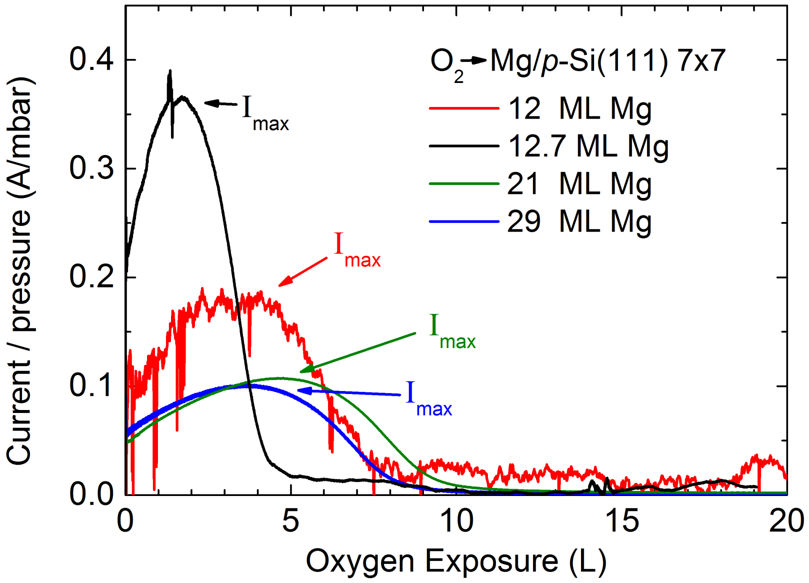

Figure 6.2.: Normalized chemicurrent signal for four diodes with different film thicknesses. The value I_{max} corresponds to the maximal current value during exposure.

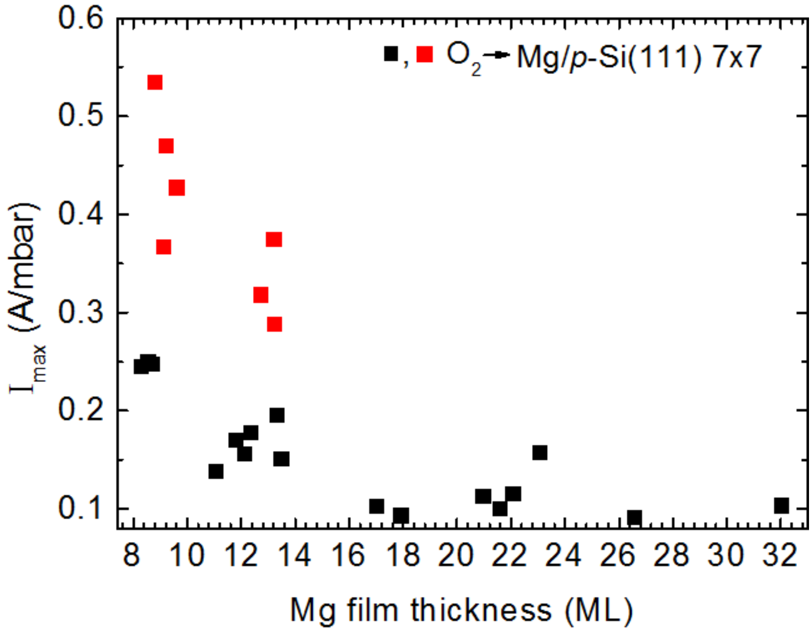

Figure 6.3.: Value of I_{max} plotted versus the film thickness of the magnesium film. Two thickness regions with large current signal can be identified (red squares).

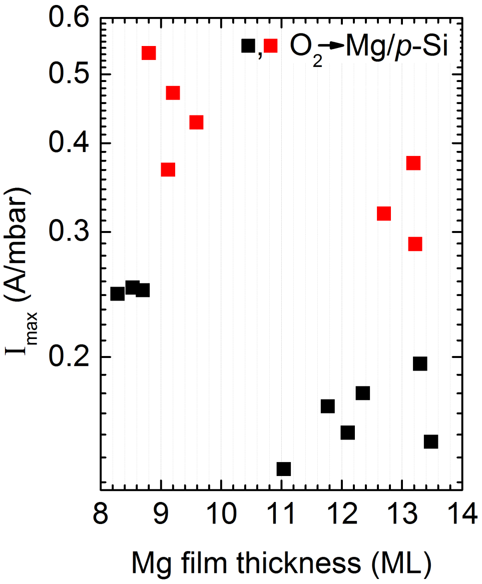

Figure 6.4.: Zoom of Figure 6.3 into the thin film regime. The y-axis is now in a logarithmic scale.

thickness. Assuming the validity of Beer's law - equation 2.14 - one can fit the black squares using an exponential function. The decay length is determined as $\lambda_{\text{cryst}} = 6.1 \pm 1$ nm - see Figure 6.10. This is, within errors, the same value as was determined by Glass *et al* for polycrystalline Mg films on Si(111) of $\lambda_{\text{poly}} = 5.4 \pm 1$ nm [GN04].

The zoom into thicknesses up to 14 ML is shown in Figure 6.4. It becomes even more evident, that the enhancement of the current is very sharply defined in a certain thickness range, when looking at the 12-13 ML region. The red squares are confined between 12.3 and 13.3 ML. Remember at this point that the film thickness is very precisely determined by the position of the first quantum well state after preparation of the film. Even if the total film thickness would be at fault for a certain diode this energetic position tells precisely which of two diodes has a larger film thickness so that the succession of the diodes is given correctly.

The empty region between 10 and 11 ML is due to the fact that the evaporation rate of Mg is not always the same from one day to another. Towards the end of this work three diodes have been made to fill this region but they ended up being slightly too thick or thin.

The main questions that arise from this experiment are: What is the mechanism behind this current increase? Is it e.g. a transport effect like reduced electron loss in the Mg film for these two thickness regions or could the reason be something like an enhanced reaction rate? If the reaction rate is larger, for a certain sample, but the reaction itself remains the same than the chemicurrent

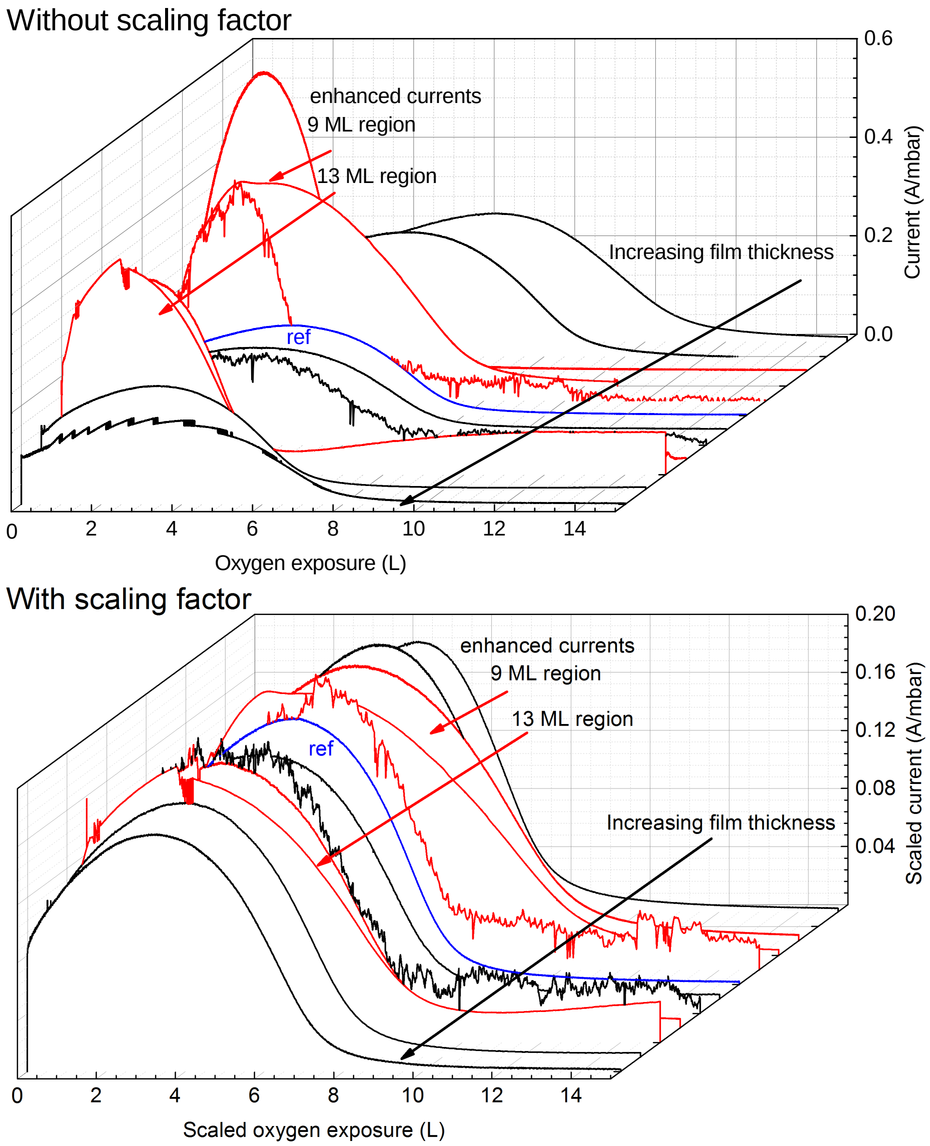

Figure 6.5.: Chemicurrent traces for different diodes. The red traces are those with an increased I_{max} value. The film thickness increases from stern most trace to the front most one. The traces in the upper graph are as recorded, in the lower graph the axes are scaled by the scaling factors L and S. As can be seen all traces can basically be scaled to look the same. When $L \approx S$ this is a clear sign that the increase in the current is due to an enhanced chemical reactivity and not due to transport effects. This means the oxidation for these film thicknesses happens faster and thus I_{max} is more intense.

traces should be scalable to resemble the same trace. By scaling the current (y)-axis by a certain factor $1/S$ and at the same time the exposure (x)-axis by the factor L it should be possible to make the different traces look similar. If for example the current for diode A is twice as large as for the reference diode B then $S = 2$. If the reaction was qualitatively the same for the two samples then $L = 2$.

The effect of the scaling is shown in Figure 6.5. The upper panel shows the chemicurrent traces for different diodes from the enhancement and their neighboring thickness regions. The thickness increase from the hindmost trace to the front. The red curves represents those diodes on which a high $\mathrm{I}_{\mathrm{max}}$ value were measured, see Figure 6.4. The blue curve is the reference to which all other traces are scaled to. For example the red line just behind it has to be roughly halved in the current to get the maxima to the same level. At the same time the exposure on the x-axis has to be doubled. The scaled traces are shown in the lower graph. All traces align and look similar. If the L and S scaling factors were equal, $L = S$, then this is evidence that the currents measured for all diodes have the same origin and that the reaction happens faster for these specific thickness regimes. The red traces, especially in the smaller thickness region show more intensity at higher exposures to the right of the maximum. This is most probably due to the oxidation of the 2nd Mg monolayer, as shown and discussed in chapter 6.4.

Figure 6.6 gives the determined values for the two scaling factors L and S. The values do align along the angle bisecting line. A linear fit shows a slope of 1 ± 0.06 with a high correlation between the two values, given by the Pearson $R = 0.96$. The deviation from the bisecting line is small. It could stem from a slight error in the attenuation length. The samples showing an enhanced $\mathrm{I}_{\mathrm{max}}$ seem to scatter around $L = S = 2$ while the other samples scatter around $L = S = 1$.

In this graph the values for the current scaling factor S and for the current $\mathrm{I}_{\mathrm{max}}$ are thickness corrected using Beers law - see 2.14 -

$$A(\mathbf{k}) \sim \mathrm{e}^{(-\frac{d}{\lambda_m})},$$

where λ_m is the attenuation length of 6.1 ± 1 nm. For the determination of the attenuation length see chapter 6.2. The exposure axis needs not to be corrected.

The scaling factor S for the current is plotted versus film thickness in 6.7. The blue circles give the scaling factor. The right y-axis and the black squares give the $\mathrm{I}_{\mathrm{max}}$ values. The dashed blue line fives the scaling factor of unity. The scaling factor follows $\mathrm{I}_{\mathrm{max}}$ rather closely, even for the extreme thicknesses of 1 ML and 44 ML. Whenever the detected current is higher than average, the scaling factor is as well.

Figure 6.8 focuses on the diodes in the region of the two enhancement regions. There seem to be

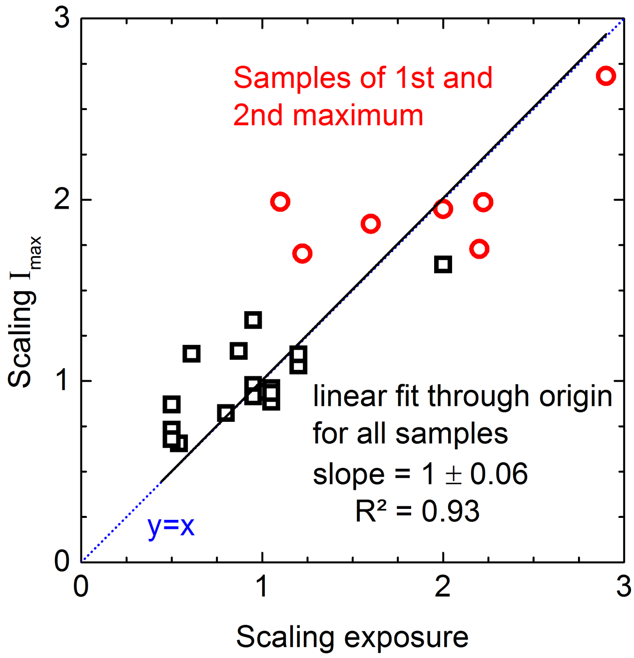

Figure 6.6.: Scaling factors L and S plotted against each other. The values align closely to the angle bisector line of $y = x$.

two different levels for the scaling factor, as already shown in Figure 6.6. Either it is two, thus the current is double that of the reference, or it is around one. One could speak of two types of Mg films. One type with a fast adsorption and reaction of oxygen molecules and a second type where the reaction rate is roughly halved.

The question that arises is, whether one can find an attribute of the film or the experiment that is responsible for this behavior. Figure 6.9 shows four different parameters plotted versus the thickness corrected $\mathrm{I}_{\mathrm{max}}$ values. From top to bottom these are the chamber pressure $p(t)$ at the time of $\mathrm{I}_{\mathrm{max}}$, the work function ϕ_{m} of the Mg film as determined in chapter 5.3.1, the homogeneous barrier height ϕ_{hom} - see chapter 5.1 -, and the density of states at the Fermi edge DOS(EF), as determined from UPS measurements shown in chapter 5.3.1. Shown in each graph is a linear fit to the data and the resulting Pearsons R, also called coefficient of correlation. Basically this value is a measure of the linear correlation of two variables. A value of ±1 is total positive/negative correlation, while 0 means no correlation at all between the values on the x- and y-axis. R close to 0 for the chamber pressure, work function and barrier height to the maximal current $\mathrm{I}_{\mathrm{max}}$. Only the density of states shows a rather strong correlation of 0.81. This is evidence that an increased density of states is in

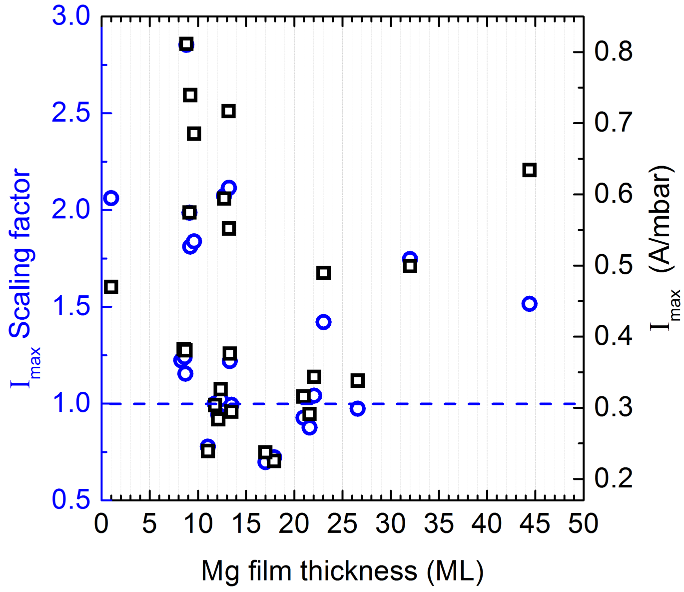

Figure 6.7.: Scaling factor S (blue) and I_{max} value (black) plotted versus the Mg film thickness. The values for S follow the values of I_{max} closely. The values for S and I_{max} are corrected by Beers law.

fact correlated with the increase in reaction rate.

That the DOS at E_F changes with thickness is obvious, when looking at Figures 5.9 and 5.10. One can see the 1st, 2nd, 3rd quantum wells show up at the Fermi edge for a certain thickness. This increases the DOS (E_F). They shift to higher energies with increasing thickness. The onset of the quantum well states can be deducted from Figure 5.10. The 1st QWS is at energetically located at the Fermi edge at a thickness of $7-8$ ML. The 2nd appears at around 14 ML. The two reactivity maxima on the other hand are found at around 9 ML and 13 ML. So while the first is shifted roughly 1 ML to higher thickness, it is the other way around for the second. In fact the quantum wells are only seen clearly, in UPS, when they have shifted $\sim$ 0.1 eV to higher binding energies. The DOS (E_F) is also not maximal when the QWS is slightly shifted. This would explain the 2 ML shift for the first reactivity maxima, but not for the second. Of course it could also be that the ML onset off the second quantum well state is slightly off. In Figure 5.10 the slopes of the quantum well positions are different and could result in a different onset. The fits used to describe the energetic positions of the QWS are empirical and do not necessarily predict the onset correctly. If the 2nd QWS showed a behavior like the 3rd QWS, in Figure 5.10, the onset would be closer to 13 ML and then align with the 2nd reactivity maximum.

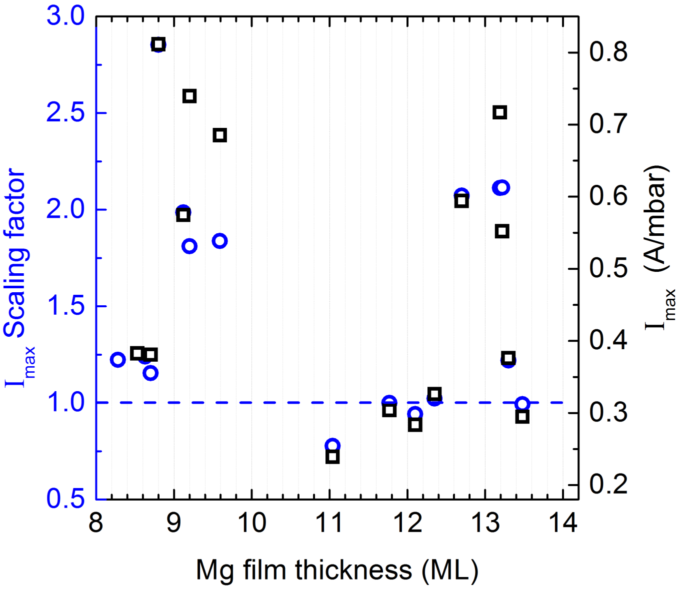

Figure 6.8.: Zoom into the smaller thickness for Figure 6.7. One can see how the scaling factor closely follows the I_{max} values as it should if it is in fact a valid description. The values for S and I_{max} are corrected by Beers law.

6.2. Comparison to polycrystalline films and hot charge carrier distribution

As has been mentioned before, similar experiments have been performed previously on polycrystalline Mg films [GN04]. Figure 6.10 shows the data from that work combined with data from this thesis. The polycrystalline data have been recorded using a chopped molecular oxygen beam instead of the back-filling method and the data have been converted via the total flux to the I_{max} [A/mbar] unit. The black and red squares are the same data as in Figure 6.3. The black line is the exponential fit (log scale) to the data for the determination of the attenuation length. The blue squares are the data points for polycrystalline films with the blue line as a fit. The attenuation lengths are $\lambda_{poly} = 5.4 \pm 1$ nm and $\lambda_{cryst} = 6.1 \pm 1$ nm and are, within errors, the same. There are not enough data points for the high I_{max} diodes to determine a decay length. However, the decay length for these also seems to be similar to the others. The black and blue squares are basically parallel to each other only with a factor of roughly 5 difference. This factor is easily explained when one considers the barrier height of the diodes. As has been shown in chapter 5.1 the homogeneous barrier height of the Mg/p-Si(111) 7x7 samples is $\Phi_{hom} = 0.567 \pm 0.04$ eV. For the polycrystalline Mg films on

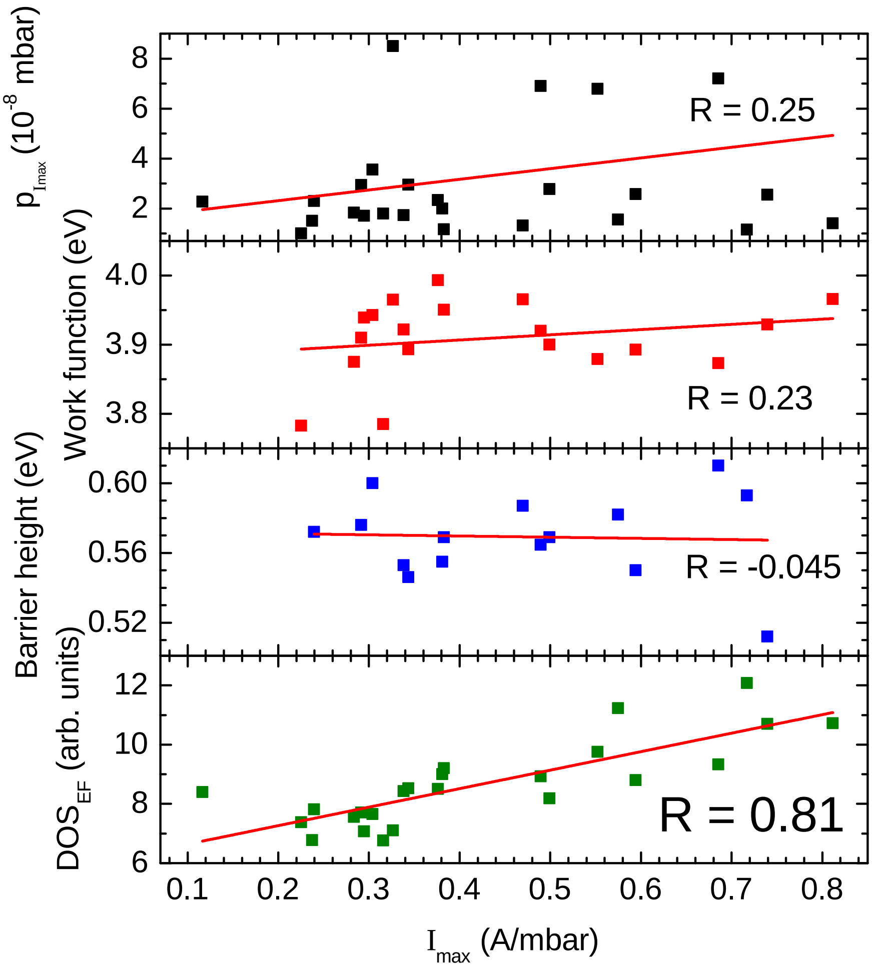

Figure 6.9.: Different values determined during the measurements plotted versus the thickness corrected I_{max} value. From top to bottom these are the chamber pressure, the work function of the Mg film, the homogeneous barrier height of the diode and the density of states at the Fermi edge, as determined by UPS. For all values the linear correlation was determined and the linear correlation is represented by the Pearson R value. Only the density of states, with an $R = 0.81$, seems to be correlated to the current.

Si(111) it was $\Phi_{hom} = 0.8 \pm 0.04$ eV. A higher barrier height results in smaller currents. It serves as a high pass filter for the charge carriers and thus the electrons have to have more energy to be detected in the polycrystalline diodes. As has been mentioned the current decays exponentially with film thickness and thus one can extrapolate the sensitivity of a film with a vanishing thickness $d = 0$ nm. This extrapolation is needed to compare this experiments here to others investigating

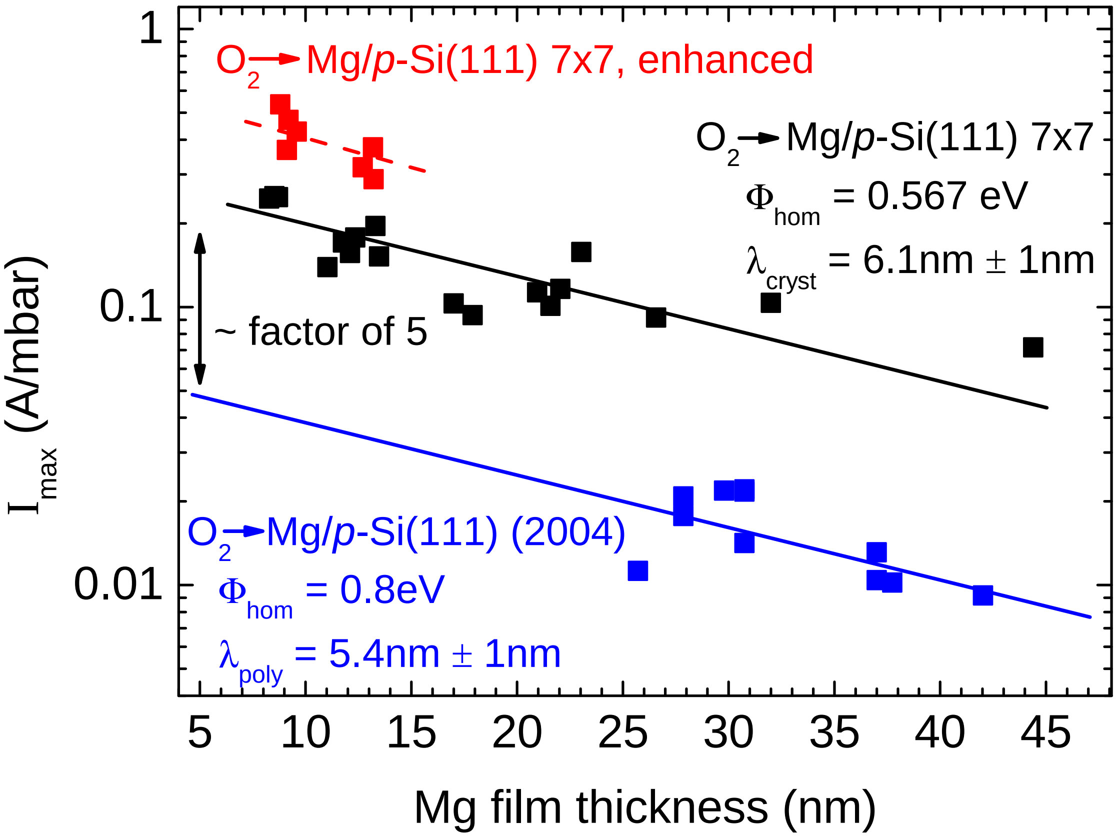

Figure 6.10.: Detected chemicurrents for the oxidation of crystalline (black) and polycrystalline (blue) Mg films [GN04]. The decay lengths, blue and black solid lines, for these two films are similar, within errors. The dashed red line denotes the possible decay length for the samples showing a high I_{max} value. There is roughly a factor of 5 between the two film types. Note the different homogeneous barrier heights of $\Phi_{hom,\ cryst} = 0.56$ eV and $\Phi_{hom,\ poly} = 0.8$ eV.

the same reaction on different kind of diodes/surfaces.

Spectroscopic analysis of the hot charge carriers is not easily done in the chemicurrent setup as it is not possible to simply change the barrier height on a single diode. But over the years different Schottky diodes, with an reactive Mg film on top, have been prepared and measured. Nienhaus and Glass showed results for the oxidation for Mg on two different Si(111) interfaces [NG06], Gesell and Arakawa measured the electron exoemission, where the surface barrier serves as the high pass filter [GA72]. In my diploma thesis I presented results on Mg/Si(001) diodes [Hag09] and in the course of this work the crystalline Mg films, which show again a different Schottky barrier hieght, have been discussed. Additionally, thin Mg films that have been evaporated onto Ag/Si(111) Schottky diodes have been investigated in this work. The silver film is not reactive to oxygen at thermal velocities and thus the detected currents originate from the reaction of O_2 with the Mg film. The data on the Mg:Ag/Si(111) diodes is presented in chapter 7.

Combing the results of all those experiments and determining the efficiency for charge carrier detection with different barrier heights allows to spectroscopically analyze the oxidation of Mg. In graph 6.11 the efficiency is plotted versus the homogeneous barrier height, or in case of the exoemission the surface barrier height. The y-axis is on a log-scale.

The filled circles are data points obtained during this work, the hollow circles represent older data. For the Mg/Ag/Si diodes see chapter 7. The data points align in a nearly perfect straight line, meaning that they can be described by a Boltzmann distribution $\propto \mathrm{e}^{-E/k_\mathrm{B}T_\mathrm{eff}}$ with an effective temperature of $T_\mathrm{eff} = 1760$ K. If one extrapolates the red line to a barrier of 0 eV it yields an efficiency of 1.03 electrons per impinging O_2 molecule. So basically every reaction excites a electron-hole pair with an energy ≥ 0 eV. For all these experiments a sticking coefficient of unity is assumed. If it is smaller than unity the efficiency would increase even further.

The effective temperature is introduced as a parameter to describe the distribution. It can not be identified as the electron or surface temperature. The Boltzmann description of this distribution has been used in the past by theoreticians and experimentalists on a variety of systems, mostly concerning the adsorption of hydrogen atoms on metal surfaces [MBPH08, TK10, LP06, KNN07, SDH11]. Independent on the method applied to calculate or measure this effective temperature it is mostly determined to be in the range of 1200-1700 K. Experimental values tend to be slightly higher than the theoretical ones.

It is possible to calculate the percentage of reaction energy that goes into the excitation of the electron system.

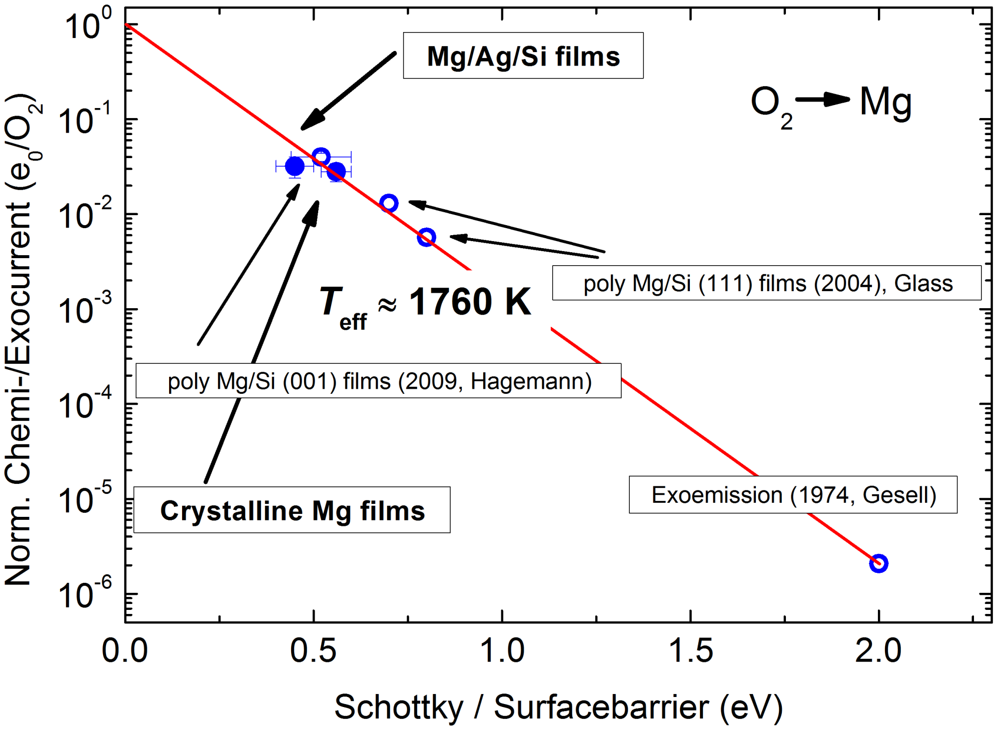

Figure 6.11.: Distribution of the hot charge carriers in the reaction of molecular oxygen with magnesium films. The data points can be described with an exponential Boltzmann-like distribution with an effective temperature of 1760 K. Extrapolation to a barrier height of zero results in one electron generated per reaction [GA72, NG06, Hag09].

To represent the probability the Boltzmann function has to be normalized.

$$f(E) = \int A e^{-\frac{E}{k_B T_{\text{eff}}}} dE = 1.03,$$
$$A = \frac{1.03}{k_B T_{\text{eff}}}.$$

The average energy is then given by

$$< E >= \frac{1.03}{k_B T_{\text{eff}}} \int_0^\infty E e^{-\frac{E}{k_B T_{\text{eff}}}} dE = \frac{1.03}{k_B T_{\text{eff}}} (k_B T_{\text{eff}})^2 = 1.03 \cdot k_B T_{\text{eff}}. \tag{6.2}$$

Inserting the effective temperature of 1760 K from graph 6.11 yields an average energy of ~165 meV per electron, or 330 meV per electron-hole pair. To estimate the reaction enthalpy of the MgO formation one has to look at the standard enthalpies of formation $\Delta_f H^0$ of oxygen atoms and magnesium oxide. Those are given in table 6.1 together with the standard Gibbs energy of formation [Lid02]. The dissociation of the oxygen molecules costs 250 kJ/mol and the reaction with a Mg

Species	Δ_fH^0	Δ_fG^0
MgO	-601.6 kJ/mol	-569.3 kJ/mol
O	249 kJ/mol	231.7 kJ/mol

Table 6.1.: Enthalpies of formation of the MgO and O [Lid02].

atom yields 600 kJ/mol. So as an estimate this reaction dissipates roughly 3.6 eV per impinging atom or 7.2 per molecule. If one takes the Gibbs free energy the value is more or less the same with 3.5 eV per atom. Both values do not strongly depend on temperature, as the main factor is the heat capacity which is does not vary strongly within between 100 K and 300 K. One can estimate the temperature dependence of the enthalpy of formation when changing from temperature T$_1$ to T$_2$ using the definition of the heat capacity

$$H(T_2) = H(T_1) + \int_{T_2}^{T_1} C_p dT \tag{6.3}$$

The temperature dependent heat capacity can be estimated at low temperatures $T < \theta_D = 760$ K by

$$C_p \sim C_v = 9NR \left(\frac{T}{\theta_D} \right)^3 \int_0^{\theta_D/T} {\frac{\tau^4 \mathrm{e}^\tau}{\mathrm{e}^\tau - 1}}^2 d\tau. \tag{6.4}$$

Calculating this yields a change of the enthalpy of formation to the standard enthalpy of formation of only $\sim$ 4 kJ/mol at a substrate temperature of 100 K. This is negligible.

The oxidation of magnesium thus has a reaction enthalpy of 7.2 eV per impinging molecule and an average excitation of the electronic system, of 330 meV. Thus a minimum of 4.5% of the total energy that is dissipated by the reaction go into direct excitations of the electronic system. This is a minimal value, because the sticking coefficient is not in fact unity. This becomes obvious when looking at Figure 6.5 where the exposure at I$_{\mathrm{max}}$ is around 3 L. If the sticking coefficient was in fact unity the maximum current value should rather be around half a ML coverage - see chapters 2.4, 6.3 and [HH74]. Thus if we assume a sticking coefficient of 0.2 the efficiency for electronic excitations would go up by a factor of 5. It might also be that the interface transmission for the charge carriers is smaller than unity. This would affect the effective temperature value only if the transmission probability differs strongly, but it immediately increases the percentage of reaction enthalpy that goes into non-adiabatic dissipation. A value of 30 % seems more realistic though this probably still underestimates the real value.

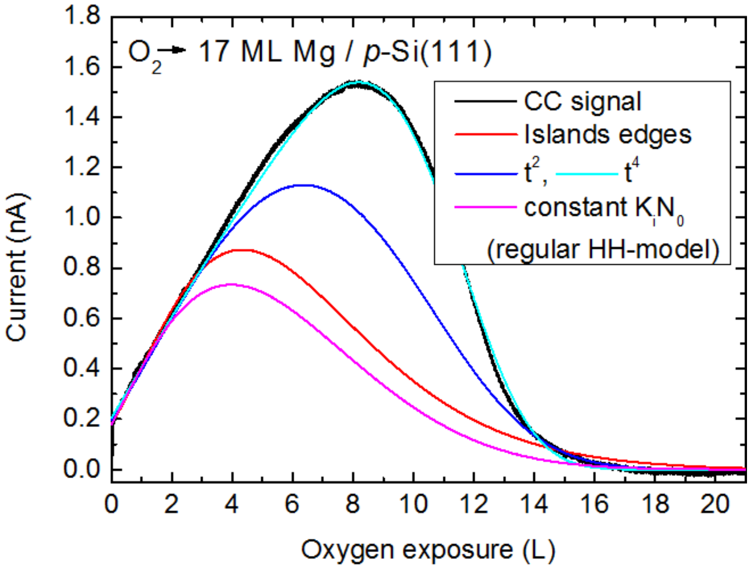

Figure 6.12.: Fit of the detected chemicurrent signal (black) during the oxidation of a 17 ML Mg film. The magenta colored fit results from the regular Hudson Holloway fit. The other colors represent different kind of fits, all of which assume a time-dependent $K_iN_0(t)$ factor. The priority for the fits was to fit the left flank of the current trace as good as possible.

6.3. Analysis of the chemicurrent trace in respect to oxide growth

The chemicurrent trace can give insight into the growth mechanism of the oxide. For polycrystalline Mg films Glass and Nienhaus have shown [GN04] that the trace can be described by the nucleation and growth model proposed by Hudson and Holloway [HH74]. This model was briefly explained in chapter 2.4.

Figure 6.12 shows the chemicurrent signal during the oxidation of a 17 ML Mg film. The colored lines represent different fits based on the nucleation and growth model. In the original description the metal and the oxide surface are treated to be completely similar. Consequently diffusion constants and mean stay time show no time dependence - see equation 2.18. This assumption leads to equation 2.19, which describes the detected chemicurrent. The fit obtained using this basic model is colored in magenta in Figure 6.12. One can see that it describes the current well for the very initial part of the trace up to an oxygen exposure of roughly 2 L. To higher exposures the nucleation and growth model clearly does not describe the data sufficiently well any more. The current is to small and the right flank is not steep enough. $K_iN_0 = 1.9 \cdot 10^{-31}$ cm^4 in this fit.

As the factor K_i is proportional to the diffusion constant D_s and if the diffusion constant was in fact time dependent $D_s(t)$, as it differs e.g. on the metal and the oxide surface, one would have to derive the time dependent equation 6.5 rather than 2.18

$$1 - \Theta = \exp(-K_i(t)N_0q(t)^2t^2). \tag{6.5}$$

For this a description of the time evolution of $D_s(t)$ and the flux $q(t)$ is required. The latter is not a problem as the chamber pressure is measured during the entire experiment and can be fitted by a polynomial function.

If one would calculate a mean diffusion constant D_s it should be equal to the pure metal surface at the beginning of the experiment. For later times the relative weight of the metal surface diffusion should diminish and the oxide surface diffusion should dominate.

As a first idea one might assume that the contribution of the oxide islands to the diffusion constant has to be proportional to the oxide island coverage of the surface. But as the reactions of oxygen with the metal take place only at the edges of those islands the time evolution could rather depend on the square root of the coverage. To describe this the chemicurrent trace in Figure 6.12 was integrated and then fitted by a Boltzmann function. This Boltzmann function was then used to describe the coverage driven transition from the metal diffusion constant D_m to that of the oxide islands D_o. The diffusion constant is proportional to the $\mathrm{K}_i\mathrm{N}_0$ factor from the nucleation and growth model and this is then given in this description by

$$D_s \propto K_i(t)N_0 \propto \frac{K_{i,m}N_0 - K_{i,o}N_0}{1 + \mathrm{e}^{(t-t0)/dt}} + K_{i,o}N_0. \tag{6.6}$$

The result of this fit is shown as the second smallest trace, which is colored in red, in Figure 6.12. It matches the measured current slightly better than the regular nucleation and growth model for low exposures. The overall agreement is still very poor though. $\mathrm{K}_{i,m}\mathrm{N}_0 = 1.74 \cdot 10^{-31}$ cm^4 for the metal and $\mathrm{K}_{i,o}\mathrm{N}_0 = 3 \cdot 10^{-32}$ cm^4 for the oxide surface in this fit.

The left and right flank of the chemicurrent trace look quite asymmetrical. The decay behind the maximum is rather steep. This is in contrast to the regular nucleation and growth model [HH74], Figure 2.10 and could be evidence for a rather strong time dependence and a t^a dependence of the mean diffusion constant, described by the following equation

$$D_s \propto K_i(t)N_0 \propto -\frac{K_{i,m}N_0 - K_{i,o}N_0}{t_k^a}t^a + K_{i,m}N_0, \tag{6.7}$$

introducing the parameter t_k as a time of inflection. The result of this fit is shown as the blue curve in Figure 6.12 for $a = 2$ and as the cyan colored trace for $a = 4$. The latter fit seems to describe the

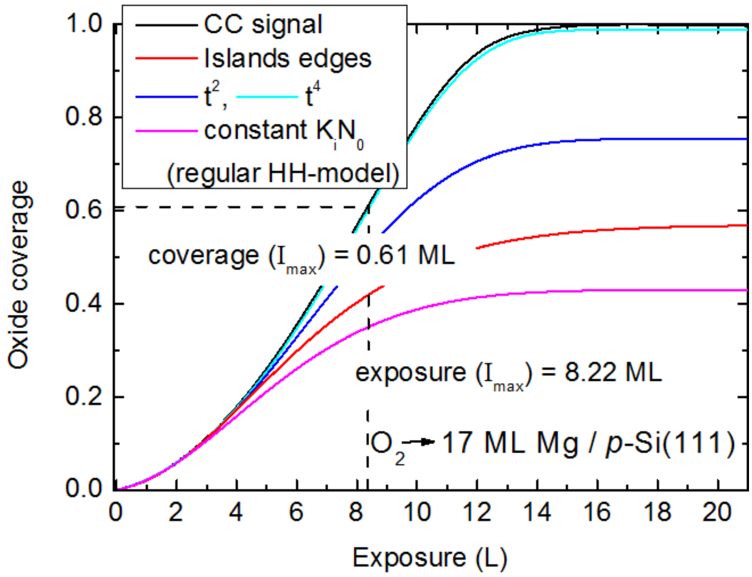

Figure 6.13.: Oxide coverage of the magnesium surface plotted versus the oxygen exposure. Here it is assumed that only the first ML is oxidized.

chemicurrent trace very well. $K_{i,m}N_0 = 6.5 \cdot 10^{-31}$ cm^4 for the metal and $K_{i,o}N_0 = 6.1 \cdot 10^{-32}$ cm^4 for the oxide surface in this fit. The quality of the fit becomes apparent when looking at the oxide coverage of the surface shown in Figure 6.13 - derived by integrating the traces in Figure 6.12. At the end of the experiment the first ML of the Mg surface is completely oxidized, when described by the nucleation and growth model. Hence the detected current is normalized to a coverage of 1 ML at high exposures. The other traces are adjusted accordingly. It will be shown in chapter 6.4 that this is not true for the samples that show a high current maximum. These samples could not be described satisfyingly by the modification to the nucleation and growth model presented here.

One can see, that the regular nucleation and growth model only satisfyingly describes the oxidation of the first tenth of a ML coverage. The other fits, using equations 6.6 and 6.7 with $a = 2$, also only manage to fit the oxidation of up to 0.3 ML. Only the t^4 fit, using equation 6.7 with $a = 4$, resembles the detected trace well.

The maximum of the chemicurrent is at an exposure of 8.22 L. Looking at Figure 6.13 this would mean that it is around a coverage of 0.6 ML. The nucleation and growth model predicts the maximum to be at around 0.4 ML, see Figure 2.10. The general form of the chemicurrent trace also differs to that of the nucleation and growth model. For the chemicurrent trace the right flank is very steep compared to the left flank. It is rather vice versa for the nucleation and growth model - see Figure

2.10 and the magenta colored line in Figure 6.12.
The tendency that the more crystalline the samples become, the less suited the nucleation and growth model is, was mentioned before in chapter 2.4. A possible explanation may run along the following line of thought:

1. First of one has to assume that the diffusion coefficient for the O_2 molecules is larger on the oxygen covered surface. The molecule is slightly decoupled from the Mg surface, thus it feels less of an attractive force from the metal. This also means it is more weakly bound, which in turn results in a higher diffusion coefficient (but possibly also smaller mean stay time).

2. Secondly, it could be that there are fewer islands present on the surface for the case of a crystalline surface.

This assumption might also be justified because the number of defects per surface area is very probably smaller. A hint that this could be the case is the fact that these films show very pronounced surface and quantum well states in UPS. If the surface was covered by a large number of defect sites/oxide islands these structures would not be present. And in fact they are not for the polycrystalline film, see Figure 5.9. If we assume the extreme case of only one oxide island, the radius of this island has eventually to become very large, basically half the sample diameter. If on the other hand many different islands are present as nucleation centers on the surface, this reduces the average distance for an adsorbate on an oxide islands to the island edge. That is why it could be, that on a sample with high island density one does not see an effect of the diffusion constant of the oxide, because the islands are just too small. Only on a surface with a small nucleation site density does the higher diffusion coefficient of the oxide surface become relevant. Hudson and Holloway mention to have had small contaminations of carbon and oxygen on their surfaces [HH74]. The number of nucleation sites could have an effect on the position of the maximum as well.
The effect of one island versus many was simulated by a simple model of a 255x255 grid. Two initial setups are compared. In one there are 10 initial oxide islands of size 1, resulting in an edge length of 40, present on the surface. The second setup is that of only one island with the same initial edge length of 40. In this simulation edges are those grid points that are adjacent along the x- or y-axis to a oxygen covered grid point. The nucleation and growth model assumes a linear growth rate independent of the island size, thus this is also assumed here. In each time step every edge position becomes covered by oxygen. This results in new edge positions which are covered in the next time step. The time development of this simple model is shown in Figure 6.14. One can see that the maximum number of edge positions for the single island setup, red solid line, is delayed in time, has

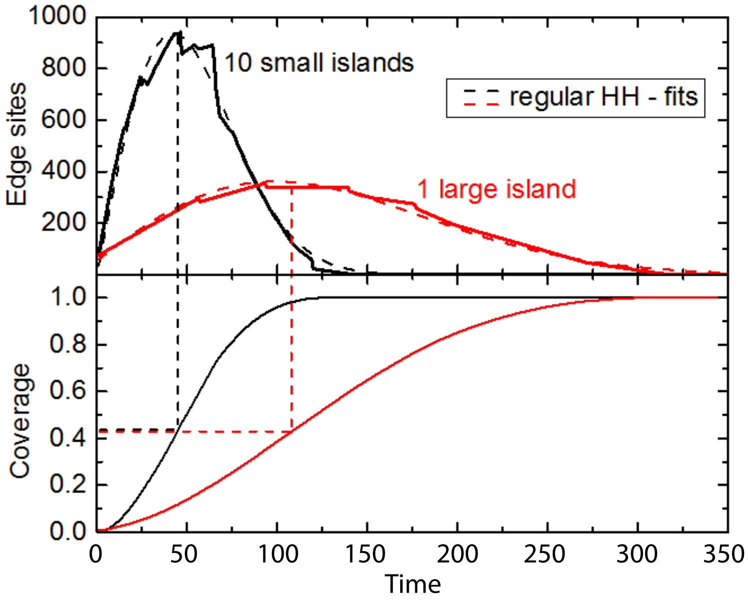

Figure 6.14.: Simulation of island growth in the extreme case of 1 island or 10 islands on a 255x255 grid. Both traces of the evolution of the number of edge positions with time can be fitted using the nucleation and growth model. The single island setup needs a smaller K_i factor. The maximal number of edge positions is at the same coverage for both initial states.

a larger FWHM and is smaller than for the 10 island setup, black solid line. This is shown in the upper panel. However, the coverages at the time of the maximum are nearly the same. The final coverage is the same for both setup, as it should be.
Both traces can be fitted by the regular nucleation and growth model, using a time independent K_i factor. K_i is roughly $1/10$ smaller for the single island than for the multiple island situation. These fits are drawn as dashed red and black lines. This result means, that the few initial island situation cannot be the singular effect resulting in the detected chemicurrent traces.

Other explanations can be discussed, that do not necessarily need two diffusion coefficients. For example it could be that by flashing the Si substrate we created a stepped surface. The growth of an oxide island on a step gets hindered and slowed down when the island radius becomes larger than half the step width. This could possibly contribute to the slow increase and the delayed current maximum compared to the nucleation and growth model.

More detailed and sophisticated theoretical calculations will have to be made to further explore the change in the chemicurrent trace from polycrystalline to crystalline films.

It should be noted here that the chemicurrent traces that were used for the above interpretation were the ones that did not show the QSE enhanced reaction rate. In the next chapter it will be shown, that these samples really only oxidize in the first monolayer. This assumption of the nucleation and growth model still holds in the description applied above.

6.4. Oxygen uptake as determined by XPS

Qualitative analysis

As was discussed earlier, in chapter 2.3, Aballe and coworkers investigated the thickness dependence of the oxidation of monolayer Mg films using x-ray photoelectron emission microscopy. They found that certain film thicknesses show a higher level of oxidation than others after the same oxygen exposure - see Figure 2.8 and [ABL$^+$04]. The oxidation experiments were performed at 50°C and consequently they showed bulk oxidation for long exposure times. This becomes obvious when looking at Figure 2.7. For longest exposure times, given in the publication as 13 L, the relative weight of the intensity of the oxide component of the Mg 2p signal is close to 100%.

This is different from the experiments shown in this work. These were done at liquid nitrogen temperatures and this effectively confines the oxidation of the Mg film to the first monolayer [GN04, NG06, Gla05, Hag09]. The oxidation of deeper lying monolayers is strongly hindered. It can only be seen weakly at high exposures for the samples showing a high reactivity, as current intensity at higher exposures than the current maximum. Hence, a comparison between the chemicurrent experiments and the work by Aballe has to be done carefully.

Figure 6.15 shows the relative weight of the oxide component of the Mg 2p peak taken from XPS measurements after the oxidation experiments were done. To transport the sample into the XPS position in the UHV chamber it could not be avoided that the sample heated to room temperature. The XPS data is recorded at room temperature as well.

The total exposure for all these samples was between 13 and 49 L. But as the bulk oxidation at liquid nitrogen temperatures is prohibited very efficiently the error due to this non calibrated exposure is supposed to be negligibly small. This will be discussed in more detail below.

In Figure 6.15 the relatively constant values in the area marked in red as '1st monolayer' are assumed to be the value of the relative weight of the $\mathrm{Mg}_{2p,ox}$ component when only the topmost layer of the Mg film is oxidized. As the bulk oxidation is very small the constant background value of this

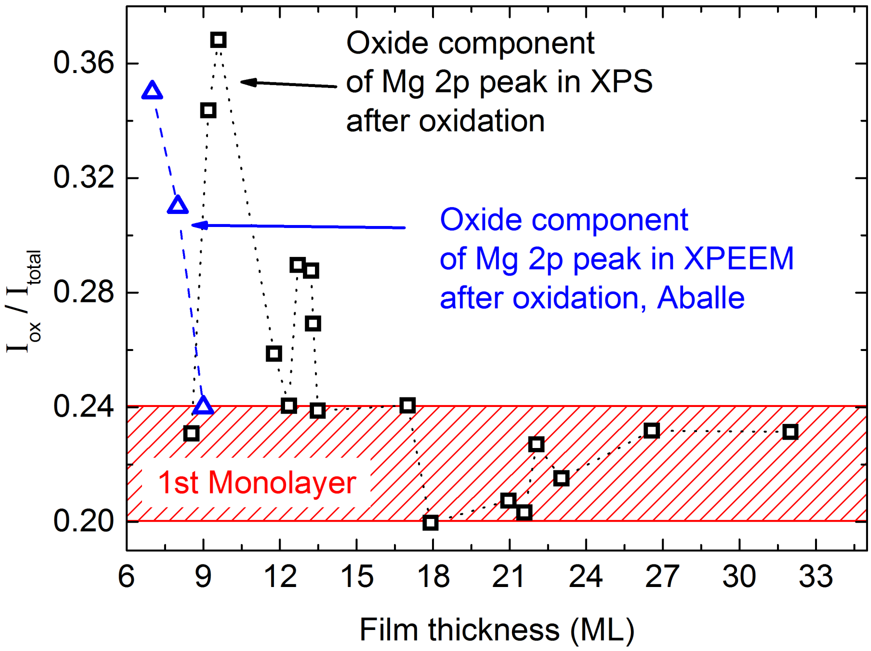

Figure 6.15.: Relative weight of the Mg 2p oxide component after oxidation. The total exposure is not the same for these samples, but the exposures are so large that the chemicurrent has diminished to basically zero. Assuming only the first ML is effectively oxidized this makes the relative error of the oxygen uptake due to different exposures after the first monolayer very small. The red area shows the relative weight of the oxide component if only the first monolayer is oxidized. This proves the above assumption to be valid. The blue triangles and lines represent data from Aballe *et al* [ABL$^+$04] for a comparable relative weight and so for an oxidation of roughly only the first monolayer.

data set can be assumed to be the first monolayer oxidation. Most samples obviously only oxidize in the 1st layer. The validity of this assumption will be discussed in more detail at the end of this section.

The blue triangles represent data by Aballe *et al* which show roughly the same background of the relative weight [ABL$^+$04]. These are shifted by about 2 ML but otherwise agree very well with our data.

The $\mathrm{Mg}_{2p,ox}$ component shows a maximum at around 9 ML and a smaller second one at around 13 ML. The increase to these maxima from the background is about 50% for the first and 20% for the second. This relative change also agrees well with the data by Aballe.

Figure 6.16 overlays the data for the maximum of the chemicurrent I_{max} - red circles - with the

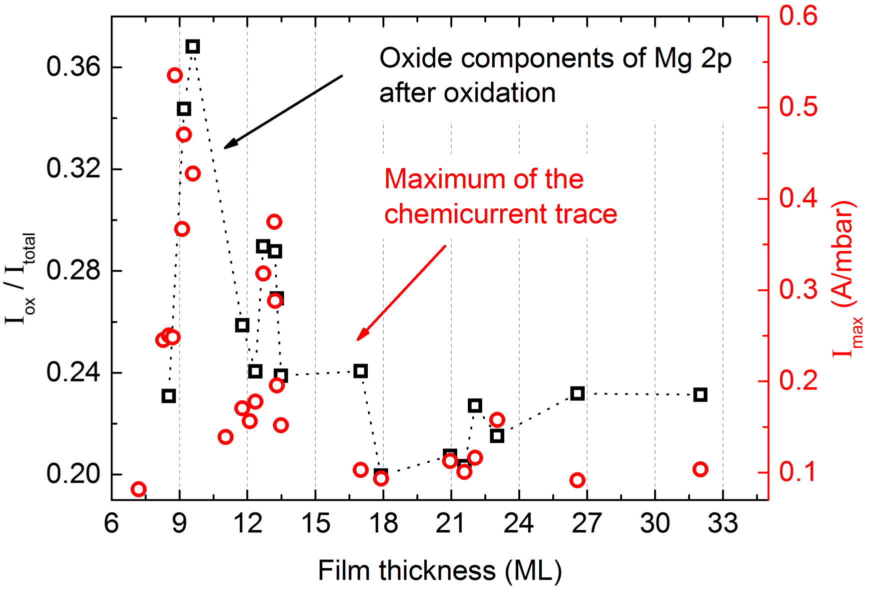

Figure 6.16.: Same as Figure 6.15 and additionally the current maxima from the chemicurrent measurements - see e.g. Figure 6.3 - are included as red circles. The oxide component follows the trend of the I_{max} value well, although they represent data taken at different times during the oxidation process. The XPS data was not recorded for all samples.

relative weight of the $\mathrm{Mg}_{2p,ox}$ component. The two data sets follow each other rather closely. The first and second maxima of the chemicurrent - see Figure 6.3 - are very well reproduced by the XPS data.

This is at first rather surprising, as the two sets of data, chemicurrent and XPS, are recorded at different times and environments, as mentioned above. Additionally, if only the first monolayer of the Mg surface was in fact oxidized then the relative weight of the oxide component should be constant. This Figure demonstrates that those samples that show a high current, thus a high reactivity and a fast reaction, show a larger oxide component in XPS as well. It seems that these samples do in fact oxidize below the first monolayer.

From this data alone one cannot say whether the oxidation rate of the second and following monolayers is increased as it is for the first one. It could be that just the onset of this slight bulk oxidation is much sooner as the first monolayer is oxidized faster, see Figure 6.5. But it actually seems as if the oxidation rate for the second monolayer is still higher for these 'fast' samples. The following argument is deducted from looking at the different trends and time values and is not sufficiently supported by hard evidence.

The total oxygen exposure of all samples is erratically different. For example for the two samples making up the first maximum in the $Mg_{2p,\,ox}$ weight the exposures are 10 L and 19 L, while the chemicurrent maximum is at 2 L and 3 L respectively. Thus the total exposure was roughly *five times* that of the exposure to the maximum. For three samples of low reactivity in the first monolayer background, with the thicknesses 8.5 ML, 21 ML and 22 ML, the maximum is at 4.7 L, 4.8 L and 3.8 L respectively. The total exposures for these samples were 49 L, 38 L and 27 L so roughly *eight to ten times* that of the exposure at the maximum. If one assumes the oxidation rate of the second monolayer to be constant for all samples, regardless of the first monolayer oxidation, than the latter three should in fact show a larger oxide component, because they were exposed to to larger amounts of oxygen in respect to the maximum exposure. The fact that they do the exact opposite and show a smaller oxide component can be seen as evidence for the higher oxidation rate of the fast samples not only for the first monolayer but also for the second.
This is possibly even more evidence for the fact that the density of states at the Fermi edge is responsible for the high currents of certain samples. The DOS_{EF} does not diminish very strongly after the oxidation experiments. Figure 6.17 shows the Fermi edge for three different samples before and after oxidation. The scans are not normalized so that the total intensities cannot be compared.

The 9 ML and 23 ML samples show some intensity of a quantum well state at the Fermi edge before oxidation. The QWS is gone after the oxidation experiment. The change is minimal and more importantly the change seems to be quiet similar for all the different samples. This means that a sample with a high DOS_{EF} before the oxidation will also show a high DOS_{EF} after oxidation when compared to other samples.
The following argument was already mentioned above and shows that an oxidation of only the first monolayer would result in an oxide component of around 0.23. If we assume an electron mean free path of 2 nm in the Mg film and furthermore assume that the emission intensity from an Mg oxide is equal to that of a Mg metal, than one can estimate the relative weight of a single, topmost, layer of magnesium oxide compared to the complete oxide signal. Both assumption seem valid, as the mean free path is given by Figure 4.1 and the ionization probability of Mg or MgO is the same [Hüf03]. The result for the relative intensity of the oxide component is 0.23 for a 2 nm film. The oxide component would show a value of 0.38 when the two topmost layers were oxidized. These values agree well with the values given in Figure 6.15 and also give evidence to the fact that the oxidation of the third and even lower layers in magnesium is basically nonexistent at these temperatures. This has been shown previously for polycrystalline films with the use of Auger electron spectroscopy and

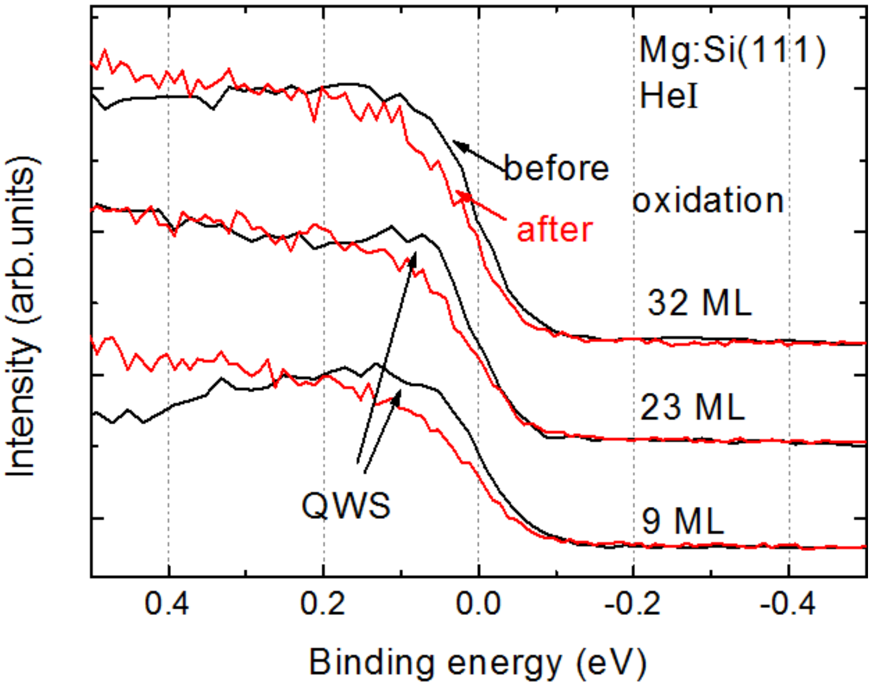

Figure 6.17.: Lo-resolution UPS scans of the Fermi edge of three different Mg films before and after the chemicurrent oxidation experiments. The change in intensity at the Fermi edge is minimal. The quantum well states disappear. These scans are not normalized so the comparability between the different samples in terms of total intensity is not given.

is still not completely understood [GN04, Gla05], as other, similar metals do show bulk oxidation, for example aluminum [Ger14].

Quantitative analysis

The QSE effect leading to more strongly oxidized films, seen in XPS and XPEEM, is about a factor of 1.5. This was shown in Figure 6.15. The effect on the detected chemicurrents is larger. As has been discussed before and can be seen in Figures 6.8 and 6.16 the increase in the chemicurrent can be up to a factor of 2.5. To start with, one might say that the chemicurrent is more sensitive to the QSE. But it has to be said again that the XPS and chemicurrents measure at different times. The chemicurrent maxima occur at an oxide coverage of roughly 0.6 ML, see chapter 6.3. The XPS or XPEEM are recorded at a coverage of between one and two monolayers of magnesium oxide. Looking closely at Figure 2.8 taken from the work by Aballe one can see that for the smallest coverages given in that graph the relative weight for the 7 ML film is about 3 times larger than for the other, neighboring layer thicknesses (lowest set of data points in the Figure). The effect of the quantum size enhancement seems to be larger for small coverages below 1 ML.

Of course the experiments by Aballe are performed on a different system (Mg on W in contrast to Mg on Si) and at a different substrate temperature (320 K to 120 K) but it seems that the XPEEM, XPS and Chemicurrent data in fact show very similar results. Namely, that the high density of states at the Fermi edge for certain film thicknesses greatly enhances the oxidation rate of the first (and second) magnesium layer. The factor of enhancement is similar for XPEEM, XPS and chemicurrent.

6.5. Discussion

In this chapter results were presented that show the influence of quantum size effects on oxidation rate of thin, crystalline magnesium layers. Certain layer thicknesses show a high electron density of states at the Fermi edge and these layer thicknesses are oxidized faster, as measured with XPS, and show a larger chemicurrent maximum than other thicknesses. The question that still has to be answered is, which part of the reaction is actually influenced by the increased electron density of states. Is it the first or the second electron transfer, see chapter 2.5, that becomes more likely?

A second question that arises is that newer publications by Aballe [ABS$^+$10], for the oxidation of aluminum, and Binggeli and Altarelli [BA06, BA08] for the oxidation of magnesium argue that it is not the electron density of states that is responsible but rather an increase in the decay length into vacuum of the electronic density of states.

The parameter that is measured in the chemicurrent is the second electron transfer, when a charged oxygen ion that moves on the metal surfaces hits an island on the surface and is incorporated into the film, chapters 2.5 and 6.3. An increase in current means that the number of oxygen atoms that react at the island edges in a certain time period increases.

That is true unless the sensitivity or the non-adiabaticity of this effect changes with time. This is not the case. The XPS measurements qualitatively reproduce the oscillations of the chemicurrent measurements although XPS and chemicurrent measure at different exposure times. This is evidence for a constant sensitivity and a non-changing non-adiabaticity of the reaction. In other words the number of electrons generated in the second electron transfer process per reacting molecule stays constant.

This said, it is plausible that an increase in current really signifies an increased number of reactions. The question remains whether this is due to an increase in the first or in the second electron transfer. Whether the number of oxygen molecules being ionized increases or the number of ionized oxygen atoms reacting at an island, without the first electron transfer being affected. In my opinion it is more likely the first process, as was also argued by the works cited above. The reason for this is, that the probability for an already ionized oxygen atom on a metal surface to desorb and leave the surface without reacting to metal oxide is unlikely, as shown by Greber *et al* [GGM+93]. Especially considering the highly mobile electron gas screening/attracting ionized particles. Thus every O^-, or O_2^-, that is on the metal surface will eventually be incorporated into the film and make a contribution to the detected current. If the incorporation rate is increased by a higher electronic density of states the incorporation rate would be slightly increased, but as the lifetime of a free ionized atom is probably very small this increase in reaction rate should be impossible to detect with our time resolution. Following this train of thought it has to be the first electron transfer that is strongly affected by the DOS. If the ionization probability of an oxygen molecule in front of the surface is increased than the consecutive steps - dissociation, second electron transfer, incorporation into the film - are also increased as the number of ionized atoms is larger. This argument is true as long as the mean stay time on the Mg surface of an O^-, or O_2^-, is much larger than the mean incorporation time.

Aballe and Binggeli explain the oscillations in the oxygen uptake also by an effect to the first electron transfer but say that the decay length into vacuum of the electronic density of states is relevant and that this value oscillates differently than the electronic density of states itself [BA08]. Figure 6.18 shows the result of density functional theory calculations on the decay length of the $\mathrm{DOS_{EF}}$ of a free standing (blue diamonds) Mg(0001) film and the same on W(110). Two maxima are present in the decay length at 9 ML and 17 ML film thickness and a minimum at 15 ML. It is unknown whether the decay length decreases or increases for thicknesses above 17 ML.

Table 6.2 gives the thicknesses for the first and second maxima from the different experiments that were mentioned in the discussion here.

One can see that for magnesium the position of the maxima/minima of the decay length, 9 and 15 ML, and the oxidation maxima/minima in XPS/XPEEM, 9 and 11 ML for XPS and 7 and 10 ML for the XPEEM, do not coincide. The position of the extrema in the $\mathrm{DOS_{EF}}$ measured by Aballe on the other hand fits their results from the XPEEM very well, as does the $\mathrm{DOS_{EF}}$ determined in this work with the XPS and chemicurrent results. This is different from the work by Aballe *et al* on the oxidation of aluminum [ABS+10], where maxima in the $\mathrm{DOS_{EF}}$ do not agree with maxima in the relative weight of the oxide component. This can be taken as evidence that in the case of magnesium the density of state has a bigger influence on the oxidation than its decay length.

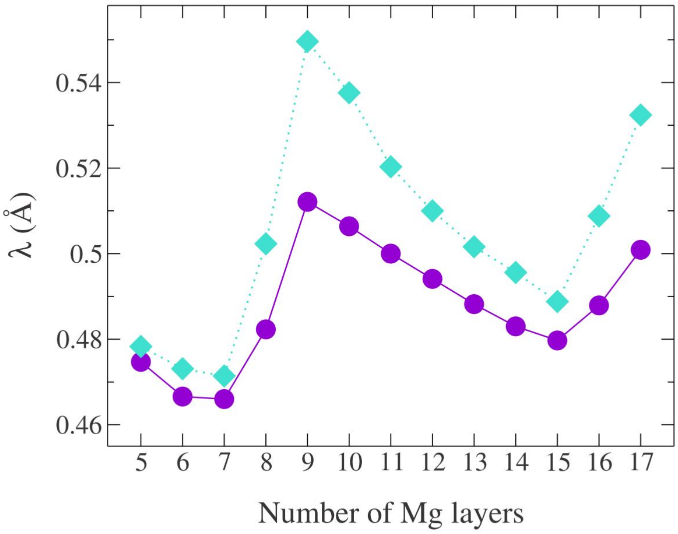

Figure 6.18.: Calculated decay length in vacuum of the electronic density of states at the Fermi edge of a Mg(0001) film on W(110) (violet circles) as a function of film thickness. The blue diamonds are the results of a free standing Mg(0001) film. Taken from [BA08].

Type	1st Max	1st Min	2nd Max
XPEEM [ABL$^+$04]	7 ML	10 ML	14-15 ML
DOS$_{\mathrm{EF}}$ [ABL$^+$04]	7 ML	10 ML	-
XPS, this work	9 ML	10-12 ML	13 ML
CC, this work	9 ML	10-12 ML	13 ML
DOS$_{\mathrm{EF}}$, this work	9 ML	10-12 ML	13 ML
Decay length [BA08]	9 ML	15 ML	≥17 ML

Table 6.2.: Values of the oscillation maxima of the oxygen uptake (XPS and XPEEM) [ABL$^+$04], the chemicurrent and the electron density decay length [BA08].

7. Oxidation of polycrystalline Mg surfaces on Ag

Recent experiments in our group, investigating the chlorination of ultrathin potassium films on Ag/p-Si(111) Schottky diodes, have shown the generation of surface plasmon coupled chemiluminescence (SPCC) and a direct influence of this radiation on the detected current [BKHN13, Bec11]. The magnitude of the SPCC depends on the thickness and structure of the intermediate silver layer. In this chapter the work on the oxidation of thin, polycrystalline magnesium films on Ag/p-Si(111) Schottky diodes is presented. For this system SPCC is found to have an effect on the detected currents as well.

7.1. Surface structure and IV-characteristics

The silicon wafer pieces used for these samples were from the same wafer as in the work on potassium films [BKHN13]. The cleaning process is similar to the one presented above in chapter 3.2, except that, instead of buffered hydrofluoric acid, regular 5% hydrofluoric acid was used. In UHV silver was deposited onto the Si at room temperature to form 10 to 60 nm thick films. The samples are then cooled to 110 K before a 1 nm thin magnesium layer is deposited. The two evaporation steps are done using different shadow masks in front of the substrate, so that the Mg layer has no direct connection to the underlying Si. This is demonstrated in the scanning electron microscopy (SEM) image of a Mg:Ag/Si multilayer, Figure 7.1. The sample was prepared in UHV and then taken out of vacuum to be measured *ex situ* in the SEM. There is no connection of the Mg layer to the underlying Si substrate and hence the Ag/Si contact is solely responsible for the rectifying behavior of the diode.

Figure 7.2 shows a SEM image of a 47 nm thick Ag film. It consists of hillocks that have an average lateral width of 50-60 nm. Additional *ex situ* atomic force microscopy measurements, an example shown in Figure 7.3, also give insight into the depth of the trenches between the hillocks. A depth of 8 nm is found, but this tip had an apex that was to large to measure the precise depth. The deepest trench measured, where the tip was small enough to reach the bottom, was 15 nm. The

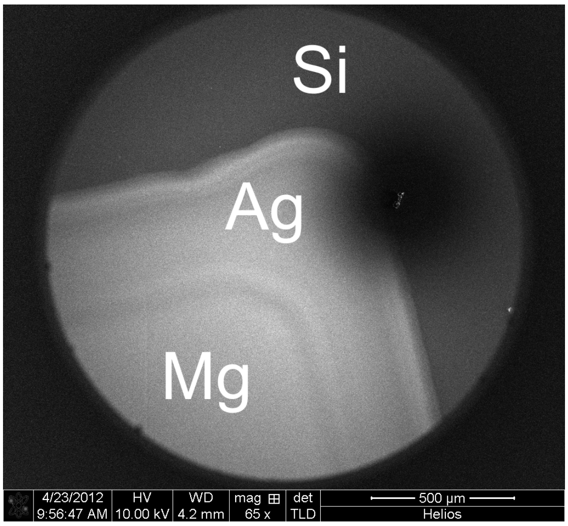

Figure 7.1.: *Ex situ* scanning electron microscopy image of the Mg:Ag/Si surface. One can easily distinguish the three different surfaces. The position shown here represents the smallest distance between the edges of the Mg and Ag film. Thus, no possible Mg/Si interface has to be considered.

characteristic width of the trenches is also roughly 10 nm. Images for different sample thicknesses are shown in appendix B and prove that these values for the width and height of hillocks and trenches are characteristic for all samples investigated, which had a thickness between 10 nm and 60 nm. Similar results were found for the same system previously [MN03] in our group.

The silver films are crystalline, as demonstrated by the LEED images in Figure 7.4. The sample is moved perpendicular to the incident electron beam to move the beam from the Ag layer to the uncovered Si substrate. The energy of the primary electron beam is 81 eV. In the central image one can see, that all the Si spots are slightly shifted to the right of the Ag spots. This shift is roughly 3 mm on the fluorescent screen. This is most probably due to the fact that the image is taken on the edge of the silver film, where we have a thickness gradient from the nominal Ag thickness of 15 nm to 0 nm. With a screen-sample distance of around 4 cm this results in an angle of 4° between the slope of the Ag film and the substrate. The length of the slope can be estimated to be 210 nm. Thus, the mean terrace width is roughly 6 nm, assuming the well known lattice constant of silver of $d_{\mathrm{Ag}} = 0.408$ nm [Kit66].

IV-curves were recorded during the cooling of the Ag film before after the oxidation. An example for an IV-curve before and after oxidation is given in the left panel of Figure 7.5 for a 1 nm Mg:

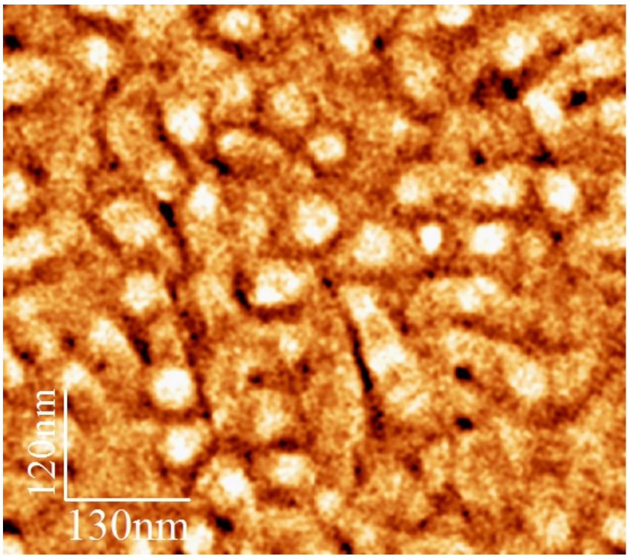

Figure 7.2.: Scanning electron microscopy image of a 47 nm Ag film on hydrogen passivated Si(111). This image was recorded with the help of Arkadius Ganczarczyk.

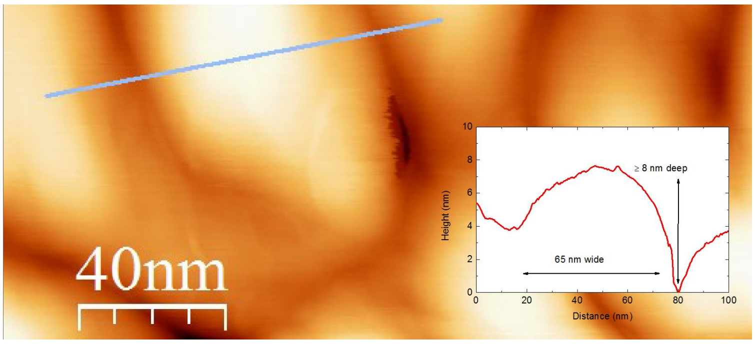

Figure 7.3.: Atomic force microscopy image of a 50 nm Ag film. The inset gives the height variation of the islands along the line drawn in the image. This image was recorded with the help of Doris Steeger.

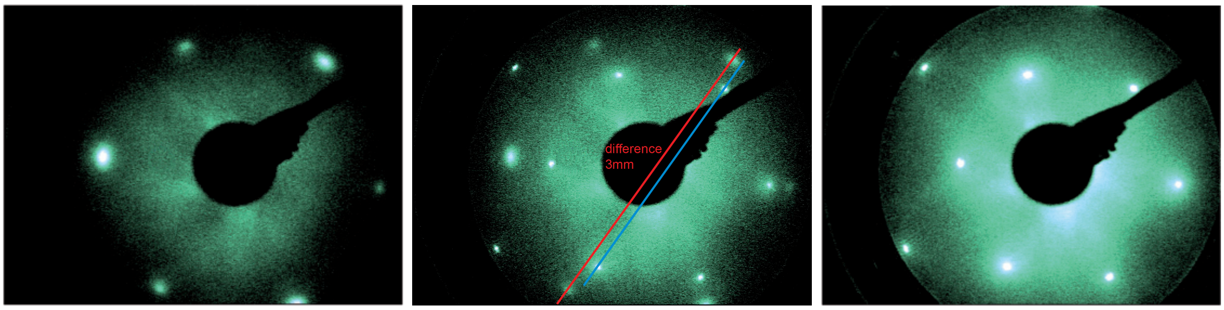

Figure 7.4.: LEED scans of a crystalline Ag film - without the Mg cover layer - prepared as described. The sample is moved perpendicular to the electron beam to move the beam from the Ag film to the uncovered Si(111) surface. The electrons have a primary beam energy of 81 eV.

17 nm Ag:*p*-Si(111) diode. The right panel shows a schematic of the experimental setup.
The IV-curves before and after oxidation are very similar and both also show a strong photocurrent when a window cover of the UHV-chamber is removed. The temperature during the two IV-curves was slightly different, which explains the difference in barrier height and photovoltage. The photovoltage of these samples - the voltage at the current minimum in the IV-curve - is slightly larger than for the crystalline Mg/Si(111) 7x7 diodes, which is evidence for the fact the the barrier height is higher for the latter. An evaluation of all the prepared silver samples yields a homogeneous barrier height of $\Phi_{\text{hom, Ag}} = 0.45 \pm 0.05$ eV. The barrier height of the Mg/Si(111) 7x7 samples was $\Phi_{\text{hom, Mg/7x7}} = 0.567 \pm 0.04$ eV.

7.2. Oxidation of Mg films on Ag/*p*-Si(111) Schottky diodes

7.2.1. Detected response currents

The oxidation experiments are performed in the same way as for the crystalline Mg films. The chamber is filled with O_2 gas through a high precision leak valve. The response current through the diode and the chamber pressure are monitored the entire time. Figure 7.6 shows the result of the oxidation of a 1 nm Mg film on a 60 nm Ag/*p*-Si(111) diode. The moment the valve is opened current and pressure increase. The chemicurrent trace resembles the traces for the crystalline Mg film, e.g. in Figure 6.1, and can be fitted by a modified nucleation and growth model, as will be shown below in section 7.2.3.
As before the chemicurrent trace has to be normalized to allow a proper comparison of different

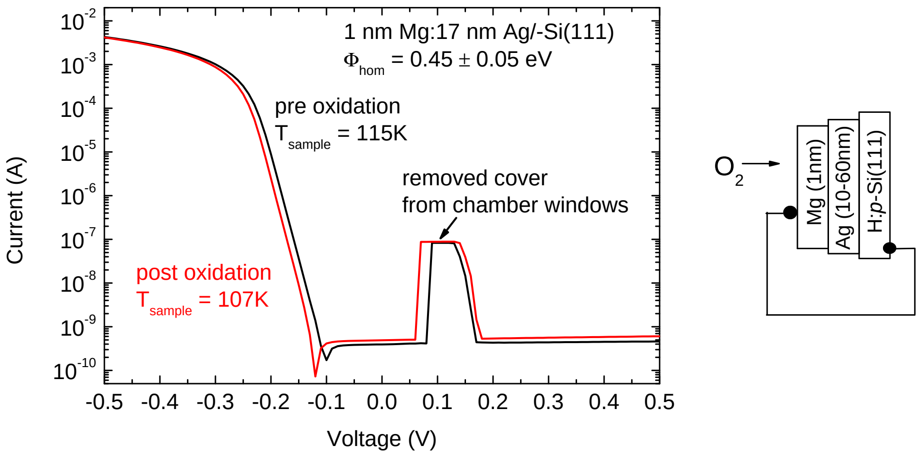

Figure 7.5.: Left panel: Typical IV-curve of Mg:Ag/p-Si diodes before and after oxidation. Both show a photocurrent when one of the window covers is removed. The photovoltage of -0.15 V is due to heat radiation from the chamber walls. Note the slight temperature difference between the two samples, responsible for the minimal shift of the lines. Right panel: Schematic of the Mg:Ag/Si diode setup. The Mg film is 1 nm thick. The silver films vary between 10 nm and 60 nm.

samples. To that end the current is divided by the chamber pressure increase and the time scale is converted into oxygen exposure. This has been done for all 15 samples measured and seven of those traces are shown in Figure 7.7. The silver thickness of the samples is between 10 nm and 60 nm. From 10 nm to 30 nm thickness the normalized current decreases roughly by a factor of 3. Then it increases towards 45 nm and finally decrease for even larger thicknesses. The shape of all the traces is similar. It is not possible to apply a scaling factor to the x- and y-axis, as in chapter 6.1, to make all the traces appear completely equal. Hence, the difference in chemicurrent intensity cannot be explained by a change in reactivity. It will be shown, that the blue lines represent samples in a thickness regime, where the current is dominated by the chemicurrent. SPCC is the main contribution to the current for the red colored traces.

From the chemicurrent traces one can deduct the maximal current value $I_{\max}$ and plot this value versus the silver film thickness, see Figure 7.8. The y-axis is on a logarithmic scale. The initial decay has a decay length of $\lambda = 12 \pm 1$ nm. This is larger than for the Mg crystalline samples from this work and the polycrystalline Mg samples used by Glass [GN04]. Between 30 and 50 nm the current increases again and decays slowly for even larger thicknesses. This increase cannot be explained within the chemicurrent framework, where the current is proportional to the reaction rate. The Mg

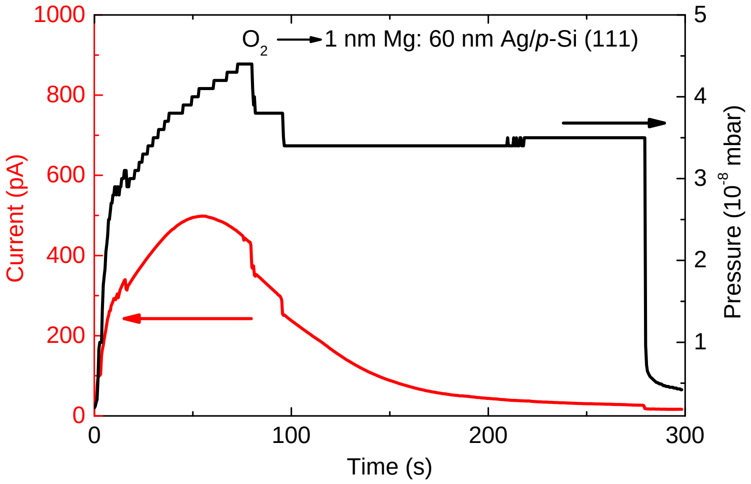

Figure 7.6.: Detected internal current through the Mg:Ag/Si diode (red curve) and chamber pressure (black curve) over time.

films in these experiments are all of the same thickness of 1 nm and thus the oxidation rate should be similar. The difference between these samples is only the silver film thickness, which does not influence the oxidation rate of the Mg surface. As is the case for the other experiments presented in this work, these samples were measured in random order.

Figure 7.9 compares the results from Figure 7.8 with data from previous publications on the oxidation of polycrystalline Mg from Glass and Nienhaus [GN04], upper panel, and with results on the chlorination of potassium on silver by Becker *et al* [BKHN13], lower panel. On the y-axis there is plotted the efficiency, detected electrons per impinging O_2 molecule, on a logarithmic scale and the x-axis represents the Mg or Ag film thickness in all panels. The yellow shaded area in the two left panels represents the thickness regime for which the chemicurrent contribution dominates the detected current. The non-shaded area in the right panels is governed by photocurrents. The black square correspond to the same data as in Figure 7.8.

The two left panels show the thickness regime, where the chemicurrent dominates the measured signal. The decay length in the chemicurrent regime detected for the oxidation of the Mg:Ag/Si (111) diodes is $\lambda_{\mathrm{Mg,\ Ag}} = 12 \pm 1$ nm. This is larger than for the polycrystalline Mg films $\lambda_{\mathrm{poly\ Mg}} = 5.4 \pm 0.7$ nm [GN04] or the chlorination of potassium $\lambda_{\mathrm{K}} = 4 \pm 0.6$ nm [BKHN13]. The reason is unclear. One difference between the setups is, that the reactive metal layer is only about 1 nm, which is 3 to 4 ML, for the Mg:Ag/Si(111) diodes. The other systems have a much thicker reactive metal layer. Why this should lead to an increased decay length is unclear.

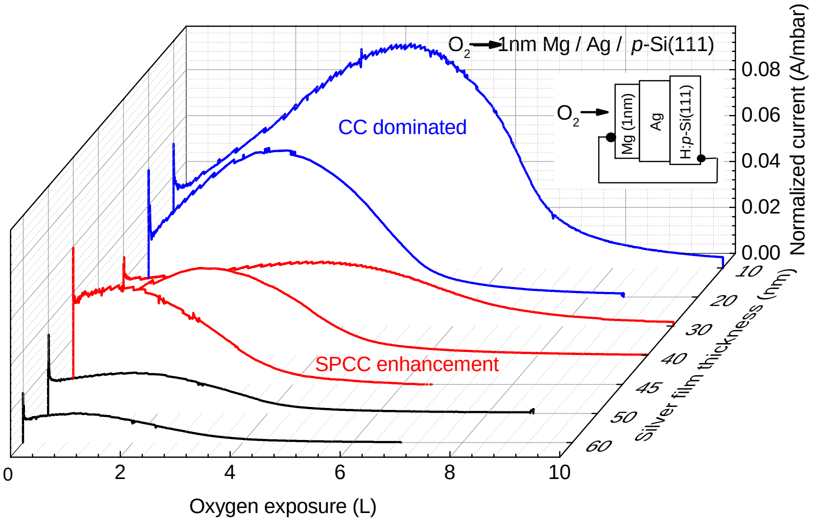

Figure 7.7.: Normalized chemicurrent traces for samples of different silver film thicknesses. The Mg on top was always 1 nm.

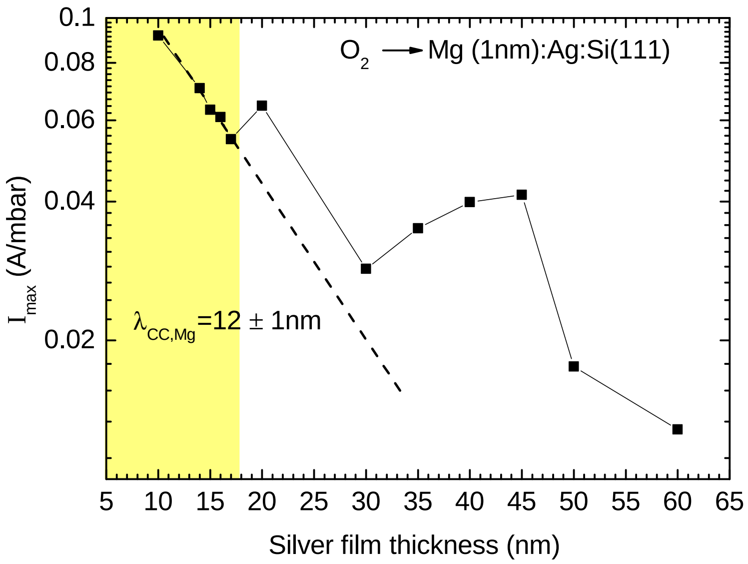

Figure 7.8.: Maximal normalized current I_{max} on a logarithmic scale versus the silver film thickness. An initial fast decrease is followed by a slight increase from 30 to 45 nm film thickness. For thicker film the current decreases again.

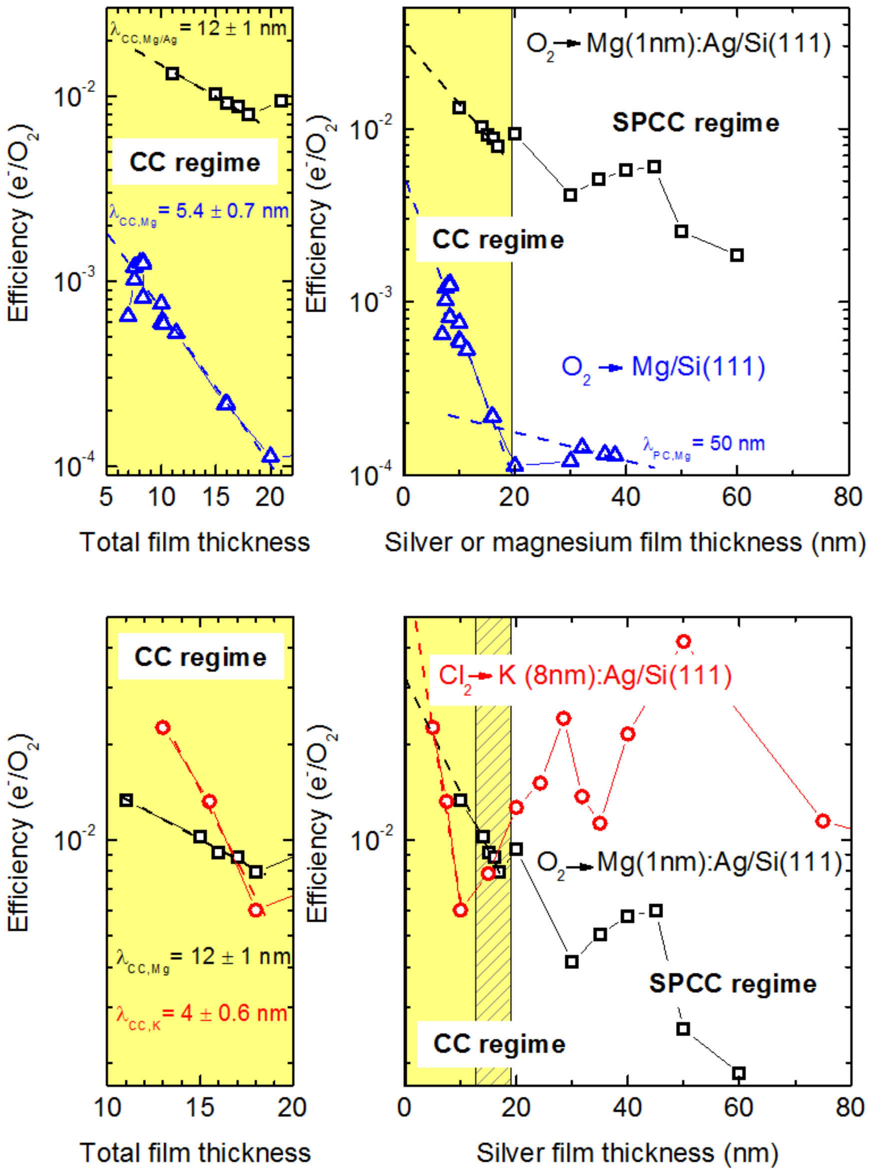

Figure 7.9.: Upper panel: Efficiency of the O_2 → Mg reaction for polycrystalline Mg films on Ag/*p*-Si(111) diodes - black squares - and on bare Si(111) - blue triangles. The initial decay in the chemicurrent region is smaller for the Mg:Ag layers. For thicknesses above 15 nm the chemicurrent on the Mg/Si films has decayed and only photocurrent remains [GN04]. The Mg layers on silver show a current increase towards 50 nm and then a, possibly exponential, decay. Lower panel: The increase towards 50 nm is also seen in the reaction of chlorine with potassium on silver Schottky diodes [BKHN13] - red squares. Two distinct maxima are found, which can be attributed to the two photon wavelengths emitted by the chlorination reaction.

Looking at the upper panels, with the comparison of the two different Mg oxidation results, two features are immediately obvious. First of all there is roughly one order of magnitude difference in the chemicurrent efficiency between the silver interlayer diodes, black squares, and the polycrystalline Mg/Si diodes, blue triangles. The reason for this are the different barrier heights of these systems. While it is $\Phi_{\text{hom, Ag}} = 0.45 \pm 0.05$ eV for the diodes with an intermediate silver layer, it is as high as $\Phi_{\text{hom, poly Mg}} = 0.8 \pm 0.04$ eV. The detected current, and with that the chemicurrent efficiency, depends exponentially on the barrier height, hence the difference. This was discussed in chapter 6.2.

The second feature to notice is the mentioned increase of the efficiency for silver thicknesses between 30 and 45 nm, shown in the upper right panel by the black squares. A similar increase is not visible for the polycrystalline films on silicon [GN04], represented by blue diamonds. As the investigated reaction is the same, the reason for this increase has to be something else.

The lower panel shows the chlorination of potassium, red circles, and the oxidation of Mg, black squares, on the same type of Ag/Si(111) diodes. In the lower right panel, where the efficiency is plotted versus the silver film thickness, the chlorination of potassium shows two distinct maxima for film thicknesses of 30 and 50 nm. The fact that any noteworthy current at all is measured for these and even larger thicknesses is surprising because the mean free path of visible light in bulk silver is approximately only 17 nm [Pal98]. Hence, as the chemicurrent has decayed already at lower thicknesses, the total current should decrease. It could be shown, that this increase can be attributed to the effect of surface plasmon coupled chemiluminescence (SPCC) [BKHN13, AG09]. The reason that the potassium chlorination has two maxima is, that this reaction emits chemiluminescence photons at two distinct wavelengths, 400 nm and 770 nm [AKW85]. Ag films show absorption maxima for light with these wavelengths at thicknesses of 48 nm and 30 nm. The oxidation of Mg shows only one maximum in the photon emission at around 470 nm [Kas74]. This results in only one maximum in the efficiency, as will be discussed in the description of the simulation below.

7.2.2. Simulation of the SPCC effect

The idea is, that light, generated at the reactive metal surface, can couple effectively to the silver surface plasmon polariton (SPP). This is due to the fact, that the silver film is rough, but with periodic structures in the 50 nm regime, which greatly enhance the excitation probability of SPPs [Rae88, MA05, Mai07]. The necessary matching of the parallel wavevectors $k_{||}$ of the light and the SPP is possible, because the emitter is close to the surface and the near field contains components

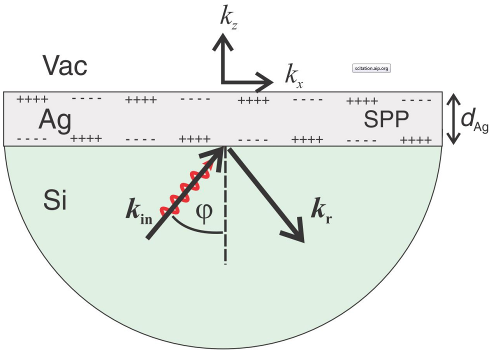

Figure 7.10.: Schematic of the attenuated total reflection (ATR) geometry used in the simulation. The light wave with the wavevector k_{in} hits the surface under an angle θ and is totally reflected, resulting in the wavevector k_r. A resulting evanescent wave travels along the Si/Ag interface and can couple to the SPPs. Also used in [BKHN13]

with large $k_{||}$ [Bar98]. The size of the near field of an emitter is in the order of magnitude of the wavelength. Here the distance of the place of reaction to the silver film is only a few nm while the emitted wavelengths are in the visible spectrum. The silver film is thus in the near field region of the reaction.

Once the SPP is generated it has to decay somehow to be detected as a current. Two possible pathways are imaginable, namely the radiative decay into the Si substrate [JBG89] and the direct excitation of single electron-hole pairs in the metal [ZZKL11, KSNH11]. When the energy of the e-h pair is large enough to cross the barrier of the diode they can be detected as reverse currents through the diode. The same is true for radiated light that has an energy larger than the band gap of silicon, thus light below ≤ 1.1 µm wavelength. The light generated by both reactions, Cl_2 on K and O_2 on Mg, is well below this value and so it is energetic enough to be absorbed in the space-charge layer of the silicon substrate. This photo-effect is in general several orders of magnitude more efficient than the internal photoemission process for detecting e-h pairs with Schottky diodes [Gla05, SN06]. This is why the radiative decay is considered to play the dominant role in the detected reverse current.

A method to describe the coupling between the Ag SPP and the radiative modes in the Si substrate has been presented in the paper by Becker *et al* [BKHN13] for the chlorination of potassium on silver films. The same argument will be given here for the oxidation of Mg on Ag.

It is not easily possible to describe the radiative decay and excitation of e-h pairs in the substrate. however, it is possible to do so with the reverse process. In the attenuated total reflection (ATR) setup, schematically drawn in Figure 7.10 in a Kretschmann-Raether like configuration [Rae88], a plane p-polarized light wave, traveling through the Si substrate with a wavevector $\mathrm{k_{in}}$ is totally reflected at the Ag-Si interface with a resulting vector $\mathrm{k_r}$. The reflectivity R of the interface depends on several factors, namely the wavelength of the incident light λ and the angle of incidence θ. Even when the wave is totally reflected at the interface an evanescent light wave, with a reduced parallel wavevector $k_{\|} = k_{\|,0}\sqrt{\epsilon_{\mathrm{Si}}}\sin\theta$, propagates along the interface and can couple to the surface plasmon, when the matching $k_{\mathrm{SP}} = k_{\|} = k_{\|,0}\sqrt{\epsilon_{\mathrm{Si}}}\sin\theta$ is fulfilled. Thus, the ATR geometry is a valid comparison to the near-field situation of the experiment. For the same reason, only the region in close proximity to the interface is of interest and we ignore light absorption in the Si substrate in the following discussion. Only the real part of the dielectric function of the substrate is needed. The reflectivity R can be calculated assuming an abrupt interface between the materials by using Maxwell's equations and the optical constants of the materials [Pal98, Pol], and is given by [Rae88]

$$R = \left| \frac{r_{\mathrm{Si/Ag}} + r_{\mathrm{Ag/Vac}}\exp(2ik_{z,\mathrm{Ag}}d_{\mathrm{Ag}})}{1 + r_{\mathrm{Si/Ag}}r_{\mathrm{Ag/Vac}}\exp(2ik_{z,\mathrm{Ag}}d_{\mathrm{Ag}})} \right|^2 . \tag{7.1}$$

The $r_{i/j}$ values are the reflection amplitudes at the respective interfaces. Those are expressed by using the frequency dependent complex dielectric functions ϵ_i of the media

$$r_{i,j} = \frac{\epsilon_j k_{z,i} - \epsilon_i k_{z,j}}{\epsilon_j k_{z,i} + \epsilon_i k_{z,j}}. \tag{7.2}$$

The z-component of the wavevector is dependent on the frequency and on $\mathrm{k}_{\|}$, given above,

$$k_{z,i} = \sqrt{\epsilon_i \frac{\omega^2}{c^2} - k_{\|}^2}. \tag{7.3}$$

The same simulations as in [BKHN13] have been done here for light with a wavelength of 470 nm, as this is the wavelength predominantly emitted by the $\mathrm{O_2} \rightarrow \mathrm{Mg}$ reaction [Kas74]. The results are shown in Figure 7.11, where the reflectivity of the interface is plotted versus the incident angle of the light. In the upper panel the thickness is increased from 5 to 100 nm in 5 nm steps. The reflectivity develops a dip with increasing thickness with a reflection very close to zero at a thickness of 65 nm and an incident angle of 13.8°. For larger thicknesses and angles the reflectivity increases again. At the same time with the reflection decrease the minimum becomes sharper. This can be seen better in the color plot in the lower panel. The incident angle is again plotted on the x-axis, while the film thickness is on the y-axis. Dark areas in the plot correspond to a small reflection. The minimum in the reflection is broad between 40 and 50 nm and then sharpens gradually. At the angle of minimal reflection, 13.8°, the entire incident light energy can be converted into SPP intensity. This means the absorption is a measure for the coupling of the radiative modes in the Si

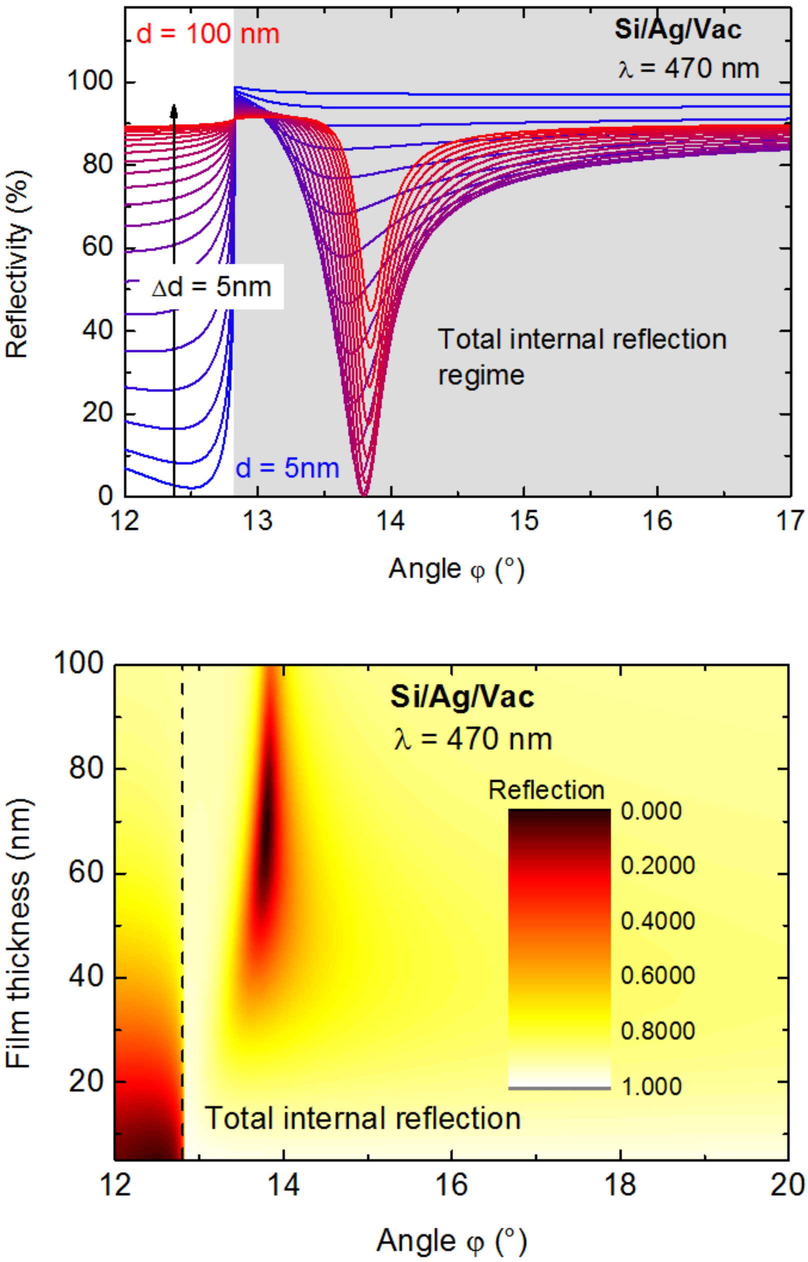

Figure 7.11.: Calculated reflectivities of the Si/Ag/Vac system for different Ag thicknesses and a wavelength of 470 nm for selected film thicknesses (upper panel) and as a color plot (lower panel).

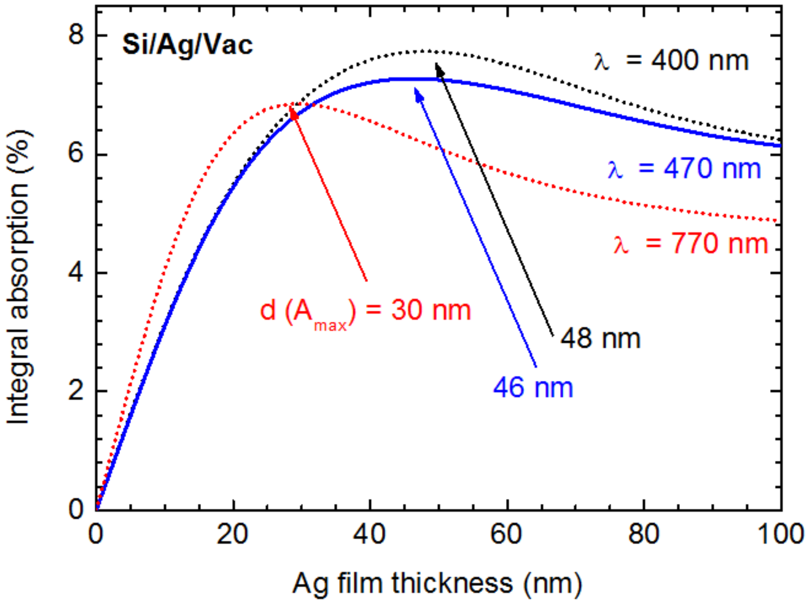

Figure 7.12.: Integral total absorption of light due to SPP excitation versus the silver film thickness for three different wavelengths. The result for the 400 and 770 nm light, dotted lines, is taken from [BKHN13]. The blue line corresponds to light with a wavelength as it is emitted dominantly by the O_2 reaction with Mg. The maximum of the absorption for this light is at 46 nm.

substrate and the Ag SPP. In the experiment light emitted from the SPP is detected in the entire half space behind the silver film. To calculate the absorption of the Si film one can integrate across the entire half space in the regime of total reflection. This integral absorption is shown in Figure 7.12 for three different wavelengths.

The dotted lines, $\lambda = 400$ nm and 770 nm, correspond to the light emitted by the chlorination reaction of potassium. The maximal absorption for these wavelengths is at $d = 30$ nm and 48 nm. These are exactly the film thicknesses at which the efficiency of current generation has its maxima as well, see red line in Figure 7.9 [BKHN13]. So for that reaction the maxima in the detected current correspond to maxima in the integral absorption of light. For the oxidation of magnesium the maxima in the total absorption of light is at 46 nm. Comparing this value to the maxima in the detected current, best seen in Figure 7.8, one can see that the thickness at which the maxima occurs is identical. This is strong evidence to support the dominant influence of SPCC on the current generation in the Schottky diode for this Ag thickness regime.

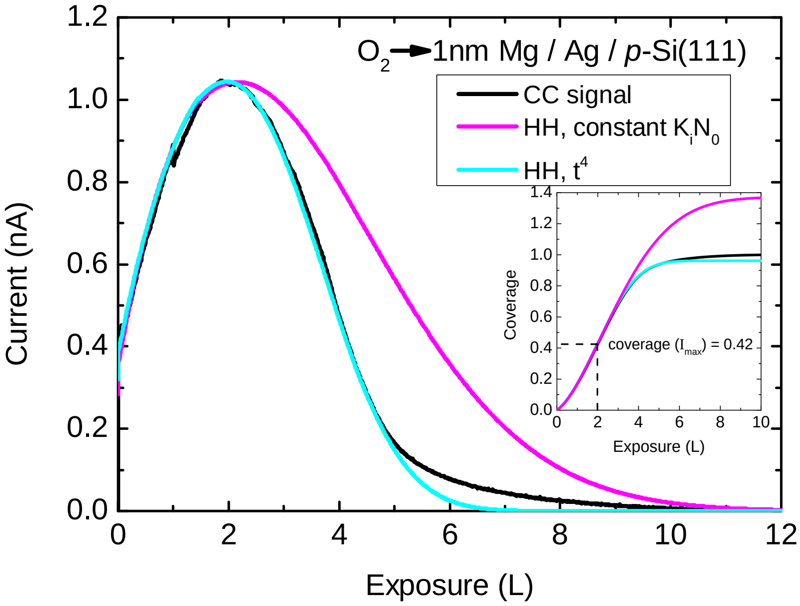

Figure 7.13.: The solid black line gives the response current versus exposure. The cyan and magenta colored lines give fits using the nucleation and growth model. The inset shows the oxide coverage of the surface. The oxide coverage at the exposure of the maximal current is 0.42.

7.2.3. Nucleation and growth model for the oxidation of Mg on Ag

The current traces in this chapter look fairly similar to the ones presented in chapter 6 on the oxidation of crystalline films. So it should be possible to describe the current by the same nucleation and growth model, equation 2.20. Figure 7.13 gives the response current through a 1 nm Mg film on a 40 nm thick Ag/p-Si(111) diode during the exposure to molecular hydrogen as a solid black line. The magenta colored line gives the best fit to the data using the regular nucleation and growth model with a constant $K_iN_0 = 6.1 \cdot 10^{-31}$ cm^4 factor, see chapters 2.4 and 6.3. Unlike the case for the oxidation of crystalline films a constant K_iN_0 describes the trace well up to exposures shortly behind the current maximum, but it strongly overestimates the detected current for higher exposure times. To describe the trace well one needs two different K_iN_0 values. For the metal one obtains $K_{i,m}N_0 = 8 \cdot 10^{-31}$ cm^4 and for the oxide $K_{i,o}N_0 = 5 \cdot 10^{-32}$ cm^4 when using a time dependent t^4 transition between the two K_iN_0 factors, see equation 6.7 with $a = 4$. As for the crystalline Mg films the time of inflection t_k is at much higher exposures than the maximum of the detected current. The values for $K_{i,o}N_0$ and $K_{i,m}N_0$ here are very similar to those for the crystalline films.

This is expected, as the surfaces, Mg and MgO, are the same and the reaction temperatures are comparable, $T \sim 100K$.

There are some differences to the previous chapter. The oxide coverage, which is given in Figure 7.13 in the inset for the detected current and the two fits, at the time of the maximum is 0.42 ML for these Mg:Ag/Si diodes. This is close to the coverage at the maximum, 0.4 ML, predicted by the regular nucleation and growth model, see Figure 2.10. For the crystalline Mg/Si the maximum was found at a coverage of 0.61 ML. This difference is the reason why the regular nucleation and growth model with a constant K_iN_0 fits the detected trace well up to the current maximum.

In chapter 6.3 the high order and crystallinity of the Mg film was proposed to be the reason for the need of two K_iN_0 factors or two different diffusion constants. For the Mg:Ag/Si films the Ag film does also show LEED spots and is hence assumed to be crystalline as well, albeit the LEED spots are more diffuse than for the Mg/Si diodes of the previous chapter. As the Mg film that is deposited onto the silver layer is only 2-3 ML thick it could retain some of the crystalline order of the silver. This would make the use of two diffusion constants necessary as assumption 4 of the nucleation and growth model is no longer valid, see chapter 6.3. If the Mg films were thicker, they could become more polycrystalline and the current traces could possibly be described by the regular nucleation and growth model again. This would be an interesting experiment to prove the effect of crystallinity on the detected current traces.

8. Oxidation of different Si(111) surfaces

In the course of this work many different interfaces and surfaces have been prepared. One idea, that lead to a short series of measurements, was to investigate the oxidation of different Si (111) surfaces. Easily obtainable by our methods of preparation are the hydrogen passivated H:Si(111) surface, that exist on the surface after the hydrofluoric acid etch. This surface should be non-reactive when oxygen impinges on it, as the hydrogen terminates the otherwise reactive clean Si surface. No current should be detectable during the exposure of this surface to oxygen in the usual chemicurrent setup and the surface should remain oxygen free.

Removing the hydrogen passivation by heating the sample to around 400°C results in the Si(111) surface. This is a highly unordered surface, as chunks of $\mathrm{Si}_x\mathrm{H}$ break away from the surface at these temperatures without the surface being able to reorganize [KMT96]. This surface should be reactive as plenty of Si atoms at the surface are missing neighbors and hence have free electron-dangling bonds. However, as no surface conductivity exists and the gold ball is only in contact with a very small portion of the wafer piece, only very small, if any, currents should be detectable during exposure to oxygen. At the same time the amount of oxygen on the surface should increase, because the free dangling bonds are saturated by oxygen atoms.

Heating the surface to around 730°, as presented earlier in chapter 3.2, allows it to reorganize and form the well known Si(111) 7x7 reconstruction. This surface is highly reactive, but in contrast to the previous two it does also show metallic surface conductivity [HTD87, HST$^+$03, Ned93, YW02]. This means that by contacting a small part of the sample one can contact the entire surface area and measure any currents that are generated during a chemical reaction. When the surface is oxidized the surface conductivity becomes smaller and with it the connection to the active diode area. Once surface conduction is lost no currents can be detected. So for the oxidation of this surface one would expect a detectable current, using the chemicurrent setup, as well as an increase in oxygen coverage. Furthermore, this surface is the thinnest film one can prepare. One monolayer of highly structured, conductive, reactive material is not easily accessible by other means.

For each of these surfaces two samples were prepared and IV-curves, chemicurrent and XPS spectra, before and after the oxygen exposure, were recorded. These experiments were done in the same

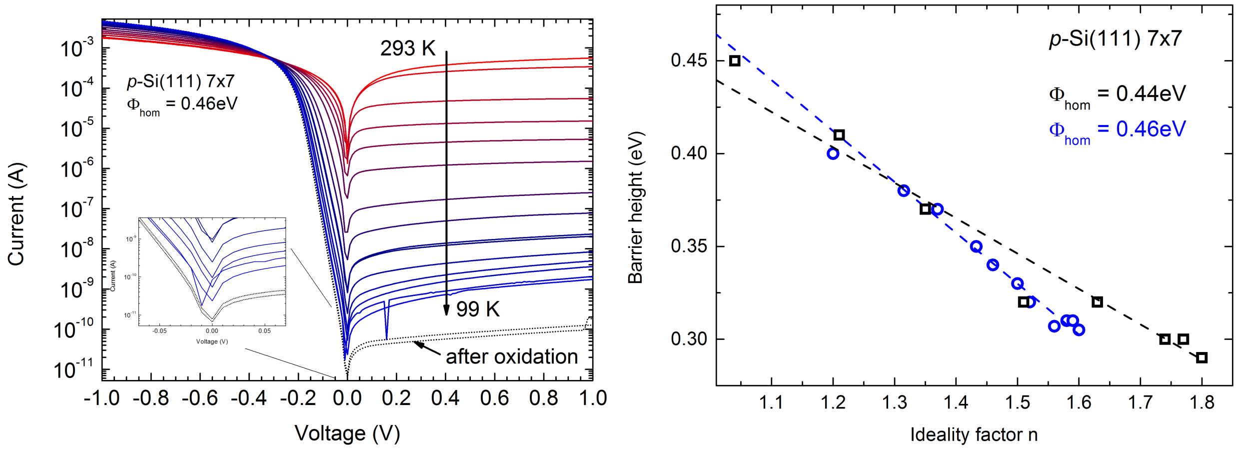

Figure 8.1.: Left panel: Set of temperature dependent IV-curves for the gold ball on the Si(111) 7x7 surface. Right panel: Effective barrier height plotted vs. the ideality factor for a Au/Si(111) 7x7 Schottky diode.

UHV-chamber as the silver interlayer measurements. As mentioned before this chamber is basically a duplicate of the one described above in chapter 3, but the hemispherical analyzer is not as good.

8.1. IV-characteristics

Measurement of the IV-characteristics is done the same way as for the other samples prepared in this work. Once the surface is prepared as desired it is cooled down to liquid nitrogen temperatures while a set of temperature dependent current-voltage curves is recorded. From these one can deduct the homogeneous barrier height of the respective sample, as presented in chapter 2.1. Examples for a set of IV-curves and the evaluation of those is given in Figure 8.1 for the *p*-Si(111) 7x7 surface. The left panel shows a set of IV-curves recorded during the cooling of the sample. At room temperature the sample is basically ohmic and it becomes gradually more rectifying with decreasing temperature. The dotted lines are two IV-curves after the surface was exposed to oxygen. The IV-characteristics do not change with oxygen uptake. The determination of the homogeneous barrier height is given in the right panel for the two 7x7 samples used in this experiment. The barrier heights are $\Phi_{\text{hom,7x7}} = 0.46$ eV and $\Phi_{\text{hom,7x7}} = 0.44$ eV, for the blue circles and black squares in Figure 8.1 respectively. The same measurements were done on the other two Si surfaces and we obtained $\Phi_{\text{hom, H:Si}} = 0.43 \pm 0.02$ eV for the hydrogen passivated surfaces. The depassivated samples were very different from each other, with barrier heights of $\Phi_{\text{hom, Si}} = 0.39$ eV and $\Phi_{\text{hom, Si}} = 0.57$ eV.

This is attributed to the very rough and unstructured nature of these surfaces.

8.2. Current measurements

The current measurements during the exposure of the three different Si surfaces to molecular oxygen are given in Figure 8.2 for all six samples. The current is plotted versus the exposure to oxygen. The sample temperature was in all cases $T_{\text{sample}} \approx 100$ K.

The hydrogen passivated and depassivated surfaces, upper and central panel, do not show a current, for all the four different samples. There is a bit of noise in the beginning when the leak valve is opened, which is most likely attributed to movement of the entire setup during the opening. The Si(111) 7x7 surface, lower panel, does show a current for both samples. The maximum of these current traces is right at the beginning and the current decays quickly to zero. The total charge flown during the experiment is 1.5 nC (black line) and 1.7 nC (red line). These values are very similar. The total charge is obtained by integrating the detected current in respect to time.

The current could be either a chemicurrent, due to e-h pair generation or chemiluminescence, or it could be a displacement current, resulting from a change in the surface band-bending and hence, a displacement of the surface-charge density.

If the current was a chemicurrent then it should be proportional to the reaction rate R(t), see chapter 2.2 [Nie02]

$$I_{\text{cc}} = \alpha(t) e_0 R(t). \tag{8.1}$$

The reaction rate can also be described as the derivative of the oxide coverage

$$R(t) = cst. \cdot \frac{d\Theta}{dt}. \tag{8.2}$$

If the chemicurrent efficiency $\alpha(t)$ is not time dependent, which is shown for many different chemicurrent experiments on other surfaces [Hag09, GN04, KNN07, SDH11], then the division of the current I by the derivative of the oxide coverage Θ, $\frac{I}{d\Theta/dt}$, should be a constant.

It was not possible to measure the oxide coverage during in this work. However, Gupta *et al* did oxygen uptake measurements on the Si(111) 7x7 surface at the same sample temperature of $T \approx 100$ K [GMCG89], using Auger electron spectroscopy. This data is shown in Figure 8.3 together with one of the current traces from this work. The oxide coverage, red solid line, increases with exposure and saturates at around 0.5 ML for high exposures - see inset. The current, black solid line, has decayed to 0 after an exposure of only ~ 0.2 to 0.3 L. The oxide coverage at these exposures is only 0.1 to 0.15 ML.

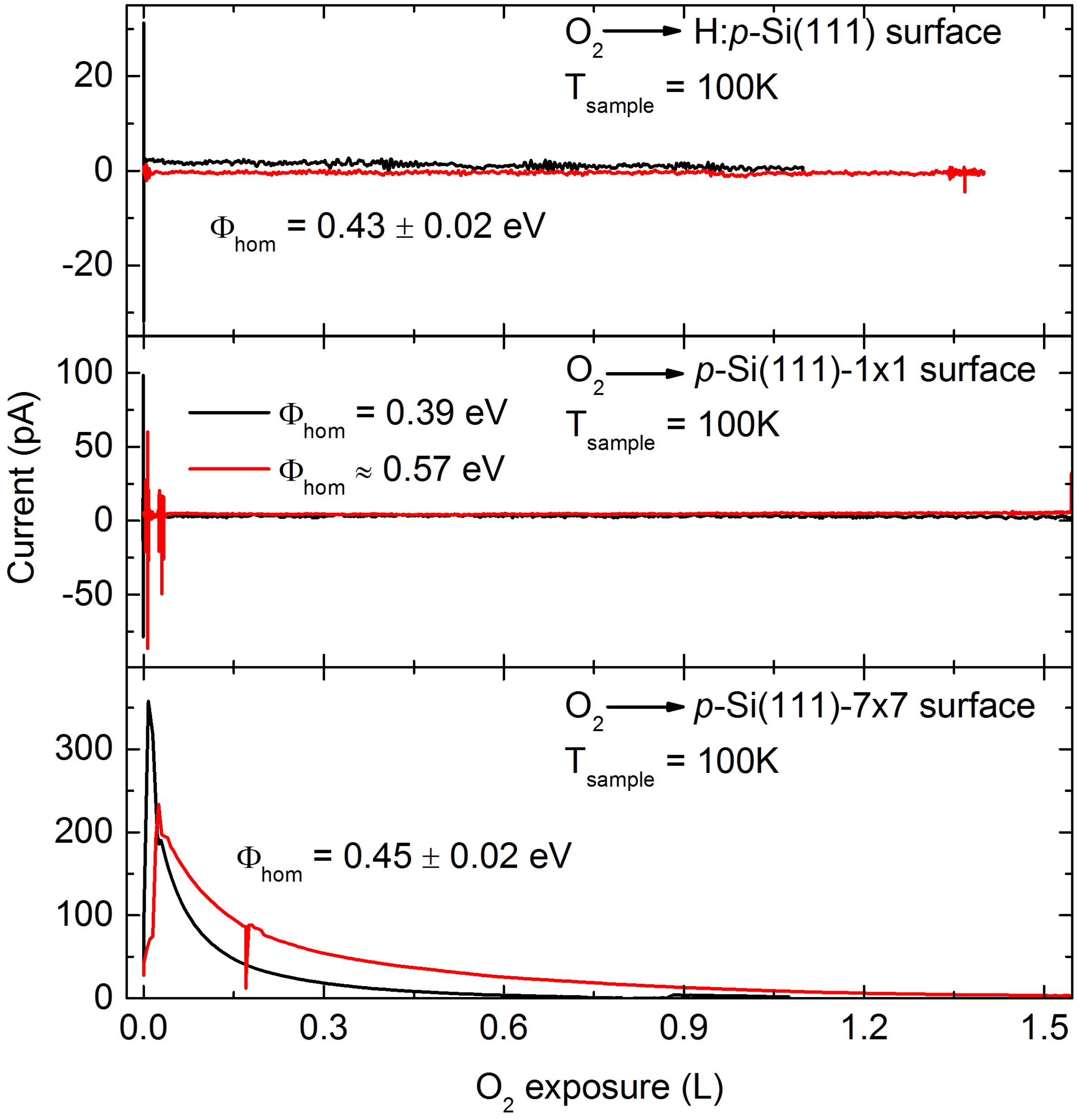

Figure 8.2.: Detected chemicurrents during the exposure of the three different Si surfaces to molecular oxygen.

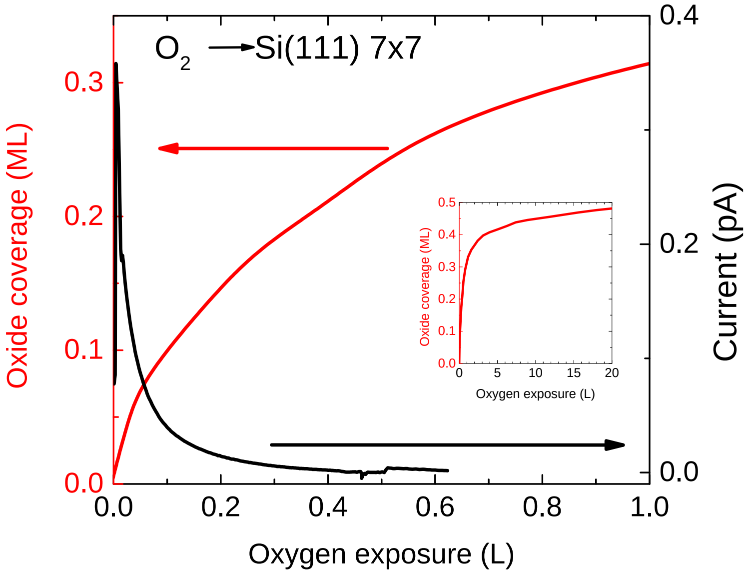

Figure 8.3.: Oxide coverage Θ as measured by Gupta *et al* [GMCG89] and the detected current in dependence on the oxygen exposure. The oxide coverage is given in red, the current trace is colored black. The inset shows the saturation of the oxide coverage at around 0.5 ML.

According to equations 8.1 and 8.2 the current divided by the derivative of the oxide coverage should be a constant, if the current is a chemicurrent. The factor $\frac{I}{d\Theta/dt}$ is plotted in Figure 8.4 versus the oxide coverage. It is obvious that this ratio is not a constant with respect to the coverage. This is strong evidence for the assumption that the detected current is not a chemicurrent. Furthermore, chemiluminescence or chemicurrent detection should continue until the surface conductivity of the Si(111) 7x7 is lost. However, the current has decayed by a factor of 7 to 10 within the first 0.2 L to 0.3 L of oxygen exposures (red and black curves in the bottom panel of Figure 8.2. These exposures correspond to oxide coverages of only 0.1 ML to 0.15 ML, see Figure 8.4.

The surface conductivity of the Si(111) 7x7 reconstruction has been studied extensively [HWWH98, TYM^{+}03, WKHH06]. The surface conductance has been studied in dependence of the adsorption of potassium [DTM^{+}09] and oxygen [YW02, HLA96]. The results are not quite clear, as the papers also measure different types of electrical conductance. All papers show a decrease of the surface conductance upon adsorption of molecules or atoms. Hasegawa *et al* [HLA96], for example, demonstrate a decrease of the conductance to a point contact in STM of roughly one order of magnitude per 0.2 ML oxide coverage until 0.6 ML. However, these results suggest that the surface conduc-

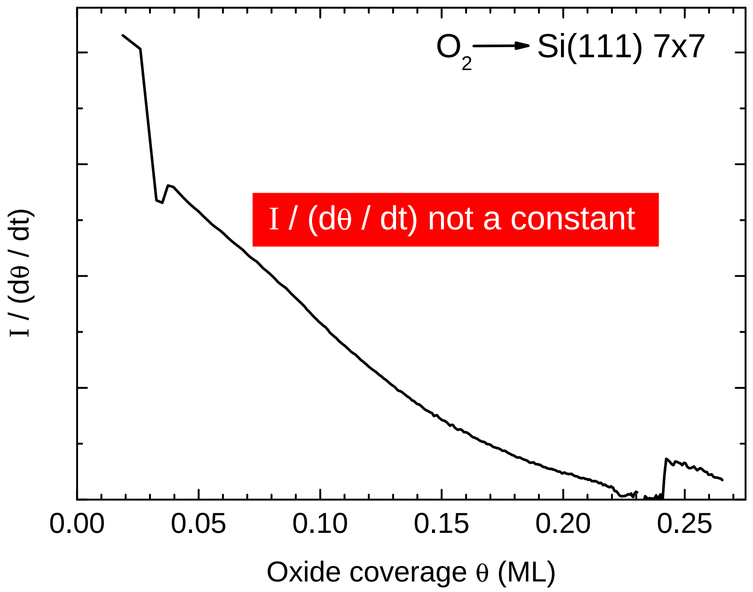

Figure 8.4.: The property $\frac{I}{d\Theta/dt}$ plotted versus the oxide coverage. The resulting trace is not constant with coverage.

tivity is not decreased to zero within the first 1/10 of a ML. Hence, a current should be detectable up to higher oxide coverages. As this is not the case, the detected current is most likely not a chemicurrent.

A displacement current on the other hand should vanish quite quickly with oxygen coverage, because of a quadratic dependence of the band-bending on the density of surface states [Mön95]. The idea of the origin of the displacement current is schematically depicted in Figure 8.5. The left panel shows a schematic of the energy-space diagram of the p-Si(111) 7x7 surface. Donor-type surface states at the Fermi energy are partially charged to neutralize the negative space-charge in the semiconductor due to the band-bending of the VBM and CBM. As will be shown below, the exposure to O_2 results in an increase in the surface band-bending. This means that the space-charge in the semiconductors space-charge layer increases. The previously existing surface state density decreases with exposure and is pushed below the Fermi energy by the band-bending. A new type of donor-type surface states, introduced by the adsorbing oxygen, now exists at the interface and is again positively charged to achieve surface neutrality. This change in surface band-bending and surface state density results in the generation of a displacement current, which would be measured as a positive current through the p-doped semiconductor.

Following the arguments by Mönch the square root of the surface band-bending is proportional

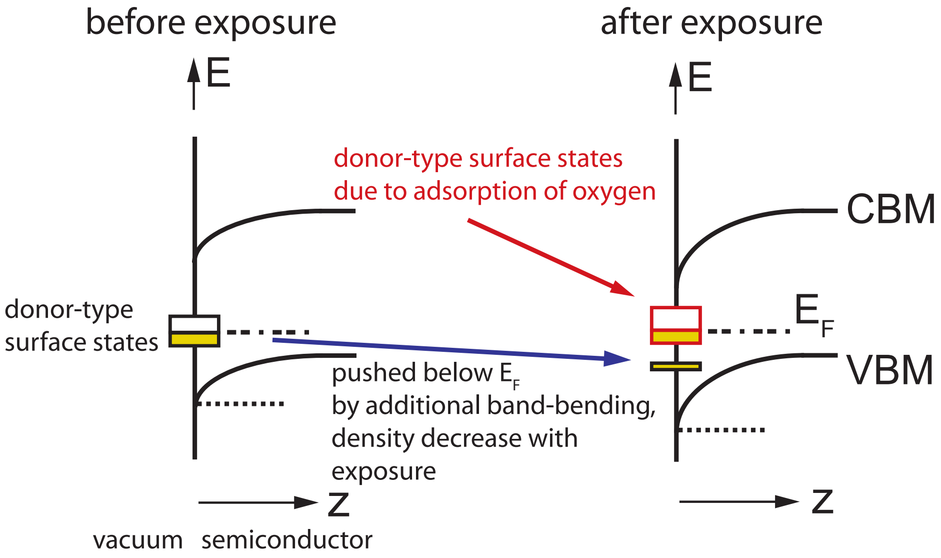

Figure 8.5.: Schematic description of displacement current upon oxygen exposure. Left panel: Energy-space diagram of the Si(111) 7x7 surface before exposure to O_2. Donor-type surface states are positively charged due to the surface band-bending and the necessity of charge neutrality at the interface Si/Vac. Right panel: Energy space diagram for same surface after O_2 exposure. This exposure introduces additional donor-type surface states, which are energetically above the existing one. The latter ones get pushed below the Fermi level with exposure and their density decreases. The new type of surface states are partially charged to achieve charge neutrality with the now increased space-charge density of the semiconductors space-charge layer.

to the surface state density [Mön95]. Hence, a displacement current I_{disp} should be equal to the derivative of the square root of the change in surface band-bending Δ V_s with respect to oxide coverage Θ [Mön95]

$$I_{\text{disp}} = \frac{dQ}{dt} \propto \frac{d\left(c\sqrt{\Delta V_{\text{s}}}\right)}{dt} = \frac{d\left(c\sqrt{\Delta V_{\text{s}}}\right)}{d\Theta}\frac{d\Theta}{dt}.I_{\text{disp}} = \frac{dQ}{dt} \propto \frac{d\left(c\sqrt{\Delta V_{\text{s}}}\right)}{dt} = \frac{d\left(c\sqrt{\Delta V_{\text{s}}}\right)}{d\Theta}\frac{d\Theta}{dt}. \tag{8.3}$$

By integrating with respect to the oxide coverage this transforms to

$$\int \frac{I_{\text{disp}}}{d\Theta/dt} d\Theta = c\sqrt{\Delta V_{\text{s}}}. \tag{8.4}$$

Squaring equation 8.4 yields

$$\left(\int \frac{I_{\text{disp}}}{d\Theta/dt} d\Theta\right)^2 = c^2 \Delta V_{\text{s}} \tag{8.5}$$

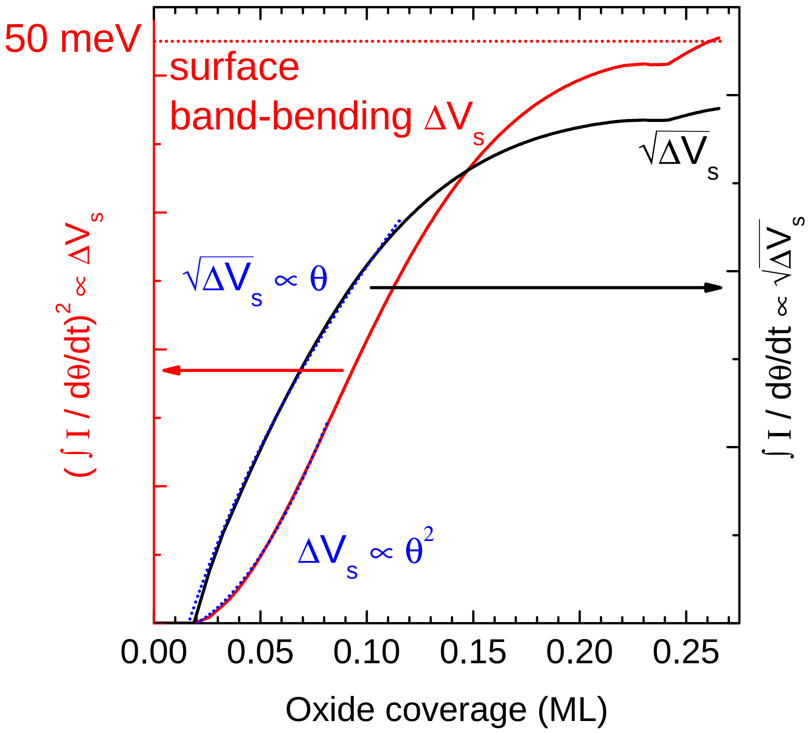

Figure 8.6.: The values $\int \frac{I_{\mathrm{disp}}}{d\Theta/dt} d\Theta$ - black line - and $(\int \frac{I_{\mathrm{disp}}}{d\Theta/dt} d\Theta)^2$ - red line - plotted versus the oxide coverage. These values are proportional to the change in surface band-bending, see equations 8.4 and 8.5. The band-bending is initially proportional to Θ^2 for small coverages - blue dashed lines.

directly the surface band-bending $\mathrm{V_s}$, when the proportionality factor c is small enough. Equations 8.4 and 8.5 have been evaluated for the current detected during the oxidation of the Si(111) 7x7, the black line in Figure 8.3. The result is plotted in Figure 8.6. The black solid line represents $\int \frac{I_{\mathrm{disp}}}{d\Theta/dt} d\Theta$ which is proportional to $\sqrt{\Delta V_{\mathrm{s}}}$. The dotted blue lines depicts a square root fit to the data, which agrees well up to a coverage of 0.1 ML. At this coverage $\sqrt{\Delta V_{\mathrm{s}}}$ has already 75% of its maximal value.

The red solid line gives the value of $\left(\int \frac{I_{\mathrm{disp}}}{d\Theta/dt} d\Theta\right)^2 \propto \Delta V_{\mathrm{s}}$. It shows an S-like increase with coverage. The cubic fit, dotted blue line, fits the data well for initial coverages. The fit crosses the x-axis at a coverage of ~ 0.02 ML. This corresponds to a coverage of 1 atom per Si(111) 7x7 unit cell. The process behind this red curve is the increase of the $\mathrm{O_2}$ exposure induced surface state density and the decrease of the previously existing surface state density, as depicted in Figure 8.5.

When this S-like curve of the band-bending seemingly saturates the Fermi level E_{F} of the substrate comes close to the energy of the new surface states E_{sd}, $E_{\mathrm{sd}} - E_{\mathrm{F}} \approx 0$ [Mön95]. In this regime, called the *Fermi level pinning* regime, changes in surface state density induce only very small variations of the surface band-bending. The change in band-bending changes from an initially quadratic behavior to a change of only 2.3 $k_{\mathrm{B}}T$ per decade of surface density [Mön95].

One can estimate the surface band-bending of a Schottky diode when the current flowing during this process is detected. If one uses the basic assumption of the depletion-layer model by Schottky [Sch42], which is that only one type of surface states is responsible for the space-charge, the band-bending can be written as [Mön95]

$$V_s[eV] = \left(\frac{Q}{A}\right)^2 \cdot \frac{1}{2\epsilon_b \epsilon_0 N_{a,d} e_0}. \tag{8.6}$$

The different values are the dopant concentration $\mathrm{N}_{a,d} = 10^{16}$ cm^{-3}, the permittivity $\epsilon_b = 12$ for silicon, the dielectric constant ϵ_0 and the surface area of $A = 72$ mm^2. As a Schottky barrier has already formed prior to the oxidation experiment, the valence and conduction band are not flat. They already show a certain band-bending. When one assumes the band-bending to be equal to the detected Schottky barrier height one can calculate the charge flow needed for this band-bending. The total charge for a band-bending of $\Phi_{\mathrm{hom,7x7}} = V_s = 0.46$ eV is $Q = 28.5$ nC and for a band-bending of $\Phi_{\mathrm{hom,7x7}} = V_s = 0.44$ eV a value of $Q = 27.9$ nC, given by equation 8.6 and the barrier heights in Figure 8.1.

During the oxidation experiments additional charges of 1.5 nC for the sample with the larger barrier height of 0.46 eV and 1.7 nC for the second sample were detected. Calculating the resulting band-bending for the total charge of the first sample 1.5 nC +28.5 nC = 30 nC yields $V_s = 0.51$ eV and hence an additional band-bending of 50 meV. This is the value that is depicted in Figure 8.6 as the total change in surface band-bending, red dashed line. For the second sample the same calculation with a total charge of 29.6 nC and a prior band-bending of 0.44 eV results in an additional band-bending of 56 meV. Both samples give very similar results. The current detected through the device is positive and this means that the band-bending of the surface is increased. Although Mönch states, that no surface-band bending was found for the oxidation of the Si(111) 7x7 surface [HH83, Mön95], as measured by XPS, shifts of only a few 10 meV were most probably not detectable in those experiments.

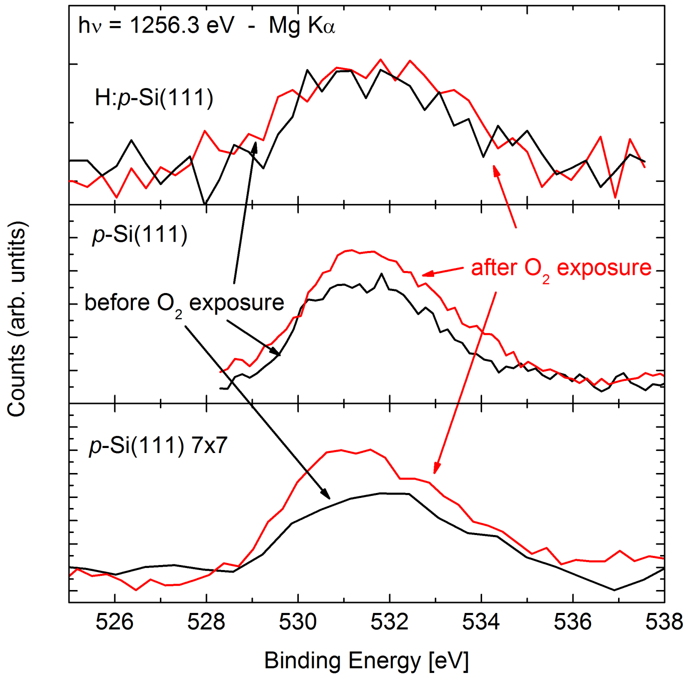

Figure 8.7.: Intensity of the O 1s XPS-peak of the H:*p*-Si(111), *p*-Si(111) and the *p*-Si(111) 7x7 surfaces before and after exposure to molecular oxygen.

8.3. Oxygen uptake

The first assumption that was made in the introduction is true. Only the oxidation of the 7x7 surface shows a detectable current through the device, because the other surfaces are either inert and/or do not exhibit surface conductivity. To determine the oxygen uptake during the exposure the samples were studied with XPS before and after the exposure to O_2.

The measured intensity of the O1s XPS-peak, at a binding energy of $\sim$ 531 eV, are shown in Figure 8.7. The black lines represent the situation before the exposure to oxygen and the red lines after. The topmost sample is a clean, hydrogen passivated surface, in the middle is shown a depassivated one and the one at the bottom is a sample showing the 7x7 reconstruction. All samples show small oxygen contamination even before the oxidation process. This is due to limitations in the analyzer setup. The spot-size of the analyzer is larger than the sample size, and hence the sample holder is partially measured as well. The exposure of a sample holder without Si substrate to molecular oxygen showed no increase in the O 1s intensity (not shown here).

The signal to noise ratio is very small for the hydrogen passivated sample, indicating a small total oxygen coverage. The increase of the O 1s signal upon O_2 exposure is also minimal. This surface seems to be inert.

The other two surfaces have a stronger initial oxygen coverage, which is probably due to the heating/flashing step during the sample preparation. For both samples the oxygen coverages increases visibly during the experiment. The relative increase for the 7x7 is slightly larger, but as the limitations of the analyzer have been mentioned, this should not be interpreted too much. That is also the reason why no percentages are given here. These measurements can only be taken as qualitative measures to show that the H-passivated surface is inert, while the other two surfaces are not.

9. UPS experiments on thin, crystalline Mg films

This chapter shows the existence of strong atomic hydrogen (Hα or Lyman α) radiation in the emission of a He, Ne or Ar plasma from a regular UV-source. This hydrogen emission is present, although the gas inlet is leak free and the gas purities were 5.0 (99.999%) or better.
Using this hydrogen emission it was possible to determine the photoyield in dependence on the incident photon energy. The samples that were investigated in this chapter were the same, or similarly prepared, crystalline Mg films as in chapter 6.
Chapter A in the appendix gives an insight into the peak fitting and background subtraction that was applied to the data.

9.1. Existence of hydrogen photon lines in UV photoemission

Figure 9.1 shows 6 different UPS spectra for Mg films of different film thickness recorded in normal emission with light emitted from a He plasma in the UV-source. The green line represents the signal of a 10 ML polycrystalline Mg film, which was deposited at room temperature. The other films were prepared at around 100 K as discussed in chapter 3.2. The film thicknesses are 8 ML - black line -, 13 ML - red -, 17 ML - blue -, 24 ML - purple - and about 300 ML - orange. The surface state at 1.6 eV binding energy becomes more intense and sharper with increasing film thickness. Between the SS and the Fermi edge the weak signal of the quantum well state(s) can be seen for the thinner films. The SS is weak for the polycrystalline film and no QWS show for this less structured surface. Between 10.5 eV and 13 eV binding energy the features named HSS and HQWS are visible. It will be shown that these peaks arise from hydrogen α radiation in the photon flux. The signal of the surface and quantum well state due to H α emission from a noble gas plasma will be called HSS and HQWS, hydrogen surface state and hydrogen quantum well state, in this chapter. SS and QWS are the surface and quantum well state due to noble gas emission - He,Ne or Ar -, unless noted otherwise. The energy of hydrogen α radiation is $h\nu = 10.2$ eV.
While the SS, measured with He I light, at 1.6 eV binding energy, increases in intensity with increasing film thickness the HSS, measured with hydrogen α light, at 12.5 eV binding energy,

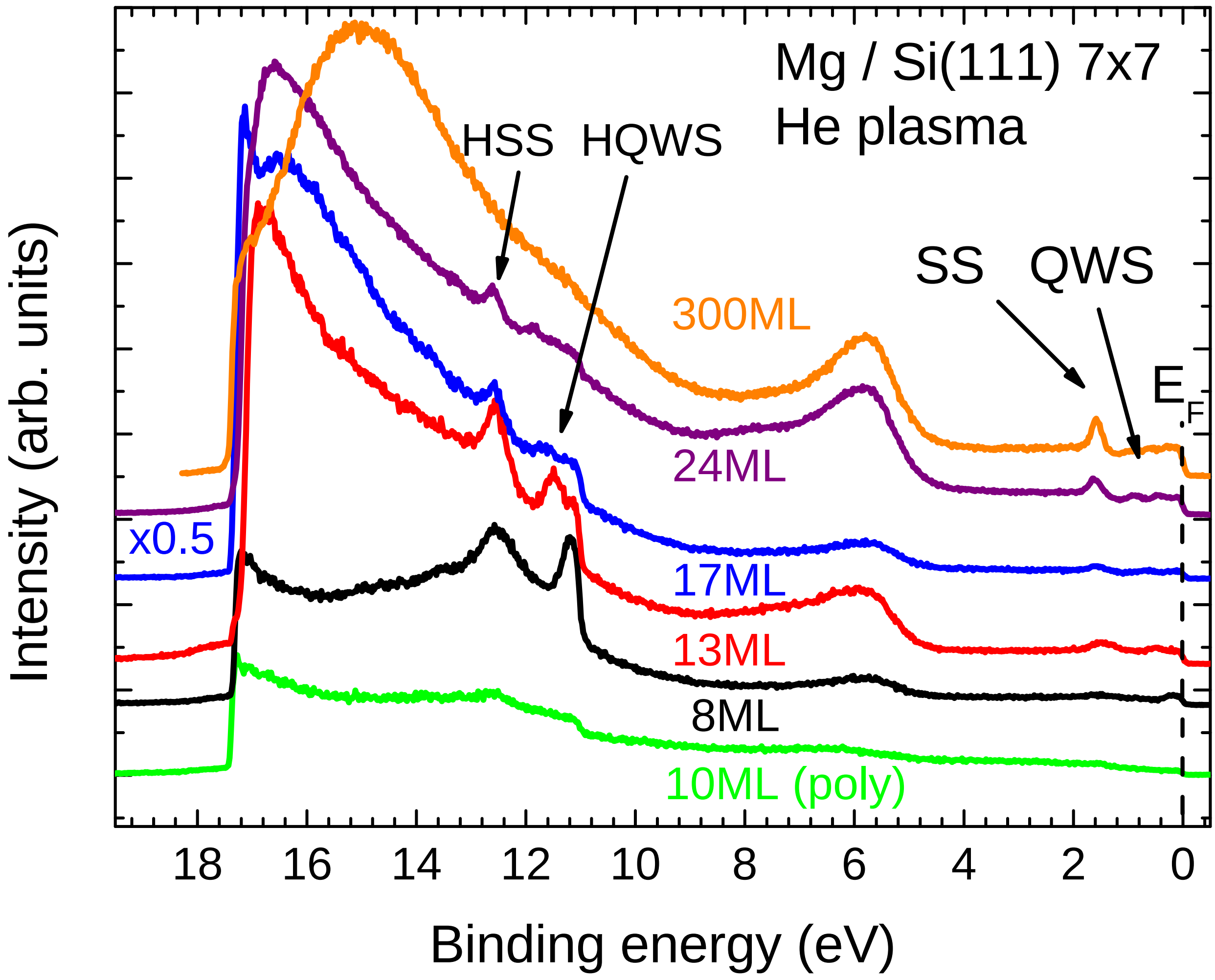

Figure 9.1.: UPS scans of Mg films of different thickness. The 10 ML polycrystalline film was deposited at room temperature, as opposed to the regular deposition at 100 K. This spectra were recorded with the He I light of 21.22 eV in normal emission. The features called HSS and HQWS are the surface and quantum well states measured with hydrogen α light, $h\nu = 10.2$ eV, that is emitted from the UV-source.

vanishes for thick films. The polycrystalline film also shows a weaker hydrogen signal than the crystalline films of comparable thickness.

To prove that the HSS and HQWS lines are in fact due to H α radiation we switched to different plasmas in the UV-source. Switching the gas that is used in the plasma source leads to a change in photon energy. As was mentioned in chapter 4 the primary lines from H, Ar, Ne, He and the secondary lines Ar II, Ne II and He II can be produced.

Figure 9.2 gives the ultraviolet photoemission spectra of an 8 ML Mg film on Si(111) 7x7 in normal emission. The primarily emitted photon energies and emission lines are H α (10.2 eV) in the top panel, Ar I (11.83 eV) in the central panel and He I (21.22 eV) in the bottom panel. The dominating part in all three spectra is a large signal to the left of the hydrogen Fermi edge E_F(H α). Around 1.55 eV to the left of this Fermi edge the signal of the Mg surface state is clearly visible. Its energetic position is the same in all three graphs. Further to the left of the SS two features, denoted A and B, emerge in the spectra. It will be shown that they belong to molecular H_2 photon emission lines, see chapter 9.3.

The He spectrum was recorded as the first of the three spectra. The gas inlet was filled with He gas for several days, purged and refilled and then used for this scan. This means that basically no large amounts of H_2 were remaining in the inlet system from previous scans and hydrogen contamination of the gas cannot be responsible for the strong H α signal. The hydrogen scan was recorded second and the Ar one last.

As the SS and HSS signals, recorded with e.g. light from a He plasma, are both stemming from the same surface state of the metal surface, their energetic position in respect to the corresponding Fermi edge has to be the same. These regions of such a scan, showing the hydrogen signal in the left and helium signal in the right panel, are shown in Figure 9.3. The data is taken from Figure 9.1 for the 8 ML and 17 ML samples. For the 8 ML sample one can clearly see the quantum well state, QWS at 0.17 eV binding energy, and less pronounced the surface state, SS at around 1.55 eV binding energy, in the helium signal - right panel. The surface state is more pronounced the thicker the samples get. The 17 ML film shows two quantum well states, at around 0.1 eV and 0.6 eV, but as this is by no means a high resolution scan they are quite noisy.

The left panel shows the 11 eV region. The step-like signal, named HFE - for H α Fermi edge - is located at 11 eV binding energy for both samples. For the 8 ML film the HQWS - H α quantum well state - is located at 11.17 eV and the HSS - H α surface state - at 12.55 eV. The positions of the different features deducted from this graph are listed in table 9.1. The features, due to H α emission, are each shifted by 11 eV compared to their equivalents close to the Fermi edge. The

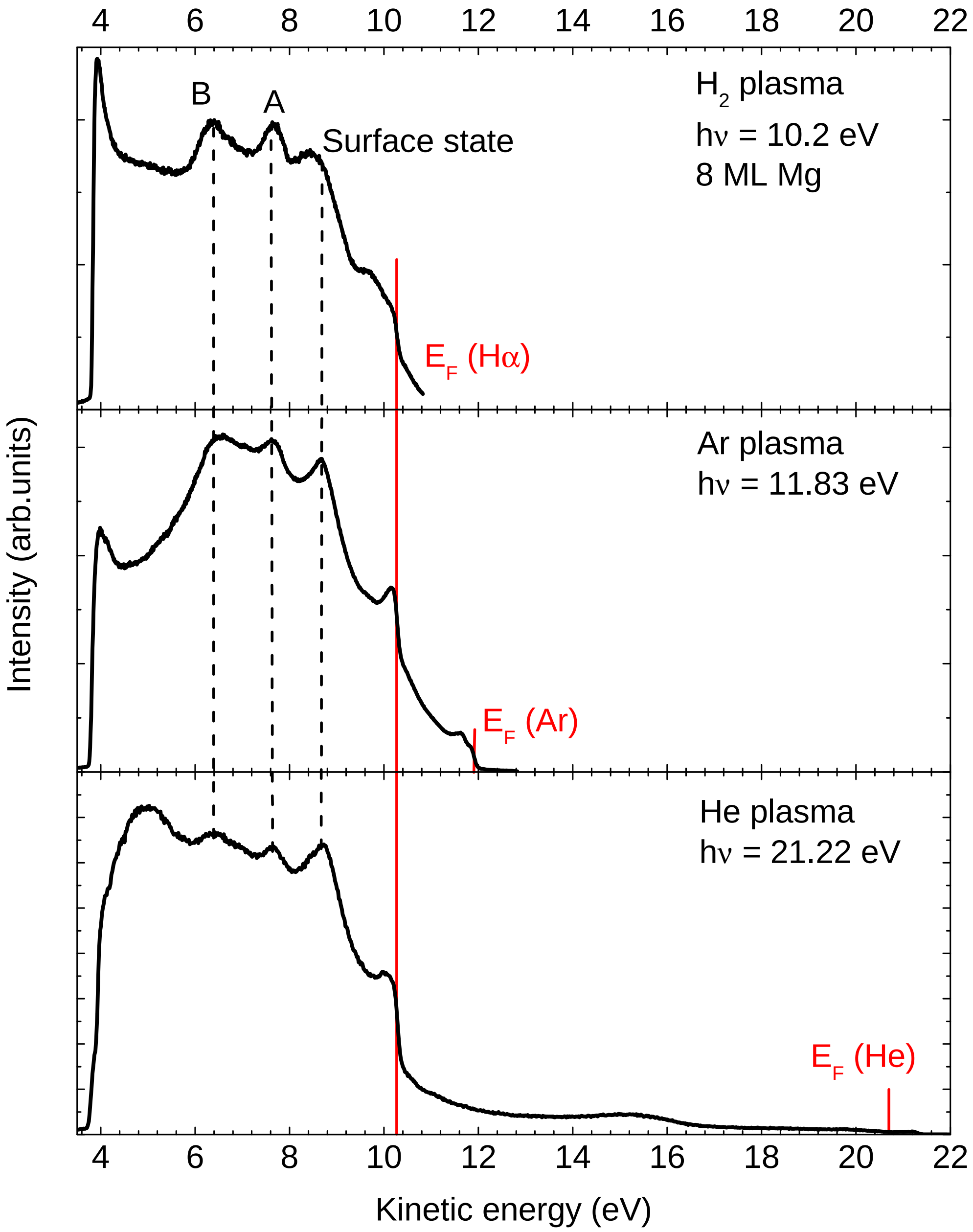

Figure 9.2.: UPS spectra in normal emission of one sample with 8 ML Mg on Si(111) 7x7. From the top to bottom panel the ignited plasmas and resulting photon energies are H (10.2 eV), Ar (11.83 eV), He (21.22 eV). The corresponding Fermi edges are given as red lines. The Fermi edge for hydrogen is drawn in all graphs. -3V are applied to the sample to make the electron onset at low electron energies visible.

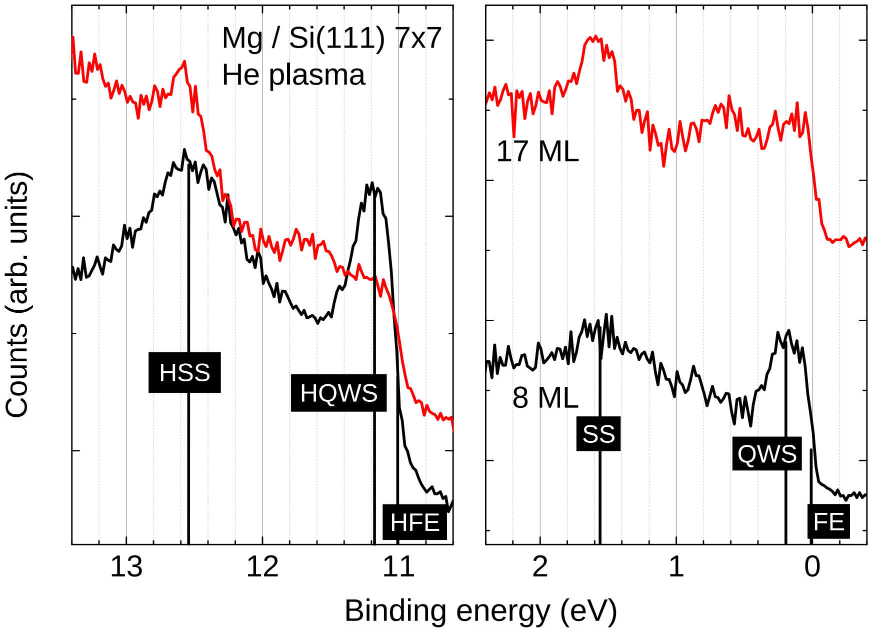

Figure 9.3.: Zoom into the Fermi edge region (He, right) and into the 11 eV (H, left) for the 8 ML and 17 ML samples from Figure 9.1. For the 8 ML sample the QWS, SS and FE are highlighted, both in the helium and hydrogen region.

Thickness	FE	QWS	SS	HFE	HQWS	HSS
8 ML	0 eV	0.17 eV	1.55 eV	11 eV	11.17 eV	12.55 eV
17 ML	0 eV	0.63 eV	1.58 eV	11 eV	11.64 eV	12.58 eV

Table 9.1.: Binding energy of the different features from Figure 9.1. QWS and HQWS represents the quantum well state closest to the surface state. Their position shift with Mg thickness, as was shown already before in Figure 5.10. The hydrogen features are shifted by 11 eV but the distance amongst themselves is exactly the same as for the 'original' features close to the He I Fermi energy.

distances between the different features in the hydrogen lines is exactly the same as the distance between the features for the He I signal. For example the SS and HSS of the 17 ML sample are both at exactly 1.58 eV binding energy from their respective Fermi edges. The explanation for the existence of the hydrogen lines will be given in chapter 9.2.

9.2. Excimer excitation of hydrogen emission

In any photon source that emits the hydrogen H α line the first step is the dissociation of the H_2 molecule with the consecutive excitation of at least one of the two H atoms. In the late 90s a source has been developed that generates a very intense and spectrally clean H α signal and is based on high-pressure microhollow cathode discharges (MHCD) [WSS$^+$98, KSB99]. A microhollow cathode consists of a cathode, that has a central hole of about 100 μm. A thin sheet of a dielectric isolates the cathode and the anode. When gas is flowing through the hole and a discharge voltage of a few 100 V is applied to the MHC the discharge is triggered. The setup is shown as an inset in Figure 9.4.

740 Torr Neon gas with only 1.5 Torr H_2, which is less than 0.3%, mixed into it that is flowing through such a MHC yields the emission spectrum shown in Figure 9.4, taken from [KSB99]. While H α at 121 nm and a little bit of Lyman β at 102.5 nm are visible basically no emission from the Ne excimer, between 75 nm and 88 nm, or the regular Ne I line at 73 nm are present. This is because the energy of a Ne_2^* excimer is between 14.1 eV and 15.5 eV and is nearly resonant to the process of dissociating an H_2 molecule,

$$\mathrm{Ne}_2^* + \mathrm{H}_2 \to 2\mathrm{Ne} + \mathrm{H} + \mathrm{H}^*(n = 2). \tag{9.1}$$

The excited hydrogen atom then relaxes by emission of H α photons

$$\mathrm{H}^*(n = 2) \to \mathrm{H}(n = 1) + h\nu(121\mathrm{nm}). \tag{9.2}$$

The dissociation of an hydrogen molecule costs about 4.55 eV [Her70] and the excitation of a single atom 10.2 eV. Hence, a total of 14.75 eV is needed for the emission of H α photons. The energy transfer happens due to collisions between the gas molecules and consequently this process is only effective at pressures where the probability of collision between the gas molecules is sufficiently high.

Although this process is off-resonance with the helium and argon excimers, H α emission has been found for these gases as well [KBO85, BKS02, MMB05, SZ12]. For our source the H α emission was most intense when the source was operated with Neon gas. Argon gas yielded the lowest emission

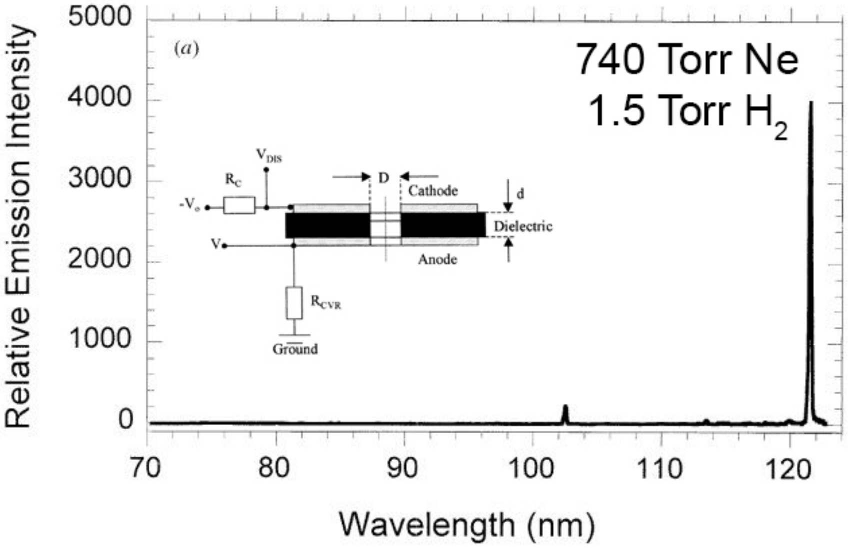

Figure 9.4.: H α emission from a MHCD driven with Neon gas with a small admixture of H_2 from [KSB99]. The inset shows the setup of such a MHCD device.

and indeed for Ar the emission could be switched off completely by changing the source parameters of operation, e.g. in Figure 9.7. The intensity of the H α signal from a helium plasma was in between the other two. We believe that the H α emission is only possible because we operate our source at larger partial pressures and with a different differential pumping scheme, than is usual for these type of discharge sources. When the source is operated in the usual way, no H α radiation can be detected. Thus we propose a similar mechanism to that of the MHCD for H α generation for the UPS experiments shown in this work, with a high gas pressure in the discharge source.

Especially for Neon the Ne I Fermi edge and the different states SS and QWS are very weak or not visible at all. At the same time the H α signal is huge, Figure 9.5. In fact the parameters under which the emission is triggered in the plasma source are crucial for the H α intensity. The gas partial pressure and the emission current of the source play an important role. When the source is operated with Ne and the source is changed from a Ne II poor to a Ne II rich photon flux the H α emission increases greatly, see Figure 9.5. These scans of a 13 ML thick Mg film show that the Ne II mode yields a much larger H α intensity than the Ne I mode. The procedure to switch to a Ne II rich photon flux is to decrease the Ne partial pressure and increase the source emission current at the same time. This also results in an increase in thedischarge voltage of the source. In a Neon plasma operated under these conditions the energy transfer from an excited Ne atom to the hydrogen molecule is obviously more probable than the radiative deexcitation of the Ne atom.

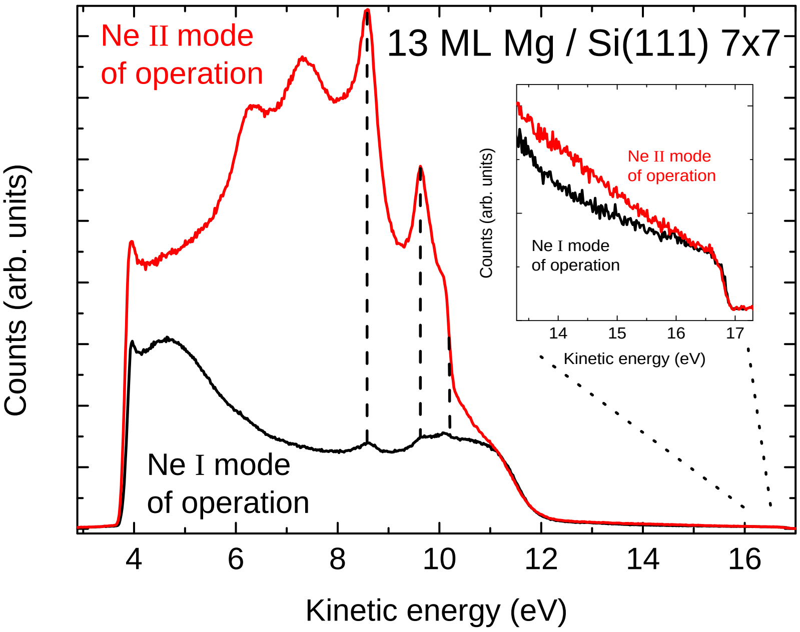

Figure 9.5.: UPS spectra of a 13 ML thick Mg film with the source operated with Neon. The mode of operation was changed from a Ne II poor to a Ne II rich photon flux by reducing the Ne partial pressure and increasing the emission current.

Hence, no strong Ne I emission is detectable.

The emission of H α photons can even be switched off completely, when operating the source with argon gas, see Figure 9.6. In the upper panel UPS spectra of a 13 ML thick Mg film are shown. The source is operated with Ar gas. The blue line, at the bottom of the graph, represents the pure Ar I mode of the source. The source parameters are slowly changed to a Ar II rich mode of operation. The stronger a line is colored red, the higher is the Ar II content. Ar II mode of operations means, similarly to Ne, that the Ar partial pressure in the source is reduced while at the same time the emission current is increased. The inset shows the Ar II Fermi edge at 13.48 eV and proves the increase in Ar II flux. At the same time H α radiation becomes visible via the H α surface state, HSS, quantum well state, HQWS, and Fermi edge, HFE. The lower panel shows He and Ne scans of the same sample to prove that the emerging peaks are in fact due to H α emission. For the source operation with argon the H α emission can thus be switched on and off by changing the operation parameters.

This is visualized in Figure 9.7. It is a contour plot of the H α quantum well state signal intensity in dependence of the chamber pressure and the sources emission current. The source is operated with

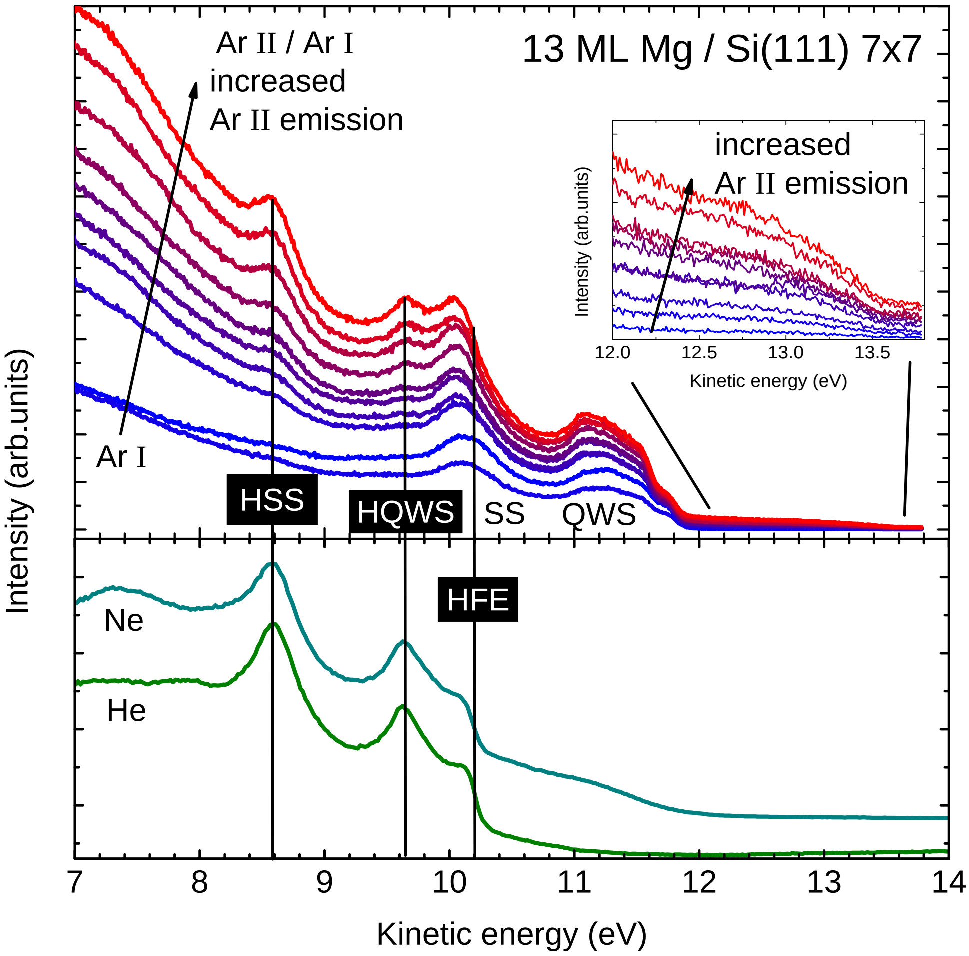

Figure 9.6.: Upper panel: UPS scans with Ar gas of a 13 ML Mg film recorded in normal emission. The amount of Ar II photons in the photon flux is increased by decreasing the Ar partial pressure and increasing the emission current in the source. The amount of Ar II radiation increases from blue to red. This is seen in the inset, which shows the Ar II Fermi edge at 13.48 eV. The H α states and Fermi edge, HSS, HQWS and HFE, become more pronounced when the source parameters are slowly changed to a Ar II mode. No H α signal is visible, when the source is driven in a pure Ar I mode. Lower panel: He and Ne scans of the same sample in the region of H α emission.

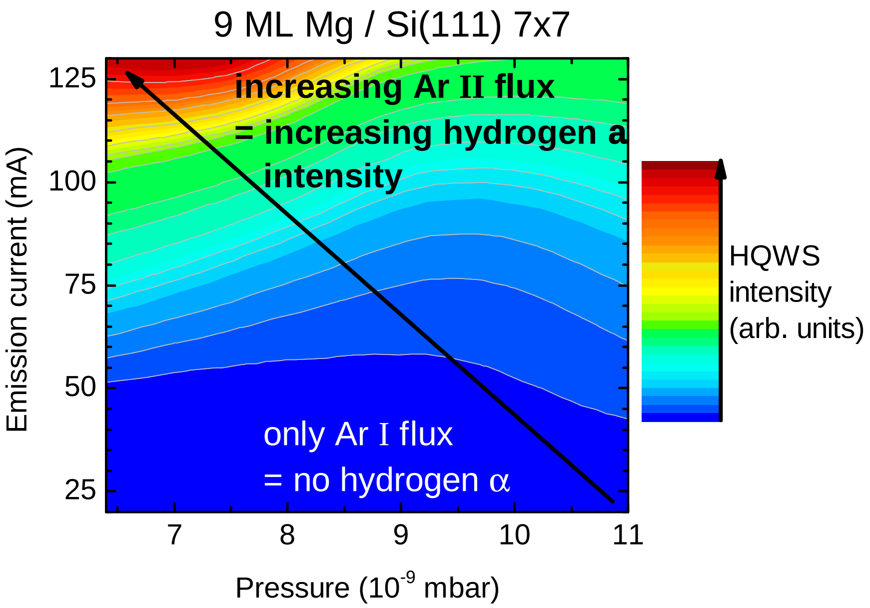

Figure 9.7.: Contour plot of the quantum well state intensity due to H α radiation of a 9 ML thick Mg film plotted in dependence of the chamber pressure and the source emission current. The change in the pressure is due to the change of the Ar partial pressure.

argon and the change in chamber pressure is due to closing/opening of the Ar leak valve, hence due to a change in the argon partial pressure. The same result is found for the intensity of the surface state. In the case of argon, one can thus switch from basically no H α emission to high emission by reducing the gas pressure in the source and increasing the emission current. This corresponds to an increase in discharge voltage in the UV source.

Similar results are found for helium and Neon. However the H α emission cannot be switched off, when the source is operated with Neon or helium gas, as it can be for argon.

9.3. Surface state dispersion with photons from a molecular hydrogen plasma

Figure 9.8 shows several UPS spectra of a 8 ML Mg film on Si(111) 7x7 recorded with light emitted when using molecular hydrogen in the discharge source. The electron emission angle is varied with respect to the analyzer between −2.5° and 17.5°. 0° corresponds to normal emission. The red solid lines are the result of a 20 point Savitzky Golay smoothing to the raw data, black solid lines

[SG64]. The HFE and HSS of the H α light are noted on the right in the graph by the blue dashed and dotted lines. The features named A and B are the same as in Figure 9.2 and their energetic shifts are given by the purple dashed and dotted lines. The HSS shifts with emission angle as does the feature B. However, the shift is somewhat smaller for feature B than for the HSS. Feature A does not shift with the angle. It is 2.41 eV from the H α Fermi edge which is in fact very close to the difference between the H α energy 10.2 eV and a molecular hydrogen emission line at around 162 nm or 7.7 eV [Ste89]. Thus, the feature A is attributed to the Fermi edge of this molecular hydrogen emission and feature B can be identified as the surface state signal for this photon energy. At normal emission this surface state is at 1.5 eV binding energy in respect to its Fermi edge. This is the same value as shown in chapter 5.3.4 for the same 8 ML film for He and H α emission in Figure 5.16.

It is not surprising that the excimer excitation of the atomic hydrogen emission described above does also excite the hydrogen molecule. The signal is weaker than that of atomic hydrogen and in fact only present for very few samples. Only for those films, that have a very small secondary electron background, which can be attributed to very clean and extremely ordered crystalline films, is this molecular signal visible. Otherwise it gets lost in the background.

It is possible to determine the dispersion relation for the surface state signal of the molecular hydrogen line, using equation 5.6. The dispersion relation is plotted in Figure 9.9 together with that of the atomic hydrogen (H α) line. The solid lines represent parabolic fits to the data, yielding slope parameters of 1.48 and 1.55 for the atomic and molecular lines. The energetic shift between the two sets of data of 0.1 eV can be attributed to the error due to the small and washed out surface state signal for both photon lines, see Figure 9.8. Qualitatively the dispersion relation with the 7.7 eV photon line agrees well with the data for atomic H α and He I light, see Figure 5.16.

9.4. Photoyield in dependence on photon energy

Using the different available photon energies from the different gas-plasmas one can measure the energy dependence of the photoyield for the different states of the Mg surface.

Figure 9.10 illustrates this, as it shows the He (top) and Ne (bottom) scans of a 12 ML thick Mg film on Si(111) 7x7. In these spectra the H α signal is dominating as before. One can see the signals of the HFE, HSS and HQWS as previously shown. The molecular hydrogen features, A and B, are also present. The insets show the area of the He I/ Ne I Fermi edge. The He I signal shows the surface an quantum well state but the Ne I does not. The two graphs on the right show the electron signal at the He II / Ne II Fermi edge from the same scans. The source is driven in the He II/ Ne II

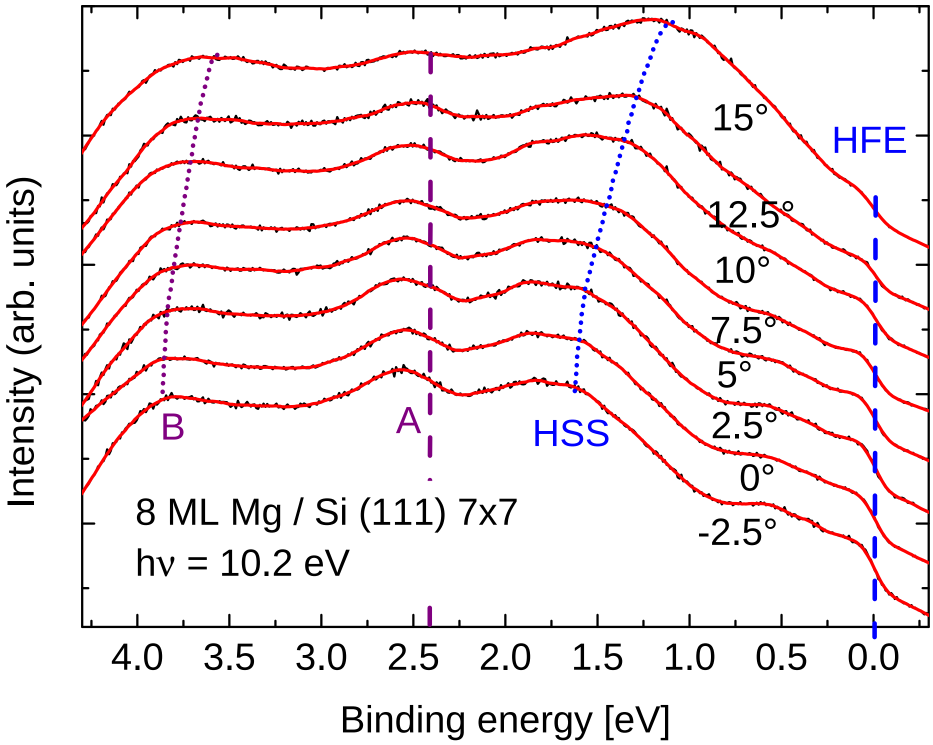

Figure 9.8.: UPS spectra with hydrogen gas in the discharge source. From top to bottom the angle of emission is varied up to 20° The surface state recorded with H α and the feature B shift with the angle. Feature A and the Fermi edge stay at a constant energy. The red lines are smoothed by a 20 point Savitzky Golay smoothing [SG64]. The original data is shown as black solid lines

mode for these scans, as described above. The surface state is visible in both cases after a 35 point Savitzky Golay smoothing, represented by the solid red line [SG64].

From measurements like this one, one can determine the intensity of the photoelectron signal from the surface and quantum well state for all these different photon energies available. For example the data in Figure 9.10 one can deduce the intensities of the molecular and atomic hydrogen lines, the primary Ne I/ He I lines and the secondary Ne II/ He II lines. For the hydrogen lines there are many different values available, as the signal is present in every scan. Hence, for the hydrogen signals, the intensity is averaged over all the scans for a single sample. The intensity of the surface and quantum well state are used, because these are the only distinguished features in the Fermi edge region.

An error is made in this evaluation of the data, as we do not know the photon fluxes. All measure-

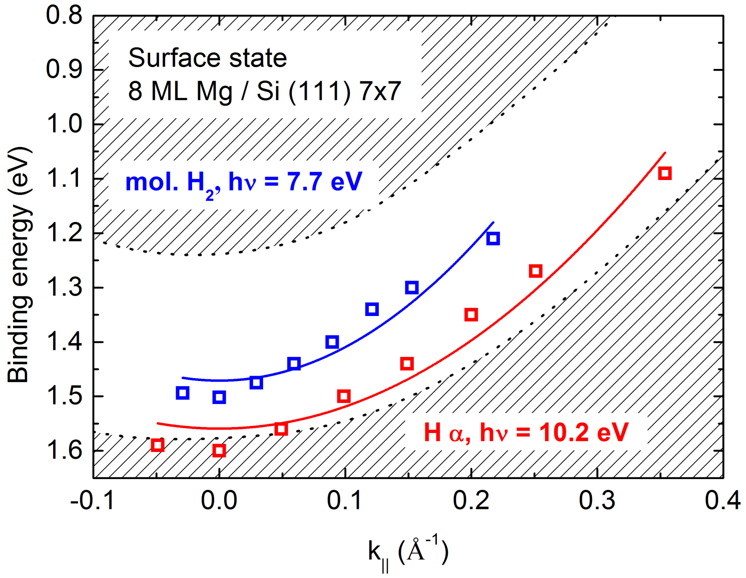

Figure 9.9.: Dispersion relation of the surface state of a 8 ML thick Mg film on Si(111) 7x7 recorded using molecular and atomic hydrogen radiation. The solid lines represent parabolic fits to the data. The shaded regions depict the projected bulk bands as determined from [BGGP86, CSFK99].

ments were made in a way, that the detected current at the sample during the measurement is the same within a factor of 2. However this value is not a very useful number for the determination of the photon flux, especially for the secondary lines. There is still dominantly He I light in the flux when scanning in He II mode. The sample current was thus only taken as a rough measure of the total photon flux. Although there is this error due to the flux difference, it is thus small for the primary I lines for the different gases. The secondary lines (Ar II, Ne II, He II) are underestimated. The result of the energy dependent intensity measurements is plotted in Figure 9.11. The intensity of all sets of data was normalized to the most intense photon energy line, which was in all cases the H α line at 10.2 eV photon energy. The surface state photoelectron intensity of a 13 ML Mg film, represented by blue hollow circles, and of a 12 ML film, green half-filled triangles. The photoelectron intensity of the quantum well state of the same 13 ML film is given by the black squares. The solid red line is taken from the publication by Aballe *et al* [ARH02b]. The photoyield of a 10 ML Mg film was recorded at the Bessy storage ring and hence the authors were able to determine precisely the photon flux. The read solid line was also normalized to the maximal value, which the authors found at an energy of 10.4 eV. The cyan line gives the photoelectron intensity at the Fermi edge of

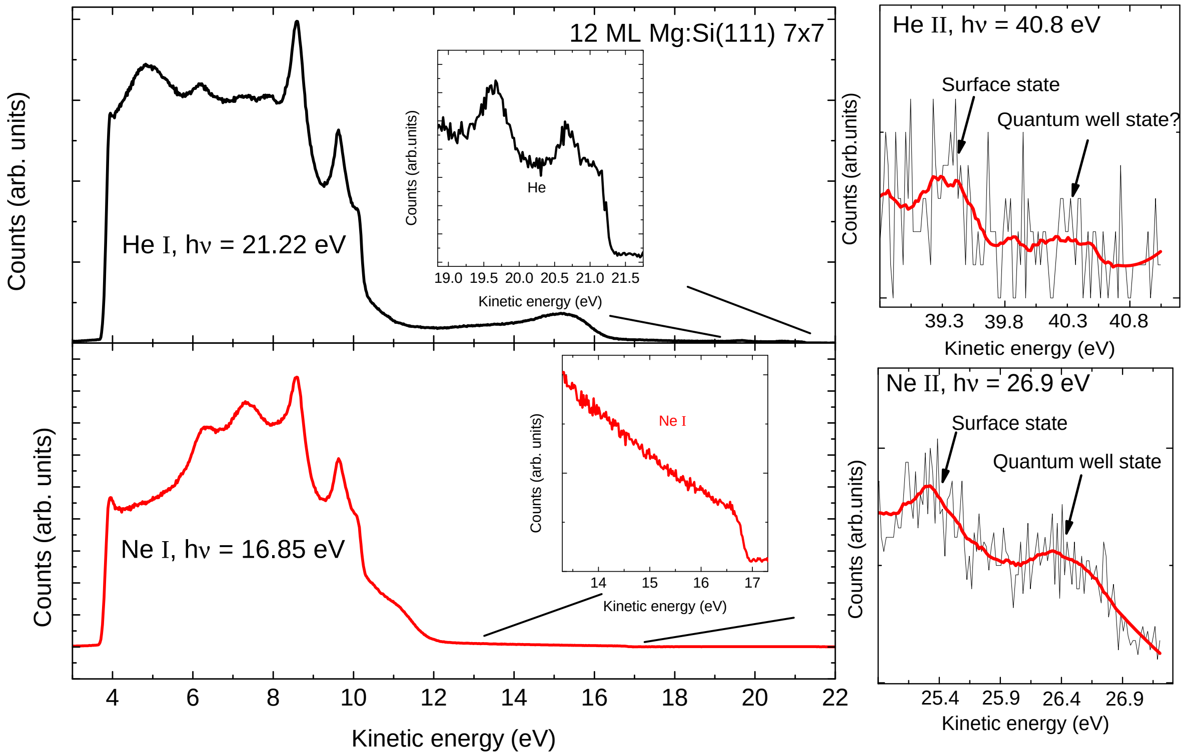

Figure 9.10.: UPS spectra of a 12 ML Mg film on Si(111) 7x7 recorded in normal emission using He, upper panel, and Ne plasma, lower panel. The graphs on the right show the He II/ Ne II Fermi edge. The red line is the result of a 35 point Savitzky Golay smoothing.

a bulk single crystal measured by Bartynski *et al* [BGGP86] and it is normalized to merge with the data from Aballe at around 18 eV.

The overall agreement between our data and the data by Aballe and Bartynski is very good, although our photon flux is not calibrated. The maximum in the photoyield lies slightly below the Mg bulk plasmon energy at 10.8 eV, see chapter 5.3.3.

For photon energies below the magnesium bulk plasmon energy $\hbar\omega_{\mathrm{bulk}} \approx 10.7$ eV, the intensity of both the surface and quantum well state is large. It drops to around zero for higher energies between 11.83 eV and 21.22 eV. The signal for He I is the most intense for photon energies above the plasmon energy. This could be due to the problem of the non existing flux normalization. This would effect the Ar II / He II / Ne II lines very strongly, because their photon flux is certainly smaller than those of the primary photon lines. However Bartynski *et al* show that the signal for

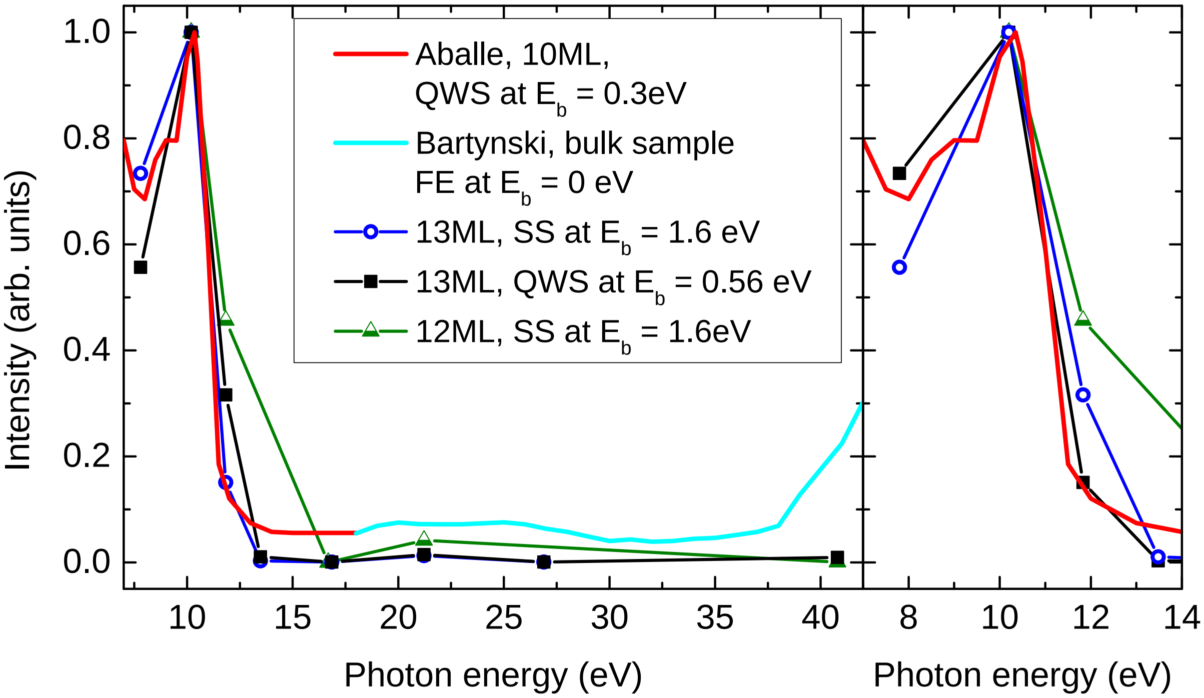

Figure 9.11.: Intensity of the photoelectron emission from the surface and quantum well state plotted versus the incident photon energy for three different sample thicknesses. The red line represents data published by Aballe *et al* [ARH02b] recorded at the Bessy storage ring. The cyan colored line represents data by Bartynski *et al* for a bulk single crystal [BGGP86]. The agreement is very good. The data points arise from scans with primary and secondary lines of H_2, Ar, Ne and He.

He I is in fact relatively more intense than for lower photon energies, but the Ne II and He II signals should not be much smaller [BGGP86]. The resonances at around 23 eV and 43 eV are attributed to an enhanced coupling to the final states at those photon energies [BGGP86].

The low energy part of the graph is shown enlarged on the right hand side. One can see that the data points here agree with the data by Aballe very well. The maximum in that work was found to be around 10.4 eV and has a width of about 0.8 eV. This energy is very close to that of the Mg bulk plasmon of $\hbar\omega_{\text{bulk}} \approx 10.7$ eV, as shown in chapter 5.3.3. It is attributed to the adlayer-related standing-wave-like bulk plasmon of Mg [BBH04]. This bulk-like mode is only present in thin films. Constant initial state photoyield measurements of bulk-like single crystal samples, on the other hand, show a minimum at this energy [LPF79]. The regular monopole bulk plasmon of an quasi infinite film cannot be excited by an electromagnetic field, as shown in chapter 2.7 [Fei82, MH70, Lie97].

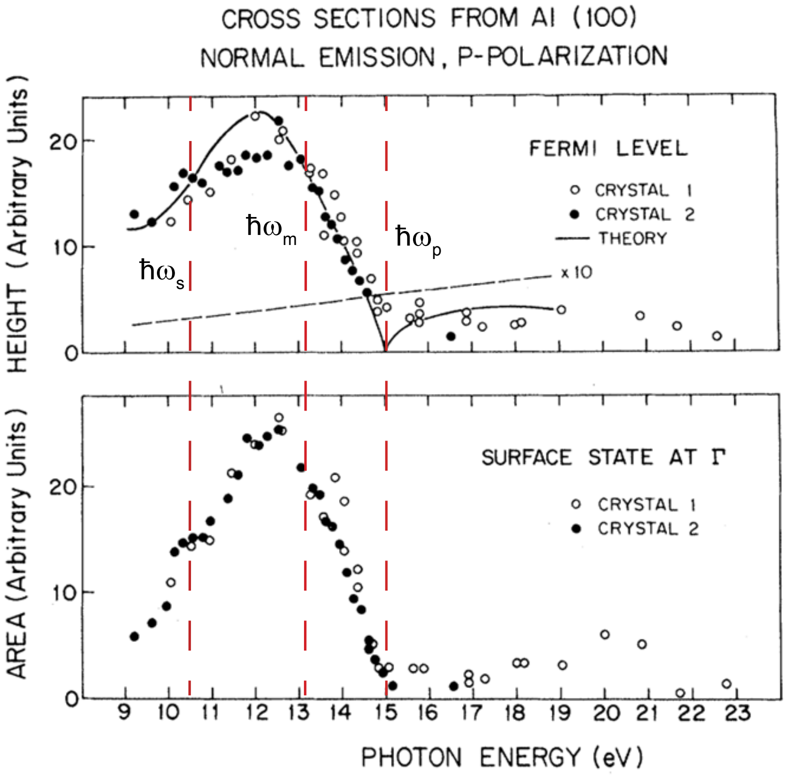

Figure 9.12.: Photoyield in dependence on photon energy of a Aluminum bulk single crystal. At the bulk plasmon energy $\hbar\omega_{\mathrm{p}} = 14.97$ eV, one finds a total minimum of the photoyield. The maximum is around the multipole surface plasmon energy $\hbar\omega_{\mathrm{m}} = 13.2$eV and the surface plasmon energy $\hbar\omega_{\mathrm{s}} = 10.55$ eV [CFS+00, Rae80]. Taken from [LPF79].

Experimental evidence is presented in Figure 9.12 for an aluminum bulk single crystal [LPF79]. At the bulk plasmon energy of Aluminum, $\hbar\omega_{p,\mathrm{Al}} = 14.97$ eV [Rae80], no photoyield is visible. Below this energy a broad emission maximum is found at $\sim 0.8 \cdot \hbar\omega_{p,\mathrm{Al}}$, which is close to the surface and surface multipole plasmon [Rae80, Lie97, CFS+00]. This is true for photoelectrons from the Fermi edge, upper panel in Figure 9.12, and the aluminum surface state, lower panel.

Obviously the situation is different for thin films. In the group of Karsten Horn it has been shown that the photoyield decreases at the plasmon energy for films larger than a certain film thickness for alkali metals and silver [LKP01, BBH04, BSH+01, BHH+98]. However, these works only cover very few selected film thicknesses and thus offer a limited thickness resolution.

The origin of this adlayer-related bulk-like plasmon mode, which is responsible for the behaviour of the photoyield of thin films, is that the transverse electromagnetic wave and the longitudinal fields in the Mg film couple when the film is very thin [Gad70]. The standing waves in the Mg layer add up due to reflection at the Mg-Si and Mg-vacuum interfaces and are spatially confined in the Mg layer [Gad70, BBH04]. With increasing Mg layer thickness the coupling between the interfaces becomes weaker and the standing waves, the bulk-like plasmon, intensity decreases.

The intensities to the left of the maximum, which are seen in the data by Aballe *et al* in Figure 9.11, can be attributed to the surface and the surface multipole plasmons, at $\hbar\omega_{\mathrm{s}} = 7.4$ eV and $\hbar\omega_{\mathrm{ms}} = 8.7$ eV, respectively. Those do not diminish with increasing film thickness, as they exist only at the surface of the Mg film [LKP01]. This is why, in Figure 9.12, the intensity maximum for the photoelectron signal of both the surface state and Fermi level from a Al semi-infinte crystal is around the energy of the surface multipole plasmon [CFS^{+}00].

The effect of the vanishing photoyield and thus vanishing cross section for photon energies around the plasmon energy can be seen in Figure 9.1 at the beginning of this chapter. The 300 ML thick Mg film does not show the H α signal. No confinement in z-direction is present, which means no standing waves can form and thus the adlayer-related plasmon does not exist. The thickness dependence and the effect of the adlayer-related plasmon will be discussed further in section 9.5.

9.5. Thickness dependence

In this chapter the thickness dependence of the He I and H α intensity is discussed. UPS spectra using Helium gas were recorded for all of the crystalline Mg samples in this work. It will be shown that the intensity of the photoelectron signal generated by hydrogen light decreases with increasing film thickness. This indicates the transition from the photoyield maximum at the plasmon energy for thin films, Figure 9.11, to the photoyield maximum at the surface (multipole) plasmon energy for bulk samples, Figure 9.12.

More than 30 samples with varying film thickness have been prepared and analyzed. The photoelectron intensity of the surface (upper panel) and the quantum well state (lower panel) is given in Figure 9.13 in dependence of the Mg film thickness in monolayers. Both the helium and hydrogen induced intensities are given. The parameters concerning gas pressure, source voltage and emission current for a single sample were the same for helium and hydrogen. Between different samples the parameters could vary, but as described before the detected sample current was kept to the same level. In Figure 9.13 the helium signal for the quantum well state is multiplied by a factor of three. In this chapter the data for the surface state is color coded in the Figures in black and green and the data for the quantum well state in red and blue.

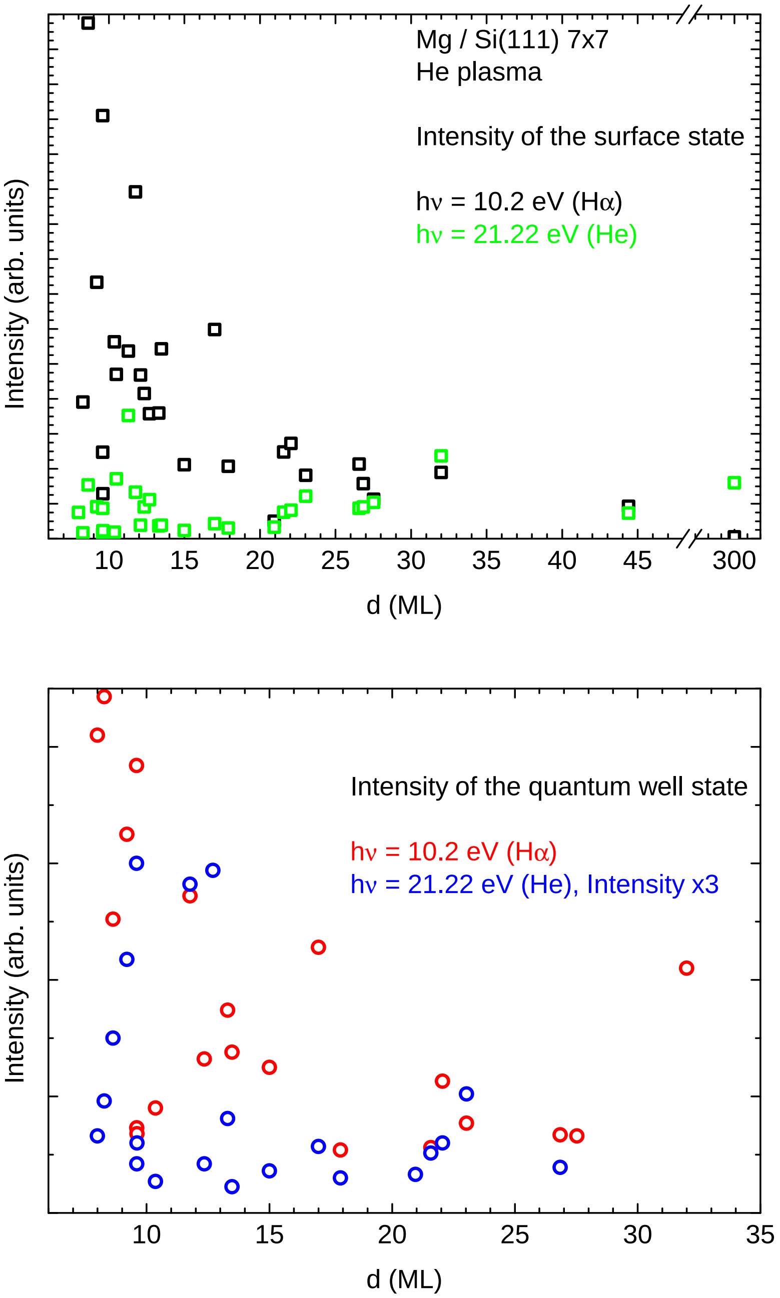

Figure 9.13.: Photoelectron intensity of the surface (upper panel, black (H) and green(He)) and quantum well (lower panel, red (H) and blue (He)) state versus the Mg film thickness. Helium was used in the UV-source. The thinner the films are, the more intense the H α photoelectron features become as opposed to those of He I. The He I photoelectron intensity of the quantum well state is multiplied by three, shown in the lower panel.

It is obvious that the thinner the Mg film is, the more intense the Hα photoelectron signal is. This is especially conspicuous for the surface state, but it holds for the quantum well state as well. On the other hand for the very thick sample, 300 ML, the surface state is not visible within the H α photoelectron signal. For thicknesses between 25 ML and 45 ML the surface state photoelectron intensity is roughly the same for hydrogen and helium light. The thinner the film gets the more intense the hydrogen induced surface state intensity becomes, while the SS intensity stays fairly constant. For the HSS signal the increase is a factor of 6, while it is only a factor of 2-3 for the SS. The situation is more or less the same for the quantum well state, but not as pronounced. This is shown in the lower panel of Figure 9.13. An increase in the HQWS intensity, similar as for the HSS, is clearly discernible - red circles. From 25 ML to 8 ML the intensity increases. Only three samples at 10 ML thickness show a low intensity as an exception. The intensity of the helium photoelectron signal on the other hand seems to be relatively constant, with a few samples between 9 ML and 14 ML showing a higher intensity. One has to bear in mind that the quantum well states become very small for larger thicknesses and finally vanishes up to a film thickness of 45 ML. The signal becomes too small for a solid evaluation after 30 ML. As was mentioned before the quantum well state denoted here is always the one closest to the surface state in kinetic energy, as its photoelectron signal is usually the most intense of the different QWS.

In general, the H α photoelectron signal is more intense than the He I photoelectron signal for both the surface and quantum well state. The intensity increase towards thin films is stronger for hydrogen light.

Error bars are not given on the data points here. It is not possible to give an estimate of the photon flux, especially for the hydrogen signal. That is why a lot of samples are needed for this type of analysis. The trends given in Figure 9.13 can be trusted, as there was no order in which these samples were prepared and measured thus eliminating any time dependent effects. The varying intensities could not be correlated to an opening and following bakeout of the chamber, a recharge of the Mg evaporation material or a switching of the gas bottle at the UV source. Basically the scatter, that can be seen at small thicknesses is a measure for the error in the intensity due to the unknown photon flux.

The difference between the hydrogen and helium photoelectron signal is better visualized when looking at the ratio of their intensities. This is shown in Figure 9.14. The upper graph shows the ratio of the surface state intensity from the hydrogen signal and the helium signal, $I_{\mathrm{HSS}}/I_{\mathrm{SS}}$. The lower graph gives the same for the photoelectron intensity of the quantum well state $I_{\mathrm{HQWS}}/I_{\mathrm{QWS}}$.

The first thing to notice is the huge scatter, roughly a factor of three from the average value, for small film thicknesses $d < 17$ ML. The unknown photon flux is of course an issue here that goes directly into the ratio. A second factor, that is also very difficult to put a number on is the crystallinity of the Mg film. If the magnesium film is not crystalline, the hydrogen signal is still present, but rather weak. This especially affects the quantum well signal, as no quantum wells exist if the film is not crystalline.

The scatter becomes somewhat smaller for films with $d > 18$ ML and decreases to around a factor of two. In this aspect the thickness dependence seems to be similar for the surface and the quantum well state. The crossing from the large to the small scatter region is very abrupt and sharp. This indicates a change in the photoelectric response to the incident photon flux.

The total increase in the intensity ratio is larger for the surface state. For $d > 18$ ML the ratio is roughly around unity and increases to a value of around 10-15 for thin films. The intensity ratio for the quantum well state starts from a much higher value of around five for $d > 18$ ML to around 10 for thin films. The increase in the ratio is thus only by a factor of 2. The intensity of the H α photoelectron signal of the quantum well state does not decay with film thickness as quickly as that of the surface state. One can see that fewer data points exist for the quantum well state. Between 20 and 30 ML only four intensity ratios could be obtained. As was mentioned, the reason is that the quantum well intensity decreases with increasing film thickness and for one of the two photoelectron signals, either for helium or hydrogen light, it was not possible to fit a quantum well peak with satisfying precision and quality.

It is obvious that thin and thick films respond differently to the incident photon energy. That has already been shown by the total photoyield measurements. With increasing film thickness the photoyield maximum, which is on the right of the hydrogen photon energy for thin films, as shown by [ARH02a] and this work, moves toward smaller photon energies, crosses the hydrogen photon energy and with further increasing the film thickness the maximum moves towards the surface plasmon energy as predicted by theory and experiment [Lie97, LPF79, Fei82]. This crossing of the hydrogen energy at 10.2 eV could be at around 17 ML. A schematic of this idea of a shift of the total photoyield is shown in Figure 9.15. For very thin films the photoyield intensity maximum is close to the (adlayer-related) bulk plasmon energy [BBH04]. Hence, the intensity of the photoelectron signal of H α light is also large. With increasing film thickness the photoyield of H α light decreases, as indicated by the red squares at 10.2 eV in Figure 9.15. For bulk samples this photoyield is basically zero. Due to the steepness of the high energy slope in the photoyield, Figure 9.11, a shift of the

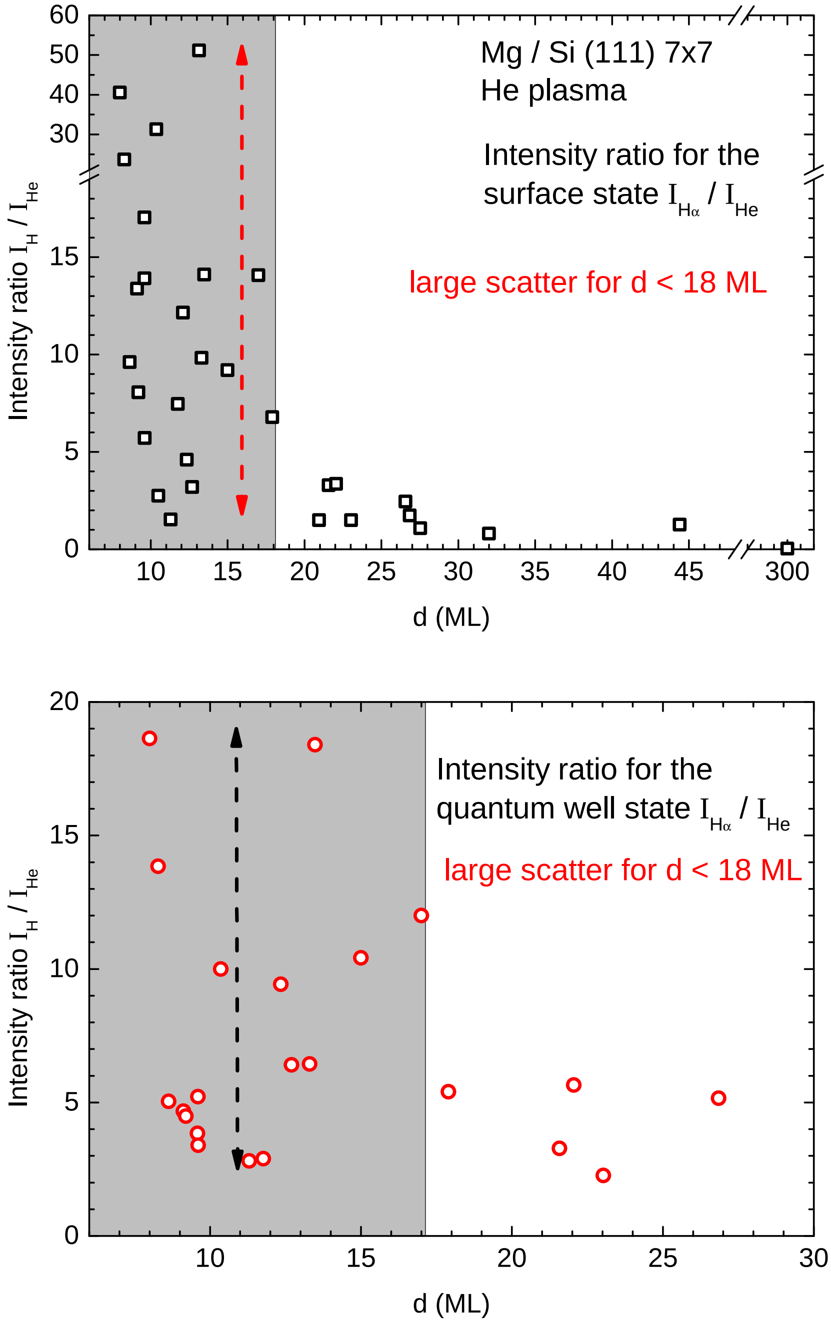

Figure 9.14.: Ratio of the intensities $I_{\mathrm{H}\alpha}/I_{\mathrm{He}}$ of the surface (upper panel) and quantum well state (lower panel). The ratio increases for the surface state from unity to 15, for the quantum well state by a factor of two from five to ten. The scatter is small for thicknesses $d > 18$ ML and large for thinner films.

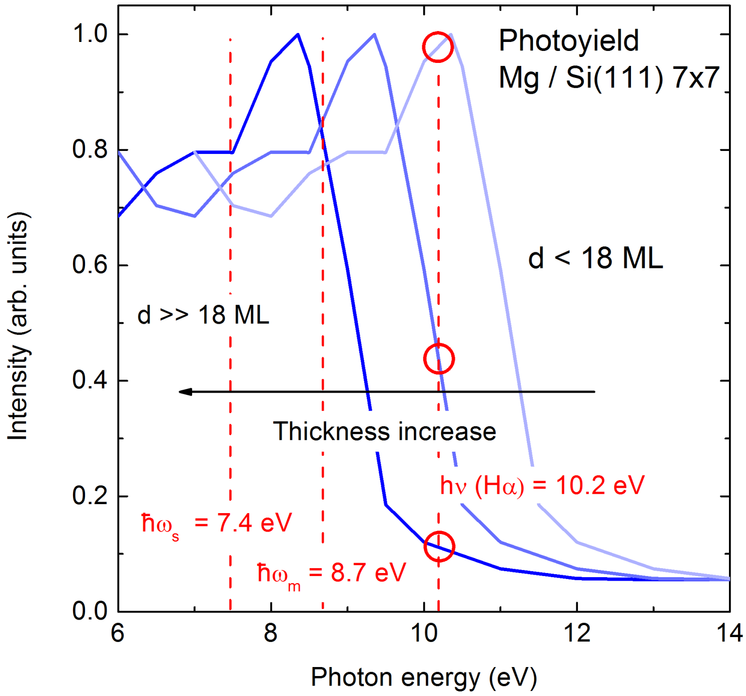

Figure 9.15.: Schematic of the thickness dependence of the photoyield. With increasing film thickness the photoyield maximum shifts from the bulk plasmon to the surface plasmon energy.

maximum, as depicted in the schematic, could result into a very quick decay of the hydrogen signal within only a few monolayers, looking like a step-like intensity decay.

There is additional evidence that something like a step-like transition around 17 ML could be correct. The first is a change in the energetic difference between the helium and hydrogen peaksm which is expected as 21.22 eV − 10.2 eV = 11.02 eV. This is presented in chapter 9.6. The second is a weak bilayer oscillation of the intensity ratio that is visible in the intensity ratio for thin films with $d < 17$ ML, show in Figure 9.16. Thicker films do not show this, but this could admittedly also just be due to the lack of data. The intensity ratio of the photoelectron signal of the surface state data is plotted in the upper panel. The red lines are given to guide the eye. Even monolayers show a high intensity ratio, odd numbers a low intensity. This means that either the H α signal becomes somehow enhanced every 2nd monolayer or the helium signal. It has to be noted that Magnesium is stacked in an ABAB configuration so that only every second monolayer shows the same electronic configuration and surface termination. As has been shown by Liebsch and Feibelmann [LKP01, Fei82] and discussed in chapter 2.7 the exact nature of the electronic potentials at the surface strongly influences the $d_\perp$ value and thus the expected photoyield. $d_\perp$ is the centroid of the fluctuating surface charge density induced by an external field, in this case the illuminating UV-light. If, by changing the surface termination through an ABAB alteration one changes the $d_\perp$ value this would be directly visible in the photoyield signal of the H α light. The He I photoelectron signal would not be affected, as the photon energy is far away from the Mg surface, multipole surface or bulk plasmon energies. The hydrogen induced photoelectron signal is much more sensitive to changes in the energy dependence of the photoyield. It is close to the maximum so all slight changes in the energy dependence have a strong effect on the hydrogen intensity, as was mentioned above 9.15. This argument results in a bilayer oscillation of the intensity ratio, due to an alterating increased/decreased H α photoelectron signal.

Overall this bilayer oscillation is very weak considering the error due to the photon flux and thus the scatter of the data points. This is why this feature should not be stressed too much.

Remembering the results from the chemicurrent experiments it should be noted that the current increase found in dependence of the film thickness does not coincide with the bilayer oscillation of the intensity ratio found here.

9.6. Kinetic energy of hydrogen alpha and helium I photoelectrons

The existence and properties of surface and quantum well states are determined by the quality and thickness of the metal film. Therefore it should not matter which photon energy is used in UPS for the determination of the energetic position of these states. The kinetic energy of the photoelectrons from the surface and quantum well state as measured by UPS with Helium gas is given in Figure 9.17. The upper panel shows the photoelectron signals by He I and H α light of the Mg surface state and the lower panel the same for the quantum well state. As before the quantum well state is the one closest to the surface state for thicker samples where more than one QWS exists. The kinetic energey difference between the HSS and SS is constant and close to the expected 21.22 eV − 10.2 eV = 11.02 eV for nearly all thicknesses. The surface state is fixed at 1.6 eV below the respective Fermi edge for thicknesses $d > 14$ ML. For thinner films the surface state shifts towards the Fermi edge and it also broadens. This is well known and the usual behavior, e.g. [ARH02a]. However for the H α light the change in the kinetic energy is stronger.

The position of the quantum well state, lower panel, changes with film thickness, as it should [PWC$^+$02]. The kinetic energy difference is seemingly farily constant for all thicknesses.

That this is not exactly the case is better visible in Figure 9.18 where the difference in the kinetic energy is plotted versus the film thickness. From top to bottom the data represent the kinetic

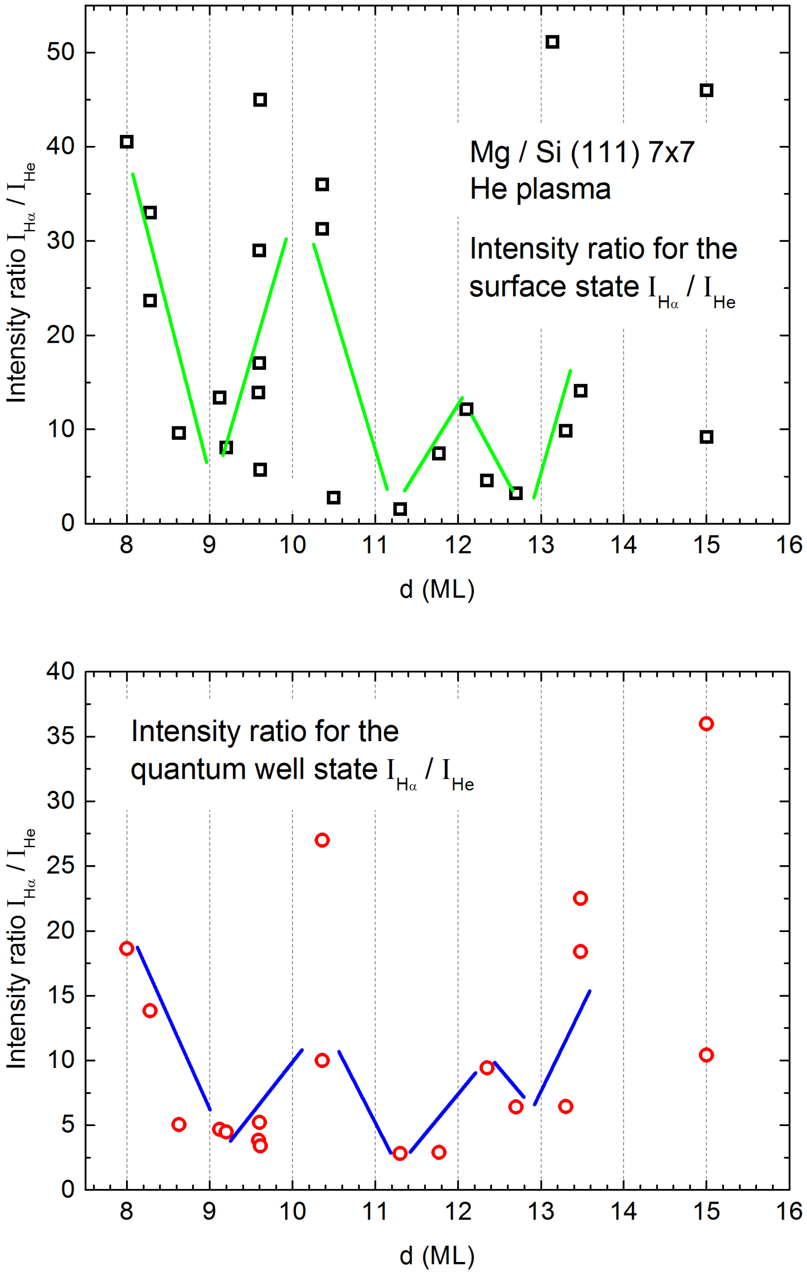

Figure 9.16.: Zoom into thicknesses below 16 ML for the intensity ratios of the surface (top) and quantum well state (bottom). The red lines indicate a bilayer oscillation of the intensity ratio.

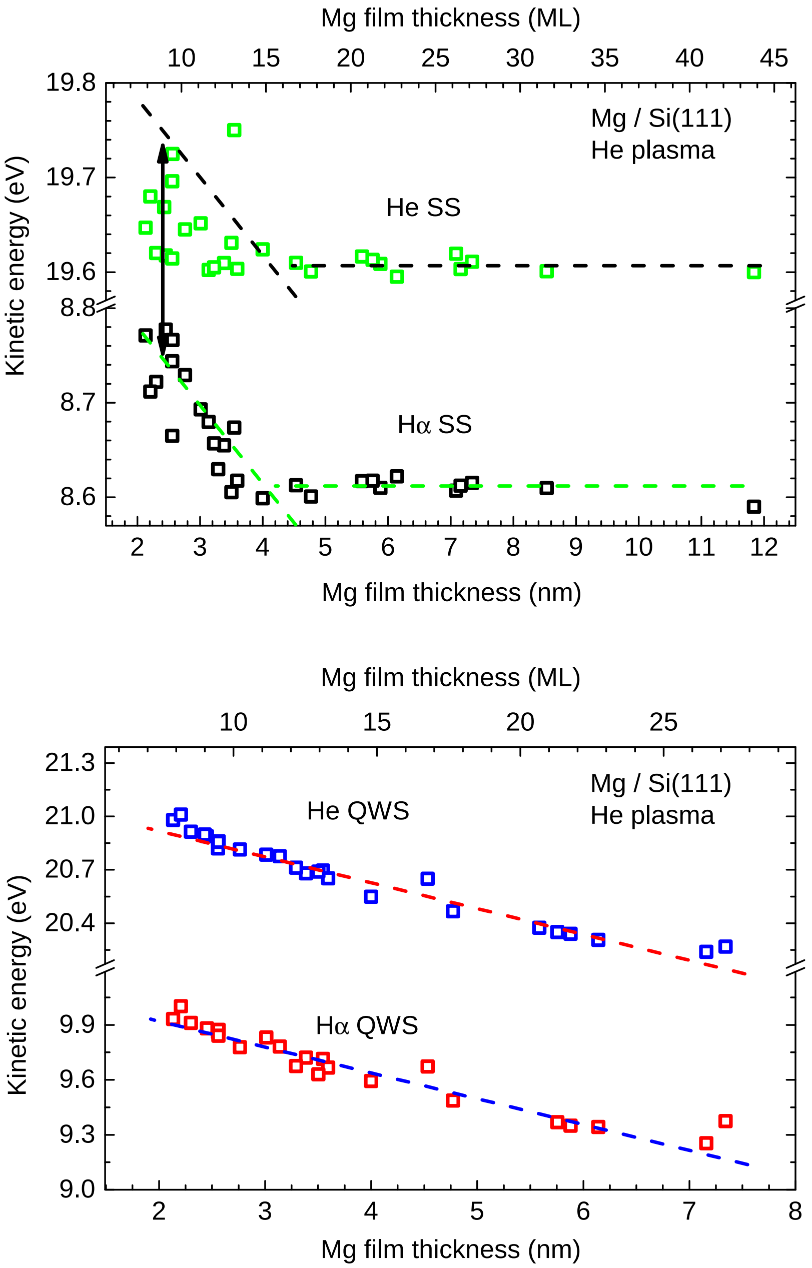

Figure 9.17.: Kinetic energy of electron emitted from the surface state (upper panel) for He I and H α light and the same for the quantum well state (lower panel) versus the thickness of the magnesium layer. The quantum well state is again the one closest to the surface state, when more than one exist.

energy difference for He I and H α photoelectrons from the surface state, quantum well state and the Fermi edge.

The latter does not change much with thickness, as is to be expected. The Fermi edge is constantly fixed at the kinetic energy corresponding to the incident light, thus the energetic difference is fixed at $\sim$ 11 eV. The 20 meV of difference between very thick and thin films is smaller than the scatter and also smaller than the resolution of the UPS setup at this temperature.

The energetic difference between the HSS and SS is constant down to thicknesses of $\sim$ 14 ML. For thinner films the difference decreases because the kinetic energy of the He I photoelectrons does not shift as strongly towards the Fermi edge. The total kinetic energy difference between $d = 8$ ML and $d > 15$ ML flims is $\sim$ 100 meV.

The situation for the photoelectrons from the quantum well state is the same as for those originating from the surface state for thick Mg films. However, below $d < 15$ ML the difference increases slightly. The difference is about 50 meV while the thickness is decreased to 8 ML. This result means that for thin films photoelectrons originating from the surface or quantum well state show a different binding energy depending on wether they were excited by H α or He I photons. The cause for this is not known. But some origins can be excluded.

It is unlikely that this behavior is an artifact due to an error in the evaluation of the peaks. Although the fitting of both the surface and the quantum well state is difficult for very thin films the fitting procedure itself is identical for both peaks, thus an error should result in the same error. The fitting is difficult because the surface state on the one hand becomes very broad and decreases in intensity when the films are very thin. The quantum well state on the other hand overlaps with the Fermi edge and thus the resulting peak is a superposition of both features. These problems are true is for a film thickness of 7 to 8 monolayers. Already for 10 ML the QWS is roughly 0.3 eV from the Fermi edge, where no overlap is possible - see Figure 5.10. The surface state is at the same time already intense enough to allow an easy fitting. Hence the change in the energetic difference is not an artifact due to the data analysis.

It is more probable that this is some kind of final state effect. The initial state of the metallic surface is independent on the photon energy. The analyzed electrons originate from the same state for helium and hydrogen light. When the screening of the photohole is good the final state energy can be calculated within a single-electron picture [Hüf03]. This is usually the case for simple metals like Magnesium. However it is imaginable that the screening of the photohole becomes insufficient when the electron density is reduced due to the reduction of the film thickness. If this was the case the detected energy could differ from the expected one-electron description. Many-body effects

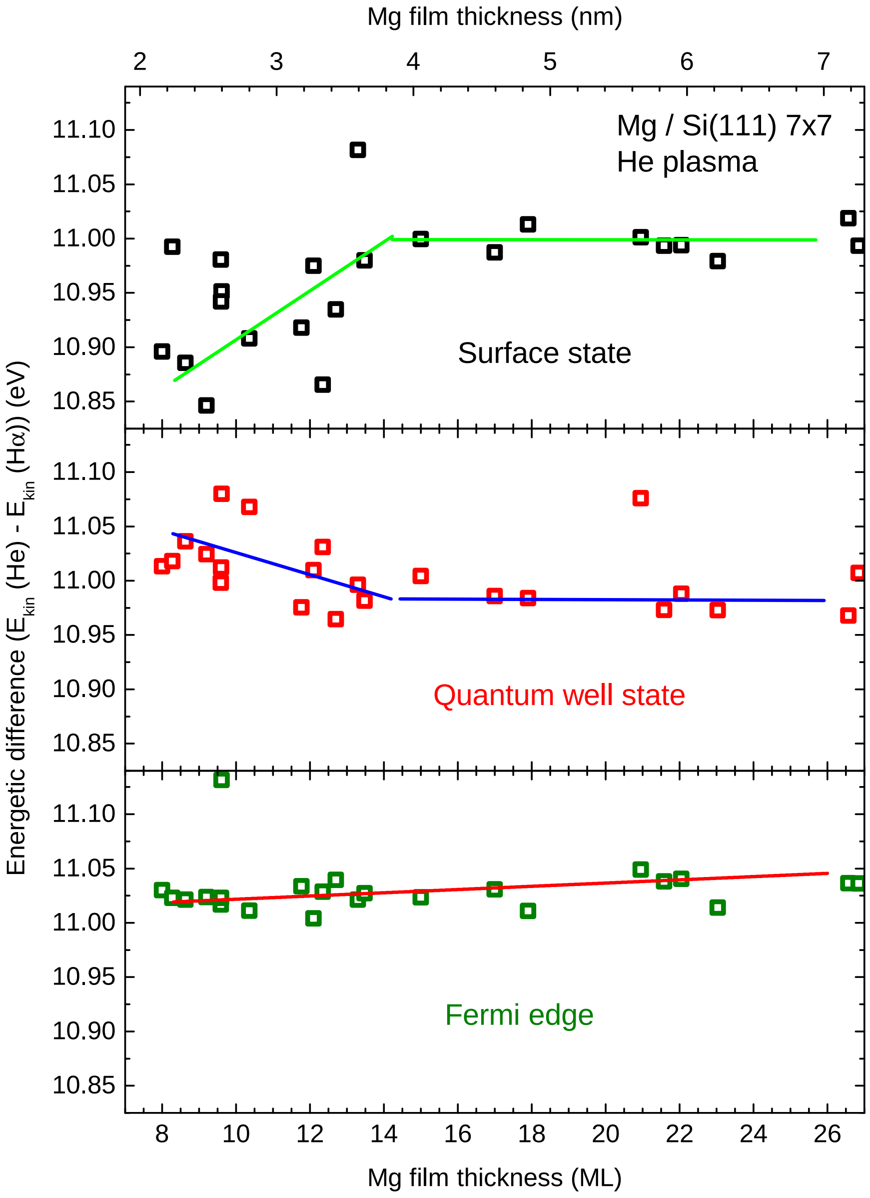

Figure 9.18.: Difference in the kinetic energy of the different states in the He I and H α parts of the spectra. The top graph shows this difference for the surface state, in the center is this value for the quantum well state and in the bottom graph for the kinetic energy difference for photoelectrons from the respective Fermi edges. The solid red lines are to guide the eyes and give the linear dependence of the energy difference on the film thickness. The quantum well state is the one closest to the surface state, when more than one exist.

could increase/decrease the detected electron kinetic energy. Why this insufficient screening of the hole should depend on the incident photon energy is unclear. As is the fact that surface and quantum well state show opposite behavior.

To determine the energy shift due to different photon energies more precisely a source/analyzer setup with a higher resolution and more photon energies would be needed. Without additional data an explanation of this weak effect is not possible.

The fact that the energy shift appears for films with a thickness $d < 15$ ML is taken as evidence, albeit unsatisfactorily explained, to support a step-like change in the intensity ratios, Figure 9.14.

Full width at half maximum of the hydrogen lines

An important parameter for describing photoemission peaks is their full width at half maximum (FWHM). Figure 9.19 plots the FWHM for the surface state signal (upper panel) and the quantum well state signal (lower panel) both for helium and hydrogen light emitted from a He plasma. The FWHM-values of the HSS and SS are basically identical. For thicker films the surface states FWHM remains constant around 0.25 eV, similar to other measurements [ARH02b, BGGP86]. QWS and HQWS show a constant FWHM of 0.25 eV for all thicknesses, albeit with a significant scatter. This is prove that the surface and the quantum well state are fundamentally different. As has been mentioned before the QWS is a bulk property, while the surface state is a surface property.

It seems that the FWHM of the two states is not affected by any final state, surface termination or surface roughness effects like the photoelectrons intensity ratios and kinetic energies.

The upper part of table 9.2 gives the FWHM values for all the different photon energies that were used to scan the surface state of a 13 ML Mg film. While the He and Ne photoelectron signals have FWHM values of 0.4 eV and 0.42 eV respectively, the Hα photoelectron peaks trend to be slighlty smaller at around 0.37 eV and 0.35 eV.

The lower part of table 9.2 gives the only available value for the FWHM of the Mg surface state for molecular hydrogen plasma along with the other photon energies used on a 8 ML sample.The surface state measured with molecular hydrogen yields a higher FWHM value 0.76 eV than the hydrogen signal when other gases, He 0.63 eV and Ar 0.64 eV, are used. This measurement has not been repeated, but it is possible that the spectral width of the hydrogen signal originating from the energy transfer through excimer excitation is smaller, hence the photon line sharper. It would be very interesting for application to investigate this behaviour in greater detail.

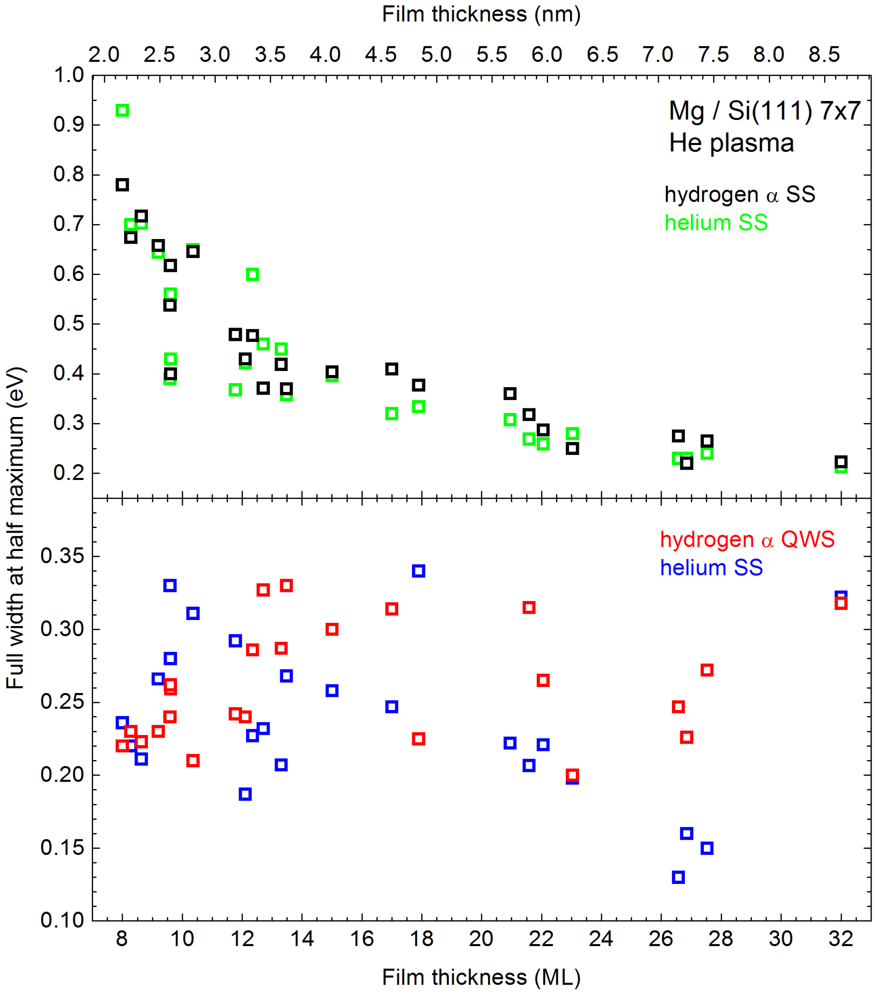

Figure 9.19.: Determined full width at half maximum of the different signals, SS (upper) and QWS (lower), from the UPS spectra plotted versus the Mg film thickness The H α (red and black squares) signals show the same FWHM as the states measured with helium light (blue and green squares).

Photon line	FWHM
He	0.40 eV
Ar	0.42 eV
H α in He	0.37 eV
H α in Ne	0.37 eV
H α in Ar	0.35 eV

Photon line	FWHM
H_2	0.76 eV
He	0.6 eV
H α in He	0.63 eV
H α in Ar	0.64 eV

Table 9.2.: upper table: Full width at half maximum of the surface state for different gases used in the UV-lamp. These measurements were done on a single sample with $d = 13$ ML. Lower table: Same for a single sample with $d = 8$ ML.

10. Summary and Outlook

10.1. Quantum size effects

This work presented the results on the preparation, characterization and oxidation of crystalline magnesium films on p-doped Si(111) 7x7 surfaces. These large area films are of high quality. LEED images show their highly ordered crystalline structure and reveal a slight rotational disorder of the metal surface of $\pm 3^\circ$. Photoemission spectroscopy data proves that the films are clean. The existence and thickness dependence of the quantum well states is another sign for the high structural quality of the films.

The thickness dependence of the work function ϕ_m was determined from ultraviolet photoelectron emission data and it follows the theoretical predictions closely [LZC07]. It oscillates by ~ 0.1 eV around a mean value of $\phi_\mathrm{m} \approx 3.92$ eV.

XPS and EELS measurements yield the surface-, multipole- and bulk-plasmon energies of these thin films to be around 7.2 eV, 8.7 eV and 10.7 eV, respectively. These values agree well with literature data [Rae80].

The parabolic dispersion relation of the surface state shows its free-electron-like nature.

A mean homogeneous barrier height of $\Phi_\mathrm{hom} = 0.567 \pm 0.04$ eV was derived from a multitude of temperature dependent current-voltage measurements. It was also shown that the IV-characteristics do not change during the oxidation experiments. The barrier height agrees very well with predictions made by the MIGS theory [Mön95].

A question that was addressed as well, was the structure of the covered Si substrate. It was previously unknown whether the 7x7 reconstruction remained intact upon the deposition of Mg atoms. Angular dependent UV-photoemission experiments indicate that this reconstruction in fact remains intact. An intensity increase for the surface state signal in UPS was found at precisely $\mathrm{k}_{||} = 0.27\text{Å}^{-1}$, which corresponds to 1/7 of the distance between two neighboring atoms in the reciprocal magnesium lattice. This agrees very well with the long range order and periodicity of the 7x7 reconstruction.

Chemicurrent measurements during the oxidation of the Mg films show a correlation between the electron density of states at the Fermi edge and the surface reactivity. A high DOS(E_F) results in a high reactivity. The entire reaction happens faster but the kinetics are qualitatively similar. By scaling down the detected current by a scaling factor $S = (1 \pm 0.06) \cdot L$ and increasing the exposure by the factor L all the chemicurrent traces look identical. As S and L are identical, this result strongly supports the claim that the chemistry for samples with a high or low DOS(E_F) is the same, when the film is exposed to oxygen. The scaling factor $S = L$ is as large as 2.5 for 9 ML thick films. The change in the DOS(E_F) is attributed to quantum size effects in the Mg film. Certain monolayer thicknesses, which are close to the value of a QWS crossing the Fermi edge, exhibit a higher density of states than others. No other parameter that correlates with the current increase is found in this work.

The intensity difference of the oxide component in the Mg 2p XPS-peak for different ML thicknesses, measured after the chemicurrent measurements, corresponds to the chemicurrent maxima. Those samples for which a high maximal current was detected also show a larger oxide component. For these samples the 2nd ML of the Mg film is also oxidized. This is in contrast to the samples displaying a low density of states or to polycrystalline Mg films.

The general trace of the chemicurrent can be described by a modified nucleation and growth model. It seems that the more crystalline a film is the higher is the discrepancy to the regular model. This modification is empirical in nature but based on the physical description of the growth process. A more detailed theoretical interpretation is needed.

Those samples which do not show a high DOS(E_F), due to quantum size effects, agree well with other data collected on the oxidation of polycrystalline magnesium films on different substrates. The hot-charge carrier distribution deducted from all these experiments can be described by a Boltzmann-like function with an effective temperature of 1760 K. This distribution intersects the y-axis at 1.03 electrons per O_2 molecule for a barrier height of 0.0 eV. Basically every reacting molecule excites an electron-hole pair with an average energy of 165 meV per electron, or 330 meV per electron-hole pair.

10.2. Intermediate silver layers

For the oxidation of 1 ML thin Mg films on Ag/p-Si(111) diodes a strong effect of surface plasmon coupled chemiluminescence (SPCC) was found.

For thin Ag layers, $d_{Ag} < 20$ nm, an increase of the Ag film thickness leads to a decrease in the current. This is in agreement with other chemicurrent data and this film thickness range is called the chemicurrent regime. A further increase of the film thickness leads to an increase in the detected current. The silver film absorbs emitted chemiluminescence light from the O_2 reaction with Mg and surface plasmon polaritons (SPP) are excited in the Ag film. These decay radiatively and are detected in the semiconductor as a photocurrent. This process is called surface plasmon coupled chemiluminescence. Simulations, that use the attenuated total reflection geometry, imply that the absorption maximum is at 46 nm Ag thickness. This agrees well with the current measurements, where the current maximum is found at a film thickness of 45 nm.

The generation of SPPs is facilitated by the periodic structure of the silver film with 50 nm wide islands separated by roughly 15 nm deep trenches, as has been shown by scanning electron microscopy and atomic force microscopy.

10.3. Si surfaces

It was possible to prepare three different silicon surfaces from the same substrate: the hydrogen passivated H:p-Si(111) surface, the moderately heated and thus depassivated and highly disordered p-Si(111) surface and the p-Si(111) 7x7 reconstruction. Two samples of each surface were made and electrically characterized by temperature dependent IV-measurements. Current measurements, in the chemicurrent setup, during the exposure of these surfaces to molecular oxygen showed that a current could only be detected on the 7x7 reconstruction. This is due to the existence of surface conductivity on the 7x7 reconstruction. The other Si surfaces do not have surface conductivity and thus no electrical connection to the Si surface is made, beyond the position of immediate contact. This also proves that the method of establishing the contact to the film, by a pivoted gold ball, is very effective, even when the conducting film is a single layer of the Si reconstructed 7x7 surface. Furthermore, the mechanical impact of the front contact onto the surface does not destroy the electrical contact to the surface conductivity.

Oxygen uptake after exposure was evaluated with XPS and revealed that, while the hydrogen passivated surfaces remained clean, the other two surfaces were contaminated with oxygen.

These results can be summarized as follows:

- H:Si(111): completely inert, so no detectable current.
- Si(111); reactive, but no existing surface conductivity and hence no detectable current.
- Si(111) 7x7: reactive and connection to the surface conductivity, thus detectable current. The current can be described as a displacement current. This is due to the generation and charging of additional surface states and the accompanying bending of the semiconductors valence band maximum and conduction band minimum.

10.4. Plasmons

This part of the thesis dealt with the existence of hydrogen radiation in the photon emission of a regular UV-light source operated with the noble gases Helium, Neon and Argon. Minimal contamination of the gases, probably just from hydrogen molecules diffusing through the walls of the inlet system, are enough to produce intense and spectroscopically very sharp hydrogen α - or Lyman α - emission, when the partial pressure in the formation chamber of the UV-source is increased. This is done by a modified pumping scheme as compared to the regular mode of operation. Excimers of the noble gas become excited by the applied high voltage and then loose their energy upon collision with a hydrogen molecule. The molecule dissociates leaving one atom in an excited state, which then emits the characteristic photons. This effect is most strongly observed for Neon. For Neon the excimer energy is very similar to the energy needed for the consecutive dissociation and photon emission from the hydrogen, so that this is basically a resonant process. Neon light emission is quenched drastically by this resonant energy transfer.

Constant initial state measurements of the Mg surface state reveal a very strong maximum in the surface state intensity vs. the photon energy, when H α light is used. The electron emission decreases almost like a step-function from maximal to nearly no emission when the incident photon energy is increased from 10.2 eV to 13.48 eV and remains very small for larger photon energies. Since theory predicts no electron emission close to the bulk plasmon energies [Lie97], which is $\hbar\omega_{\text{bulk}} = 10.7$ eV, the high intensity for H α light was surprising. However, this is only true for semi-infinite samples. For thin films, the photoyield maximum is found close to the bulk-plasmon energies.

The data presented here is the first, to the authors knowledge, to address the thickness dependence of the photoemission cross-section in a wide thickness range of up to 44 ML or ~ 10 nm, for thin metal films. It seems that a rather abrupt decrease in the emission probability occurs at around 16 ML Mg film thickness, where the intensity of the hydrogen signal drops to the same level as for the helium signal.

For films with $d \leq 16$ ML a possible bilayer oscillation is found, that would agree with the bilayer structure of crystalline magnesium. However, the evidence for this is not very strong.

While the full width at half maximum for the surface and quantum well states are the same for Helium and Hydrogen emission, the energetic position of the states is not. For very thin films, $d_{\text{Mg}} < 15$ ML, the surface state, detected by H α emission, shifts energetically closer to the surface state measured by He I light. This shift is roughly 0.1 eV. To complicate things even further the energetic position of the quantum well state behaves exactly the opposite way. However, the shift of 0.05 eV is smaller and less pronounced. The Fermi edges for the two photon energies do not shift with the Mg film thicknesses. This effect is not yet understood.

10.5. Outlook

The influence of quantum size effects on the detected chemicurrent can be investigated for different metal-semiconductor systems. Aluminum exhibits similar oscillatory oxygen uptake effects as magnesium [ABS^{+}10], due to a change in the decay length of the electron density of states with film thickness. With the newly constructed molecular beam chamber in our laboratory this reaction could be investigated via the detection of chemicurrents.

A more sophisticated description of the oxide growth on crystalline surfaces would facilitate the interpretation of the detected chemicurrent traces. The nucleation and growth model, albeit perfectly capable of describing the oxidation of polycrystalline quality films, is pushed to its limit when applied to crystalline films.

A possible experiment to further analyze the interplay of crystallinity and the detected current traces would be to prepare Ag/p-Si(111) diodes with a fixed silver thickness. Increasing the magnesium thickness on these diodes could result in a decrease of the Mg film quality due to relaxation of the lattice strain induced by the crystalline silver film. In chapter 7 the Mg layers were only 2-3 ML thick. Consequently the crystal structure was strongly influenced by the Ag layer underneath. Hence, thicker films should be better suited for modeling within the nucleation and growth model. In this way, one could possibly follow the change in film structure by monitoring the change in the current traces.

Ultraviolet synchrotron radiation would be the ideal tool to investigate the thickness dependence of the photoyield from thin Mg surfaces. With its tunable photon energy range the transition of the energy of the photoyield maximum from a value close the bulk plasmon energy, for thin films, to a value close to the surface plasmon energy, for semi-infinite samples, could be followed perfectly.

Appendices

A. Background subtraction for UPS spectra

Many samples with varying film thickness were prepared in the cause of this study. To eliminate the contribution of the secondary electron background and just compare the true replica signals a total inelastic background was deducted from the spectra [LZH93]. This procedure needs two defined energies in the spectrum. A E_{max} above which there is no signal. Usually this is chosen to be slightly above the Fermi energy. The other energy E_{min} is the one below which the signal consists only of secondary electron background. This background correction was used to evaluate the He and H_2 signals.

The total spectrum is the sum of the signal and the background:

$$I_{\mathrm{tot}}(E) = I_{\mathrm{b}}(E) + I_{\mathrm{s}}(E). \tag{A.1}$$

If we define

$$I'_{\mathrm{tot}}(E) = I_{\mathrm{tot}}(E) - I_{\mathrm{tot}}(E_{\mathrm{max}}), \tag{A.2}$$

the background function is

$$I_{\mathrm{b}}(E) = I_{\mathrm{tot}}(E_{\mathrm{max}}) + A \int\limits_{E}^{E_{\mathrm{max}}} I'_{\mathrm{tot}}(E')dE'. \tag{A.3}$$

The constant A can be determined from

$$I_{\mathrm{b}}(E_{\mathrm{min}}) = I_{\mathrm{tot}}(E_{\mathrm{min}}) \tag{A.4}$$

as the spectrum at E_{min} consists only of inelastically scattered background. The total background function can finally be written as:

$$I_{\mathrm{b}} = I_{\mathrm{tot}}(E_{\mathrm{max}}) + (I_{\mathrm{tot}}(E_{\mathrm{min}}) - I_{\mathrm{tot}}(E_{\mathrm{max}})) \cdot \frac{\int\limits_{E}^{E_{\mathrm{max}}} I'_{\mathrm{tot}}(E')dE'}{\int\limits_{E_{\mathrm{min}}}^{E_{\mathrm{max}}} I'_{\mathrm{tot}}(E')dE'}. \tag{A.5}$$

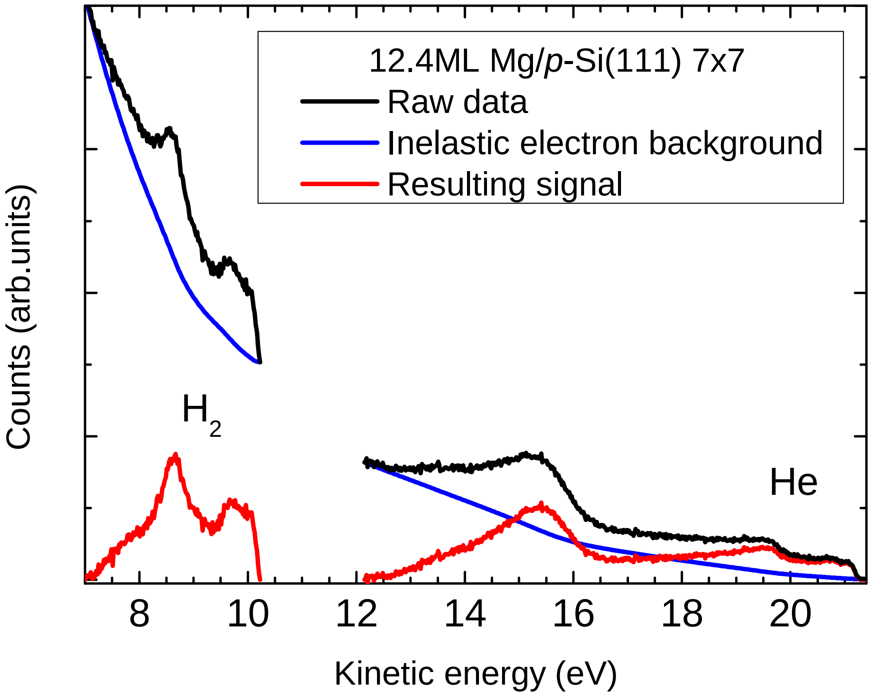

Figure A.1.: Result of the background correction. The black line gives the raw data, blue represents the calculated total inelastic electron background calculated by equation A.5. The red line is the resulting data.

An example of this background correction is given in Figure A.1. $E_{\text{min, H}_2}$ - signal consists only of background - was chosen to be roughly 3 eV to the left of the Fermi edge for H_2. $E_{\text{max, H}_2}$ just to its right. For the Helium part $E_{\text{min, He}}$ was selected to include the oxygen footprint. $E_{\text{max, He}}$ is just to the high kinetic energy side of the He Fermi edge.

The software CasaXPS was used to fit the resulting spectra. The result of the fit to the scan is shown in Figures A and A.3 for the helium and the hydrogen line respectively. The line shapes are 75% Gaussian - 25% Lorentzian sum function. Linear backgrounds are used, shown in blue, and the resulting fits to the SS and QWS are shown in green. Sometimes, as in this case for the surface state in the He spectrum, the electron background is not constant, even after the applied background correction. If this was the case two approaches were made to fit the data as is shown in the left and right panels of Figure A. Either one component with a tilted linear background, left panel, or two components with the second one representing the electron background were used. The parameters for the SS fit for each are given in the graphs and are the same. This twofold fitting procedure was applied every time when the electron background was not constant.

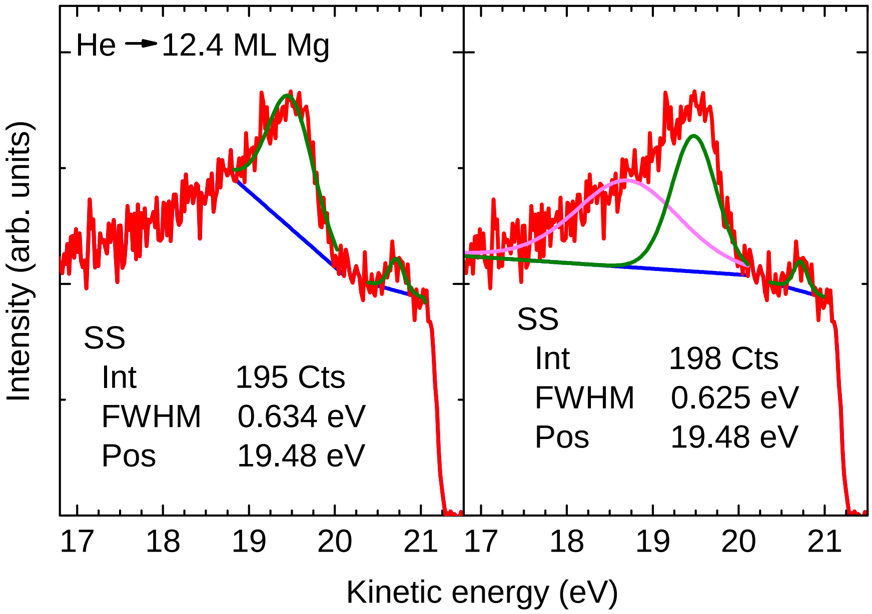

Figure A.2.: Result of fitting the He data from Figure A.1. The red line is the background corrected data. Green lines represent the fits to the QWS and SS applying a Gaussian Lorentzian sum function. The linear background is colored blue. Often the electron background rises towards the surface state like in this case. Then the SS is fitted in two ways: One with a tilted linear background to just use one component to fit the data and a 2 component fit, where the second represents the electron background increase. Both type of fits yield the same result.

The background correction presented in this chapter is used to determine the position, intensity and width of the surface and quantum well state signals in the scans using Helium gas both for the He and the H_2 signal in these scans. The correction can not be applied as easily to the Ne and Ar scans as here the surface state - for Ar- and the oxygen signal - for Ne - overlap with the hydrogen signal. Ar, Ne and H_2 in the plasma source were only used on a few samples. Most of the data originates from He scans.

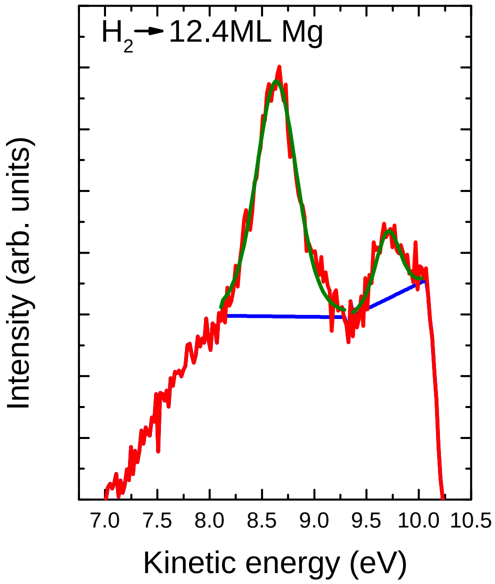

Figure A.3.: Result of fitting the Hα data from Figure A.1. The red line is the background corrected data. Green lines represent the fits to the QWS and SS applying a Gaussian Lorentzian sum function. The linear background is colored blue.

B. SEM images of Ag films on Si

The following Figures show SEM images of different Ag films, between 15 nm and 65 nm, of the kind prepared and used for the experiments described in chapter 7. The size and height/depth of the islands and trenches is apparently very similar for all thickness.
In Figure B.4 the Ag layer is etched of in steps with a focused ion beam, revealing similar width and height values as the AFM measurements shown above in chapter 7.1.

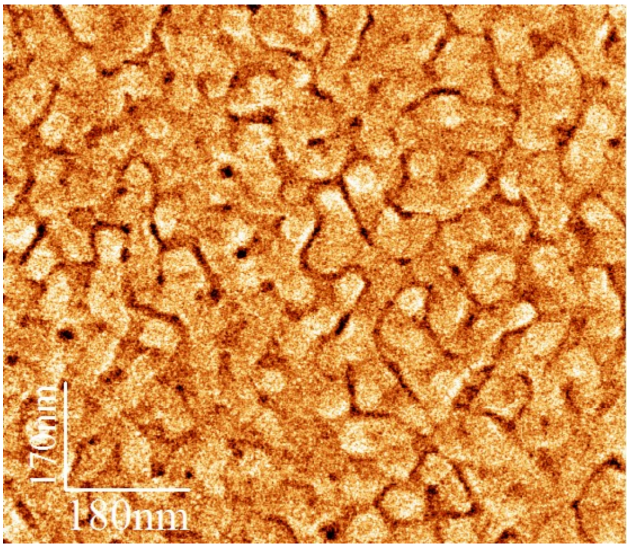

Figure B.1.: SEM image of a 25nm Ag film on Si(111).

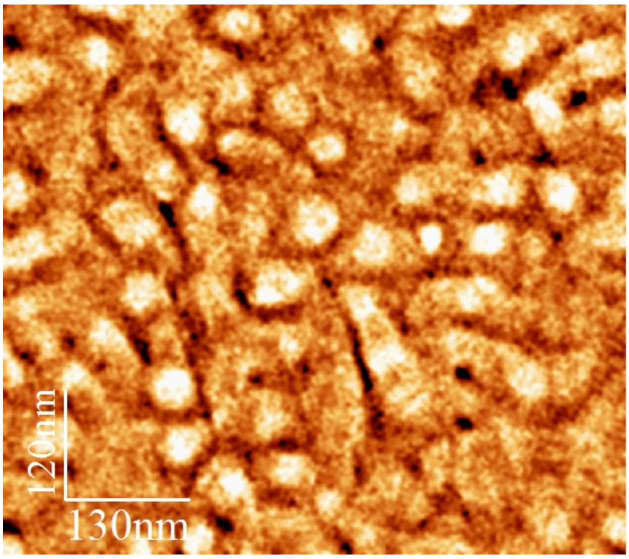

Figure B.2.: SEM image of a 47 nm Ag film on Si(111).

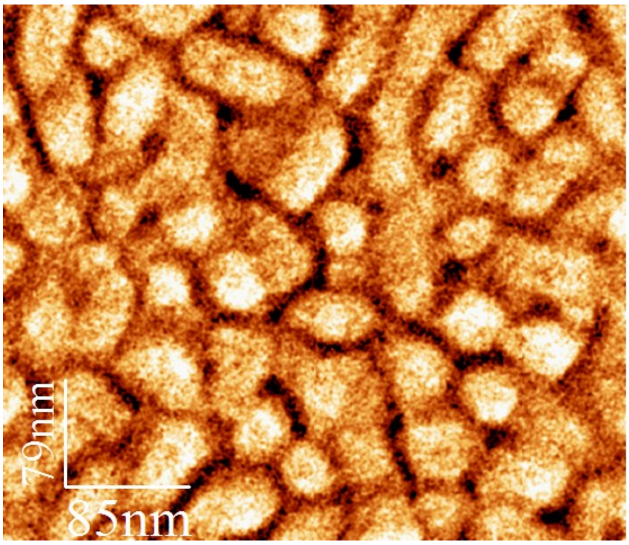

Figure B.3.: SEM image of a 65nm Ag film on Si(111).

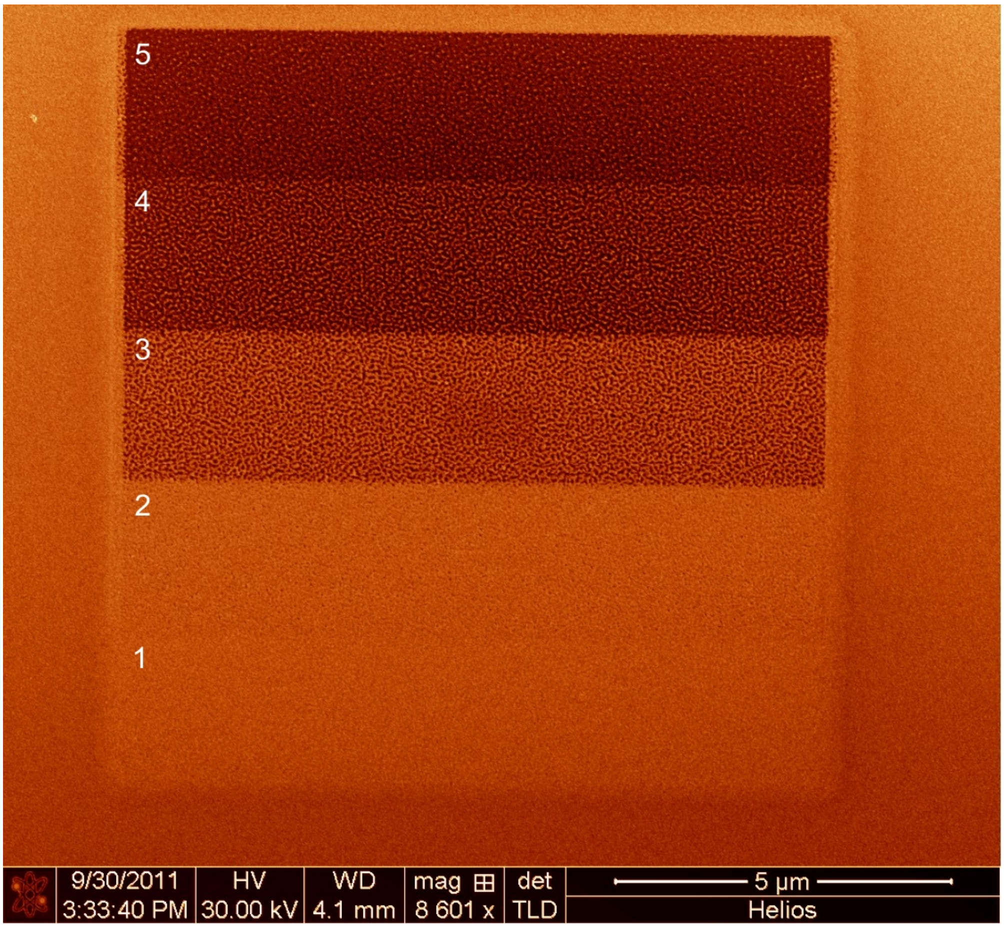

Figure B.4.: Large area scan of a 15 nm Ag layer on Si. From bottom to top the silver is etched off using a focused ion beam. The structure of the Ag islands becomes clearly visible.

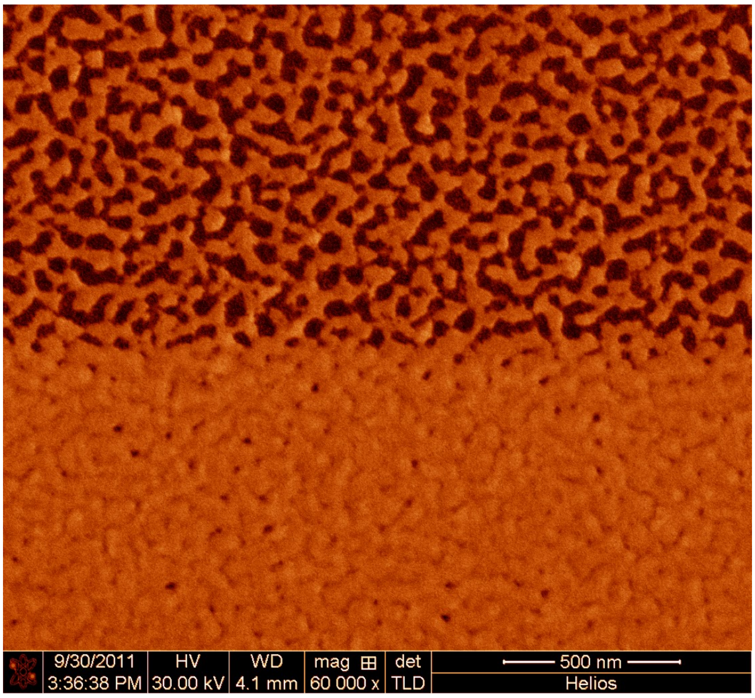

Figure B.5.: SEM image of the step between areas two and three in figure B.4.

C. Backsidedoping Profiles

Profiles of the backside-doping of the Si wafers used in this work.

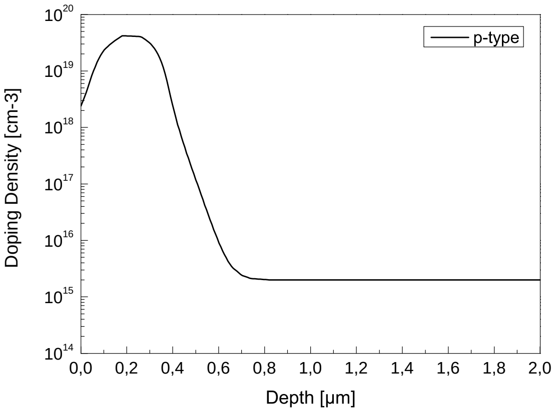

Figure C.1.: Backsidedoping Profile for p-doped Si samples used in this work.

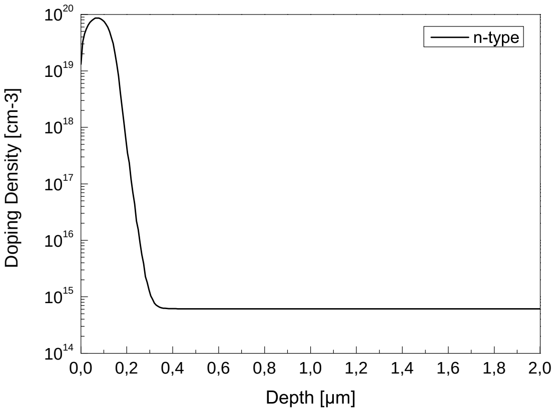

Figure C.2.: Backsidedoping Profile for n-doped Si samples used in this work.

Bibliography

[ABL$^+$04] L. Aballe, A. Barinov, A. Locatelli, S. Heun, and M. Kiskinova, *Tuning Surface Reactivity via Electron Quantum Confinement*, Phys. Rev. Lett. **93** (2004), 196103, DOI 10.1103/PhysRevLett.93.196103.

[ABS$^+$10] L. Aballe, A. Barinov, N. Stojic, N. Binggeli, T.O. Mentes, A. Locatelli, and M. Kiskinova, *The electron density decay length effect on surface reactivity*, Journal of Physics: Condensed Matter **22** (2010), 015001, DOI 10.1088/0953-8984/22/1/015001.

[AG09] Kadir Aslan and Chris D. Geddes, *Metal-enhanced chemiluminescence: advanced chemiluminescence concepts for the 21st century*, Chemical Society Reviews **38** (2009), 2556–2564, DOI 10.1039/B807498B.

[AKW85] D. Andersson, B. Kasemo, and L. Wallden, *Surface chemiluminescence in the Ksolid + Cl2gas reaction*, Surface Science **152-153, Part 1** (1985), 576 – 586, DOI 10.1016/0039-6028(85)90190-6.

[Anp96] M. Anpo (ed.), *Surface photochemistry*, Wiley, Chichester, 1996.

[ARH02a] L. Aballe, C. Rogero, and K. Horn, *Quantum size effects in ultrathin epitaxial Mg films on Si(111)*, Phys. Rev. B **65** (2002), 125319, DOI 10.1103/PhysRevB.65.125319.

[ARH02b] L. Aballe, C. Rogero, and K. Horn, *Quantum-size effects in ultrathin Mg films: electronic structure and collective excitations*, Surface Science **518** (2002), 141–154, DOI 10.1016/S0039-6028(02)02119-2.

[Avr39] Melvin Avrami, *Kinetics of Phase Change. I General Theory*, The Journal of Chemical Physics **7** (1939), 1103–1112, DOI 10.1063/1.1750380.

[Avr40] Melvin Avrami, *Kinetics of Phase Change. II Transformation Time Relations for Random Distribution of Nuclei*, The Journal of Chemical Physics **8** (1940), 212–224, DOI 10.1063/1.1750631.

[Avr41] Melvin Avrami, *Granulation, Phase Change, and Microstructure Kinetics of Phase Change. III*, The Journal of Chemical Physics **9** (1941), 177–184, DOI 10.1063/1.1750872.

[AY74] Tetsuji Aiyama and Keiji Yada, *Plasmon Damping in Be, Mg, Al, Si, Ge and Sn*, Journal of the Physical Society of Japan **36** (1974), 1554–1562, DOI 10.1143/JPSJ.36.1554.

[BA06] N. Binggeli and M. Altarelli, *Surface Reactivity and Quantum-Size Effects on the Electronic Density Decay Length of Ultrathin Metal Films*, Phys. Rev. Lett. **96** (2006), 036805, DOI 10.1103/PhysRevLett.96.036805.

[BA08] N. Binggeli and M. Altarelli, *Quantum-size effects in ultrathin Mg films*, Phys. Rev. B **78** (2008), 035438, DOI 10.1103/PhysRevB.78.035438.

[Bar98] W.L. Barnes, *Fluorescence near interfaces: The role of photonic mode density*, Journal of Modern Optics **45** (1998), 661–699, DOI 10.1080/09500349808230614.

[BBH04] S.R. Barman, C. Biswas, and K. Horn, *Electronic excitations on silver surfaces*, Phys. Rev. B **69** (2004), 045413, DOI 10.1103/PhysRevB.69.045413.

[Bec11] Felix Becker, *Energietransfer bei der Reaktion von Halogenen mit Alkalimetalloberflächen*, Master's thesis, Universität Duisburg-Essen, Dezember 2011.

[Bee52] August Beer, *Bestimmung der Absorption des rothen Lichts in farbigen Flüssigkeiten*, Annalen der Physik **162** (1852), 78 – 88, DOI 10.1002/andp.18521620505.

[Bel03] A.T. Bell, *The impact of nanoscience on heterogeneous catalysis*, Science **299** (2003), 1688 – 1691, DOI 10.1126/science.1083671.

[Ber12] Alexander Bernhart, *Mikroskopie mit ballistischen Elektronen und Löchern*, Ph.D. thesis, University of Duisburg-Essen, 2012.

[BGGP86] R.A. Bartynski, R.H. Gaylord, T. Gustafsson, and E.W. Plummer, *Angle-resolved photoemission study of the surface and bulk electronic structure of Mg(0001) and Mg(11¯0)*, Phys. Rev. B **33** (1986), 3644–3656, DOI 10.1103/PhysRevB.33.3644.

[BH99] S.R. Barman and K. Horn, *Photoemission study of electronic excitations at clean metal surfaces and thin metal films*, Applied Physics A **69** (1999), 519 – 527 (English), DOI 10.1007/s003390051458.

[BHH$^+$98] S.R. Barman, K. Horn, P. Häberle, H. Ishida, and A. Liebsch, *Photoinduced plasmon excitations in alkali-metal overlayers*, Phys. Rev. B **57** (1998), 6662–6665, DOI 10.1103/PhysRevB.57.6662.

[BKHN13] Felix Becker, David Krix, Ulrich Hagemann, and Hermann Nienhaus, *Internal detection of surface plasmon coupled chemiluminescence during chlorination of potassium thin films*, The Journal of Chemical Physics **138** (2013), 034710, DOI 10.1063/1.4776156.

[BKS02] Kurt H. Becker, Peter F. Kurunczi, and Karl H. Schoenbach, *Collisional and radiative processes in high-pressure discharge plasmas*, Physics of Plasmas **9** (2002), 2399–2404, DOI 10.1063/1.1449464.

[Bra75] Ferdinand Braun, *Ueber die Stromleitung durch Schwefelmetalle*, Annalen der Physik **229** (1875), 556–563, DOI 10.1002/andp.18752291207.

[BSH$^+$01] S.R. Barman, C. Stampfl, P. Häberle, W. Iba nez, Y.Q. Cai, and K. Horn, *Collective excitations in alkali metals on Al(111)*, Phys. Rev. B **64** (2001), 195410, DOI 10.1103/PhysRevB.64.195410.

[CFS$^+$00] Gennaro Chiarello, Vincenzo Formoso, Anna Santaniello, Elio Colavita, and Luigi Papagno, *Surface-plasmon dispersion and multipole surface plasmons in Al(111)*, Phys. Rev. B **62** (2000), 12676–12679, DOI 10.1103/PhysRevB.62.12676.

[Che76] C.H. Chen, *Plasmon dispersion in single-crystal magnesium*, Journal of Physics C: Solid State Physics **9** (1976), L321, DOI 10.1088/0022-3719/9/12/005.

[Chi00] T.-C Chiang, *Photoemission studies of quantum well states in thin films*, Surface Science Reports **39** (2000), 181–235, DOI 10.1016/S0167-5729(00)00006-6.

[CL78] M. Cardona and L. Ley, *Photoemission in Solids*, Topics in Applied Physics, vol. 26, Springer, Berlin, Heidelberg, Germany, 1978.

[CMA$^+$07] Mustafa H. Chowdhury, Stuart N. Malyn, Kadir Aslan, Joseph R. Lakowicz, and Chris D. Geddes, *First observation of surface plasmon-coupled chemiluminescence (SPCC)*, Chemical Physics Letters **435** (2007), 114–118, DOI 10.1016/j.cplett.2006.12.063.

[CSFK99] S.A. Canney, V.A. Sashin, M.J. Ford, and A.S. Kheifets, *Electronic band structure of magnesium and magnesium oxide: experiment and theory*, Journal of Physics: Condensed Matter **11** (1999), 7507, DOI 10.1088/0953-8984/11/39/308.

[DCB04] A. G. Danese, F. G. Curti, and R. A. Bartynski, *Quantum size effect induced modification of the chemisorption properties of thin metal films*, Phys. Rev. B **70** (2004), 165420, DOI 10.1103/PhysRevB.70.165420.

[DTM$^+$09] Marie D'angelo, Keiko Takase, Nobuhiro Miyata, Toru Hirahara, Shuji Hasegawa, Akinori Nishide, Manami Ogawa, and Iwao Matsuda, *Conductivity of the Si(111) 7x7 dangling-bond state*, Phys. Rev. B **79** (2009), 035318, DOI 10.1103/PhysRevB.79.035318.

[Ein05] Albert Einstein, *Über einen die Erzeugung und Verwandlung des Lichtes betreffenden heuristischen Gesichtspunkt*, Annalen der Physik **322** (1905), 132–148, DOI 10.1002/andp.19053220607.

[Fei82] Peter J. Feibelman, *Surface electromagnetic fields*, Progress in Surface Science **12** (1982), 287–407, DOI 10.1016/0079-6816(82)90001-6.

[GA72] T.F. Gesell and E.T. Arakawa, *Work function changes during oxygen chemisorption on fresh magnesium surfaces*, Surface Science **33** (1972), 419–421, DOI 10.1016/0039-6028(72)90219-1.

[Gad70] J.W. Gadzuk, *Resonance-Tunneling Spectroscopy of Atoms Adsorbed on Metal Surfaces: Theory*, Phys. Rev. B **1** (1970), 2110–2129, DOI 10.1103/PhysRevB.1.2110.

[Ger14] Achim Gerstenberg, *Oxidation von Aluminium Schichten*, Master's thesis, Universität Duisburg-Essen, 2014.

[GFG$^+$94] T. Greber, K. Freihube, R. Grobecker, A. Böttcher, K. Hermann, G. Ertl, and D. Fick, *Nonadiabatic processes during the oxidation of Li layers*, Phys. Rev. B **50** (1994), 8755–8762, DOI 10.1103/PhysRevB.50.8755.

[GGM$^+$93] T. Greber, R. Grobecker, A. Morgante, A. Böttcher, and G. Ertl, *O- escape during the oxidation of cesium*, Phys. Rev. Lett. **70** (1993), 1331 – 1334, DOI 10.1103/PhysRevLett.70.1331.

[GKG$^+$07] K.N. Galkin, Mahesh Kumar, Govind, S.M. Shivaprasad, V.V. Korobtsov, and N.G. Galkin, *A study of the temperature dependence of adsorption and silicidation kinetics at the Mg/Si(111) interface*, Thin Solid Films **515** (2007), 8192–8196, DOI 10.1016/j.tsf.2007.02.041.

[Gla05] Stefan Glass, *Detektion von elektronischen Anregungen bei chemischen Reaktionen an Metalloberflächen*, Ph.D. thesis, University of Duisburg-Essen, 2005.

[GMCG89] P. Gupta, C. H. Mak, P. A. Coon, and S. M. George, *Oxidation kinetics of Si(111) 7x7 in the submonolayer regime*, Phys. Rev. B **40** (1989), 7739 – 7749, DOI 10.1103/PhysRevB.40.7739.

[GN04] S. Glass and H. Nienhaus, *Continuous Monitoring of Mg Oxidation by Internal Exoemission*, Phys. Rev. Lett. **93** (2004), 168302, DOI 10.1103/PhysRevLett.93.168302.

[GNWM01] Brian Gergen, Hermann Nienhaus, Henry W. Weinberg, and Eric W. McFarland, *Chemically Induced Electronic Excitations at Metal Surfaces*, Science **294** (2001), 2521–2523, DOI 10.1126/science.1066134.

[Gre94] T. Greber, *Chemical hole diving*, Chemical Physics Letters **222** (1994), 292–296, DOI 10.1016/0009-2614(94)00344-0.

[Gre97] T. Greber, *Charge-transfer induced particle emission in gas surface reactions*, Surface Science Reports **28** (1997), 1–64, DOI 10.1016/S0167-5729(97)00005-8.

[Hag09] Ulrich Hagemann, *Chemostrom-Messungen an Mg/ p -Si(001) Schottky-Dioden bei Mg-Deposition und Oxidation und Charakterisierung epitaktischer Oxid-Schichten auf Si*, Master's thesis, University of Duisburg-Essen, 2009.

[Hen96] M. Henzler, *Growth of epitaxial monolayers*, Surface Science **357 - 358** (1996), 809–819, DOI 10.1016/0039-6028(96)00270-1.

[Her87] H. Hertz, *Ueber einen Einfluss des ultravioletten Lichtes auf die electrische Entladung*, Annalen der Physik **267** (1887), 983–1000, DOI 10.1002/andp.18872670827.

[Her70] G. Herzberg, *The dissociation energy of the hydrogen molecule*, Journal of Molecular Spectroscopy **33** (1970), 147–168, DOI 10.1016/0022-2852(70)90060-3.

[HG94] Martin Henzler and Wolfgang Göpel, *Oberflächenphysik des Festkörpers*, vol. 1, Teubner, Stuttgart, Germany, 1994.

[HH74] P.H. Holloway and J.B. Hudson, *Kinetics of the reaction of oxygen with clean nickel single crystal surfaces: I. Ni(100) surface*, Surface Science **43** (1974), 123–140, DOI 10.1016/0039-6028(74)90223-4.

[HH83] G. Hollinger and F.J. Himpsel, *Multiple-bonding configurations for oxygen on silicon surfaces*, Phys. Rev. B **28** (1983), 3651 – 3653, DOI 10.1103/PhysRevB.28.3651.

[HHV07] Carl H. Hamann, Andrew Hamnett, and W. Vielstich, *Electrochemistry*, 2nd ed., Wiley, Weinheim, 2007.

[HKN10] Ulrich Hagemann, David Krix, and Hermann Nienhaus, *Electronic Excitations Generated by the Deposition of Mg on Mg Films*, Phys. Rev. Lett. **104** (2010), 028301, DOI 10.1103/PhysRevLett.104.028301.

[HL08] E. Hasselbrink and B.I. Lundqvist (eds.), *Handbook of Surface Science: Dynamics*, Handbook of Surface Science, vol. 3, Elsevier Science, Amsterdam, Netherlands, 2008.

[HLA96] Yukio Hasegawa, In-Whan Lyo, and Phaedon Avouris, *Measurement of surface state conductance using STM point contacts*, Surface Science **357 - 358** (1996), 32 – 37, DOI 10.1016/0039-6028(96)00052-0.

[HST$^+$03] S. Hasegawa, I. Shirak, F. Tanabe, R. Hobara, T. Kanagawa, T. Tanikawa, I. Matsuda, C.L. Petersen, T.M. Hansen, P. Boggild, and F. Grey, *Electrical Conduction Through Surface Superstructures Measured by Microscopic Four-Point Probes*, Surface Review and Letters **10** (2003), 963–980, DOI 10.1142/S0218625X03005736.

[HTD87] R.J. Hamers, R.M. Tromp, and J.E. Demuth, *Electronic and geometric structure of Si(111)-(7 x 7) and Si(001) surfaces*, Surface Science **181** (1987), 346 – 355, DOI 10.1016/0039-6028(87)90176-2.

[Hüf03] Stephan Hüfner, *Photoelectron spectroscopy: principles and applications*, Advanced Texts in Physics, Springer, Berlin, Heidelberg, Germany, 2003.

[HWC$^+$03] H. Hong, C.M. Wei, M.Y. Chou, Z. Wu, L. Basile, H. Chen, M. Holt, and T.-C. Chiang, *Alternating Layer and Island Growth of Pb on Si by Spontaneous Quantum Phase Separation*, Phys. Rev. Lett. **90** (2003), 076104, DOI 10.1103/PhysRevLett.90.076104.

[HWWH98] S. Heike, S. Watanabe, Y. Wada, and T. Hashizume, *Electron Conduction through Surface States of the Si(111)-(7x7) Surface*, Phys. Rev. Lett. **81** (1998), 890 – 893, DOI 10.1103/PhysRevLett.81.890.

[IL90] H. Ishida and A. Liebsch, *Linear and nonlinear response of alkali-metal adlayers on metal surfaces to a static electric field*, Phys. Rev. B **42** (1990), 5505 – 5515, DOI 10.1103/PhysRevB.42.5505.

[IM82] H. Ibach and D.L. Mills, *Electron energy loss spectroscopy and surface vibrations*, vol. 1, Academic press, New York, 1982.

[JBG89] M. Jestl, W. Beinstingl, and E. Gornik, *Leaky modes in metal semiconductor junctions*, Journal of Applied Physics **65** (1989), 1805–1808, DOI 10.1063/1.342912.

[JL75] R.C. Jaklevic and J. Lambe, *Experimental study of quantum size effects in thin metal films by electron tunneling*, Phys. Rev. B **12** (1975), 4146–4160, DOI 10.1103/PhysRevB.12.4146.

[JM39] W.A. Johnson and R.F. Mehl, *Reaction kinetics in processes of nucleation and growth*, Transactions of the american instituteof mining and metallurgical engineers **135** (1939), 416–442, DOI 10.1007/s11663-010-9421-1.

[Jou12] Karl Jousten (ed.), *Handbuch Vakuumtechnik*, Springer, Vieweg, Braunschweig, Wiesbaden, 2012.

[Kas74] Bengt Kasemo, *Photon Emission during Chemisorption of Oxygen on Al and Mg Surfaces*, Phys. Rev. Lett. **32** (1974), 1114–1117, DOI 10.1103/PhysRevLett.32.1114.

[KB88] W.J. Kaiser and L.D. Bell, *Direct investigation of subsurface interface electronic structure by ballistic-electron-emission microscopy*, Phys. Rev. Lett. **60** (1988), 1406–1409, DOI 10.1103/PhysRevLett.60.1406.

[KBO85] Jules Z. Klose, John M. Bridges, and William R. Ott, *Monochromatic source of Lyman-alpha radiation*, Appl. Opt. **24** (1985), 2263–2266, DOI 10.1364/AO.24.002263.

[KGK$^+$10] Domocos Kovacs, Artur Golczewski, Gregor Kowarik, Friedrich Aumayr, and Detlef Diesing, *Low-energy ion-induced electron emission in metal-insulator-metal sandwich structures*, Phys. Rev. B **81** (2010), 075411, DOI 10.1103/PhysRevB.81.075411.

[KGM03] M. Kurth, P.C.J. Graat, and E.J. Mittemeijer, *Determination of the intrinsic bulk and surface plasmon intensity of XPS spectra of magnesium*, Applied Surface Science **220** (2003), 60–78, DOI 10.1016/S0169-4332(03)00804-3.

[KHPF82] U.O. Karlsson, G.V. Hansson, P.E.S. Persson, and S.A. Flodström, *Surface electronic structure of Mg(0001)*, Phys. Rev. B **26** (1982), 1852–1858, DOI 10.1103/PhysRevB.26.1852.

[Kit66] Charles Kittel, *Einführung in die Festkörperphysik*, 3rd ed., Oldenbourg Verlag, München, Wien, Germany/Austria, `http://www.degruyter.com/view/product/231310?rskey=xMerGI&result=1`, 1966.

[KMT96] T. Komeda, Y. Morita, and H. Tokumoto, *Surface roughening and metastable superstructures on wet-processed Si(111) surface induced by hydrogen desorption*, Surface Science **348** (1996), 153–160, DOI 10.1016/0039-6028(95)00992-2.

[KNN07] D. Krix, R. Nünthel, and H. Nienhaus, *Generation of hot charge carriers by adsorption of hydrogen and deuterium atoms on a silver surface*, Phys. Rev. B **75** (2007), 073410, DOI 10.1103/PhysRevB.75.073410.

[Kri11] David Krix, *Non-adiabatic Effects in the Oxidation of Alkali Metal Surfaces*, Ph.D. thesis, University of Duisburg-Essen, 2011.

[KSB99] P. Kurunczi, H. Shah, and K. Becker, *Hydrogen Lyman- alpha and beta emissions from high-pressure microhollow cathode discharges in Ne-H 2 mixtures*, Journal of Physics B: Atomic, Molecular and Optical Physics **32** (1999), L651, DOI 10.1088/0953-4075/32/22/103.

[KSNH11] Mark W. Knight, Heidar Sobhani, Peter Nordlander, and Naomi J. Halas, *Photodetection with Active Optical Antennas*, Science **332** (2011), 702–704, DOI 10.1126/science.1203056.

[Lak07] Joseph R. Lakowicz, *Principles of fluorescence spectroscopy*, Springer, New York, USA, 2007.

[Len00] P. Lenard, *Erzeugung von Kathodenstrahlen durch ultraviolettes Licht*, Annalen der Physik **307** (1900), 359–375, DOI 10.1002/andp.19003070611.

[Len02] P. Lenard, *Ueber die lichtelektrische Wirkung*, Annalen der Physik **313** (1902), 149–198, DOI 10.1002/andp.19023130510.

[Lid02] David R. Lide, *CRC Handbook of Chemistry and Physics*, 83 ed., CRC press, Baton Rouge, USA, 2002.

[Lie97] Ansgar Liebsch, *Electronic excitations at metal surfaces*, Physics of Solids and Liquids, Springer, Berlin, Heidelberg, Germany, 1997.

[LKP01] A. Liebsch, Bong-Ok Kim, and E. W. Plummer, *Collective excitations in adsorbed alkali-metal films: Critical analysis of photoyield and electron-energy-loss spectra for K on Al(111)*, Phys. Rev. B **63** (2001), 125416, DOI 10.1103/PhysRevB.63.125416.

[LM] P.J. Linstrom and W.G. Mallards (eds.), *NIST Chemistry Webbook, NIST Standard Reference Database Number 69*, National Institute of Standards and Technology, Gaithersburg MD, 20899, `http://webbook.nist.gov`, (retrieved November 8, 2009).

[LP06] M. Lindenblatt and E. Pehlke, *Ab Initio Simulation of the Spin Transition during Chemisorption:* H/Al(111), Phys. Rev. Lett. **97** (2006), 216101, DOI 10.1103/PhysRevLett.97.216101.

[LPF79] Harry J. Levinson, E. W. Plummer, and Peter J. Feibelman, *Effects on Photoemission of the Spatially Varying Photon Field at a Metal Surface*, Phys. Rev. Lett. **43** (1979), 952–955, DOI 10.1103/PhysRevLett.43.952.

[LSS$^+$95] P. Lahnor, K. Seiter, M. Schulz, W. Dorsch, and R. Scholz, *Barrier-height nonuniformities of PtSi/Si(111) Schottky diodes*, Applied Physics A **61** (1995), 369–375 (English), DOI 10.1007/BF01540110.

[Lüt10] Hans Lüth, *Solid surfaces, interfaces and thin films*, Graduate Texts in Physics, vol. 8431, Springer, Berlin, Heidelberg, Germany, 2010.

[LZC07] Xiang-Gui Li, Ping Zhang, and C.K. Chan, *First-principles calculation of Mg(0001) thin films: Quantum size effect and adsorption of atomic hydrogen*, Physica B: Condensed Matter **390** (2007), 225–230, DOI 10.1016/j.physb.2006.08.019.

[LZH93] Xiaomei Li, Zhaoming Zhang, and Victor E. Henrich, *Inelastic electron background function for ultraviolet photoelectron spectra*, Journal of Electron Spectroscopy and Related Phenomena **63** (1993), 253–265, DOI 10.1016/0368-2048(93)87007-M.

[MA05] Stefan A. Maier and Harry A. Atwater, *Plasmonics: Localization and guiding of electromagnetic energy in metal/dielectric structures*, Journal of Applied Physics **98** (2005), DOI 10.1063/1.1951057.

[Mai07] Stefan Alexander Maier, *Plasmonics: Fundamentals and Applications*, Springer, New York, USA, 2007.

[Mas96] Richard I. Masel, *Principles of adsorption and reaction on solid surfaces*, vol. 3, John Wiley & Sons, 1996.

[MBPH08] M.S. Mizielinski, D.M. Bird, M. Persson, and S. Holloway, *Newns-Anderson model of chemicurrents in H/Cu and H/Ag*, Surface Science **602** (2008), 2617–2622, DOI 10.1016/j.susc.2008.06.015.

[McC01] Elaine M. McCash, *Surface chemistry*, vol. 1, Oxford University Press, Oxford, United Kingdom, 2001.

[MH70] Andrew R. Melnyk and Michael J. Harrison, *Theory of Optical Excitation of Plasmons in Metals*, Phys. Rev. B **2** (1970), 835–850, DOI 10.1103/PhysRevB.2.835.

[MHDW11] Mario Marpe, Christian Heuser, Detlef Diesing, and Andreas Wucher, *Internal electron emission in metal-insulator-metal thin film tunnel devices bombarded with keV argon and gold-cluster projectiles*, Nuclear Instruments and Methods in Physics Research Section B: Beam Interactions with Materials and Atoms **269** (2011), 972–976, DOI 10.1016/j.nimb.2010.12.045.

[MMB05] N. Masoud, K. Martus, and K. Becker, *VUV emission from a cylindrical dielectric barrier discharge in Ar and in Ar/N 2 and Ar/air mixtures*, Journal of Physics D: Applied Physics **38** (2005), 1674, DOI 10.1088/0022-3727/38/11/006.

[Mön95] W. Mönch, *Semiconductor Surfaces and Interfaces*, Springer Series in Surface Science, vol. 26, Springer, Berlin, Heidelberg, Germany, 1995.

[MN03] T. Müller and H. Nienhaus, *Ultrathin Ag films on H:Si(111)-1x1 surfaces deposited at low temperatures*, Journal of Applied Physics **93** (2003), 924–929, DOI 10.1063/1.1530714.

[Mön04] Winfried Mönch, *Electronic properties of semiconductor interfaces*, Springer Series in Surface Science, vol. 43, Springer, Berlin, Heidelberg, Germany, 2004.

[Mor01] Philip Moriarty, *Nanostructured materials*, Reports on Progress in Physics **64** (2001), 297, DOI 10.1088/0034-4885/64/3/201.

[MRB$^+$14] Vivian Merk, Christoph Rehbock, Felix Becker, Ulrich Hagemann, Hermann Nienhaus, and Stephan Barcikowski, *In Situ Non-DLVO Stabilization of Surfactant-Free, Plasmonic Gold Nanoparticles: Effect of Hofmeisters Anions*, Langmuir **30** (2014), 4213–4222, DOI 10.1021/la404556a.

[MSSB95] John F. Moulder, William F. Stickle, Peter E. Sobol, and Kenneth D. Bomben, *Handbook of X-ray Photoelectron Spectroscopy*, Physical Electronics, Inc., 6509 Flying Cloud Drive, Eden Prairie, MN 55344, USA, 1995.

[NBG$^+$99] H. Nienhaus, H.S. Bergh, B. Gergen, A. Majumdar, W.H. Weinberg, and E.W. McFarland, *Electron-Hole Pair Creation at Ag and Cu Surfaces by Adsorption of Atomic Hydrogen and Deuterium*, Phys. Rev. Lett. **82** (1999), 446–449, DOI 10.1103/PhysRevLett.82.446.

[NBG$^+$00] H. Nienhaus, H.S. Bergh, B. Gergen, A. Majumdar, W.H. Weinberg, and E.W. McFarland, *Direct detection of electron-hole pairs generated by chemical reactions on metal surfaces*, Surface Science **445** (2000), 335–342, DOI 10.1016/S0039-6028(99)01078-X.

[Ned93] H. Neddermeyer, *Scanning Tunneling Microscopy*, Perspectives in Condensed Matter Physics, vol. 6, Dordrecht, Netherlands, 1993.

[NG06] H. Nienhaus and S. Glass, *Probing the distribution of hot charge carriers generated in Mg surfaces by oxidation*, Surface science **600** (2006), 4285–4289, DOI 10.1016/j.susc.2006.01.155.

[Nie02] Hermann Nienhaus, *Electronic excitations by chemical reactions on metal surfaces*, Surface Science Reports **45** (2002), 1–78, DOI 10.1016/S0167-5729(01)00019-X.

[NKG07] H. Nienhaus, D. Krix, and S. Glass, *Varying the Schottky barrier of thin film Mg/H:p-Si(111) contacts: Properties and applications*, Journal of Vacuum Science & Technology A **25** (2007), 950–954, DOI 10.1116/1.2484574.

[NSS57] Carl Nordling, Evelyn Sokolowski, and Kai Siegbahn, *Precision Method for Obtaining Absolute Values of Atomic Binding Energies*, Phys. Rev. **105** (1957), 1676–1677, DOI 10.1103/PhysRev.105.1676.

[Pal98] Edward D. Palik, *Handbook of optical constants of solids*, vol. 3, Academic press, San Diego, USA, 1998.

[Pol] M.N. Polyanskiy, *Refractive index database*, http://refractiveindex.info/.

[PSCE07] J.M. Pitarke, V.M. Silkin, E.V. Chulkov, and P.M. Echenique, *Theory of surface plasmons and surface-plasmon polaritons*, Reports on Progress in Physics **70** (2007), 1, DOI 10.1088/0034-4885/70/1/R01.

[PWC$^+$02] J.J. Paggel, C.M. Wei, M.Y. Chou, D.-A. Luh, T. Miller, and T.-C. Chiang, *Atomic-layer-resolved quantum oscillations in the work function: Theory and experiment for Ag/Fe(100)*, Phys. Rev. B **66** (2002), 233403, DOI 10.1103/PhysRevB.66.233403.

[Rae80] Heinz Raether, *Excitation of plasmons and interband transitions by electrons*, Springer Tracts in Modern Physics, vol. 88, Springer, Berlin, Heidelberg, Germany, 1980.

[Rae88] Heinz Raether, *Surface plasmons on smooth surfaces*, Springer Tracts in Modern Physics, vol. 111, Springer, Berlin, Heidelberg, Germany, 1988.

[Ros04] Federico Rosei, *Nanostructured surfaces: challenges and frontiers in nanotechnology*, Journal of Physics: Condensed Matter **16** (2004), S1373, DOI 10.1088/0953-8984/16/17/001.

[RT90] D Roy and D Tremblay, *Design of electron spectrometers*, Reports on Progress in Physics **53** (1990), 1621, DOI 10.1088/0034-4885/53/12/003.

[SB10] C. Scales and P. Berini, *Thin-Film Schottky Barrier Photodetector Models*, Quantum Electronics, IEEE Journal of **46** (2010), 633–643, DOI 10.1109/JQE.2010.2046720.

[Sch39] Walter Schottky, *Zur Halbleitertheorie der Sperrschicht- und Spitzengleichrichter*, Zeitschrift für Physik **113** (1939), 367–414 (German), DOI 10.1007/BF01340116.

[Sch42] Walter Schottky, *Vereinfachte und erweiterte Theorie der Randschicht-Gleichrichter*, Zeitschrift für Physik **118** (1942), 539–592 (German), DOI 10.1007/BF01329843.

[SDH11] Beate Schindler, Detlef Diesing, and Eckart Hasselbrink, *Electronic excitations induced by hydrogen surface chemical reactions on gold*, The Journal of Chemical Physics **134** (2011), DOI 10.1063/1.3523647.

[SDH13] Beate Schindler, Detlef Diesing, and Eckart Hasselbrink, *Electronic Excitations in the Course of the Reaction of H with Coinage and Noble Metal Surfaces: A Comparison*, Zeitschrift für Physikalische Chemie **227** (2013), DOI 10.1524/zpch.2013.0408.

[SG64] Abraham. Savitzky and M.J.E. Golay, *Smoothing and Differentiation of Data by Simplified Least Squares Procedures.*, Analytical Chemistry **36** (1964), 1627–1639, DOI 10.1021/ac60214a047.

[Sie81] Kai Siegbahn, *Electron Spectroscopy for Atoms, Molecules and Condensed Matter*, Nobel Lecture (1981), DOI 10.1103/RevModPhys.54.709.

[SKM97] R.F. Schmitsdorf, T.U. Kampen, and W. Mönch, *Explanation of the linear correlation between barrier heights and ideality factors of real metal-semiconductor contacts by laterally nonuniform Schottky barriers*, Journal of Vacuum Science & Technology B: Microelectronics and Nanometer Structures **15** (1997), 1221–1226, DOI 10.1116/1.589442.

[SLG$^+$03] A. Schlapka, M. Lischka, A. Gross, U. Käsberger, and P. Jakob, *Surface Strain versus Substrate Interaction in Heteroepitaxial Metal Layers: Pt on Ru(0001)*, Phys. Rev. Lett. **91** (2003), 016101, DOI 10.1103/PhysRevLett.91.016101.

[SM99] R.F. Schmitsdorf and W. Mönch, *Influence of the interface structure on the barrier height of homogeneous Schottky contacts*, The European Physical Journal B-Condensed Matter and Complex Systems **7** (1999), 457–466, DOI 10.1007/s100510050634.

[SN06] Simon M. Sze and Kwok K. Ng, *Physics of semiconductor devices*, Wiley, Hoboken, New Jersey, USA, 2006.

[SNS58] Evelyn Sokolowski, Carl Nordling, and Kai Siegbahn, *Chemical Shift Effect in Inner Electronic Levels of Cu Due to Oxidation*, Phys. Rev. **110** (1958), 776–776, DOI 10.1103/PhysRev.110.776.

[Som94] G.A. Somorjai, *Introduction to Surface Chemistry and Catalysis*, A Wiley-Interscience publication, Wiley, 1994.

[SPEa] SPECS GmbH, 13355 Berlin, *Manuals: Phoibos Hemispherical Analyzer Series*.

[SPEb] SPECS GmbH, 13355 Berlin, *Manuals: UV-Source UVS 10/35 and X-Ray Source XR50*.

[Ste89] A. Sternberg, *Ultraviolet fluorescent molecular hydrogen emission*, apj **347** (1989), 863–874, DOI 10.1086/168177.

[Sue65] Osamu Sueoka, *Plasma Oscillation of Electrons in Be, Mg, Al, Si, Ge, Sn, Sb and Bi*, Journal of the Physical Society of Japan **20** (1965), 2203–2211, DOI 10.1143/JPSJ.20.2203.

[SWP92] P.T. Sprunger, G.M. Watson, and E.W. Plummer, *The normal modes at the surface of Li and Mg*, Surface Science **269-270** (1992), 551–555, DOI 10.1016/0039-6028(92)91307-W.

[SZ12] K.H. Schoenbach and WeiDong Zhu, *High-Pressure Microdischarges: Sources of Ultraviolet Radiation*, Quantum Electronics, IEEE Journal of **48** (2012), 768–782, DOI 10.1109/JQE.2012.2185686.

[TK10] Matthias Timmer and Peter Kratzer, *Theoretical investigation of the influence of isotope mass on chemicurrents during adsorption of H on K(110)*, Surface Science **604** (2010), 1452–1458, DOI 10.1016/j.susc.2010.05.008.

[Tun91] R.T. Tung, *Electron transport of inhomogeneous Schottky barriers*, Applied Physics Letters **58** (1991), 2821–2823, DOI 10.1063/1.104747.

[TYM$^+$03] T. Tanikawa, K. Yoo, I. Matsuda, S. Hasegawa, and Y. Hasegawa, *Nonmetallic transport property of the Si(111) 7x7 surface*, Phys. Rev. B **68** (2003), 113303, DOI 10.1103/PhysRevB.68.113303.

[Wal11] Dirk Wall, *High Temperature Structure Formation and Surface Diffusion of Silver on Silicon Surfaces*, Ph.D. thesis, University of Duisburg-Essen, 2011.

[WKHH06] J.W. Wells, J.F. Kallehauge, T.M. Hansen, and Ph. Hofmann, *Disentangling Surface, Bulk, and Space-Charge-Layer Conductivity in Si(111)-(7x7)*, Phys. Rev. Lett. **97** (2006), 206803, DOI 10.1103/PhysRevLett.97.206803.

[WSS$^+$98] J. Wieser, M. Salvermoser, L.H. Shaw, A. Ulrich, D.E. Murnick, and H. Dahi, *Lyman-alpha emission via resonant energy transfer*, Journal of Physics B: Atomic, Molecular and Optical Physics **31** (1998), 4589, DOI 10.1088/0953-4075/31/20/017.

[YL85] J.J. Yeh and I. Lindau, *Atomic subshell photoionization cross sections and asymmetry parameters: 1<= Z <= 103*, Atomic Data and Nuclear Data Tables **32** (1985), 1–155, DOI 10.1016/0092-640X(85)90016-6.

[YW02] K. Yoo and H.H. Weitering, *Electrical conductance of reconstructed silicon surfaces*, Phys. Rev. B **65** (2002), 115424, DOI 10.1103/PhysRevB.65.115424.

[ZZF$^+$08] Z. Zhang, Y. Zhang, Q. Fu, H. Zhang, Y. Yao, T. Ma, D. Tan, Q. Xue, and X. Bao, *Modulation of surface reactivity via electron confinement in metal quantum well films: O2 adsorption on Pb/Si(111)*, The Journal of Chemical Physics **129** (2008), DOI 10.1063/1.2919992.

[ZZKL11] Igor Zoric, Michael Zäch, Bengt Kasemo, and Christoph Langhammer, *Gold, Platinum, and Aluminum Nanodisk Plasmons: Material Independence, Subradiance, and Damping Mechanisms*, ACS Nano **5** (2011), 2535–2546, DOI 10.1021/nn102166t.

List of Figures

List of Tables

Der Lebenslauf ist in der Online-Version aus Gründen des Datenschutzes nicht enthalten

Veröffentlichungen

1. Electronic excitations in magnesium epitaxy: Experiment and theory, U. Hagemann, M. Timmer, D. Krix, P. Kratzer and Hermann Nienhaus, Phys. Rev. B **82**, 15 (2010) 155420.
2. Electronic excitations generated by the deposition of Mg on Mg films, U. Hagemann, D. Krix, and H. Nienhaus, Phys. Rev. Lett. **104** (2010) 028301.
3. Internal detection of surface plasmon coupled chemiluminescence during chlorination of potassium thin films
   F. Becker, D. Krix, U. Hagemann, H. Nienhaus, Journal of Chemical Physics **138**, 3 (2013) 034710.
4. Low temperature diffusion of Li atoms into Si nanoparticles and surfaces
   H. Nienhaus, H. Karacuban, D. Krix, F. Becker, U. Hagemann, D. Steeger, R. Bywalez, C. Schulz, H. Wiggers, Journal of Applied Physics **114** (2013) 034310.
5. In situ non-DLVO Stabilization of Surfactant-free, Plasmonic Gold Nanoparticles: The Effect of Hofmeister's Anions
   Vivian Marina Merk, Christoph Rehbock, Felix Becker, Ulrich Hagemann, Hermann Nienhaus, Stephan Barcikowski, Langmuir **30,** 15 (2014) 4213–4222
6. Quantum size effects in chemicurrent measurements during low-temperature oxidation of Mg(0001) epilayers
   U.Hagemann and H. Nienhaus, New Journal of Physics, **16** (2014) 113035

Danksagung

Mein besonderer Dank gilt Prof. Hermann Nienhaus. Er gab mir die Möglichkeit selbständig und eigenverantwortlich an hochinteressanten wissenschaftlichen Themen zu arbeiten. Jederzeit war er für Diskussionen, auch mal außerhalb des wissenschaftlichen Treibens, offen und unterstützte mich und meine Arbeit durchgängig. Vielen Dank für die sehr gute Zusammenarbeit in den vergangenen Jahren.

Über die Jahre haben mich viele tolle Kollegen begleitet. Hervorheben möchte ich hier vor allem David Krix, der mich die Geheimnisse des wissenschaftlichen Arbeitens gelehrt hat (ich habe ihm dafür ein paar Tricks beim Fußball beigebracht :)), und Kornelia Huba, mit der ich lange das Büro und das Labor geteilt und dabei viele schöne Lieder gesungen habe.

Auch allen anderen Mitarbeitern der Arbeitsgruppen Nienhaus und Möller danke ich für die jederzeit große Hilfsbereitschaft, die schönen Arbeitsgruppenausflüge, den Grillveranstaltungen auf dem Dach der Universität, und für die vielen schönen Abende bei diversen Mitarbeiterworkshops und Tagungen und den damit verbundenen Gesprächen und Diskussionen. Viele sind mir, über die Arbeit hinaus, zu guten Freunden geworden.

Weiterhin möchte ich mich bei allen Mitarbeitern, vor allem und zuerst bei Frau Maria Dunke, des Sonderforschungsbereich 616 bedanken. Die Möglichkeit zum Austausch über verschiedenste experimentelle und theoretische Methoden und die vielen tollen Abende bei den Mitarbeiterworkshops in Papenburg haben meine Zeit als Doktorand sehr bereichert.

Ich danke allen Personen, die diese Arbeit zur Korrektur gelesen haben.

Prof. Rolf Möller danke ich herzlich für die Bereitstellung der Räumlichkeiten.

Prof. Klaus Schierbaum danke ich für die Bereitschaft diese Arbeit als zweiter Gutachter zu bewerten.

Meinen Eltern danke ich ganz besonders für ihre wertvolle Unterstüzung während meiner Schul- und Studienzeit, ohne die es mir nicht möglich gewesen wäre, Physik zu studieren.

Simone, dir danke ich für deine volle Unterstützung zu jeder Zeit in den vergangenen Jahren. Deine Motivation, Zuspruch und der Rückhalt, den du mir gegeben hast, waren mir die größte Hilfe. Danke für unsere gemeinsame Zeit. Ich liebe dich.

Erklärung

Hiermit versichere ich, dass ich die Arbeit selbständig verfasst, Zitate kenntlich gemacht und keine anderen als die angegebenen Quellen und Hilfsmittel benutzt habe. Die Arbeit wurde bisher weder im Inland noch im Ausland in gleicher oder ähnlicher Form einer anderen Prüfungsbehörde vorgelegt. Die Arbeit wurde unter wissenschaftlicher Betreuung durch Herrn Prof. Dr. Hermann Nienhaus an der Fakultät für Physik der Universität Duisburg-Essen angefertigt.

Duisburg, 11. Juli 2014